

Copyright  
by  
Zachary John Liptak  
2014

The Dissertation Committee for Zachary John Liptak  
certifies that this is the approved version of the following dissertation:

**Search for Neutrinoless Double Beta Decay of  $^{116}\text{Cd}$  and  
 $^{82}\text{Se}$  and Calorimeter Simulations for the SuperNEMO  
Experiment**

Committee:

---

Karol Lang, Supervisor

---

Jack Ritchie

---

Roy Schwitters

---

Duane Dicus

---

Pawan Kumar

**Search for Neutrinoless Double Beta Decay of  $^{116}\text{Cd}$  and  
 $^{82}\text{Se}$  and Calorimeter Simulations for the SuperNEMO  
Experiment**

by

**Zachary John Liptak, B.S.; B.A.**

**DISSERTATION**

Presented to the Faculty of the Graduate School of  
The University of Texas at Austin  
in Partial Fulfillment  
of the Requirements  
for the Degree of

**DOCTOR OF PHILOSOPHY**

THE UNIVERSITY OF TEXAS AT AUSTIN

May 2014

Dedicated to Mina and Kenshin E.

## Acknowledgments

This dissertation owes a great deal to many people. First and foremost is my advisor, Karol Lang, whose experience with, understanding of, and enthusiasm for physics have proven a consistent guide in the development of my research. I am grateful for his guidance, which has countless times provided insights into and a deeper understanding of the physics at hand. I also thank R.B. Pahlka, who laid the groundwork for many of these studies and helped to develop my research skills; his help has many times proved to be an invaluable resource. I am also grateful to the entire NEMO-3/SuperNEMO collaboration, and for the opportunity to participate in collaboration meetings in France, the United Kingdom, Russia, the Czech Republic, and Slovakia, which was made possible by Karol, as was the opportunity to present a talk at the INFO13 workshop in Santa Fe, New Mexico. I would also like to thank my wife, Mina, whose patience and support greatly aided in the development of my work.

# Search for Neutrinoless Double Beta Decay of $^{116}\text{Cd}$ and $^{82}\text{Se}$ and Calorimeter Simulations for the SuperNEMO Experiment

Publication No. \_\_\_\_\_

Zachary John Liptak, Ph.D.  
The University of Texas at Austin, 2014

Supervisor: Karol Lang

Using the NEMO-3 detector, 410.4 g of  $^{116}\text{Cd}$  with a total exposure of 1.65 kg·y and 932 g of  $^{82}\text{Se}$  with a total exposure of 3.75 kg·y were used to measure the half-life of two-neutrino double beta decay ( $2\nu\beta\beta$ ) to the ground states of  $^{116}\text{Sn}$  and  $^{82}\text{Kr}$  and to place a lower limit on the neutrinoless double beta decay ( $0\nu\beta\beta$ ) to the same ground states. In the single-states dominance hypothesis, the  $2\nu\beta\beta$  half-lives are found to be  $T_{1/2}^{2\nu}(^{116}\text{Cd}) = (2.90 \pm 0.03^{stat} \pm 0.15^{syst}) \times 10^{19}$  yr and  $T_{1/2}^{2\nu}(^{82}\text{Se}) = (10.62 \pm 0.11^{stat} \pm 0.56^{syst}) \times 10^{19}$  yr.  $0\nu\beta\beta$  is excluded to 90% confidence level at  $T_{1/2}^{0\nu} \geq 1.12 \times 10^{23}$  yr for  $^{116}\text{Cd}$  and  $T_{1/2}^{0\nu} \geq 3.90 \times 10^{23}$  yr for  $^{82}\text{Se}$ , corresponding to effective Majorana neutrino masses of  $\langle m_\nu \rangle \leq (4.33 - 5.54)$  eV and  $\langle m_\nu \rangle \leq (2.28 - 2.82)$  eV, respectively, in the light Majorana exchange mechanism.

# Table of Contents

<b>Acknowledgments</b>	<b>v</b>
<b>Abstract</b>	<b>vi</b>
<b>List of Tables</b>	<b>xiii</b>
<b>List of Figures</b>	<b>xvi</b>
<b>Chapter 1. Introduction</b>	<b>1</b>
1.1 Neutrino Phenomenology . . . . .	2
1.1.1 A History of Neutrino Physics . . . . .	2
1.1.2 Neutrinos in the Standard Model . . . . .	3
1.1.3 Neutrino Oscillations . . . . .	4
1.2 Neutrino Mass . . . . .	5
1.2.1 Dirac Neutrinos . . . . .	5
1.3 Majorana neutrinos . . . . .	7
1.3.1 The Seesaw Mechanism . . . . .	8
1.4 Neutrino Mass Hierarchy . . . . .	9
<b>Chapter 2. Double Beta Decay</b>	<b>12</b>
2.1 Single Beta Decay . . . . .	12
2.1.1 Electron and Positron Emission . . . . .	13
2.2 Other Emissions . . . . .	14
2.2.1 Electron Capture . . . . .	14
2.2.2 Internal Conversion . . . . .	14
2.3 Double Beta Decay . . . . .	15
2.3.1 Two-Neutrino Double Beta Decay . . . . .	15
2.3.2 Neutrinoless Double Beta Decay . . . . .	17
2.3.3 Right-handed Current Mechanism . . . . .	18

2.3.4	Majoron Mechanisms . . . . .	19
2.4	Nuclear Matrix Elements . . . . .	20
2.4.1	Quasi-Random Phase Approximation . . . . .	24
2.4.2	Shell Model . . . . .	24
2.4.3	Hartree-Fock Method . . . . .	25
2.4.4	Interacting Boson Model . . . . .	25
2.4.5	NME Values . . . . .	25
2.5	Single and Higher States Dominance Hypotheses . . . . .	26
2.6	Previous Double Beta Experiments . . . . .	29
2.6.1	Semiconductor Experiments . . . . .	29
2.6.2	Scintillation Experiments . . . . .	31
2.6.3	Bolometer Experiments . . . . .	32
2.6.4	Time Projection Chamber Experiments . . . . .	33
2.6.5	Previous $^{116}\text{Cd}$ Results . . . . .	34
2.6.6	Previous $^{82}\text{Se}$ Results . . . . .	35
2.7	NEMO-3 . . . . .	36
<b>Chapter 3. The NEMO-3 Detector</b>		<b>37</b>
3.1	Detector Description . . . . .	38
3.2	Source Foils . . . . .	41
3.2.1	Choice of Isotopes . . . . .	42
3.2.2	Source Preparation . . . . .	43
3.2.3	$^{82}\text{Se}$ . . . . .	44
3.2.4	$^{116}\text{Cd}$ . . . . .	44
3.3	Tracking Chamber . . . . .	45
3.3.1	Elementary Geiger Cell . . . . .	46
3.4	Calorimeter . . . . .	47
3.4.1	Scintillator Characteristics . . . . .	48
3.4.2	Photomultiplier Tube Characteristics . . . . .	49
3.4.3	Light Guide Characteristics . . . . .	49
3.4.4	Coupling Between Scintillator and PMT . . . . .	49
3.4.5	Energy Calibration . . . . .	50
3.5	Laser Time Corrections . . . . .	52



<b>Chapter 4. NEMO-3 Analysis Strategy</b>	<b>59</b>
4.1 NEMO-3 Analysis Flow . . . . .	59
4.1.1 Event Generation and Reconstruction . . . . .	61
4.1.2 Topology Selection Requirements . . . . .	62
4.1.3 Analysis Requirements . . . . .	62
4.2 Scaling and Fitting . . . . .	63
4.3 Half-life Calculation . . . . .	64
4.4 Neutrinoless Double Beta Decay Limit Determination . . . . .	65
4.4.1 Neutrinoless Double Beta Decay Half-life Sensitivity . . . . .	66
4.4.2 Limit Calculation . . . . .	67
<b>Chapter 5. NEMO-3 backgrounds</b>	<b>69</b>
5.1 Background overview and measurements . . . . .	70
5.2 Internal backgrounds . . . . .	72
5.2.1 $^{116}\text{Cd}$ foil . . . . .	73
5.2.2 $^{82}\text{Se}$ foil . . . . .	75
5.3 External backgrounds . . . . .	77
5.3.1 Neutron flux . . . . .	78
5.4 Radon backgrounds . . . . .	79
5.4.1 Phase I . . . . .	81
5.4.2 Phase II . . . . .	83
<b>Chapter 6. Single Electron Background Measurements</b>	<b>85</b>
6.1 Single-Electron Selection Requirements . . . . .	86
6.1.1 Foil Vertex Requirements . . . . .	86
6.1.2 Tracking Requirements . . . . .	87
6.1.3 Calorimetry Requirements . . . . .	87
6.2 $^{116}\text{Cd}$ Foil Description . . . . .	88
6.2.1 Phase I . . . . .	91
6.2.2 Phase II . . . . .	94
6.3 $^{82}\text{Se}$ Foil Description . . . . .	97
6.4 $^{82}\text{Se}$ One-Electron Results . . . . .	97
6.4.1 Phase I . . . . .	97

6.4.2	Phase II . . . . .	101
6.5	Single-electron Measurement Summary . . . . .	103
<b>Chapter 7. Electron-<math>\gamma</math> Background Measurements</b>		<b>104</b>
7.1	Electron- $\gamma$ Selection Requirements . . . . .	104
7.1.1	Foil Vertex Cuts . . . . .	105
7.1.2	Tracking Cuts . . . . .	105
7.1.3	Calorimetry Cuts . . . . .	106
7.2	$^{116}\text{Cd}$ Electron- $\gamma$ Results . . . . .	107
7.2.1	Phase I . . . . .	107
7.2.2	Phase II . . . . .	112
7.3	$^{82}\text{Se}$ Electron- $\gamma$ Results . . . . .	117
7.3.1	Phase I . . . . .	117
7.3.2	Phase II . . . . .	118
7.4	Electron- $\gamma\gamma$ Channel . . . . .	123
7.4.1	$^{116}\text{Cd}$ Electron- $\gamma\gamma$ Results . . . . .	123
7.4.2	$^{82}\text{Se}$ Electron- $\gamma\gamma$ Results . . . . .	126
7.5	Electron- $\gamma$ Measurement Summary . . . . .	131
<b>Chapter 8. Two Electron Channel Analysis</b>		<b>132</b>
8.1	Two Electron Selection Requirements . . . . .	133
8.1.1	Vertex requirements . . . . .	133
8.1.2	Tracking requirements . . . . .	133
8.1.3	Calorimeter requirements . . . . .	134
8.2	Selection criteria optimization . . . . .	135
8.3	Systematic uncertainties . . . . .	136
8.4	Two-Electron Results . . . . .	138
8.4.1	$^{116}\text{Cd}$ Two-Electron Measurements . . . . .	138
8.5	SSD and HSD hypotheses . . . . .	146
8.5.1	$^{82}\text{Se}$ Two-Electron Measurements . . . . .	148
8.6	Summary and Conclusions . . . . .	153

<b>Chapter 9. Search for the Neutrinoless Transition</b>	<b>154</b>
9.1 Limit Calculation . . . . .	154
9.1.1 Selection Criteria and Data Set . . . . .	155
9.1.2 NEMO-3 Sensitivity . . . . .	155
9.1.3 Nuclear Matrix Elements and Phase-Space Values . . . . .	155
9.2 Neutrinoless Transition Search Results for $^{116}\text{Cd}$ . . . . .	156
9.2.1 Light Majorana Exchange Mechanism . . . . .	157
9.2.2 Signal Windows . . . . .	159
9.2.3 Effective neutrino Mass Calculation . . . . .	159
9.2.4 Right-Handed Currents . . . . .	160
9.2.5 Majoron-Emitting Models . . . . .	161
9.3 Neutrinoless Transition Search Results for $^{82}\text{Se}$ . . . . .	163
9.3.1 Light Majorana Exchange Mechanism . . . . .	163
9.3.2 Effective Neutrino Mass Calculation . . . . .	164
9.3.3 Right-Handed Currents . . . . .	164
9.3.4 Majoron-Emitting Models . . . . .	164
9.4 Discussion and Conclusions . . . . .	167
<b>Chapter 10. The SuperNEMO Detector</b>	<b>170</b>
10.1 Detector Description . . . . .	170
10.2 Source Material . . . . .	172
10.3 Tracker . . . . .	172
10.4 Calorimeter . . . . .	173
10.5 Radiopurity . . . . .	175
10.6 SuperNEMO versus NEMO-3 . . . . .	175
<b>Chapter 11. Simulations of SuperNEMO Scintillators</b>	<b>177</b>
11.1 Scintillator Types . . . . .	177
11.1.1 Photomultiplier Tubes . . . . .	178
11.2 Materials . . . . .	179
11.2.1 Material Properties . . . . .	180
11.2.2 Simulation Results . . . . .	180
11.3 Summary and Conclusion . . . . .	183

<b>Chapter 12. Conclusions and Outlook</b>	<b>185</b>
<b>Appendices</b>	<b>188</b>
<b>Appendix A. Scintillator details</b>	<b>189</b>
<b>Appendix B. Double beta decay candidate isotopes</b>	<b>192</b>
<b>Appendix C. Time-of-Flight Calculation Details</b>	<b>196</b>
<b>Appendix D. Neutrinoless Decay Kinetic Observables</b>	<b>199</b>
<b>Appendix E. Cut Optimization Details</b>	<b>206</b>
E.1 Cut Descriptions and Values . . . . .	207
<b>Appendix F. Details of the <math>^{207}\text{Bi}</math> Calibration Source</b>	<b>211</b>
<b>Appendix G. <math>^{214}\text{Bi}</math> and <math>^{208}\text{Tl}</math> decay information</b>	<b>215</b>
G.1 Introduction . . . . .	215
G.2 Decay of $^{214}\text{Bi}$ . . . . .	215
G.3 Decay of $^{208}\text{Tl}$ . . . . .	217
<b>Appendix H. Background Details</b>	<b>218</b>
H.1 $^{116}\text{Cd}$ . . . . .	218
H.1.1 Internal Backgrounds . . . . .	219
H.1.2 External Backgrounds . . . . .	220
H.1.3 Radon Backgrounds . . . . .	221
H.1.4 Backgrounds Listed by Number of Events . . . . .	222
H.2 $^{82}\text{Se}$ . . . . .	224
H.2.1 Internal Backgrounds . . . . .	224
H.2.2 External Backgrounds . . . . .	225
H.2.3 Radon Backgrounds . . . . .	226
<b>Bibliography</b>	<b>227</b>
<b>Vita</b>	<b>240</b>

## List of Tables

1.1	Summary of neutrino mixing matrix parameters. . . . .	6
3.1	Double beta decay isotopes used in the NEMO-3 detector, with Q-values and abundance. . . . .	53
3.2	Description of sector 6 in NEMO-3 (Se(I)) . . . . .	54
3.3	Description of sector 6 in NEMO-3 (Se(II)) . . . . .	55
3.4	Description of sector 8 strips in NEMO-3 containing selenium. Both Se(I) and Se(II) are present in strip 1 of sector 8. . . . .	56
3.5	Description of the $^{116}\text{Cd}$ foil (sector 18 in NEMO-3) . . . . .	57
3.6	Measured FWHM resolution at 1 MeV by block type . . . . .	58
5.2	Description of the radon background model distribution in NEMO-3. . . . .	83
5.1	Description of the external background model with accompanying Monte Carlo designation. . . . .	84
6.1	Summary of background isotopes measured in the single-electron channel for $^{116}\text{Cd}$ in Phase I. . . . .	91
6.2	Summary of background isotopes measured in the single-electron channel for the low-energy region. . . . .	94
6.3	Summary of background isotopes measured in the single-electron channel. . . . .	98
6.4	Summary of background isotopes measured in the single-electron channel. . . . .	101
7.1	Summary of measured background activities in the electron- $\gamma$ channel for Phase I. . . . .	108
7.2	Summary of measured background activities in the $^{116}\text{Cd}$ electron- $\gamma$ channel for Phase II. . . . .	112
7.3	Summary of measured background activities for $^{82}\text{Se}$ in the electron- $\gamma$ channel for Phase I. . . . .	117

7.4	Summary of measured background activities for $^{82}\text{Se}$ in the electron- $\gamma$ channel for Phase II. . . . .	118
8.1	Summary of systematic uncertainties for $^{116}\text{Cd}$ . . . . .	139
8.2	Summary of systematic uncertainties for $^{82}\text{Se}$ . . . . .	140
8.3	Summary of $^{116}\text{Cd}$ results for the combined data set. . . . .	145
8.4	$\chi^2$ results for SSD and HSD spectra for relevant observables. . . . .	146
8.5	Summary of $^{82}\text{Se}$ results for the combined data set. . . . .	151
9.1	Phase-space factor and nuclear matrix element values for $^{116}\text{Cd}$ . . . . .	156
9.2	Phase-space factor and nuclear matrix element values for $^{82}\text{Se}$ . . . . .	157
9.3	Results of calculating the $^{116}\text{Cd}$ $0\nu\beta\beta$ half life for various signal windows. . . . .	159
9.4	Summary of results for Majoron-emitting models in $^{116}\text{Cd}$ . . . . .	161
9.5	Summary of results for Majoron-emitting models in $^{82}\text{Se}$ . . . . .	165
9.6	Summary of effective neutrino masses by calculated nuclear matrix element for $^{116}\text{Cd}$ . . . . .	168
9.7	Summary of effective neutrino masses by calculated nuclear matrix element for $^{82}\text{Se}$ . . . . .	169
10.1	Comparison of NEMO-3 and SuperNEMO parameters. . . . .	176
11.1	Description of scintillator blocks in SuperNEMO. . . . .	179
11.2	Summary of SuperNEMO scintillator simulation results. . . . .	183
A.1	Mass fraction of scintillator materials by block type. . . . .	189
A.2	Vertical wall scintillator characteristics. . . . .	190
A.3	Petal scintillator characteristics. . . . .	191
B.1	Table of double beta decay isotopes, with $Q_{\beta\beta}$ values, isotopic abundance and phase space factors G for $2\nu\beta\beta$ and $0\nu\beta\beta$ processes. . . . .	192
B.1	Table of double beta decay isotopes, with $Q_{\beta\beta}$ values, isotopic abundance and phase space factors G for $2\nu\beta\beta$ and $0\nu\beta\beta$ processes. . . . .	193
B.1	Table of double beta decay isotopes, with $Q_{\beta\beta}$ values, isotopic abundance and phase space factors G for $2\nu\beta\beta$ and $0\nu\beta\beta$ processes. . . . .	194

B.1	Table of double beta decay isotopes, with $Q_{\beta\beta}$ values, isotopic abundance and phase space factors $G$ for $2\nu\beta\beta$ and $0\nu\beta\beta$ processes. . . . .	195
E.1	Optimization details for Minimum Single-electron Energy cuts. . . . .	208
E.2	Optimization details for internal time-of-flight cuts. . . . .	209
E.3	Optimization details for Minimum First Geiger Layer cuts. . . . .	210
E.4	Optimization details for charge cuts. . . . .	210
F.1	Summary of X-rays resulting from electron capture in the $^{207}\text{Bi} \rightarrow ^{207}\text{Pb}$ decay. . . . .	212
F.2	Binding energies for the K,L,M shell electrons of $^{207}\text{Pb}$ . . . . .	213
F.3	Summary of conversion electrons in $^{207}\text{Bi} \rightarrow ^{207}\text{Pb}$ decay. . . . .	213
H.1	Table of backgrounds present in the $^{116}\text{Cd}$ foils. . . . .	219
H.2	Summary of external BG model. 'modelf' refers to default value from recorded measurement. . . . .	220
H.3	Summary of Radon background model. . . . .	221
H.4	Summary of backgrounds by final number of expected events in $^{116}\text{Cd}$ for Phase I. . . . .	223
H.5	Summary of external BG model. 'modelf' refers to default value from recorded measurement. . . . .	225

## List of Figures

1.1	Illustration of the possible neutrino mass hierarchy cases assuming three neutrino flavors. The left figure describes the normal mass hierarchy, while the right describes the inverted mass hierarchy. . . . .	9
1.2	Mass hierarchy splitting in parameter space of minimum neutrino mass and effective neutrino mass. For certain values, a measurement or limit of sufficient sensitivity would be able to distinguish between the normal and inverted hierarchies. . .	11
2.2	Feynman diagram for $2\nu\beta\beta$ decay. . . . .	16
2.3	Feynman diagram for $0\nu\beta\beta$ decay. . . . .	17
2.4	Feynman diagram for $0\nu\beta\beta$ decay with Majoron emission. . .	20
2.1	Z versus M plot illustrating the split between even-even and odd-odd isobaric nuclei giving rise to double beta decay for mass numbers 116 and 82. . . . .	23
2.5	Comparison of $0\nu$ calculated nuclear matrix elements for a selection of $0\nu\beta\beta$ candidate isotopes using a variety of models. .	26
2.6	Calculated single-electron energy spectra for the SSD and HSD hypotheses in $^{116}\text{Cd}$ . . . . .	27
2.7	Level scheme for $^{116}\text{Cd}\rightarrow^{116}\text{Sn}$ decay showing the HSD and SSD contributions. . . . .	28
3.1	Cutaway of the NEMO-3 detector showing the tracking chamber, calorimeter, shielding, and support structure. . . . .	40
3.2	Distribution of isotopic source foils in NEMO-3 by sector. . . .	41
3.3	Spectrum of natural radioactivity, demonstrating the 2615 keV $\gamma$ line due to $^{208}\text{Tl}$ . . . . .	43
3.4	Detail of the Geiger cell and petal layout in the NEMO-3 tracking chamber. . . . .	45
3.5	Illustration of an elementary Geiger cell. . . . .	46
5.1	Decay chains of $^{238}\text{U}$ , $^{232}\text{Th}$ , and $^{235}\text{U}$ . . . . .	71



5.2	Diagram of major processes by which contamination in the isotopic source foil can mimic double-beta decay. . . . .	73
5.3	Spectra of backgrounds known to be present in the $^{116}\text{Cd}$ foils.	74
5.4	Spectrum of internal backgrounds in the $^{116}\text{Cd}$ sector of the source foil. . . . .	75
5.5	Spectra of backgrounds known to be present in the $^{82}\text{Se}$ foils. .	76
5.6	Diagram of major processes by which contamination in the detector volume can mimic double-beta decay. . . . .	78
5.7	Event displays of an external $\gamma$ ray Compton scattering in the foil and an external crossing electron. . . . .	79
5.8	Spectra of $^{214}\text{Bi}$ and $^{208}\text{Tl}$ combined energies for events mimicking two-electron decays. . . . .	80
5.9	Example of a $^{214}\text{Bi}$ - $^{210}\text{Po}$ event in NEMO-3, shown in a top-down event display. . . . .	81
5.10	Measured $^{222}\text{Rn}$ by run in Phases I and II of NEMO-3. . . . .	82
6.1	Positions of $^{116}\text{Cd}$ single-electron events on the source foil. . .	89
6.2	Vertex positions of single-electron events in the low- and medium-activity regions of the $^{116}\text{Cd}$ foil. . . . .	90
6.3	Electron energy spectrum for the low-activity Phase I data set.	92
6.4	Electron energy spectrum for the medium-activity Phase I data set. . . . .	93
6.5	Electron energy spectrum for the low-activity Phase II data set.	95
6.6	Electron energy spectrum for the medium-activity Phase II data set. . . . .	96
6.7	Single-electron event vertices projected onto the source foil in the $^{82}\text{Se}$ sectors before and after removing high-activity “hot spots”. . . . .	99
6.8	Electron energy spectrum for the $^{82}\text{Se}$ Phase I data set. . . . .	100
6.9	Electron energy spectrum for the $^{82}\text{Se}$ Phase II data set. . . . .	102
7.1	Combined electron- $\gamma$ energy for the Phase I low-activity region $^{116}\text{Cd}$ data set. . . . .	108
7.2	Electron (top) and $\gamma$ (bottom) energy for the Phase I low-activity region $^{116}\text{Cd}$ data set. . . . .	109
7.3	Electron (top) and $\gamma$ (bottom) energy for the Phase I medium-activity region $^{116}\text{Cd}$ data set. . . . .	110

7.4	Combined electron- $\gamma$ energy for the Phase I medium-activity region $^{116}\text{Cd}$ data set. . . . .	111
7.5	Electron energy for the Phase II low-activity region $^{116}\text{Cd}$ data set. . . . .	113
7.6	Combined electron- $\gamma$ energy for the Phase II low-activity region $^{116}\text{Cd}$ data set. . . . .	114
7.7	Electron energy for the Phase II medium-activity region $^{116}\text{Cd}$ data set. . . . .	115
7.8	Combined electron- $\gamma$ energy for the Phase II medium-activity region $^{116}\text{Cd}$ data set. . . . .	116
7.9	Electron and $\gamma$ energy for the Phase I $^{82}\text{Se}$ data set. . . . .	119
7.10	Combined electron- $\gamma$ energy for the Phase I $^{82}\text{Se}$ data set. . . . .	120
7.11	Electron and $\gamma$ energy for the Phase II $^{82}\text{Se}$ data set. . . . .	121
7.12	Combined electron- $\gamma$ energy for the Phase II $^{82}\text{Se}$ data set. . . . .	122
7.13	Electron and energy spectrum for the $e\gamma\gamma$ channel in $^{116}\text{Cd}$ . . . . .	124
7.14	Combined $\gamma$ energy spectra for the $e\gamma\gamma$ channel in $^{116}\text{Cd}$ . . . . .	125
7.15	$e\gamma\gamma$ channel electron energy distributions for the Se(I) sample. . . . .	127
7.16	$e\gamma\gamma$ channel electron energy distributions for the Se(I) sample. . . . .	128
7.17	$e\gamma\gamma$ channel electron energy distributions for the Se(II) sample. . . . .	129
7.18	$e\gamma\gamma$ channel electron energy distributions for the Se(II) sample. . . . .	130
8.1	Two-electron combined energy for the combined $^{116}\text{Cd}$ data set. . . . .	141
8.2	Energy of the lesser-energy electron for the combined $^{116}\text{Cd}$ data set. . . . .	142
8.3	Cosine between electron tracks and internal probability for the combined $^{116}\text{Cd}$ data set. . . . .	143
8.4	Vertex sector and Z position for the combined $^{116}\text{Cd}$ data set. . . . .	144
8.5	Total and minimum electron energies for fitted $^{116}\text{Cd}$ signal under the higher states dominance hypothesis. . . . .	147
8.6	Two-electron combined energy for the combined $^{82}\text{Se}$ data set. . . . .	148
8.7	Energy of the lesser- and greater-energy electrons for the combined $^{82}\text{Se}$ data set. . . . .	149
8.8	Cosine between electron tracks and internal probability for the combined $^{82}\text{Se}$ data set. . . . .	150
8.9	Vertex sector and Z position for the combined $^{82}\text{Se}$ data set. . . . .	152

9.1	$0\nu\beta\beta$ spectrum of $^{116}\text{Cd}$ excluded at 90% C.L. shown as an overlay on the total background. . . . .	158
9.2	Right-Handed Current (V + A) spectrum of $^{116}\text{Cd}$ excluded at 90% C.L. shown in red as an overlay on the total background. . . . .	160
9.3	Spectra of Majoron-emitting modes in $^{116}\text{Cd}$ . . . . .	162
9.4	$0\nu\beta\beta$ spectrum of $^{82}\text{Se}$ excluded at 90% C.L. shown as an overlay on the total background. . . . .	163
9.5	Right-handed current (V + A) spectrum of $^{82}\text{Se}$ excluded at 90% C.L. shown as an overlay on the total background. . . . .	165
9.6	Majoron-emitting model spectra for $^{82}\text{Se}$ . . . . .	166
10.1	Exploded view of the SuperNEMO detector. . . . .	171
10.2	Predicted SuperNEMO half-life sensitivity as a function of calorimeter resolution at 1 MeV. . . . .	173
10.3	Exploded view of a main wall optical module in SuperNEMO. . . . .	174
11.1	Simulated energy resolution for a main wall block to be used in SuperNEMO. . . . .	181
11.2	Simulated energy resolution for an X and V-wall block to be used in SuperNEMO. . . . .	182
D.1	Total electron energy distributions for Light Majorana Exchange, Right Handed Current, and Majoron-emitting $0\nu\beta\beta$ models. . . . .	200
D.2	Individual electron energy distributions for Light Majorana Exchange, Right Handed Current, and Majoron-emitting $0\nu\beta\beta$ models. . . . .	201
D.3	Maximum electron energy distributions for Light Majorana Exchange, Right Handed Current, and Majoron-emitting $0\nu\beta\beta$ models. . . . .	202
D.4	Minimum electron energy distributions for Light Majorana Exchange, Right Handed Current, and Majoron-emitting $0\nu\beta\beta$ models. . . . .	203
D.5	Maximum vs. Minimum electron energy distributions for Light Majorana Exchange, Right Handed Current, and Majoron-emitting $0\nu\beta\beta$ models. . . . .	204
D.6	Cosine between electron tracks distributions for Light Majorana Exchange, Right Handed Current, and Majoron-emitting $0\nu\beta\beta$ models. . . . .	205

F.1	Decay scheme of $^{207}\text{Bi}$ . . . . .	214
G.1	$^{214}\text{Bi}$ decays contributing background to the $\beta\beta$ spectrum. . .	216
G.2	Three most common decays of $^{208}\text{Tl}$ contributing background to the $\beta\beta$ spectrum. . . . .	217

# Chapter 1

## Introduction

The development of the Standard Model (SM) of particle physics has provided the most complete description of fundamental physics to date. However, the observation of neutrino oscillations proves that neutrinos possess a nonzero mass [1], providing a first confirmation of physics beyond the Standard Model. Some fundamental questions regarding neutrino properties remain unanswered, however, including the absolute mass, mass hierarchy, and the nature of neutrinos as Dirac or Majorana particles. Observation of neutrinoless double beta decay ( $0\nu\beta\beta$ ) would provide both direct confirmation of neutrinos as Majorana particles as well as a direct measurement of effective neutrino mass, in addition to aiding in the determination of the mass hierarchy.

Because  $0\nu\beta\beta$  decay is to date the only avenue for direct measurement of neutrino mass, a great effort has been made in the search for a signal, utilizing a wide range of technologies.

In the effort to answer these questions, the NEMO-3 experiment utilized seven isotopes in the measurement of two-neutrino double beta decay ( $2\nu\beta\beta$ ) and the search for  $0\nu\beta\beta$  with a half-life sensitivity of  $10^{25}$  years, corresponding to an effective neutrino mass at the level of 0.1 eV. NEMO-3 utilized

a setup unique among  $0\nu\beta\beta$  detectors, allowing for measurement of a suite of observables and discrimination between signal and background contamination.

This dissertation is concerned with the measurement of  $2\nu\beta\beta$  decays of  $^{116}\text{Cd}$  to the ground state of  $^{116}\text{Sn}$  and of  $^{82}\text{Se}$  to the ground state of  $^{82}\text{Kr}$ . Chapter 2 describes beta-decay phenomena, including a theoretical description of  $2\nu\beta\beta$  and several  $0\nu\beta\beta$  models. Chapter 3 details the NEMO-3 detector setup and operation. Chapter 4 presents the analysis strategy and framework for NEMO-3 data, including Monte Carlo methods and calculation of half-life limits. Chapter 5 describes the NEMO-3 background model and its measurement. Chapters 6 and 7 provide measurements of the backgrounds in the  $^{116}\text{Cd}$  and  $^{82}\text{Se}$  sectors *in situ* using NEMO-3 data. Chapter 8 presents measurements of  $2\nu\beta\beta$  decays for  $^{116}\text{Cd}$  and  $^{82}\text{Se}$ , and chapter 9 shows the limit calculations for  $0\nu\beta\beta$  models in both isotopes. Chapter 10 discusses the upcoming SuperNEMO detector and Chapter 11 gives the results simulations done for research and development of its calorimeter.

## 1.1 Neutrino Phenomenology

### 1.1.1 A History of Neutrino Physics

After the discovery of  $\beta$  decay, the reaction was believed to be of the form

$$(A \rightarrow B + e^-) \tag{1.1}$$

where a and B are the parent and daughter nuclei, respectively. However, in 1914 the spectrum of electron energy was shown by Chadwick to be continuous

via the application of a magnetic field [2], an apparent violation of energy conservation. In 1930 Wolfgang Pauli proposed a resolution in the form of a then-unknown chargeless particle which could carry away energy undetected. In 1933 Enrico Fermi developed a theory of  $\beta$  decay incorporating this particle, now dubbed a neutrino, in a reaction of the form [3]

$$(A \rightarrow B + e^- + \nu) \tag{1.2}$$

The first observation of neutrinos by Frederick Reines and Clyde Cowan occurred in 1956 using a large liquid scintillation experiment to detect electron antineutrinos from the Savannah River nuclear reactor [4, 5]. The existence of an additional flavor of neutrino was confirmed in 1962 with the observation of  $\mu$  antineutrinos by Leon Lederman, Melvin Schwartz, and Jack Streinberger [6]. Following the discovery of the  $\tau$  in 1975, the  $\tau$  neutrino was observed in 2000 by the DONUT experiment [7].

### 1.1.2 Neutrinos in the Standard Model

The Standard Model (SM) of particle physics refers to the  $SU(3) \times SU(2) \times U(1)$  gauge theory describing the interactions of the strong, weak, and electromagnetic forces [8]. The SM is built upon the theoretical description of the weak interaction by Weinberg, Glashow, and Salam [9, 10, 11, 12] and has succeeded in describing a wide variety of physical phenomena.

Within the SM framework, each lepton pair is a left-handed  $SU(2)$  doublet containing a charged particle (electron, muon, or tau) and an associated (massless) neutrino. an  $SU(2)$  singlet describes right-handed charged

particles, but right-handed neutrinos are absent. The observation of neutrino oscillations, and thus massive neutrinos [1], offered the first evidence of physics beyond the SM, indicating that a modification to the theory is necessary.

### 1.1.3 Neutrino Oscillations

In 1968, Raymond Davis, Don Harmer, and Kenneth Hoffman observed a deficit of neutrinos with respect to the expectation from theoretical calculations [13, 14]. The discrepancy was eventually resolved using a theory originally proposed by Pontecorvo [15, 16], and later elaborated upon by Maki, Nakagawa, and Sakata in 1962 [17], in which massive neutrinos can oscillate between flavor states. In a manner analogous to CKM quark mixing [18, 19], the mass eigenstates  $(\nu_1, \nu_2, \nu_3)$  and flavor eigenstates  $(\nu_e, \nu_\mu, \nu_\tau)$  can be related to one another by a unitary matrix U:

$$|\nu_\alpha\rangle = \sum_{i=1}^3 U_{\alpha i} |\nu_i\rangle \quad (1.3)$$

where  $i$  spans three mass eigenstates and  $\alpha$  spans the three flavor eigenstates. The mixing matrix U is parametrized as the Pontecorvo-Maki-Nakagawa-Sakata (PMNS) matrix:

$$U = \begin{pmatrix} c_{12}c_{13} & s_{12}c_{13} & s_{13}e^{i\delta} \\ -s_{12}c_{23} - c_{12}s_{23}s_{13}e^{i\delta} & c_{12}c_{23} - s_{12}s_{23}s_{13}e^{i\delta} & s_{23}c_{13} \\ s_{12}s_{23} - c_{12}c_{23}s_{13}e^{i\delta} & -c_{12}s_{23} - s_{12}c_{23}s_{13}e^{i\delta} & c_{23}c_{13} \end{pmatrix} \cdot D_M \quad (1.4)$$

where  $c_{ij}$  and  $s_{ij}$  correspond to  $\cos(\theta_{ij})$  and  $\sin(\theta_{ij})$ , respectively,  $\delta$  is the Dirac CP violating phase and  $D_M$  is the Majorana phase matrix

$$D_M = \begin{pmatrix} 1 & 0 & 0 \\ 0 & e^{i\phi_2} & 0 \\ 0 & 0 & e^{i\phi_3} \end{pmatrix} \quad (1.5)$$



where  $\phi_i$  are Majorana CP violating phases. Such phases appear only in processes which violate lepton number conservation.

In the case of two-neutrino oscillation in a vacuum, the probability that a neutrino initially in flavor eigenstate  $\alpha$  with energy  $E$  will oscillate to flavor state  $\beta$  after length  $L$  is given by

$$P(\nu_\alpha \rightarrow \nu_\beta) = \sin^2(2\theta_{ij})\sin^2\left(\frac{1.27\Delta m_{ij}^2 L}{E}\right) \quad (1.6)$$

with  $(\Delta m_{ij})^2$  equal to the difference of squared mass eigenstates  $i$  and  $j$ , and the mixing angles  $\theta_{ij}$  obtained experimentally. Oscillation parameters are typically described in terms of the neutrino source: solar, atmospheric, accelerator, or reactor.

Current best parameters for neutrino mixing and mass-squared splitting are shown in table 1.1.

## 1.2 Neutrino Mass

The observation of neutrino oscillations strongly implies that at least one neutrino has a nonzero mass. Although predicted by the SM to be massless, neutrino masses can be constructed via the inclusion of Dirac or Majorana mass terms in the electroweak Lagrangian.

### 1.2.1 Dirac Neutrinos

Following the standard model construction, a Dirac neutrino mass term requiring four independent components  $\nu_L, \nu_R, \bar{\nu}_L, \bar{\nu}_R$  can be constructed. Us-

Parameter	Value	Neutrino Type	Experiment	Reference
$\sin^2(\theta_{12})$	$0.312^{+0.017}_{-0.015}$	solar + reactor	SNO, KamLAND	[20, 21]
$\sin^2(\theta_{23})$	$0.52 \pm 0.06$	atm., accel.	Super-K, MINOS	[22, 23]
$\sin^2(2\theta_{13})$	$0.089 \pm 0.01 \pm 0.005$	reactor	Daya Bay	[24]
$\Delta m_{21}^2$	$7.59 \pm 0.21 \times 10^{-5} \text{ eV}^2$	solar + reactor	SNO, KamLAND	[20, 21]
$ \Delta m_{23}^2 $	$2.41 \times 10^{-3} \text{ eV}^2$	atm.	MINOS, T2K	[22, 23]

Table 1.1: Summary of neutrino mixing matrix parameters.

ing the Dirac equation for massive fermions, with chirality eigenstates  $\psi_R, \psi_L$  coupled and forming a four-component object of mass  $m$  [25]:

$$i(\hat{\sigma}^\mu \partial_\mu)\psi_R - m\psi_L = 0, \quad i(\sigma^\mu \partial_\mu)\psi_L - m\psi_R = 0 \quad (1.7)$$

where  $\hat{\sigma}^\mu = (\sigma^0, \vec{\sigma}^\mu)$  and  $\sigma^\mu = (\sigma^0, -\vec{\sigma}^\mu)$  and  $\psi_{L(R)}$  are 2-component spinors.

These are related via the four-component bispinors

$$\Psi = \begin{pmatrix} \psi_R \\ \psi_L \end{pmatrix}, \quad \Psi_R = \begin{pmatrix} \psi_R \\ 0 \end{pmatrix}, \quad \Psi_L = \begin{pmatrix} 0 \\ \psi_L \end{pmatrix} \quad (1.8)$$

If one defines a left (right) handed projection operator  $P_{L(R)}$ ,

$$P_{L(R)} = \frac{1}{2}(1 \mp \gamma^5) \quad (1.9)$$

then the chiral projections of  $\Psi$ ,  $\Psi_{L(R)}$  are eigenstates of  $P_{L(R)}$ .

Using  $\nu_L + \nu_R$ , defined as

$$\nu_R = \begin{pmatrix} \nu_{e_R} \\ \nu_{\mu_R} \\ \nu_{\tau_R} \end{pmatrix} \quad \nu_L = \begin{pmatrix} \nu_{e_L} \\ \nu_{\mu_L} \\ \nu_{\tau_L} \end{pmatrix} \quad (1.10)$$

the mass term in the neutrino Lagrangian for a Dirac neutrino becomes

$$\mathcal{L}^D = \bar{\nu}_R M^D \nu_L + h.c. \quad (1.11)$$

where  $M^D$  is a complex non-diagonal  $3 \times 3$  matrix and  $\nu_L \neq \nu_R$ .

This Lagrangian is gauge invariant, implying that lepton number is conserved, and leads to a small coupling to the Higgs field consistent with charged leptons; small neutrino masses with respect to other leptons, however, are unaccounted for. In addition, the Dirac formulation of neutrino mass requires right-handed fields which do not occur in the SM, and therefore these right-handed neutrinos are sterile [26].

### 1.3 Majorana neutrinos

In contrast to the Dirac case, massive fermions without conserved quantum numbers may be written as  $\psi_R$  with mass  $m$  or  $\psi_L$  with mass  $m'$ , obeying independent equations [25]:

$$i(\hat{\sigma}^\mu \partial_\mu) \psi_R - m \epsilon \psi_L^* = 0, \quad i(\sigma^\mu \partial_\mu) \psi_L + m' \epsilon \psi_R^* = 0 \quad (1.12)$$

where  $\epsilon \equiv i\sigma_y$ . Expressed in the four-component form, the Majorana fields are

$$\Psi_L(x) = \begin{pmatrix} -\epsilon \psi_L^*(x) \\ \psi_L(x) \end{pmatrix}, \quad \Psi_R(x) = \begin{pmatrix} \psi_R(x) \\ \epsilon \psi_R^*(x) \end{pmatrix} \quad (1.13)$$

which are self-conjugate under the charge conjugation operator  $i\gamma^2\gamma^0$ .

The left-handed Majorana mass term can then be written [27]:

$$\mathcal{L}^M = -\frac{1}{2}\bar{\nu}_L^c M_{M_L} \nu_L + h.c. \quad (1.14)$$

where  $\nu^c$  denotes a charge conjugate. Similarly, the right-handed mass term can be written

$$\mathcal{L}^M = -\frac{1}{2}\bar{\nu}_R^c M_{M_R} \nu_R + h.c. \quad (1.15)$$

In both cases, the mass term can be constructed entirely from one two-component field  $\Psi_{L(R)}$ , removing the need for sterile neutrinos. Consequently, in the Majorana case neutrinos and antineutrinos are identical ( $\nu = \bar{\nu}$ ). Because neutrinos are the only neutral SM leptons, they are the only particles for which Majorana mass terms can be written.

### 1.3.1 The Seesaw Mechanism

The most general extension of the SM to include massive neutrinos is by the addition of the Lagrangians listed in the preceding sections. Additionally, any theory of massive neutrinos must account for the disparity between neutrino masses ( $<1$  eV) and all other leptons (511 keV and above). The most common mechanism considered involves assumes a mass matrix of the form [28, 29]

$$M = \begin{pmatrix} 0 & m_D \\ m_D & m_R \end{pmatrix} \quad (1.16)$$

Diagonalizing this matrix yields

$$M \approx \begin{pmatrix} (m_D^2/m_R) & 0 \\ 0 & m_R + (m_D^2/m_R) \end{pmatrix} \quad (1.17)$$

A Majorana neutrino is considered to consist of the eigenvalues  $m_1 = m_D^2/m_R$  and  $m_2 = m_R$ , where  $m_D$  is taken at the scale of other SM fermions. The seesaw mechanism arises from the dependence of  $m_1$  on  $m_2$ ; as  $m_2$  grows,  $m_1$ , the left-handed Majorana neutrino, is correspondingly suppressed. The large mass of the right-handed counterpart renders it unobservably large, often considered on the order of GUT scales ( $10^{15}$  GeV) and at least  $10^3 - 10^9$  GeV for a 1 eV neutrino.

## 1.4 Neutrino Mass Hierarchy

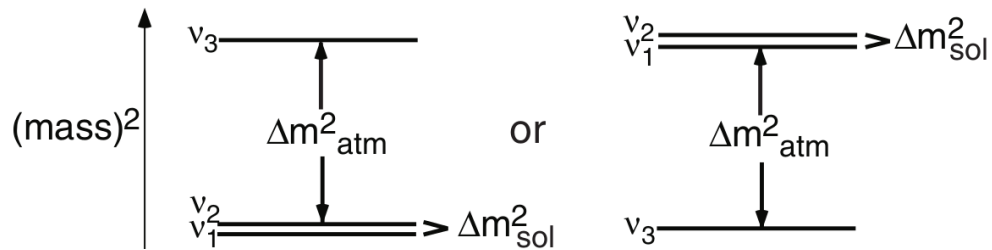


Figure 1.1: Illustration of the possible neutrino mass hierarchy cases assuming three neutrino flavors. The left figure describes the normal mass hierarchy, while the right describes the inverted mass hierarchy [30].

The question of the neutrino mass hierarchy remains an important unresolved question in neutrino physics. Oscillation data provides mass-squared splitting as described previously, but thus far the absolute scale of neutrino masses has yet to be determined.

In addition, assuming there are no as-yet unknown neutrino flavors, the measured mass-squared differences give rise to two possibilities for a mass hierarchy:

- The normal hierarchy:  $\nu_1 < \nu_2 < \nu_3$
- The inverted hierarchy:  $\nu_3 < \nu_1 < \nu_2$

Figure 1.1 shows a representation of the two possible cases [30]. A measurement of effective neutrino mass would provide an estimate as to the absolute scale of neutrino masses. Furthermore, an effective mass measurement may be used to distinguish between the two hierarchies, as shown in Figure 1.2.

Because the effective neutrino mass is inversely proportional to the neutrinoless double beta transition half-life, measurements or lower limits of neutrinoless half-lives can be used to constrain the available parameter space on the Y axis in the figure. A full discussion of limits in this parameter space is contained in reference [31].

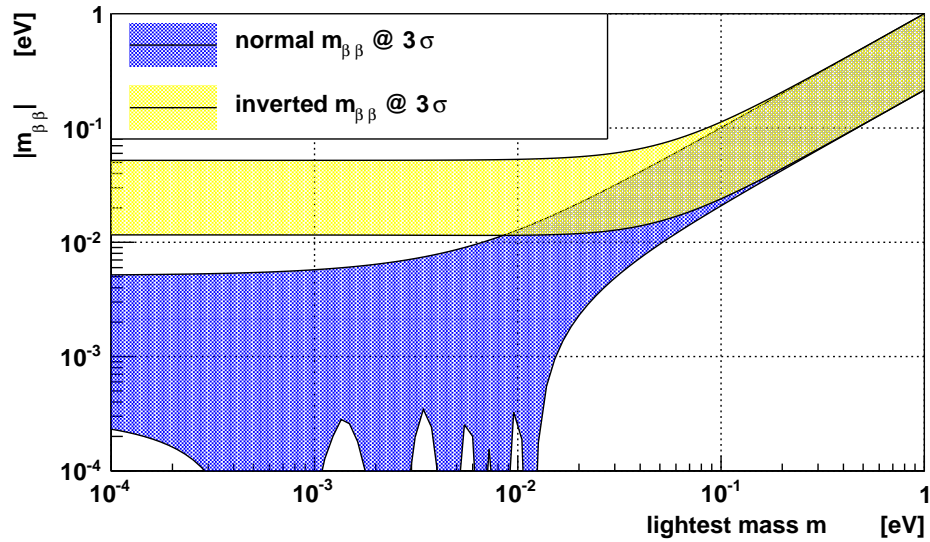
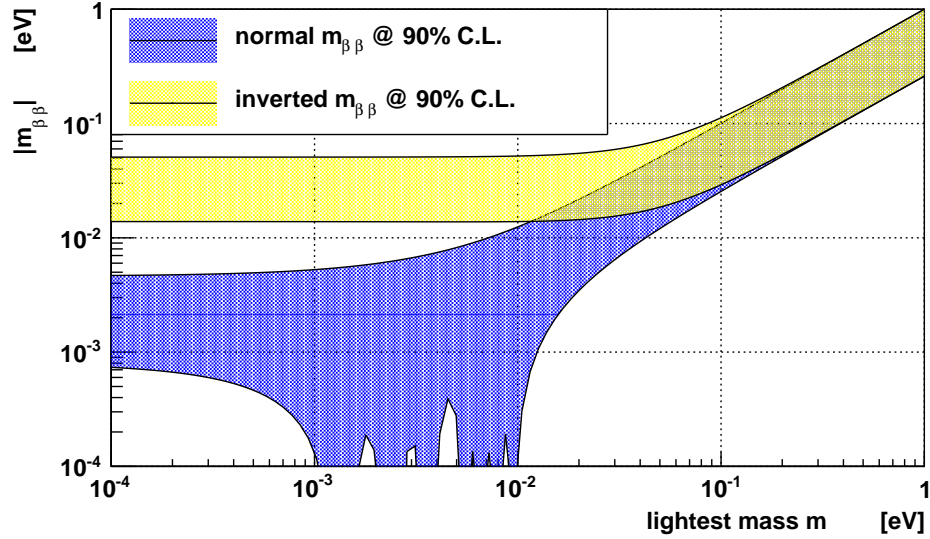


Figure 1.2: Mass hierarchy splitting in parameter space of minimum neutrino mass and effective neutrino mass. For certain values, a measurement or limit of sufficient sensitivity would be able to distinguish between the normal and inverted hierarchies. Parameters are shown at 90% (top) and  $3\sigma$  (99%) (bottom) confidence levels.

# Chapter 2

## Double Beta Decay

To provide a background to neutrinoless double beta decay, this chapter describes the mechanics of several types of well-known  $\beta$ -radiation before moving on to a discussion of two-neutrino double- $\beta$  ( $2\nu\beta\beta$ ) decay. Neutrinoless double-beta ( $0\nu\beta\beta$ ) decay in the Light Majorana Exchange framework is introduced, followed by a discussion of right-handed currents and Majoron-emitting  $0\nu\beta\beta$  models. The single-states dominance and higher-states dominance hypotheses are also discussed, and results from previous double beta measurements are presented.

### 2.1 Single Beta Decay

Beta emission describes a type of radioactive decay mediated by the weak force and resulting in the change of the atomic number by one unit. Three forms of  $\beta$  decay are possible:  $\beta^-$  emission,  $\beta^+$  emission, and electron capture. In addition,  $\beta$  decays can be categorized by the difference between initial and final nuclear total angular momentum  $J$  and the overall emitted lepton spin state [32, 33]. Transitions in which the electron and antineutrino have antiparallel spins in a relative singlet state are known as Fermi transitions, while



those in which the electron and neutrino have parallel spins in a triplet state are known as Gamow-Teller transitions.

### 2.1.1 Electron and Positron Emission

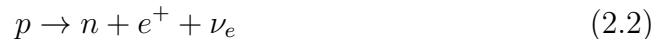
Beta emission is the process by which a parent nucleus transitions to a more stable daughter via emission of an electron or a positron and mediated by a  $W^\pm$  boson. In addition, lepton number is conserved by emission of an electron antineutrino for electron-emitting nuclei and an electron neutrino for positron-emitting nuclei.

Nuclei with excess neutrons decay via conversion of a neutron to a proton, with the emission of the associated leptons:



Consequently, the atomic number  $Z$  of the nucleus is increased by one, while its overall number of nucleons remains constant.

Nuclei with an excess of protons decay in an analogous manner, with a proton decaying to a neutron:



Positron emission requires that the daughter nucleus has a greater binding energy than the parent, as energy must be extracted from the parent nucleus to make up the difference between the neutron and positron mass. In this case,  $Z$  is decreased by one, while again the overall number of nucleons is unchanged.

## 2.2 Other Emissions

### 2.2.1 Electron Capture

In contrast to direct emission of  $\beta$  particles, a third process known as electron capture (EC) exists in which only a neutrino is emitted. In this case low-lying atomic electrons are absorbed directly into the nucleus with the emission of a monoenergetic neutrino. The vacant K-shell (or less frequently, L- or M-shell) is filled in by a higher-level electron, with corresponding release of an X-ray or Auger electron [34]. Alternately, this process may be known as K-capture, as in most cases the captured electron comes from the K shell.

### 2.2.2 Internal Conversion

While not a  $\beta$  decay, a further process allowing for the release of an electron known as internal conversion is possible. In this case, excitation energy of the nucleus is transmitted directly to an inner shell electron, which is released from the atom with kinetic energy  $h\nu - B$ , where  $h\nu$  is the de-excitation energy and  $B$  is the binding energy of the electron, given by

$$\frac{Z^2 \times 13.6 \text{ eV}}{n^2} \tag{2.3}$$

for an electron in level  $n$ . As in the case of EC, the vacated electron state is filled in by a higher-level electron, accompanied with the emission of an X-ray or Auger electron.  $A$  and  $Z$  both remain constant in IC, and the process is entirely electromagnetic and thus competes with  $\gamma$  emission in nuclear de-excitation. Because no neutrinos are involved in the decay, ejected electrons carry discrete energy values [34].

## 2.3 Double Beta Decay

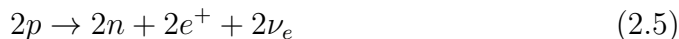
In certain cases for nuclei with an even number of protons and neutrons, there is a chance for a decay to a daughter of  $Z \pm 2$  via double  $\beta$  decay, a process which can be considered as two simultaneous  $\beta$  decays. If the masses of isotopes around a given atomic number  $Z_0$  are plotted with respect to mass, a parabola is formed; in the case of odd-odd and even-even nuclei, a nuclear pairing energy term causes a splitting into two parabolæ, as shown in Figure 2.1. In such cases, for even-even isotopes (i.e., isotopes on the bottom parabola)  $\beta$  decay is energetically unfavorable, but decays to next-nearest-neighbor isotopes are possible. Because all even-even isotopes have a ground state of spin 0 and positive parity, double  $\beta$  decay ground state transitions are all  $(0^+ \rightarrow 0^+)$  transitions and thus a necessary requirement for double  $\beta$  decay is that  $m(Z,A) > m(Z+2,A)$ . Because double  $\beta$  decay is a higher-order process with a significantly longer half-life than  $\beta$  decay, a *de facto* requirement is also that  $\beta$  decay is either forbidden or strongly suppressed. [30]

### 2.3.1 Two-Neutrino Double Beta Decay

As was the case with  $\beta$  decay as discussed in the previous section, double  $\beta$  decay also proceeds via three processes:  $\beta^-\beta^-$ ,  $\beta^+\beta^+$ , and double electron capture.  $\beta^-\beta^-$  emitters decay as [30]



while  $\beta^+\beta^+$  decay as



and double EC proceeds as

$$2p + 2e^- \rightarrow 2n + 2\bar{\nu}_e \quad (2.6)$$

A Feynman diagram for the  $2\nu\beta\beta$  decay of a double electron emitting nucleus is shown in Figure 2.2. The half-life for this process can be represented by

$$[T_{1/2}^{2\nu}]^{-1} = G^{2\nu} |M^{2\nu}|^2 \quad (2.7)$$

where  $G^{2\nu}$  is an exactly-calculable phase space factor and  $M^{2\nu}$  is the  $2\nu\beta\beta$  nuclear matrix element given by [35]

$$M^{2\nu} = \sum_i \frac{\langle GD(J) | \vec{\sigma}t^- | 1_i^+ \rangle \langle 1_i^+ | \vec{\sigma}t^- | P \rangle}{\Delta E_i} \quad (2.8)$$

for parent nucleus P and final granddaughter nucleus GD with J=1, 2, or 3. See section 2.4 for further discussion of nuclear matrix elements.

There are 35 known  $2\nu\beta^-\beta^-$  and 6 known  $2\nu\beta^+\beta^+$  emitting isotopes. a summary of these isotopes and their phase space values is given in table B.1.

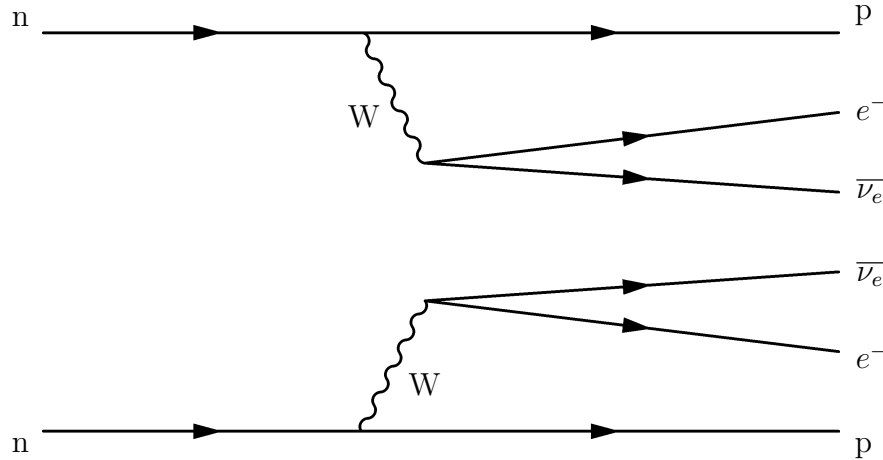


Figure 2.2: Feynman diagram for  $2\nu\beta\beta$  decay.

### 2.3.2 Neutrinoless Double Beta Decay

In a case analogous to  $2\nu\beta\beta$  decay, neutrinoless double  $\beta$  decay ( $0\nu\beta\beta$ ) is two-electron emission process changing the atomic number  $Z$  of the parent nucleus by two. In this case, however, no neutrinos are emitted:



In the most commonly discussed model of  $0\nu\beta\beta$ , known as the  $V - A$  Light Majorana Exchange, the process is mediated by the emission of one left-handed virtual neutrino which undergoes a chirality flip and is absorbed as a right-handed neutrino [36].

As a consequence, lepton number is violated by two units, requiring that neutrinos be Majorana particles, as discussed in section 1.3.  $0\nu\beta\beta$  decay is therefore forbidden by the standard model, and its observation would be a major probe into physics beyond the standard model. a Feynman diagram of  $0\nu\beta\beta$  mediated by Light Majorana Exchange is shown in Figure 2.3.

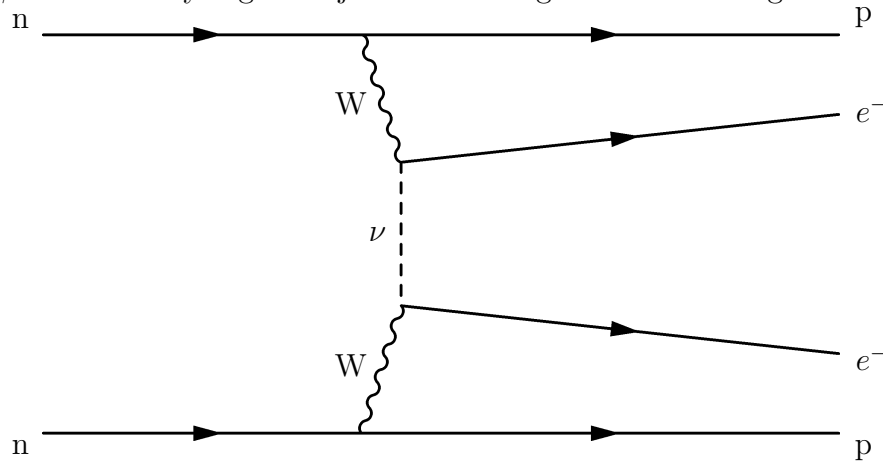


Figure 2.3: Feynman diagram for  $0\nu\beta\beta$  decay.

The half-life for this process is given by [30]:

$$(T_{1/2}^{0\nu})^{-1} = G^{0\nu} |M^{0\nu}|^2 \left(\frac{\langle m_{\nu_e} \rangle}{m_e}\right)^2 \quad (2.10)$$

As was the case in the  $2\nu\beta\beta$  case,  $G^{0\nu}$  is a calculable phase-space element and  $M^{0\nu}$  is a nuclear matrix element which will be discussed in section 2.4.

### 2.3.3 Right-handed Current Mechanism

An alternative formulation of double beta decay posits that neutrinos can couple to right-handed lepton currents, an interaction absent from the SM. From this possibility arise three dimensionless parameters describing new couplings [28, 36]:

- $\lambda$ : coupling between right-handed lepton current and right-handed quark current;
- $\eta$ : coupling between right-handed lepton current and left-handed quark current;
- $\kappa$ : coupling between left-handed lepton current and right-handed quark currents.

In this model, the neutrino can couple directly to either emitted W in the double beta decay process and requires no helicity flip. However, such couplings are generally negligibly small and only visible in the event that other mechanisms are either forbidden or vanishingly small.

The NEMO-3 detector considers the case of only a nonzero  $\lambda$  parameter, for which the double-beta decay half-life is given by

$$(T_{1/2}^{0\nu})^{-1} = G^{0\nu\lambda} |M^{0\nu\lambda}|^2 \langle \lambda \rangle^2 \quad (2.11)$$

where  $G^{0\nu\lambda}$  and  $M^{0\nu\lambda}$  are the right-handed current specific phase-space factor and NME, respectively.

### 2.3.4 Majoron Mechanisms

There also exist several models in which global baryon-lepton symmetry is spontaneously broken and a boson which couples to the neutrino is emitted. In general, such models proceed as

$$2n \rightarrow 2p + 2e^- + \xi\chi^0, \quad \xi = (1, 2) \quad (2.12)$$

with  $\chi^0$  denoting the emitted boson, known as a Majoron. Majorons are generally predicted to be light or massless, and may potentially be Goldstone bosons. Majoron mechanisms which conserve and violate lepton number both exist, and both scalar- and fermion-mediated mechanisms exist as well [37, 36].

Models are denoted by a spectral index  $n$ , with the cases considered in NEMO-3 as follows:

- $n = 1$ : single Majoron emission [38];
- $n = 2$ : bulk Majoron emission in a supersymmetric framework [39];
- $n = 3$ : emission of two massless Majorons [40, 41];

- $n = 7$ : emission of two light Majorons [40].

The phase space factor  $G^{0\nu\chi^0}$  for Majoron-emitting processes depends on the spectral index  $n$  and is proportional to  $(Q_{\beta\beta} - E_{sum})^n$ , the difference between the Q-value for the decay and the summed electron kinetic energies.

A Feynman diagram describing a general Majoron mechanism decay is shown in Figure 2.4.

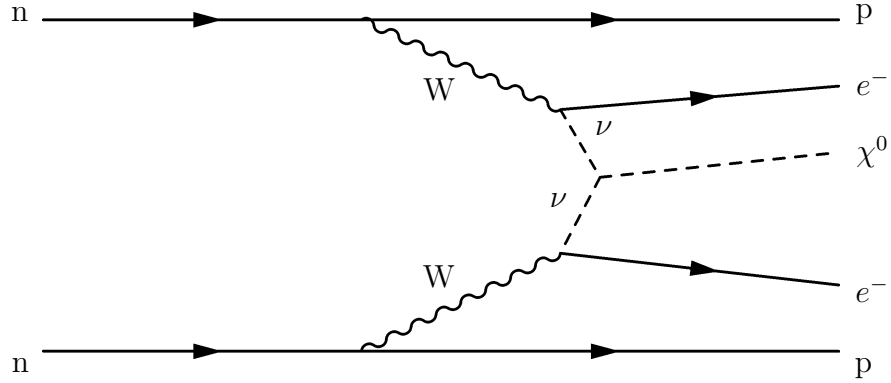


Figure 2.4: Feynman diagram for  $0\nu\beta\beta$  decay with Majoron emission.

Half-lives for Majoron-emitting  $0\nu\beta\beta$  decay are given as

$$T_{1/2}^{0\nu\chi^0} = G^{0\nu\chi^0} |M^{0\nu\chi^0}|^2 \langle g_{\chi^0} \rangle^2 \quad (2.13)$$

given a Majoron-neutrino coupling constant  $g_{\chi^0}$ .

## 2.4 Nuclear Matrix Elements

The accurate calculation of the  $0\nu\beta\beta$  nuclear matrix element  $M^{0\nu}$  is a crucial component in relating the measured  $0\nu\beta\beta$  half-life to the effective



neutrino mass. To begin consideration of this matrix element, one can consider first the individual  $\beta$ -decay transition element before moving to the  $\beta\beta$  cases.

Weak interaction decays proceed in the (V - A) theory via two components [33, 42] a polar vector term with coupling constant  $G_V$  and an axial-vector term  $G_A$ . The operator for  $\beta^\pm$  decay then has the form

$$\mathbf{O}_{\lambda\mu}(\beta^\pm) = G_V \sum_{j=1}^A \boldsymbol{\tau}_\mp(j) + G_A \sum_{j=1}^A \boldsymbol{\sigma}(j) \boldsymbol{\tau}_\mp(j) \quad (2.14)$$

where  $\boldsymbol{\tau}_\mp$  is the isospin raising/lowering operator, giving the nuclear matrix element the form

$$\langle P|H'|D\rangle \approx \frac{G_V}{V} \sum_{\mu M_f} \left\{ \langle P| \sum_{j=1}^A \boldsymbol{\tau}_\mp(j)|D\rangle + g_A \langle P| \sum_{j=1}^A \boldsymbol{\sigma}(j) \boldsymbol{\tau}_\mp(j)|D\rangle \right\} \quad (2.15)$$

for parent nucleus P and daughter D. More succinctly, the matrix element  $M$  can be represented by

$$M^\beta = \langle P| -\frac{M_F}{g_A^2} + M_{GT}|D\rangle \quad (2.16)$$

where  $M_F$  and  $M_{GT}$  are known as the Fermi and Gamow-Teller operators. The constant  $g_A$  is equal to  $\frac{G_A}{G_V}$  and is known as the Gamow-Teller coupling constant. There is a known discrepancy between calculated values of  $g_A$  and those measured experimentally, with the value from calculation at

$$|g_A| \approx 1.31 \quad (2.17)$$

compared to the measured value from  $\beta$  decay of  $-1.259 \pm 0.004$ .

This matrix element can be extended to  $\beta\beta$  decays by considering the combination of interactions between nucleons in the parent and intermediate nuclei [36]. The Fermi term considers only contributions of the lowest-lying  $0^+$  state of the intermediate nucleus, giving

$$M_F^{2\nu} = \sum_a \mu_a^{-1} \langle 0_D^+ | \sum_n n \tau_n^+ | 0_I^+ \rangle \langle 0_I^+ | \sum_n \tau_n^+ | 0_P^+ \rangle \quad (2.18)$$

the Gamow-Teller term can contribute via higher-energy states of the intermediate nucleus  $I$ , and is given by

$$M_F^{2\nu} = - \sum_a \mu_a^{-1} \langle 0_D^+ | \sum_n n \tau_n^+ \sigma_n | 1_I^+ \rangle \langle 1_I^+ | \sum_n \tau_n^+ \sigma_n | 0_P^+ \rangle \quad (2.19)$$

for the  $2\nu\beta\beta$  case these are combined to give equation 2.8.

In the  $0\nu$  case, neutrino potentials must also be considered in the NME, leading to a matrix element of the form [36]

$$M_{GT}^{0\nu} = \sum_a \langle 0_D^+ | h(r_{nm}, E_a) \sigma_n \cdot \sigma_m | 0_P^+ \rangle \quad (2.20)$$

$$\chi_F = \sum -a \langle 0_D^+ | h(r_{nm}, E_a) | 0_P^+ \rangle \left( \frac{G_V}{g_A} \right)^2 / M_{GT}^{0\nu} \quad (2.21)$$

for a neutrino potential  $h$ , and where  $\chi_F$  is a Fermi-type NME.

Because calculation of NMEs explicitly involves solving a many-body Schrödinger equation containing terms for all nucleon-nucleon interactions, it quickly becomes intractable for even small nuclei. To combat this problem, several approximation techniques have been developed to calculate NME values.

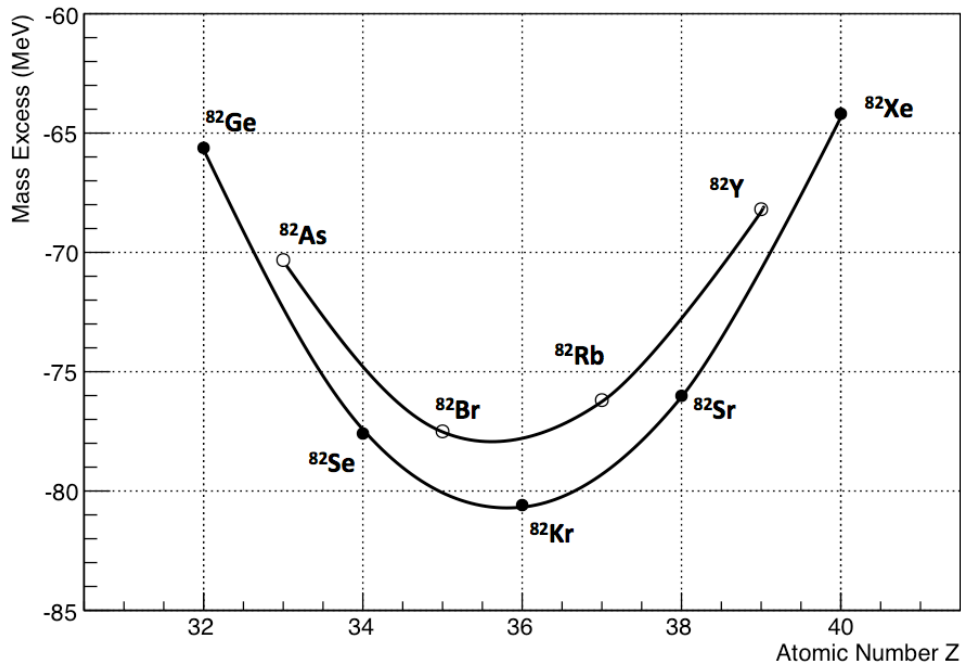
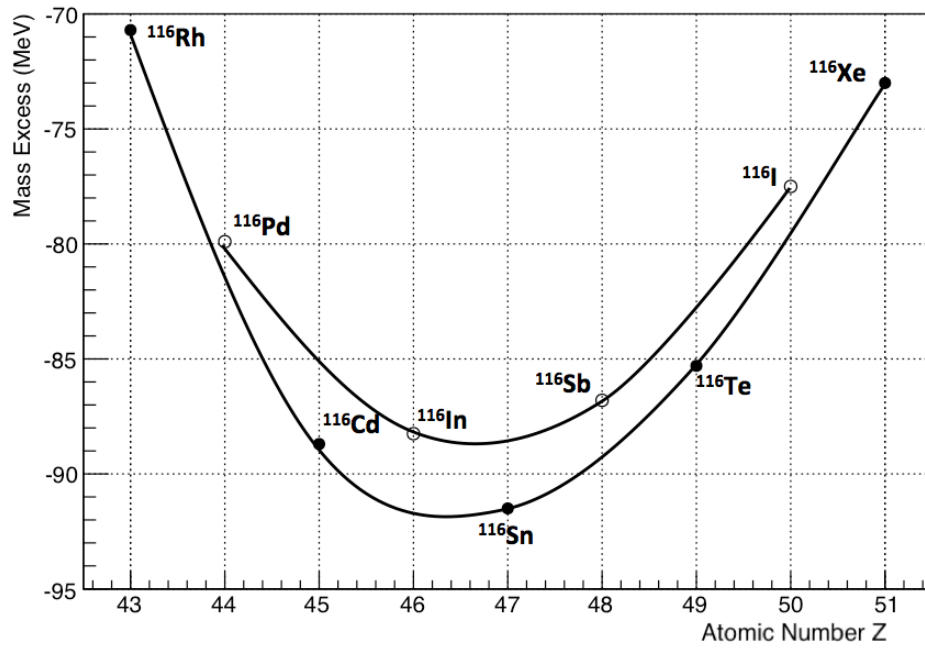


Figure 2.1: Z versus M plot illustrating the split between even-even and odd-odd isobaric nuclei giving rise to double beta decay for mass numbers 116 (top) and 82 (bottom).

### 2.4.1 Quasi-Random Phase Approximation

The Quasi-Random Phase Approximation (QRPA) method uses mean-field theory to describe a large single model space, but truncates available configurations. In this model, the mean field corresponding to the minimum energy is calculated with the quasiparticle representation and equations of motion for vibrations around that minimum are solved. Extensions of the model including the renormalized QRPA (RQRPA) and self-consistent renormalized QRPA (SRQRPA) remove problems related to non-conservation of nucleon number and violation of the Pauli exclusion principle. A thorough discussion of QRPA and its extensions is available in references [43, 44, 45].

### 2.4.2 Shell Model

An alternative to the QRPA framework is the Shell model, in which an assumption of weak coupling between proton and neutron systems is assumed [28]. This assumption has the advantages of providing wavefunctions with important quantum numbers such as parity, angular momentum, and isospin. Provided the model space is sufficiently large, correlations contained in the interaction Hamiltonian are automatically included; however, a major drawback is that providing a sufficiently large model space quickly becomes very difficult. In practice, only  $^{48}\text{Ca}$  can realistically be treated very well in this model for  $\beta\beta$  purposes.

### 2.4.3 Hartree-Fock Method

Another approach, in which a central nuclear wave function and wave functions for nuclear shells are approximated, is known as the Hartree-Fock method. The resulting solutions are in the form of a Slater determinant usually formed by the product of central and shell wave functions. Various other considerations including the shape of the Fermi surface are accounted for by further additions, such as introducing the Bogoliubov transformation, giving the Hartree-Fock-Bogoliubov (HFB) method. In general the shell method is restricted to spherical and lightly-deformed nuclei; ellipsoidal nuclei are not described as well. A thorough description of Hartree-Fock techniques are available in reference [46].

### 2.4.4 Interacting Boson Model

Another calculation known as the interacting boson model (IBM) aims to produce wave functions based on the interactions of nucleon pairs. For the purposes of double beta decay, even-even nuclei with atomic mass  $A \geq 60$ , realistic wave functions can be produced which are subsequently used to produce the NME for double beta decay. A thorough discussion of the IBM method as it relates to double beta decay is available in reference [47].

### 2.4.5 NME Values

Calculated NMEs for common double  $\beta$  decay nuclei with several approximation methods are shown in Figure 2.5.

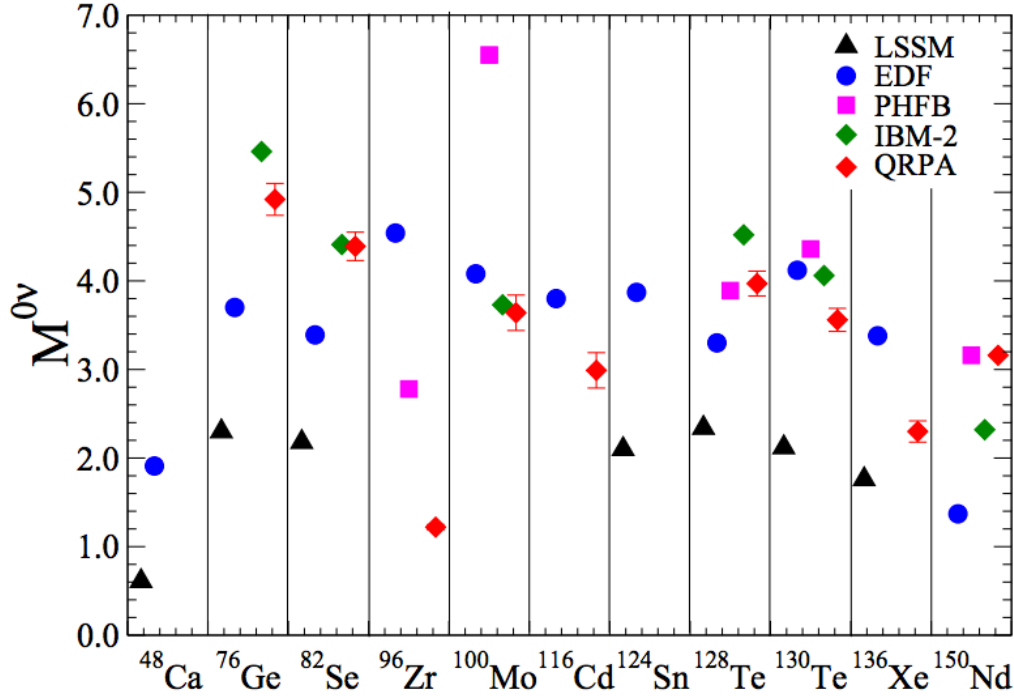


Figure 2.5: Comparison of  $0\nu$  calculated nuclear matrix elements for a selection of  $0\nu\beta\beta$  candidate isotopes using a variety of models [45].

## 2.5 Single and Higher States Dominance Hypotheses

As discussed in section 2.3.1, the  $2\nu\beta\beta$  process can be considered as two successive  $\beta$  decays proceeding through an intermediate nucleus. The general calculation of this process [48], known as the higher-states dominance (HSD) hypothesis, considers the sum of all states of the intermediate nucleus. an alternative known as the single-states dominance (SSD) hypothesis, applicable to transitions with intermediate nuclei with  $1^+$  ground states reachable via

the Gamow-Teller transition, posits that only the ground state of the intermediate nucleus contributes to the NME [49, 50].

Because the NMEs for the SSD and HSD processes differ in the contribution of individual lepton kinetic energies in the denominator, the single-electron spectrum may be used as a more sensitive observable for differentiation of the hypotheses. The largest separation between the spectra can be observed at low energies, as shown in Figure 2.6 [51].

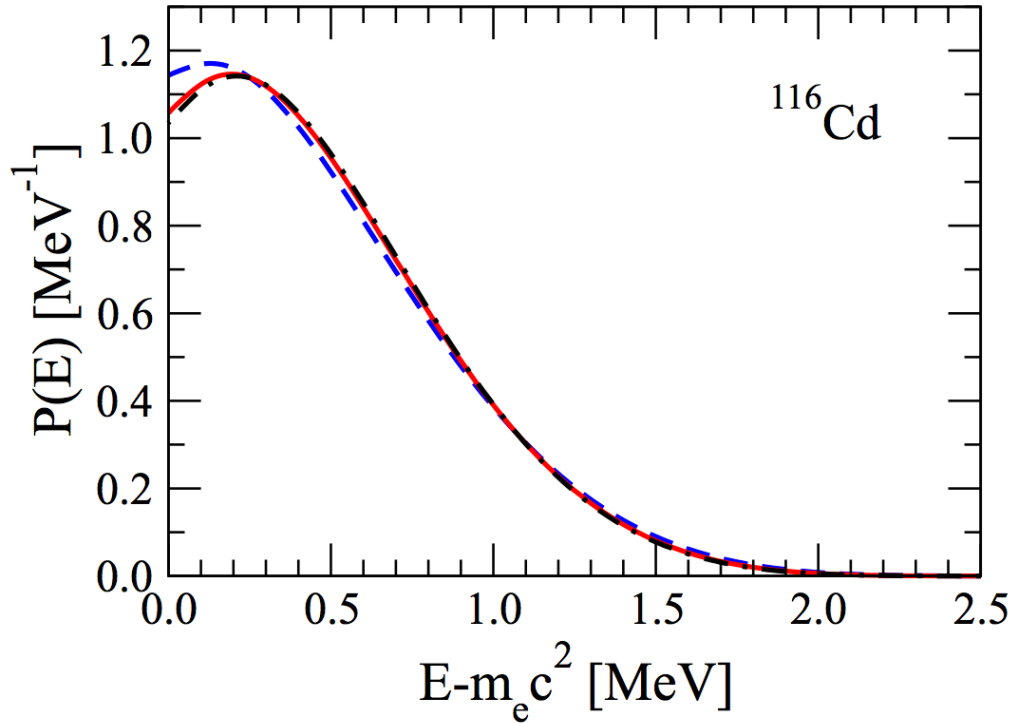


Figure 2.6: Calculated single-electron energy spectra for the SSD and HSD hypotheses in  $^{116}\text{Cd}$ . The solid red line represents the spectrum under the SSD hypothesis and the dashed lines represent several models of HSD spectra [51].

Among NEMO-3 isotopes,  $^{100}\text{Mo}$  and  $^{116}\text{Cd}$  have  $1^+$  intermediate nuclei, with  $^{116}\text{Cd}$  proceeding through the  $1^+$  state of  $^{116}\text{In}$ . Previous experiments have measured the Gamow-Teller matrix elements for the transition  $^{116}\text{Cd} \rightarrow ^{116}\text{In}$  using  $(^3\text{He}, t)$  reactions [52] and for the transition  $^{116}\text{In} \rightarrow ^{116}\text{Sn}$  using  $(d, ^2\text{He})$  reactions [53]. Figure 2.7 demonstrates the HSD and SSD levels for  $^{116}\text{Cd}$ .

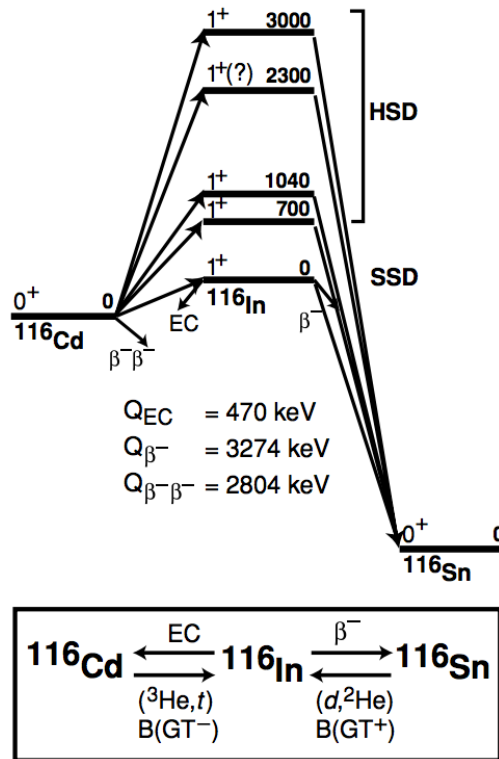


Figure 2.7: Level scheme for  $^{116}\text{Cd} \rightarrow ^{116}\text{Sn}$  decay showing the HSD and SSD contributions.



## 2.6 Previous Double Beta Experiments

Experiments designed with the goal of measuring  $\beta\beta$  lifetimes are chiefly designed with considerations of minimizing background radioactivity and maximizing sensitivity to  $\beta\beta$  signals. In practice, these goals are often at odds with each other, and a compromise must be made between background rejection and signal detection. Because of this compromise, a number of different methods have been developed, each with its own advantages and drawbacks. This section will briefly describe the major types of  $\beta\beta$  experiments and summarize past results, with a particular focus on those concerning  $^{116}\text{Cd}$  and  $^{82}\text{Se}$ .

The NEMO-3 and SuperNEMO experiments, which make use of a tracking chamber and a calorimeter system for tracking electron motion and measuring energy, will be described in detail in chapters 3 and 10, respectively.

### 2.6.1 Semiconductor Experiments

Semiconductor experiments exploit candidate isotopes which can be used as semiconductors, most often  $^{76}\text{Ge}$ . The source material is positioned between a pair of electrodes to form a diode, and incident radiation creates electron-hole pairs which migrate to the electrodes to generate a signal. Enriched Germanium crystals can be produced relatively easily with total absorption of  $\gamma$ -rays up to 5 MeV, and can provide energy resolution of approximately 0.3%. However, to reduce electronic noise they must be kept at cryogenic temperatures.

A well known and controversial example of semiconductor experiments

is the Heidelberg-Moscow experiment [54], which used high-purity Germanium enriched to 86-88% purity with a total exposure of 35.5 kg yr to obtain a limit of

$$T_{1/2}^{0\nu}(^{76}\text{Ge}) = 1.9 \times 10^{25} \text{ yr}, \quad (2.22)$$

corresponding to an effective neutrino mass of  $\langle m_\nu \rangle \leq 250 - 500 \text{ meV}$ .

In 2001, a group within the Heidelberg-Moscow collaboration claimed to have observed a signal of  $0\nu\beta\beta$  decay [55], using an exposure of 71.7 kg yr to obtain a  $T_{1/2}$  of

$$T_{1/2}^{0\nu}(^{76}\text{Ge}) = 1.19_{-0.50}^{+2.99} \times 10^{25} \text{ yr}. \quad (2.23)$$

Other experiments, however, have failed to reproduce this claim. The IGEX experiment [56] utilized a similar setup, using six HPGe detectors enriched to 86% to achieve an exposure of 8.9 kg yr with 2.0 kg of  $^{76}\text{Ge}$ , setting a lower half-life limit of

$$T_{1/2}^{0\nu}(^{76}\text{Ge}) \geq 1.57 \times 10^{25} \text{ yr}. \quad (2.24)$$

The GERDA experiment utilized repurposed HPGe detectors from Heidelberg-Moscow and IGEX, in addition to new Broad Energy Germanium (BEGe) detectors for a total mass of 21.3 kg. An improved background rejection system, including a liquid argon cryostat which doubled as coolant for the scintillators and 3 m water overhead instrumented with PMTs for cosmic ray muon rejection served to reduce backgrounds significantly.

Recent results from GERDA [57] strongly disfavor the claim from the Heidelberg-Moscow experiment, finding a half-life limit of

$$T_{1/2}^{0\nu}(^{76}\text{Ge}) \geq 2.1 \times 10^{25} \text{ yr}. \quad (2.25)$$

MAJORANA is a next-generation Germanium-semiconductor experiment aiming to improve on the sensitivity of Heidelberg-Moscow and IGEX by improving radiopurity, background shielding and rejection, and pulse shape discrimination.

### 2.6.2 Scintillation Experiments

An alternate approach to the measurement of  $\beta\beta$  decays is to include the candidate isotope directly inside a solid or liquid scintillator. Electrons ejected during decays of the source isotope are absorbed in the scintillating material, causing excitations in the material which are emitted as light that is subsequently detected by PMTs.

Elegant VI and CANDLES III are examples of scintillation experiments utilizing solid scintillators. In both cases,  $\text{CaF}_2$  crystals are used as both source and scintillator to detect decays of  $^{48}\text{Ca}$ . ELEGANT VI [58] used 6.6 kg of  $\text{CaF}_2(\text{Eu})$  for a total of 7.6 g of  $^{48}\text{Ca}$  to produce a half-life limit of

$$T_{1/2}^{0\nu} \geq 5.8 \times 10^{22} \text{ yr} \quad \langle m_{\beta\beta} \rangle \leq (3.5 - 22) \text{ eV}. \quad (2.26)$$

CANDLES III [59] uses 305 kg of undoped  $\text{CaF}_2$  for a total of 300 g of  $^{48}\text{Ca}$  immersed in liquid scintillator and is currently taking data.

In the case of liquid scintillators, candidate isotopes are dissolved directly into a scintillating medium, such as liquid Argon (LAr) which is instrumented with PMTs to observe scintillation. The liquid scintillator itself generally serves to self-shield the fiducial volume of the detector. This technique allows for measurement of relatively large amounts of candidate isotope, at the cost of reduced energy resolution.

KamLAND-Zen [60] contains 13 t of Xe-loaded liquid scintillator contained in a nylon balloon, with a total of 300 kg of  $^{136}\text{Xe}$ . The balloon is surrounded by 1000 t of liquid scintillator to act as a background suppressant as well as a water-Cherenkov detector to veto cosmic-ray muons. KamLAND-Zen has produced a half-life limit of

$$T_{1/2}^{0\nu} \geq 1.9 \times 10^{25} \text{ yr} \quad \langle m_{\beta\beta} \rangle \leq (160 - 330) \text{ meV}. \quad (2.27)$$

SNO+ [61] uses a similar model, loading  $^{130}\text{Te}$  dissolved into liquid scintillator contained in a 12 m diameter acrylic sphere shielded with a water bath instrumented with 9,500 PMTs. The first phase plans to use 800 kg of  $^{130}\text{Te}$  (0.3% concentration), to be increased to 8,000 kg (3%) in a second phase.

### 2.6.3 Bolometer Experiments

Bolometer experiments make use of changing material properties of detectors upon absorption of energy emitted during particle decays. Particles incident on the detector cause changes in the temperature of the material, with the resulting increase detected as a change in electrical properties [62]. This

technique typically allows for good resolution, but poor particle identification. Furthermore, because heat capacity is proportional to  $T^3$  at low temperatures, detectors must be maintained at the milliKelvin level.

CUORICINO [63, 64] used an array of 62  $\text{TeO}_2$  crystals with a total of 10.7 kg of  $^{130}\text{Te}$  surrounded by passive shielding to set a half-life limit of

$$T_{1/2}^{0\nu} \geq 3.0 \times 10^{24} \text{ yr} \quad \langle m_{\beta\beta} \rangle \leq (190 - 680) \text{ meV}. \quad (2.28)$$

CUORE [65] plans to build on the CUORICINO principle by increasing the array to 988 bolometers for a total of 206 kg of  $^{130}\text{Te}$ .

#### 2.6.4 Time Projection Chamber Experiments

Time projection chamber (TPC) experiments track the path of electrons as they move through an ionized medium. An electric field is applied to the medium to drive ionization electrons to a collection device. Drift time measurements allow for reconstruction of the electron track, and the amount of ionization is proportional to electron energy, allowing for energy measurements. Current experiments also utilize a medium which is also a scintillator, such as liquid Xenon.

EXO-200 [66] is a TPC experiment filled with liquid Xenon enriched with 80 kg of  $^{136}\text{Xe}$  (80% concentration). The TPC uses a cathode grid with planes of wires and avalanche photodiodes (APDs) symmetric at each end of the detector for detection of ionization signals and scintillation light. EXO-200

set a half-life limit of

$$T_{1/2}^{0\nu} \geq 1.6 \times 10^{25} \text{ yr} \quad \langle m_{\beta\beta} \rangle \leq (170 - 360) \text{ meV}. \quad (2.29)$$

The next iteration of EXO-200 is the EXO experiment, which plans to scale EXO-200 to the ton scale.

Additionally, NEXT-100 [67] plans to use pressurized gaseous Xenon as the detector medium, with an array of PMTs to measure energy resolution on one side of the detector with the other end instrumented with silicon photomultipliers which read electroluminescent signals proportional to the ionization signal. The detector plans to use 100 kg of gaseous  $^{136}\text{Xe}$  enriched to 91%, with the possibility of scaling to the ton scale in the future.

### 2.6.5 Previous $^{116}\text{Cd}$ Results

Several experiments have previously reported measured values for  $^{116}\text{Cd}$ , utilizing several of the techniques described above. A summary of these experiments and their results is given in this section.

An early search for  $2\nu\beta\beta$  decay [68] was performed in a Wilson cloud chamber containing a 30 g  $^{116}\text{Cd}$  foil. The background was too high to make a definite claim of observation, and the experiment was able to place a lower limit of

$$T_{1/2}^{2\nu} \geq 1 \times 10^{17} \text{ yr}. \quad (2.30)$$

ELEGANT V [69], a scintillator-type experiment which used  $^{116}\text{Cd}$  foils placed

between NaI scintillators, measured a  $2\nu\beta\beta$  half-life of

$$T_{1/2}^{2\nu} = 2.6_{-0.5}^{0.9} \times 10^{19} \text{ yr}, \quad (2.31)$$

and to place a  $0\nu\beta\beta$  half-life limit of

$$T_{1/2}^{0\nu}(68\%C.L.) \geq 6.3 \times 10^{21} \text{ yr} \quad (2.32)$$

The COBRA experiment [70, 71] is a semiconductor-type experiment using CdZnTe semiconductors. a prototype of this detector consisting of four  $1 \text{ cm}^3$  semiconductor crystals has been constructed, producing a  $0\nu\beta\beta$  limit of

$$T_{1/2}^{0\nu}(90\%C.L.) \geq 3.14 \times 10^{19} \text{ yr} \quad (2.33)$$

The Solotvina experiment [72, 73, 74] used  $\text{CdWO}_4$  scintillators containing a total mass of 330 g of  $^{116}\text{Cd}$ . The measured  $2\nu\beta\beta$  half-life reported by the experiment was

$$T_{1/2}^{2\nu} = 2.9_{-0.3}^{+0.4} \times 10^{19} \text{ yr} \quad (2.34)$$

and the current best  $0\nu\beta\beta$  half-life limit of

$$T_{1/2}^{0\nu} \geq 1.7(2.6) \times 10^{23} \text{ yr} \quad 90\% (68\%) \text{ C.L.} \quad (2.35)$$

### 2.6.6 Previous $^{82}\text{Se}$ Results

Geochemical evidence for  $2\nu\beta\beta$  decay of  $^{82}\text{Se}$  was observed by Lin *et al.* in 1988 [75], measuring a half-life of

$$T_{1/2}^{\beta\beta} = (1.2 \pm 0.1) \times 10^{20} \text{ yr} \quad (2.36)$$

for the combined  $0\nu + 2\nu$  double beta decay.

A TPC experiment at the University of California at Irvine [76] made the first observation of  $2\nu\beta\beta$  events, measuring a half-life of

$$T_{1/2}^{2\nu}(68\%C.L.) = 1.08_{-0.06}^{+0.26} \times 10^{20} \text{ yr} \quad (2.37)$$

and set a lower limit on  $0\nu\beta\beta$  decay half-life at

$$T_{1/2}^{0\nu} \geq 2.7 \times 10^{22} \text{ yr} \quad (2.38)$$

corresponding to an upper  $\langle m_{\beta\beta} \rangle$  limit of 5 eV.

Additionally, the NEMO-2 experiment [77], using a tracker-calorimeter setup similar to that of NEMO-3, measured a  $2\nu\beta\beta$  half-life of

$$T_{1/2}^{2\nu} = (8.3 \pm 1.0 \pm 0.7) \times 10^{19} \text{ yr} \quad (2.39)$$

and set a lower  $0\nu\beta\beta$  half-life limit of

$$T_{1/2}^{0\nu} \geq 2.8 \times 10^{21} \text{ yr}. \quad (2.40)$$

## 2.7 NEMO-3

The NEMO-3 experiment built off of the experiences from NEMO-2, utilizing a tracker-calorimeter setup to measure a total of seven isotopes. This experiment will be described in detail in chapter 3.



## Chapter 3

### The NEMO-3 Detector

Central to the effort of measuring double beta decay is the detector used to carry out the measurement. The NEMO-3 detector was the culmination of years of research and development, as well as experience gained from the previous NEMO-2 experiment. Extensive research and development was carried out to ensure that the detector would be able to achieve maximum sensitivity, in areas such as source foil purification and production, drift chamber optimization, and calorimeter development, measurement, and calibration. In addition, preventing the introduction of unwanted radioactive contaminants was also a major concern, and both the source purification and detector construction were developed with this in mind.

Development of the NEMO-3 detector was carried out with the purpose of designing a unique detector that could take advantage of multiple measurement techniques to provide more sensitive measurements of double beta decay through a variety of observables. NEMO-3 was thus unique, incorporating both a tracker to measure trajectories of particles emitted during decays of the isotopic foil as well as a calorimeter to measure energy. This combination made it possible to distinguish between signal and background events *in*

*situ* based on event topologies, as well as on time-of-flight hypotheses for rejecting backgrounds originating outside of the source foils. Furthermore, the cylindrical design of NEMO-3 made it possible to study multiple isotopes simultaneously, ultimately allowing for the determination of limits of seven isotopes.

This chapter describes each component of the NEMO-3 detector, along with background reduction considerations. Beginning with an overall description of the detector and its surroundings and then moving through the isotopic source foils, drift chamber, and calorimeter, each individual section of the detector will be discussed in detail to provide a full understanding of the mechanics used in double-beta decay measurement.

### **3.1 Detector Description**

The NEMO-3 detector was located in the Fréjus Underground Laboratory (known as the Laboratoire Souterrain de Modane, or LSM) in Modane, France, until its disassembly in 2011. It was designed as a cylinder divided azimuthally into 20 equal wedge-shaped sectors, with each sector containing a double beta candidate isotopic foil surrounded by a tracking chamber and calorimeter. The total mass of candidate isotopes in the detector was approximately 10 kg. The detector measured 3.1 m in diameter and 2.5 m in height. The combination of tracking chamber and calorimeter allows for particle tracking, energy measurement, and time-of-flight calculation, which combined allow for discrimination between electrons, positrons, gamma rays, and  $\alpha$  particles

and for *in situ* background rejection.

The source foils were fixed vertically in the detector. 18 of the 20 sectors contained candidate double beta decay isotopes, while the remaining two contained copper and natural tellurium for background measurement. Each foil was either metallic or composite, with a density between 30 and 60 mg/cm<sup>2</sup>.

The source foils were surrounded on either side by a tracking volume composed of 6,180 drift cells operating in Geiger mode. Drift cells were 270 cm long stainless steel wires and the tracking chamber was filled with a mixture of helium, ethyl alcohol, and argon at 7 mbar above atmospheric pressure.

Surrounding the tracking volume were 1,940 plastic scintillators coupled to low-radioactivity photomultiplier tubes for measurement of particle energy and time-of-flight. Both the internal and external walls were covered hermetically, and the top and bottom iron petals of the tracker chamber were also partially covered.

The detector was enclosed by a solenoid producing a 25 G magnetic field parallel to the foil axis to distinguish particle charges and reject positrons. a 20 cm external low-radioactivity iron shield surrounded the detector to suppress external  $\gamma$ -rays and thermal neutrons. Outside the iron shield was a borated water shield to capture thermal neutrons and thermalize fast neutrons. a 28 cm shield of wood surrounded the borated water tank. Finally, to prevent background interference from cosmic-ray particles, the detector had an overhead of 4,800 meters of water equivalent.

Figure 3.1 shows a cutaway of the NEMO-3 detector, showing the positions of the tracking chamber, scintillator, shielding, and support structure.

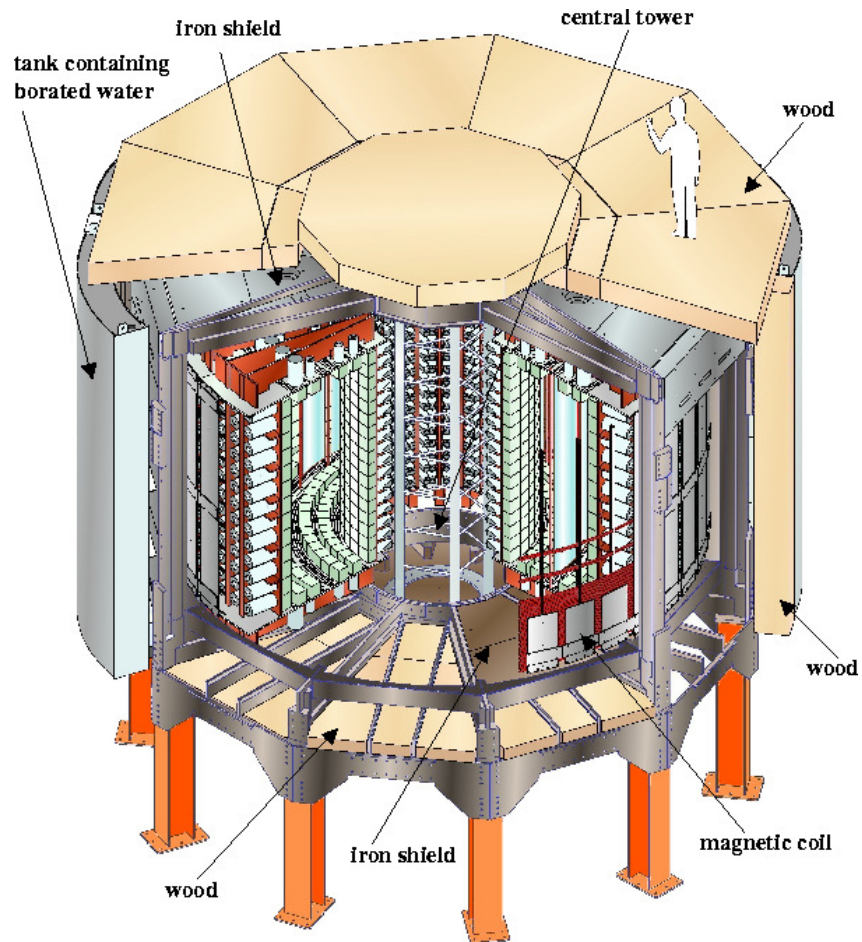


Figure 3.1: Cutaway of the NEMO-3 detector showing the tracking chamber, calorimeter, shielding, and support structure.

### 3.2 Source Foils

Each of the 20 sectors contained seven strips of isotopic foils. The two strips on the edge of each sector had a width of 63 mm, and the five in the center were each 65 mm in width. The mean length of the strips was 2480 mm. All source foils had a mean density from 30-60 mg/cm<sup>2</sup>, giving a thickness of < 60 μm for metallic foils (density 10 g/cm<sup>3</sup>) and < 300 μm for composite foils (density 2 g/cm<sup>3</sup>). It was demonstrated that efficiency for the  $0\nu\beta\beta$  process was not compromised given foil surface densities under 60 mg/cm<sup>2</sup> [78].

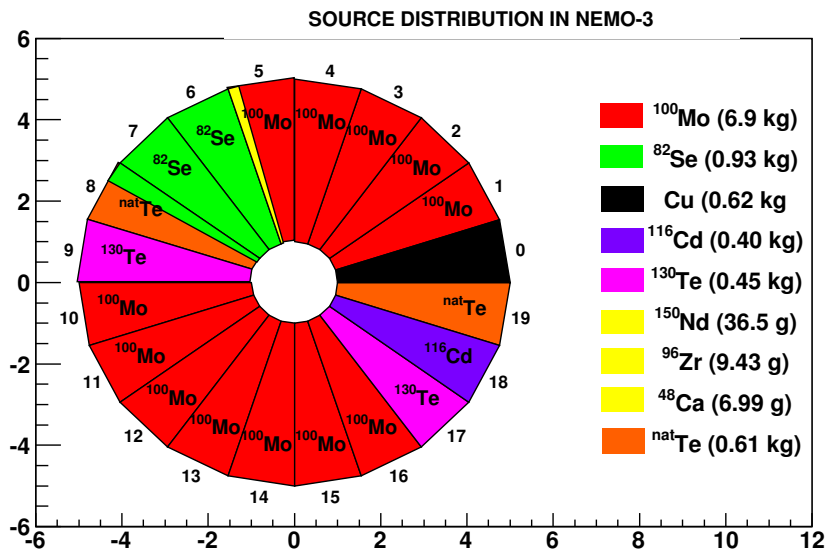


Figure 3.2: Distribution of isotopic source foils in NEMO-3 by sector.

### 3.2.1 Choice of Isotopes

At the time of this writing, there are 35 known  $\beta^-\beta^-$  isotopes and six known  $\beta^+\beta^+$  isotopes. The choice of isotopes to use in NEMO-3 was determined by several factors, chiefly the double beta transition energy ( $Q_{\beta\beta}$ ), background in the energy region around  $Q_{\beta\beta}$ , natural isotopic abundance, and the ability to sufficiently purify the candidate isotope to acceptable levels. Because of the ubiquitous presence of natural thorium, the 2615 keV  $\gamma$ -ray produced by its decay product  $^{208}\text{Tl}$  contributes a consistently troublesome background; to avoid contamination from this isotope,  $Q_{\beta\beta}$  values above 2.6 MeV were highly desirable. Figure 3.3 demonstrates the background spectrum from naturally-occurring radiation.

Additionally, in most cases isotopes with an abundance greater than 2% were considered; however, because of improvements in the enrichment process in Russia and an extremely high  $Q_{\beta\beta}$  value,  $^{48}\text{Ca}$  was also added despite its extremely low abundance. Finally,  $^{130}\text{Te}$  was added for  $2\nu\beta\beta$  studies and to attempt to give a reliable resolution to historical tension between measured geochemical half-lives [79, 80].

A table of isotopes chosen for inclusion in NEMO-3 is given in table 3.1. a full reference of all double beta decay isotopes is given in table B.1

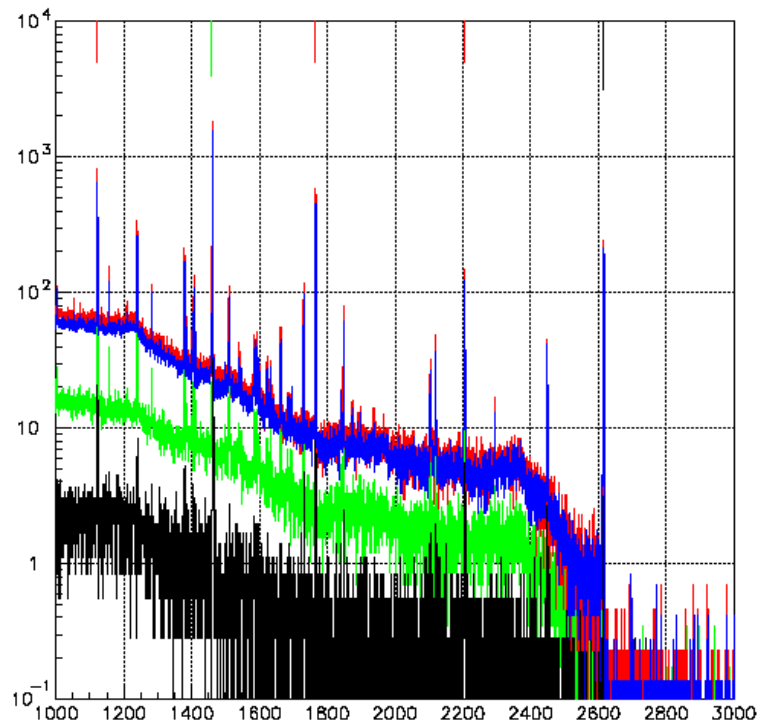


Figure 3.3: Spectrum of natural radioactivity, demonstrating the 2615 keV  $\gamma$  line due to  $^{208}\text{Tl}$ .

### 3.2.2 Source Preparation

The isotopic source foils were at the literal and figurative center of the NEMO-3 experiment. To observe a double beta signal, a large number of candidate atoms must be present in the source, and the source must also be free of undesirable radioisotopes which can mimic the signal. Additionally, an even distribution of source across the foil was also required for accuracy in tracking and event vertex determination.

Because each isotope in NEMO-3 exists in different forms and abundances, each required individual treatment and preparation. This section will discuss the preparation of  $^{82}\text{Se}$  and  $^{116}\text{Cd}$  and the composition of their foils. a thorough discussion of the preparation of all isotopes in NEMO-3 is available in reference [78].

### 3.2.3 $^{82}\text{Se}$

To obtain enriched  $^{82}\text{Se}$ , a chemical purification process beginning with metallic powder was used with a focus on removing long-lived radioisotopes of the  $^{238}\text{U}$  and  $^{232}\text{Th}$  decay chains while filling Ra sites with Ba. The selenium powder was dissolved in an aqueous solution and heated to produce  $^{82}\text{SeF}_6$  gas. an electrical discharge in the gas obtained the enriched selenium powder. Two different runs were produced, known as Se(I) and Se(II), with enrichments of  $97.02 \pm 0.05\%$  and  $96.82 \pm 0.05\%$ , respectively. a portion of Se(I) had already been used in the NEMO-2 prototype and found to have small "hot spots" of  $^{214}\text{Bi}$  contamination which could be rejected in the data analysis [81].

$^{82}\text{Se}$  foils are contained in sectors 6 and 7, as well as the first two strips in sector 8. a description of the  $^{82}\text{Se}$  foils is contained in tables 3.2, 3.3, and 3.4.

### 3.2.4 $^{116}\text{Cd}$

Metallic cadmium was enriched to  $(93.2 \pm 0.2)\%$  of isotope 116 via centrifuge. Strips were glued between Mylar foils to provide mechanical strength in the vertical position. Overall, a total of 441.5 g of cadmium with an enrich-



ment of 93.2% are included in the source foils, for a total of  $(410.4 \pm 1)$  g of  $^{116}\text{Cd}$  in NEMO-3 [82]. Note that reference [78] erroneously reports a value of  $(405 \pm 1)$  g. a description of the sector in NEMO-3 containing  $^{116}\text{Cd}$  foil is contained in table 3.5.

### 3.3 Tracking Chamber

The NEMO-3 tracking chamber was comprised of 18 concentric layers of vertical wire drift cells working in Geiger mode, totaling 6,180 cells and 39,820 wires. There were nine layers of drift cells between each side of the isotopic foil and the calorimeter, arranged as four layers followed by a gap, two layers, another gap and a final three layers.

An illustration of this layout is shown in Figure 3.4

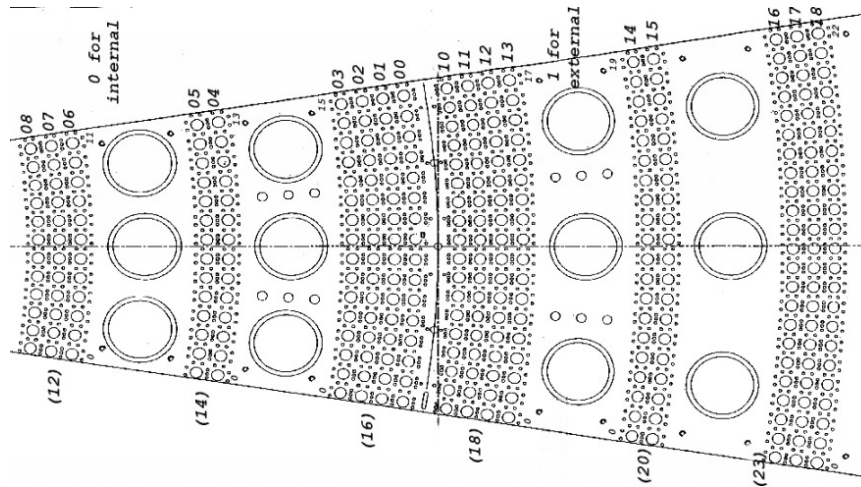


Figure 3.4: Detail of the Geiger cell and petal layout in the NEMO-3 tracking chamber.

### 3.3.1 Elementary Geiger Cell

Each cell was octagonal, with a diameter of 3 cm defined by 8 grounded cathode wires with a central anode wire. Adjacent cells shared cathode wires to reduce the overall number of wires, minimizing electron scattering. To reduce electrostatic cross talk between layers, an extra ground wire was added to each cell between layers, but not within the same layer.

All wires were stainless steel, 50  $\mu\text{m}$  in diameter and 270 cm long. Wires were strung between the iron petals at the top and bottom of the detector. At the end of each cell, there was a cylindrical cathode ring 3 cm in length and 2.3 cm in diameter. The anode wire ran through the center of the ring, with the cathode wires supported immediately outside it. An illustration of a cell is shown in Figure 3.5.

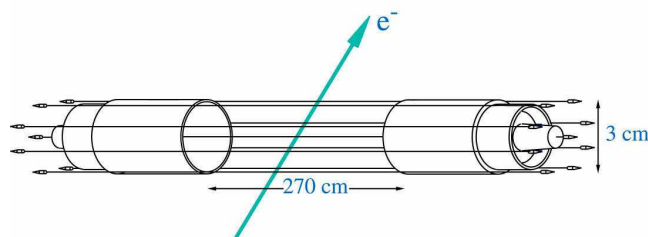


Figure 3.5: Illustration of an elementary Geiger cell.

The cells were run in Geiger mode, with an operating voltage on the anode wires of 1800 V. In this regime, charged particles such as electrons ionize some of the helium in the cell, which develops into a Geiger plasma which propagates along the wire with a speed of 5 cm/ $\mu\text{s}$ . Plasma creation

and propagation creates a voltage on the anode wire, which in turn develops a current which is collected in the cathode rings.

In NEMO-3, the anode pulse amplitude was approximately 50 mV measured on 270  $\Omega$ , providing a current of 200  $\mu\text{A}$  for a total propagation time of 40 ns. The total charge of the plasma was approximately  $10^{-8}$  C, or equivalently about  $6 \times 10^{10}$  electrons. After triggering, each cell had a dead time of about 500 ms, corresponding to the total ion collection time. The anode and cathode signals for fired cells were converted to drift and propagation times by the readout electronics, using the fast calorimeter signal as a trigger.

### 3.4 Calorimeter

The NEMO-3 calorimeter was composed of 1,940 optical modules designed for the cylindrical geometry of the detector. They served the simultaneous functions of particle energy measurement, time-of-flight measurements, and providing a fast trigger signal. Each module was composed of a plastic scintillator block and a light guide bonded to a 3 inch or 5 inch PMT, with the scintillator face oriented towards the isotopic foil. The scintillators hermetically covered the inner and outer cylindrical walls of the detector, and also had limited coverage on the top and bottom.

There were three types of scintillator blocks in the main calorimeter walls: IN, EC, and EE. The inner detector wall was comprised of two columns of IN blocks which were mirror-symmetric, while the exterior contained two columns of mirror-symmetric EE (edge) blocks placed symmetrically about

a center column of EC (center) blocks. On the top and bottom of the detector, there were four layers of scintillator blocks, each of a different type, known as L1 - L4, increasing radially from the center. L1 and L2 were considered 'interior' blocks, while L3 and L4 were considered exterior. Scintillator block details are provided in tables A.2 and A.3.

The scintillator blocks were placed inside the gas in the tracking chamber to minimize energy loss in the detected electrons. The blocks were supported by the rigid detector frame, making it possible to position the PMTs outside of the damaging helium gas.

To prevent loss of transparency to scintillation light while maintaining a high enough efficiency for  $\gamma$ -ray tagging, all blocks were produced with a thickness of 10 cm. While only about 2 cm of scintillator are necessary for measurement of any electrons in the regime of 1-10 MeV, the low Z of the plastic scintillator results in a greatly reduced efficiency for  $\gamma$ -rays, with the only interactions being Compton scattering.

### 3.4.1 Scintillator Characteristics

The polystyrene (PS) scintillator material was chosen for its radiopurity and to minimize electron backscattering. In addition to the PS, each scintillator contains a primary dopant p-terphenyl (pTP) and a wavelength shifter 1,4-di-(5-phenyl-2-oxazolyl) benzene (POPOP) chosen to move the fluorescence to a frequency better suited to the PMT photocathode. Table A.1 shows the mass fraction of PS, pTP, and POPOP by scintillator type.

### 3.4.2 Photomultiplier Tube Characteristics

The IN, L1, L2, and L3 scintillator blocks were coupled to Hamamatsu R6091 3" PMTs. These tubes have 12 dynodes and a flat photocathode ( $\phi = 76$  mm). The EE, EC, and L4 scintillator blocks were coupled to 6594 5" PMTs, which have 10 dynodes and a hemispherical photocathode ( $\phi = 127$  mm) for structural integrity. Therefore, to match the design of the PMT and the light guide, a second interface guide was necessary.

### 3.4.3 Light Guide Characteristics

For the scintillator-PMT interface, a polymethylmethacrylate (PMMA) plexiglass light guide 60 mm thick was installed, and served a secondary purpose by protecting the PMTs from helium in the tracking chamber. For 5" PMTs, a second PMMA interface had to be constructed to fit the hemispherical shape of the PMT. To ensure rigidity, the light guide was glued to an iron ring, which also served to complete the magnetic shield around the PMT. For the L4 row of scintillators, a second iron ring was glued to the petals and then on the 5" PMT's light guide. The light guide was then optically glued to the scintillator and checked for bubbles or other irregularities.

### 3.4.4 Coupling Between Scintillator and PMT

A major goal of the NEMO-3 calorimeter was to provide as uniform an ADC response as possible across all optical modules. To account for variations in both PMT and scintillator response, PMTs with good quantum effi-

iciencies and electron collection where paired with scintillators with poor light efficiency and vice versa.

The process of matching PMTs and scintillators began by measuring the ADC response at 1 MeV of each scintillator block, giving a mean value and variance for all scintillators of  $\langle ADC \rangle$  and  $\sigma_{ADC}$ . Using these quantities, a quantity  $\mu$  was defined for each scintillator:

$$\mu = \frac{ADC - \langle ADC \rangle}{\sigma_{ADC}} \quad (3.1)$$

To characterize PMTs in an analogous fashion, the sensitivity was defined as a ratio of photocathode current to photon flux, measured by the Corning Blue value provided by Hamamatsu for each PMT and confirmed by testing. As before, the mean and variance of CB values  $\langle CB \rangle$ ,  $\sigma_{CB}$  were used to define a quantity  $\nu$  for each PMT:

$$\nu = \frac{CB - \langle CB \rangle}{\sigma_{CB}} \quad (3.2)$$

An ideal association between PMT and scintillator was the case where  $\mu \approx \nu$ . However, the procedure was constrained by the limited number of PMTs and the requirement that three PMTs be attached to each HV channel.

### 3.4.5 Energy Calibration

To accurately and consistently measure the absolute energy released in double beta decay, an absolute calibration system was installed in the NEMO-3 detector. In addition, to monitor PMT gain fluctuations between absolute calibrations, a laser energy survey was also used more frequently.

The absolute calibration system consisted of 60  $^{207}\text{Bi}$  sources of 222 Bq deployed into copper tubes between foil sectors. Calibration runs lasted approximately 24 hours and were carried out monthly. Between calibration runs, the  $^{207}\text{Bi}$  sources were stored outside the detector volume.

$^{207}\text{Bi}$  emits conversion electrons with 482, 976, and 1682 keV energies. Of these, the 482 and 976 keV lines are useful calibration points. Due to multiple coulomb scattering in the tracking volume gas, in addition to energy losses in the calibration tube windows, these electrons lose approximately 45 keV and 40 keV, respectively.

The full width at half maximum (FWHM) energy resolution at 1 MeV is calculated from the width of the 976 keV peak assuming

$$R_{FWHM}(E) = \frac{FWHM(E)}{E} = \sqrt{\frac{A}{E}} \quad (3.3)$$

where  $a$  is a constant varying from 0.014 - 0.032 for all blocks. This energy resolution is assumed to have two main contributions: a principal component from the statistical fluctuations of the scintillation photons and the number of photoelectrons at the PMT anode, and a lesser dependence of 1 - 2 % (3" PMTs) up to 10% for 5" blocks. The component from statistical fluctuations increases as the square root of energy.

To account for the impact point dependence, the front face of each scintillator was divided into nine (25) bins for blocks with 3" (5") PMTs, arranged as a  $3 \times 3$  ( $5 \times 5$ ) grid. ADC histograms were constructed for

each impact bin and the 976 keV electron peak was refit to obtain  $A$  for the resolution function.

For energies of 3 MeV or more, a  $^{90}\text{Sr}$  source (with its daughter,  $^{90}\text{Y}$ ) was used less frequently for an additional high-energy data point. The end point of the  $\beta$  spectrum of  $^{90}\text{Sr}$  is 2.283 MeV.

For a more detailed description of the  $^{207}\text{Bi}$  calibration source, see Appendix F.

### 3.5 Laser Time Corrections

To ensure accurate timing in the detector, a laser was used to determine the relative time offset for each optical module. Light was sent through quartz optical fibers to each module, and the timing offset was used to produce a laser time correction (LTC) to be stored in the NEMO-3 database.

The offset was calculated as [83]

$$(TDC \times k + T(ADC) + TT(laserlight) + \epsilon) = constant \quad (3.4)$$

with  $TDC$  the mean digital value of the TDC in channels,  $k$  is the TDC channel constant of 0.053 ns/channel,  $T(ADC)$  the transit time of the light from laser to PMT, and  $\epsilon$  the constant necessary to keep the value constant for all PMTs. The time resolution is between 265-290 ns. Laser calibration runs were performed twice daily over the running time of NEMO-3 [78].



Transition	$Q_{\beta\beta}$ (keV)	Abundance (%)
$^{130}\text{Te} \rightarrow ^{136}\text{Xe}$	$2528.8 \pm 2.1$	33.8
$^{116}\text{Cd} \rightarrow ^{116}\text{Sn}$	$2804.7 \pm 4.2$	7.5
$^{82}\text{Se} \rightarrow ^{82}\text{Kr}$	$2995.2 \pm 3.3$	9.2
$^{100}\text{Mo} \rightarrow ^{100}\text{Ru}$	$3034.8 \pm 6.3$	9.6
$^{96}\text{Zr} \rightarrow ^{96}\text{Mo}$	$3350.0 \pm 3.5$	2.8
$^{150}\text{Nd} \rightarrow ^{150}\text{Sm}$	$3367.1 \pm 4.9$	5.6
$^{48}\text{Ca} \rightarrow ^{48}\text{Ti}$	$4272.0 \pm 4.1$	0.187

Table 3.1: Double beta decay isotopes used in the NEMO-3 detector, with Q-values and abundance.

Sector 06							
Strip number	1	2	3	4	5	6	7
Length	2425	2425	2423	2426	2425	2425	246
Width	63	65	65	65	65	65	63
$M_1$ (g)	58.34	62.15	65.15	75.03	71.33	62.88	60.79
$M_2$ (g)	48.83	52.23	55.08	64.41	60.91	52.92	50.93
$M_3$ (g)	47.37	50.67	53.43	62.49	59.09	51.34	49.41
$\eta$ (%)	97.02	97.02	97.02	97.02	97.02	97.02	97.02
Material	Se(I)						

Table 3.2: Description of sector 6 in NEMO-3 (Se(I)). Mass and  $\eta$  values are taken from reference [78].

Sector 07							
Strip number	1	2	3	4	5	6	7
Length (mm)	2426	2423	2424	2423	2423	2423	225
Width (mm)	63	65	65	65	65	65	63
$M_1$	74.60	77.31	77.54	78.05	77.66	76.90	72.98
$M_2$	64.21	66.58	66.79	67.28	66.91	66.19	62.69
$M_3$	62.19	64.46	64.67	65.14	64.78	64.09	60.70
$\eta$ (%)	96.82	96.82	96.82	96.82	96.82	96.82	96.82
Material	Se(II) (Composite)						

Table 3.3: Description of sector 7 in NEMO-3 (Se(II)). Mass and  $\eta$  values are taken from reference [78].

Sector 08		
Strip number	1	2
Length (mm)	2428	2428
Width (mm)	63	65
$M_1$ (g)	73.58	62.78
$M_2$ (g)	63.24	52.82
$M_3$ (g)	61.31	51.25
$\eta$ (%)	96.95 (mean value)	97.02
Material	Se(I) (1600 mm) Se(II) (828 mm)	Se(I)

Table 3.4: Description of sector 8 strips in NEMO-3 containing selenium. Both Se(I) and Se(II) are present in strip 1 of sector 8. Mass and  $\eta$  values are taken from reference [78].

Sector 18							
Strip number	1	2	3	4	5	6	7
Length (mm)	2432	2458	2456	2458	2458	2458	2433
Width (mm)	63	65	65	65	65	65	63
$M_1$ (g)	56.03	68.64	70.39	83.96	78.11	69.47	64.58
$M_2$ (g)	47.69	59.76	61.45	76.09	70.50	61.88	57.05
$M_3$ (g)	44.45	55.70	57.27	70.92	65.71	57.67	53.17
$\eta$ (%)	93.2	93.2	93.2	93.2	93.2	93.2	93.2

Table 3.5: Description of the  $^{116}\text{Cd}$  foil (sector 18 in NEMO-3). Mass and  $\eta$  values are taken from reference [78].

Block Type	Measured $R_{FWHM}$	Measured R (No Impact Corrections)
EC	$13.8 \pm 0.3$	$15.6 \pm 0.3$
EE	$13.5 \pm 0.2$	$14.9 \pm 0.2$
IN	$16.7 \pm 0.2$	$16.8 \pm 0.2$
L1	$14.9 \pm 0.2$	$16.6 \pm 0.2$
L4	$13.4 \pm 0.2$	$14.7 \pm 0.2$

Table 3.6: Measured FWHM resolution at 1 MeV by block type [78].

## Chapter 4

### NEMO-3 Analysis Strategy

The analysis of NEMO-3 data relies upon the accurate simulation of physical processes to develop a model for expected signal and background present in the detector. Relevant nuclear decays are generated using Monte Carlo (MC) techniques to produce events of the type observed in NEMO-3. Data and Monte Carlo events are reconstructed to generate tracks which are associated to scintillators and subsequently used to select signal-like and reject background-like events. From the selected data set, statistical tools are used to calculate results for desired physics quantities, including signal efficiency and purity, decay process half-lives, and likelihoods. This chapter details the analysis flow in NEMO-3, signal fitting procedures, decay half-life calculation and  $0\nu\beta\beta$  decay limits.

#### 4.1 NEMO-3 Analysis Flow

NEMO-3 follows a multi-step analysis path which begins with simulation of relevant processes, including  $\beta\beta$  decays and contaminant radiation to generate a model of observable spectra from known or postulated decay parameters. Generated events are digitized by simulating detector effects and

the output of electronics based on the true MC data. Using this information, a basis for comparison between data and MC is made available.

A tracking algorithm is used to reconstruct particle paths in the tracking chamber and extrapolate tracks to positions on both the source foil and calorimeter, to ensure to high probability that events are generated in the source foil and deposit energy in the calorimeter. The energy deposited in the calorimeter is measured by the emission of scintillation light detected by PMTs in the optical module for data events, and for MC events the deposited energy is simulated based on detailed photon transport modeling of the NEMO-3 scintillators [84].

Tracking and calorimetric data are used to discriminate between electrons,  $\alpha$  particles,  $\gamma$  rays, and positrons. Internal and external time-of-flight hypotheses are constructed and tested using these data to discriminate against backgrounds originating outside of the source foils. At this stage, broad topology requirements for event types being studied, such single- or double-electron events, electron- $\gamma$  events, or electron- $\alpha$  events.

More specific analysis requirements may then be performed over the reduced data and MC sets, allowing for selection of parameters which maximize the efficiency, purity, and signal to background ratio of the selected data. The final selected background spectra are then combined to produce an overall background model in the detector, and the signal MC is fitted to the (data - background) spectrum to generate a best-fit activity value, from which a double beta decay half-life is calculated.



The final  $0\nu\beta\beta$  analysis relies upon a limit-setting routine to determine the likelihood of signal observation in the presence of expected background, including an irreducible tail from the  $2\nu\beta\beta$  signal spectrum. If no events are reliably observed, the fit is used to generate a limit at 90% confidence level from which a number of excluded signal events and lower half-life limit can be deduced.

#### 4.1.1 Event Generation and Reconstruction

NEMO-3 analysis begins with the simulation of Monte Carlo events via the *DECAY0* [85] program. The  $2\nu\beta\beta$  and  $0\nu\beta\beta$  signals as well as all known or suspected background contaminants are generated and then propagated through a virtual detector constructed in GEANT3 [86] to simulate the effects of moving through the isotopic foils as well as multiple scattering in the tracking chamber gas.

Data events and simulated Monte Carlo events that have been thus digitized are then passed to the reconstruction algorithm, where information from the Geiger cells and calorimeters is used to reconstruct a track from the foil to the calorimeter. Because of the 25 G magnetic field in the detector, electron tracks follow curved helices with a radius proportional to the energy of the ejected electron. Tracks which reach the calorimeter are associated with the specific scintillator activated.

### 4.1.2 Topology Selection Requirements

To reduce the size of the data set under consideration, a first set of selection requirements is submitted to select events which meet broad criteria for the channel being studied. This step allows for selection of general event types, while reducing the size of the data set and allowing more specific requirements to be performed in a reasonable amount of time. The selection algorithm loops over each event, rejecting events not meeting all criteria. Events which pass all requirements are saved as a root ntuple containing a user-defined set of histograms which can be used for further analysis.

At this level, events are selected based on the number and type of particles reconstructed, such as two-electron or electron-gamma events. Information requiring a connection to the NEMO-3 database, such as laser time corrections, scintillator impact corrections, and presence or lack of  $\alpha$ s is also selected at this stage. Additionally, events are selected based on their position on the foil, removing all events except those in the sector containing the desired isotope. a detailed list of requirements for each analysis channel will be presented in their respective chapters.

### 4.1.3 Analysis Requirements

After the initial selection requirements as described in the previous subsection, requirements based on specific observables can be performed for selection of the final data set. In addition, because the most time-consuming portion of the analysis process has already been performed, cut selection can be

optimized at this stage on a blinded data set before being applied to all data. At this stage, kinematic requirements based directly on physics observables are applied, along with time of flight calculations, which are in turn used to calculate probabilities for the internal and external hypotheses, described in the next section. Once all requirements have been applied, the remaining events are stored in histograms for final scaling and signal fitting.

## 4.2 Scaling and Fitting

To provide an acceptable background and signal model, an arbitrarily large number of MC events are generated to minimize statistical fluctuations. The resulting curve is then scaled based on the measured time  $t$  and, in the case of background, activity  $A$  measured via HPGe or within NEMO-3. To account for detector inefficiency, each distribution is also scaled by its simulated efficiency

$$\epsilon = \frac{N_f}{N_g} \quad (4.1)$$

where  $N_f$  is the number of selected events and  $N_g$  is the total number of events generated in the MC. The final number of scaled events for background channel  $i$  is given by

$$N_i = \epsilon_i A_i t \quad (4.2)$$

In the case of a measured signal, the activity is unknown and must be determined by a fit to the spectrum of (data - background). The TMinuit routine in ROOT is used to calculate a log-likelihood minimization based on

the probability of observing  $d$  events given a signal  $s$  and backgrounds  $b$  in each bin  $i$ :

$$p_i = \frac{-(s_i + b_i)(s_i + b_i)^{d_i}}{d_i!} \quad (4.3)$$

The likelihood  $L$  is the product of probabilities in all bins:

$$L = \prod_{i=0}^k p_i \quad (4.4)$$

giving a log-likelihood

$$\ln(L) = \sum_{i=0}^k -(s_i + b_i) + d_i \ln(s_i + b_i) - \ln(d_i!) \quad (4.5)$$

The quantity  $-\ln(L)$  is minimized numerically with respect to the signal to find the expected number of  $2\nu\beta\beta$  events:

$$\frac{\partial -\ln(L)}{\partial S} = -1 + \sum_{i=0}^k \frac{d_i}{s_i + b_i} \frac{\partial s_i}{\partial s} = 0 \quad (4.6)$$

and its uncertainty  $\sigma_s$  is determined by the value of  $s$  such that  $\ln(L)$  is  $\frac{1}{2}$  its maximum:

$$\ln(L(S)) - \ln(L(s \pm \sigma_s)) = \frac{1}{2} \quad (4.7)$$

### 4.3 Half-life Calculation

The overall goal of the  $2\nu\beta\beta$  and  $0\nu\beta\beta$  decay channels is the measurement of a decay half-life, which is determined based on the number of signal events observed during the running time. Given a sample of  $N$  atoms with

activity  $a$  and decay constant  $\lambda$ ,

$$A = N\lambda = \frac{N\ln(2)}{T_{1/2}} \quad (4.8)$$

Activity can also be measured given a number of measured signal events  $N_s$  in time  $t$ , in a detector with efficiency  $\epsilon$ :

$$A = \frac{N_s}{t \cdot \epsilon} \quad (4.9)$$

Equating 4.8 and 4.9 allows for calculation of the half-life given measurable observables:

$$T_{1/2} = \frac{N\ln(2)\epsilon t}{N_s} \quad (4.10)$$

The number of atoms in a sample of mass  $m$  of an isotope with atomic mass  $A$  is given by

$$N = \frac{N_A m}{A} \quad (4.11)$$

where  $N_A$  is Avogadro's number.

The final formula for a measured half-life is thus

$$T_{1/2} = \frac{\epsilon \cdot m \cdot \ln(2) N_A t}{N_s \cdot A} \quad (4.12)$$

#### 4.4 Neutrinoless Double Beta Decay Limit Determination

The final goal of any neutrinoless double beta decay experiment is to observe a  $0\nu\beta\beta$  signal. In order to conclusively make such a claim, it is necessary to be able to discriminate between signal-like and background-like events

to a reasonable certainty. In the event that no events above background are observed, only a lower half-life limit may be set. The statistical tools for these determinations are presented in this section.

#### 4.4.1 Neutrinoless Double Beta Decay Half-life Sensitivity

In cases where a clear signal above background is not observed, only a lower limit can be placed on the half-life. This limit is given with respect to standard deviations corresponding to a desired confidence level. The sensitivity with which a detector can be expected to set a limit is given as [87, 88]:

$$T_{1/2}^{0\nu}(n_\sigma) = \frac{\ln(2) \times N_A \epsilon \eta}{n_\sigma} \frac{1}{A} \sqrt{\frac{Mt}{b\Delta(E)}} \quad (4.13)$$

where

- $n_\sigma$  is the number of standard deviations
- $N_A$  is Avogadro's number
- $\epsilon$  is the signal efficiency
- $M$  is the total source mass
- $\eta$  is the source enrichment
- $b$  is the expected background, in units of  $\text{Bq} \cdot \text{kg}^{-1} \cdot \text{yr}^{-1}$
- $\Delta(E)$  is the energy resolution at the  $Q_{\beta\beta}$  value
- $t$  is the total time in years

#### 4.4.2 Limit Calculation

To determine the actual likelihood of signal exclusion in the case where both expected number of signal and background events are small, a modified frequentist confidence level calculation [89] is employed, using the test statistic of the likelihood ratio to discriminate signal-like outcomes from background-like ones. This calculation is too onerous to perform by hand, and is carried out using the TLimit class in ROOT.

To define the likelihood ratio, first the probability of observing  $d_i$  events in channel  $i$  given signal  $s_i$  and expected background  $b_i$  is defined as

$$P_{s+b} = \frac{e^{-(s_i+b_i)}(s_i + b_i)^{d_i}}{d_i!} \quad (4.14)$$

and the probability given only background is defined as

$$P_b = \frac{e^{-b_i}b_i^{d_i}}{d_i!} \quad (4.15)$$

The likelihood ratio  $X$  is then calculated as the product of the ratio of these quantities for all channels:

$$X = \prod_{i=1}^n X_i = \prod_{i=1}^n \frac{e^{-(s_i+b_i)}(s_i + b_i)^{d_i}}{d_i!} / \frac{e^{-b_i}b_i^{d_i}}{d_i!} \quad (4.16)$$

The CL for excluding the possibility of the simultaneous presence of both signal and background events is

$$CL_{s+b} = P_{s+b}(X \leq X_{obs}) = \sum_{X(d'_i) \leq X(d_i)} \prod_{i=1}^2 \frac{e^{-(s_i+b_i)}(s_i + b_i)^{d'_i}}{d'_i!} \quad (4.17)$$

where the sum runs over all possible outcomes ( $d'_i$ ) with test statistics less than or equal to the observed one.

A similar CL for the background-only hypothesis,  $CL_b$ , is defined similarly:

$$CL_b = P_b(X \leq X_{obs}) \quad (4.18)$$

The modified frequentist confidence level for observing a signal is then taken as the ratio of the two hypotheses:

$$CL_s = \frac{CL_{s+b}}{CL_b} \quad (4.19)$$

and the quoted CL for exclusion is  $CL = 1 - CL_s$ .



## Chapter 5

### NEMO-3 backgrounds

The  $2\nu\beta\beta$  and, to an even greater extent,  $0\nu\beta\beta$  processes are very highly suppressed, and as a consequence have extremely long half-lives: on the order of  $10^{18-20}$  years for  $2\nu\beta\beta$  and constrained to be greater than  $10^{22}$  years for the theorized  $0\nu\beta\beta$ . To make an accurate observation of such rare processes, reduction of background contamination and accurate modeling of irreducible contaminants is of the utmost importance.

In general, a background as it concerns NEMO-3 is anything which can mimic the double- $\beta$  processes being measured. In the case of the  $2\nu\beta\beta$  analysis, this definition applies to unwanted radioisotopes, a description of which will be provided in this chapter. Additionally, in the cases of the light Majorana exchange V-A and Right handed current  $0\nu\beta\beta$  processes, the  $2\nu\beta\beta$  spectrum provides an irreducible background due to finite detector resolution confounding the spectra. The ability to differentiate this background from signal is a major factor in sensitivity to  $0\nu\beta\beta$  detection.

The NEMO-3 detector was designed with the aim of background reduction. As described in section 3.1, several layers of shielding, including the placement of the detector itself, were put in place to reduce natural back-

ground. The LSM, with an overhead of 4,800 m.w.e, was well protected against background radiation from cosmic rays. External shielding composed of layers of iron, water, and wood protected the tracking chamber from both thermal and fast neutrons and external  $\gamma$  rays. To reduce the level of radon and its daughter nuclei from natural  $^{238}\text{U}$  decay in the rock surrounding the laboratory, a radon tent was installed in September 2004.

Measurement of the remaining backgrounds in NEMO-3 is a crucial part of the analysis of NEMO-3 data. This chapter will describe the types of backgrounds present in NEMO-3 during its runs, their mechanisms for mimicking double-beta decay, and their measurement using both HPGe detectors and detector data.

A full description of backgrounds in the entirety of NEMO-3 can be found in reference [90].

## 5.1 Background overview and measurements

The NEMO-3 analysis divided backgrounds into three types based on their position of origin:

- Internal: Backgrounds originating from impurities in the isotopic source foil. This dissertation will only discuss internal backgrounds originating in the  $^{116}\text{Cd}$  and  $^{82}\text{Se}$  source foils.
- External: Backgrounds originating from outside of the source foil, including the source frame, PMTs, and scintillators.

- Radon: Backgrounds whose source is the emanation of  $^{222}\text{Rn}$  into the NEMO-3 detector. The decays giving rise to these backgrounds and their daughters are shown in Figure 5.1.

	$^{238}\text{U}$				$^{232}\text{Th}$				$^{235}\text{U}$					
U	U-238 4.47 $10^9$ yr		U-234 2.455 $10^5$ yr							U-235 7.04 $10^8$ yr				
Pa	↓	Pa-234m 1.17 m	↓							↓	Pa-231 3.27 $10^4$ yr			
Th	Th-234 24.10 d		Th-230 7.538 $10^4$ yr	α ↓		Th-232 14 $10^9$ yr	Th-228 1.912 yr			Th-231 25.52 h		Th-227 18.72 d		
Ac			↓			↓	Ac-228 6.15 h	↓		↓	Ac-227 21.773 yr	↓		
Ra			Ra-226 1600 yr			Ra-228 5.75 yr	Ra-224 3.66 d					Ra-223 11.435 d		
Fr			↓				↓					↓		
Rn			Rn-222 3.8235 d				Rn-220 55.6 s					Rn-219 3.96 s		
At			↓				↓					↓		
Po			Po-218 3.10 m	Po-214 164.3 μ s	Po-210 138.376 d		Po-216 145 ms	Po-212 299 ns				Po-215 1.781 ms		
Bi			↓	Bi-214 19.9 m	↓	Bi-210 5.013 d	↓	Bi-212 60.55 m	↓			↓	Bi-211 2.14 m	
Pb			Pb-214 26.8 m	0.021 μ s ↓	Pb-210 22.3 yr	Pb-206 stable		Pb-212 10.64 h	36% ↓	Pb-208 stable		Pb-211 36.1 m	↓	Pb-207 stable
Tl				Tl-210 1.3 m		Tl-206 4.199 m		Tl-208 3.053 m					Tl-207 4.77 m	

Figure 5.1: Decay chains of  $^{238}\text{U}$ ,  $^{232}\text{Th}$ , and  $^{235}\text{U}$ . Pernicious daughters contributing to the radon background in NEMO-3 are highlighted.

NEMO-3 detector components were measured by HPGe detector to determine the amount of background they could be expected to contribute. In several cases, only limits on radioactivity were possible by this method, and in such cases it can be more effective to measure the contamination by developing

best-fit models in single-electron or electron- $\gamma$  topologies which are sensitive to particular background isotopes.

## 5.2 Internal backgrounds

*Internal backgrounds* arise from the contamination of the isotopic source foil during the enrichment process. Events originating from inside the source foil typically mimic double- $\beta$  decay in several ways, with three principal channels:

- $\beta$  decay with emission of an internal conversion electron.
- $\beta$  decay with Möller scattering within the foil.
- $\beta$  decay with emission of a  $\gamma$  with subsequent Compton scattering inside the foil.

In all three cases, the final-state topology visible to the detector is that of two electrons, identical to that of double-beta decay. a diagram of internal decays in NEMO-3 is shown in Figure 5.2

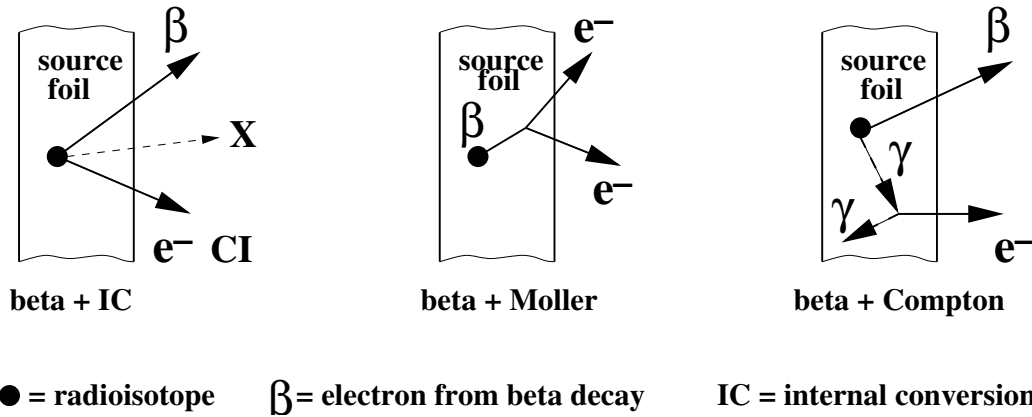


Figure 5.2: Diagram of major processes by which contamination in the isotopic source foil can mimic double-beta decay.

Prior to installation in the detector, the source foils were measured with a HPGe detector [78]. While this technique is very useful for measurement of  $\gamma$  radiation, it is less sensitive to pure  $\beta$  emitters which cause the bulk of the background events as described above. To perform a more sensitive measurement, the NEMO-3 detector itself was utilized.

Because internal backgrounds vary with foil position and isotope enrichment process, the  $^{116}\text{Cd}$  and  $^{82}\text{Se}$  foil background models will be discussed separately.

### 5.2.1 $^{116}\text{Cd}$ foil

The  $^{116}\text{Cd}$  foils are enriched to a value of 93.2%, with the remainder giving rise to a small amount of contaminant  $^{113}\text{Cd}$ . In addition, other impurities are known to exist, including  $^{234m}\text{Pa}$  and  $^{228}\text{Ac}$ , whose decay chains

include  $^{214}\text{Bi}$  and  $^{208}\text{Tl}$ . Additional backgrounds include  $^{40}\text{K}$ ,  $^{137}\text{Cs}$ , and  $^{212}\text{Bi}$ . Normalized spectra of these backgrounds are shown in figures 5.3 and 5.8.

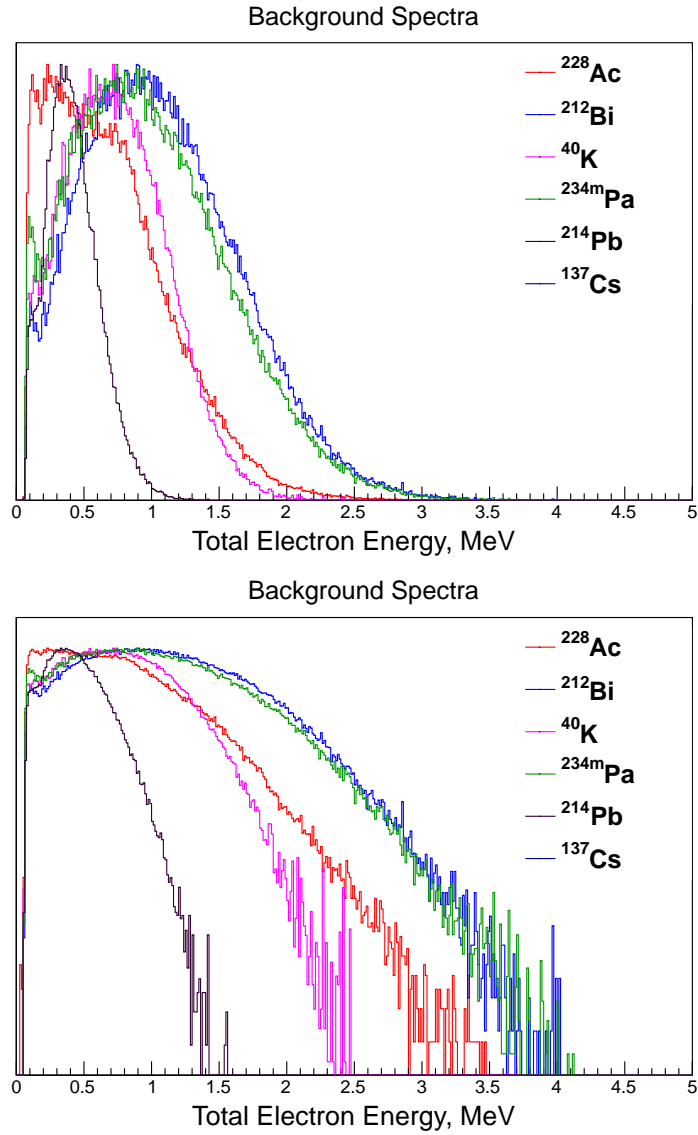


Figure 5.3: Spectra of backgrounds known to be present in the  $^{116}\text{Cd}$  foils in linear (top) and log (bottom) scales.

A description of backgrounds in the cadmium foils, including their measured activities, is given in table H.1. a sample of expected background events remaining after selection is presented graphically in Figure 5.4.

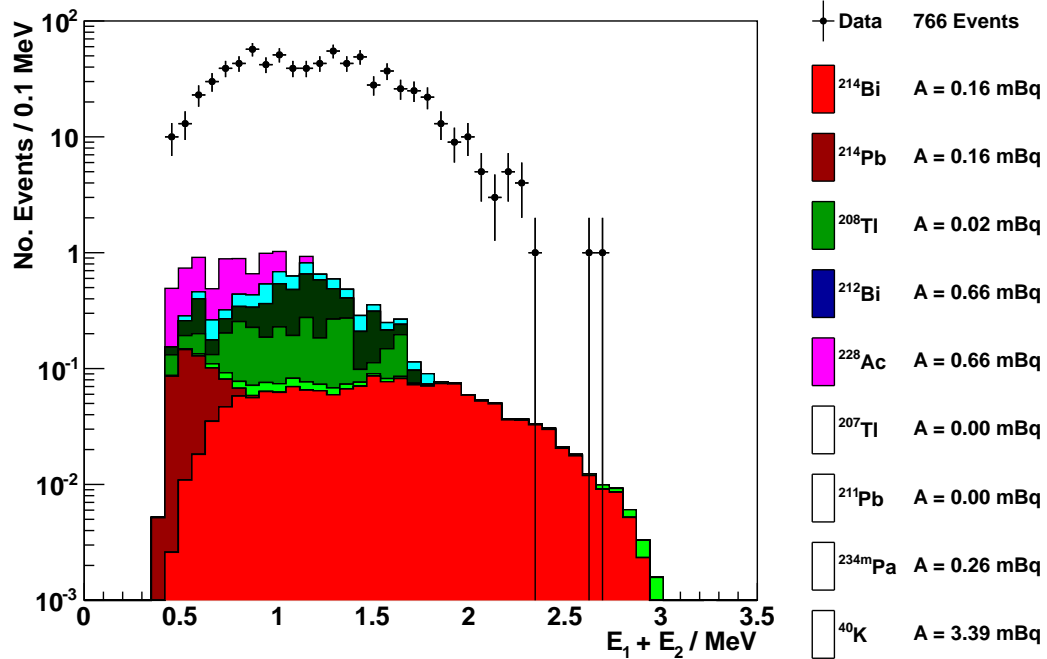


Figure 5.4: Spectrum of internal backgrounds remaining in the  $^{116}\text{Cd}$  sector of the source foil after event selection.

### 5.2.2 $^{82}\text{Se}$ foil

The  $^{82}\text{Se}$  foils are enriched to varying values, depending on their production run. Se(I), some of which was recovered from the prior NEMO-2 experiment, was enriched to 97.02%, while Se(II) was enriched to 96.82%. Details of the  $^{82}\text{Se}$  foil enrichments and positions are provided in tables 3.2, 3.3,

and 3.4. The remainder of the foil gives rise to the presence of several natural impurities, again including  $^{234m}\text{Pa}$  and  $^{228}\text{Ac}$ , along with their pernicious daughters  $^{214}\text{Bi}$  and  $^{208}\text{Tl}$ . Normalized spectra of backgrounds present in the  $^{82}\text{Se}$  foils are shown in figures 5.5 and 5.8.

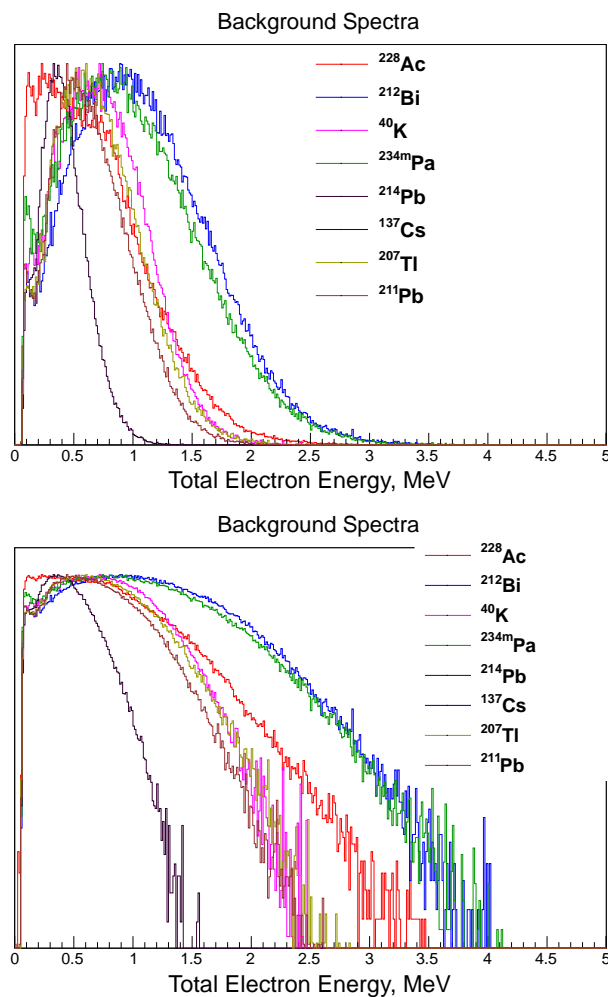


Figure 5.5: Spectra of backgrounds known to be present in the  $^{82}\text{Se}$  foils in linear (top) and log (bottom) scales.



### 5.3 External backgrounds

*External background* events originate outside the source foil and mimic double beta event final topologies. Because they do not originate inside the source foil, a particle from the decay must interact with the foil in such a way as to produce a final topology with two electrons, both of which cross the tracking chamber and interact with a scintillator with sufficient energy to register as an event.

In addition to contamination from  $^{222}\text{Rn}$  and  $^{220}\text{Rn}$ , which will be discussed separately,  $^{40}\text{K}$ , a naturally-occurring  $\gamma$ ,  $\beta^-$ , and  $\beta^+$  emitter present with a  $T_{1/2}$  of  $1.248 \times 10^9$  years, is a major contaminant which exists in many components of the detector, including the frame, shields, scintillators, and particularly the PMT glass.

Gamma rays originating from background events can interact with the foil to mimic background events in several ways, principally:

- Pair production in the foil, with the positron misidentified as an electron.
- Double Compton scattering, resulting in two electrons being ejected from the foil.
- Compton scattering, with the ejected electron subsequently Möller scattering in the foil.

These processes are illustrated in Figure 5.6.

In addition, high-energy electrons or positrons can also cross the source foil and interact with multiple scintillators. Such crossing electron events re-

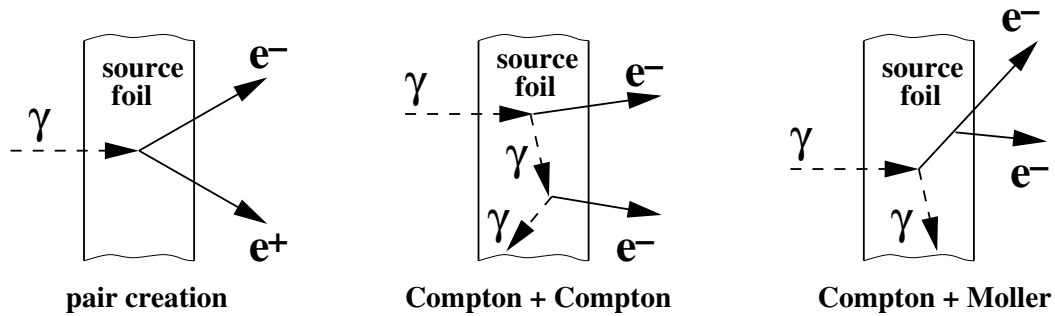


Figure 5.6: Diagram of major processes by which contamination in the detector volume can mimic double-beta decay.

semble two-electron events originating in the foil, but can be differentiated by the timing difference between the PMTs, as discussed in section C.

An example of an external  $\gamma$  ray compton scattering in the source foil and a crossing electron event are shown in Figure 5.7.

To accurately model the contamination in the detector, a background model was developed based on measurements made with HPGe detectors in NEMO-3 [90]. Monte Carlo events were generated in each individual component of the detector with measured contamination. a brief description of each MC component is provided in table 5.1.

### 5.3.1 Neutron flux

External neutrons can also contribute to the measurable background in NEMO-3 via neutron capture, resulting in  $\gamma$ -ray emission. Neutron flux in the LSM was measured [91, 92] and an analysis of the data concluded that for energies below 4 MeV, neutron backgrounds account for only 0.03% of total

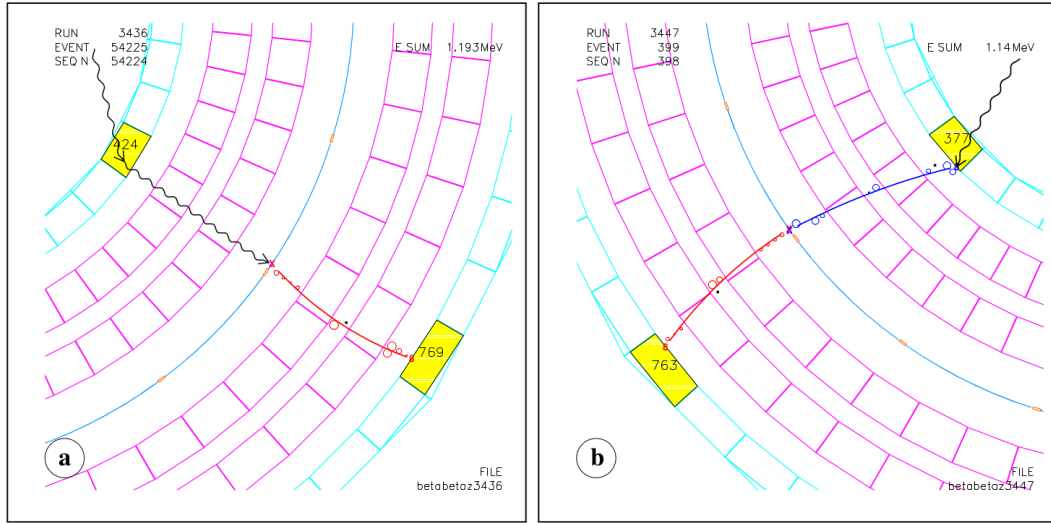


Figure 5.7: Top-down event displays of an external  $\gamma$  ray Compton scattering in the foil (left) and an external crossing electron (right). Reconstructed electron (positron) tracks, shown as red (dark blue) helices, are reconstructed with a vertex on the source foil, shown in blue. After crossing the tracking chamber, they deposit energy in a calorimeter, shown as cyan boxes. Pink boxes represent petal calorimeters.

events and can be neglected for double beta analysis [90].

## 5.4 Radon backgrounds

In addition to the contaminants discussed in section 5.3, events originating from the decay chains of naturally-occurring  $^{238}\text{U}$  and  $^{232}\text{Th}$  are accounted separately. These isotopes decay to gaseous  $^{222}\text{Rn}$  and  $^{220}\text{Rn}$ , respectively, which ultimately give rise to  $^{214}\text{Bi}$  and  $^{208}\text{Th}$ , both of which are troublesome isotopes which emit high-energy  $\beta$  and  $\gamma$  rays. These isotopes are of particular concern because they can mimic double-beta events in the range of  $Q_{\beta\beta}$  of

candidate isotopes in NEMO-3.  $^{210}\text{Bi}$ , a product of natural  $^{238}\text{U}$  decay chain, is also included as a radon background.

Background events originating from the  $^{214}\text{Bi} \rightarrow ^{214}\text{Po}$  (BiPo) chain are readily identified by the emission of a delayed  $\alpha$  particle emitted from the daughter  $^{214}\text{Po}$  nucleus.

The background model for the distribution of these isotopes is described in table 5.2 and a description of the most relevant decays of  $^{214}\text{Bi}$  and  $^{208}\text{Tl}$  as they relate to NEMO-3 is contained in Appendix G.

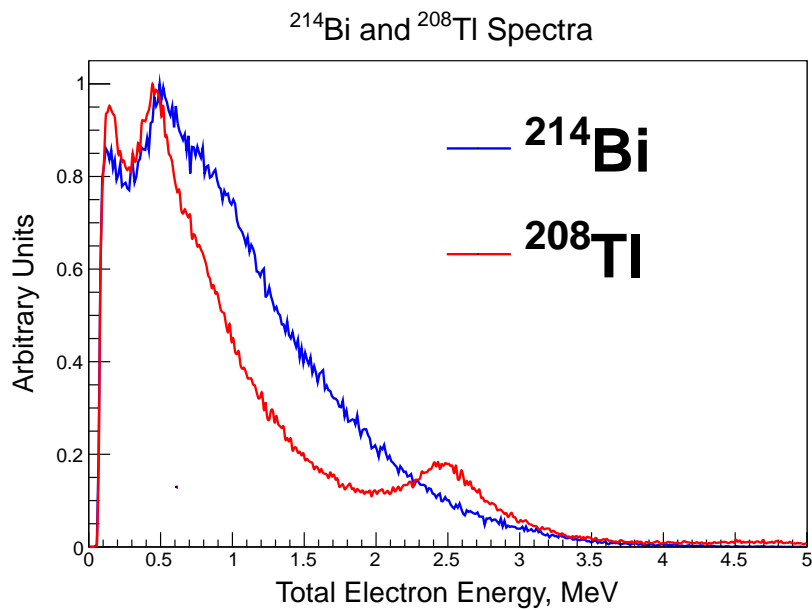


Figure 5.8: Spectra of  $^{214}\text{Bi}$  and  $^{208}\text{Tl}$  combined energies for events mimicking two-electron decays.

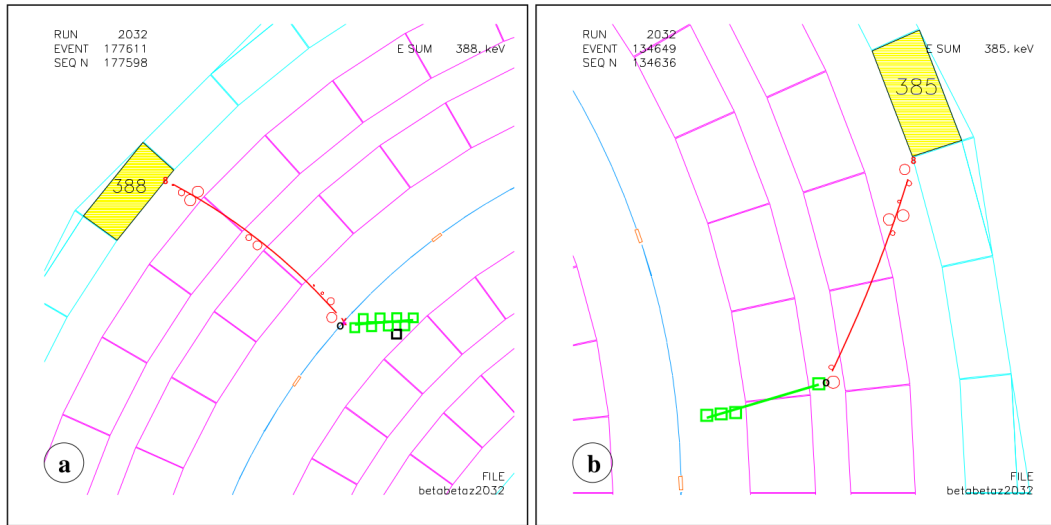


Figure 5.9: Example of  $^{214}\text{Bi}$ - $^{210}\text{Po}$  events in NEMO-3, shown in a top-down event display. A reconstructed electron track is shown in red, and a delayed  $\alpha$  track, shown in green, leave the source foil, shown in blue (left) or tracking chamber wire (right). Inner and outer wall scintillators are shown in cyan and petal scintillators are shown in pink.

#### 5.4.1 Phase I

The initial phase of data taking in NEMO-3, termed Phase I, commenced in February 2003. However, measurements of  $^{222}\text{Rn}$  in the detector remained unacceptably high due to outgassing from the rock surrounding the laboratory. Measurements of  $^{222}\text{Rn}$  during this phase are shown by run in Figure 5.10.

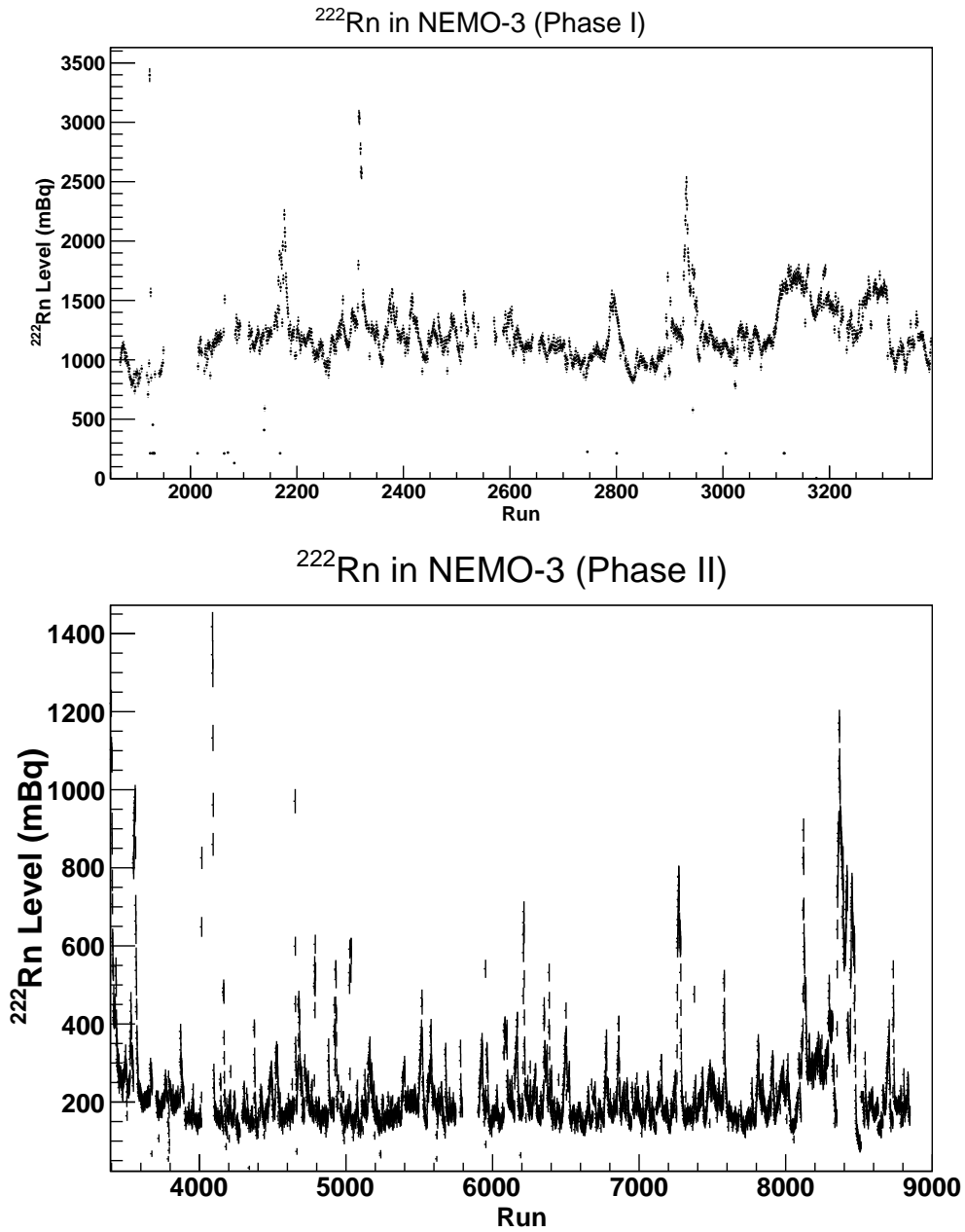


Figure 5.10: Measured  $^{222}\text{Rn}$  by run in Phase I (April 2003 - September 2004, top) and Phase II (October 2004 - December 2010, bottom). Spikes in the  $^{222}\text{Rn}$  level correspond to dates for which the anti-radon system was turned off as a result of power loss, calibration, or other perturbations [93].

### 5.4.2 Phase II

After September 2004, a radon tent was installed around NEMO-3 to reduce the contamination within the detector. The period from the installation of this tent until the end of data taking is known as Phase II, and as a consequence the average radon level in NEMO-3 was demonstrably lower, as shown in the lower half of Figure 5.10. Several periods of markedly increased  $^{222}\text{Rn}$  activity occurred during Phase II, including during and after a fire in the Fréjus tunnel in June 2005. In cases where Radon activity is above acceptable levels, data runs are rejected as unacceptable for inclusion in the analysis. For included runs, the measured Radon levels are accounted for during the analysis by weighting the the contribution of Radon-chain backgrounds at the time of selection.

MC designation	Description
swire	Geiger wire surfaces
sfoil	Source foil surface
sscin	Scintillator surfaces

Table 5.2: Description of the radon background model distribution in NEMO-3.

MC designation	Description
exbg2	LSM air
exbg4	Iron shield
exbg6	Central tower
exbg7	Iron petals
exbg8	PMT magnetic shields
exbg11	PMT glass
exbg17	Copper above petals
scii	Internal wall scintillators
scio	External wall scintillators
scip	Petal scintillators

Table 5.1: Description of the external background model with accompanying Monte Carlo designation.



## Chapter 6

### Single Electron Background Measurements

Of paramount importance in the measurement of  $2\nu\beta\beta$  and  $0\nu\beta\beta$  signals is a thorough understanding of the backgrounds present in the detector. To achieve this goal, a major component in the analysis of NEMO-3 data is the measurement of all known contaminant radioisotopes. The initial background model as measured by high-purity Germanium (HPGe) detectors is comprised entirely of isotopes which are either pure  $\beta$  emitters or  $\beta$  emitters to an excited state, with subsequent release of a  $\gamma$ . However, in several cases the HPGe measurements were only able to set upper limits on background levels, and thus a more accurate measurement using the *in situ* capabilities of NEMO-3 was possible.

As such, this chapter seeks to describe measurements of background contaminants using only events for which a single electron is detected. Measurements of emitters which decay to an excited state and subsequently release a  $\gamma$ -ray are described in chapter 7.

## 6.1 Single-Electron Selection Requirements

To accurately select background-like events, single-electron events are selected to best model the contamination expected in the detector. Note that unlike channels which contain multiple electrons or electrons and  $\gamma$  rays, time of flight calculations cannot be constructed for single electron selection. Selection cuts to achieve this goal can be divided into several categories, moving outward from the foil:

### 6.1.1 Foil Vertex Requirements

Beginning in the source foil, events are selected to match final-state topologies of desired two-electron events. Electron tracks are extrapolated to an origin in the source foil, selecting only those that arise in an appropriate position for the analysis. Selection requirements are also applied to select against high-energy “hot spots” which display unacceptably high levels of background contaminants. a description of individual selection requirements on track vertices is presented below.

- Event origins are reconstructed on the source foil.
- Events originate in the correct sector of the source foil (Sector 18 for  $^{116}\text{Cd}$ , and Sectors 6 - 8 for  $^{82}\text{Se}$ , as described in sections 3.2.4 and 3.2.3, respectively).
- Events must not originate in high-contamination hot spots (see section 6.2 and 6.3 for descriptions).

- Events originate with a vertical foil position of  $< \pm 120$  cm from the center.

### 6.1.2 Tracking Requirements

Selection requirements are applied on the reconstructed particle tracks within the tracking chamber, requiring that particles have tracks characteristic of electrons which exit the source foil, traverse the tracking chamber, and enter the calorimeter. Individual selection requirements are described below.

- Events contain one track consistent with electron curvature and associated to one scintillator.
- Events must register a hit in the first two layers of Geiger cells (0 or 1).
- Events which hit inner layer petals are rejected.
- Events which hit outer layer petals must register a hit in Geiger layer 4 or 5.
- Events which hit main wall calorimeters must register a hit in the last two Geiger layers (7 or 8).
- Electron tracks must be a minimum of 50 cm.

### 6.1.3 Calorimetry Requirements

Calorimetric requirements are applied to ensure that each selected electron deposits sufficient energy for accurate measurement by the NEMO-3 calorimeter, as well as to reduce scattering from neighboring scintillators and mis-measurement from noisy PMTs. Additionally, laser time corrections must also exist in the database to ensure accurate event timing.

- Electrons must deposit a minimum of 500 keV in the scintillator.

- Electrons must enter the front face of the scintillator.
- The PMT associated with the track must have a laser time correction.
- The PMT associated with the track must not have excessive electronic noise.

## 6.2 $^{116}\text{Cd}$ Foil Description

Projecting the vertex of all selected 1e events from the  $^{116}\text{Cd}$  sector reveals that there are distinct regions of high activity, resulting from contamination occurring largely at the end of individual foil strips and visible clearly in Figure 6.1. In addition, contaminated areas at the top and bottom of the foil are also evident; these events originate in the clips with which the source foil is attached to the frame. As described in section 6.1.1, events originating in either foil hot spots or in the foil clips (defined as events outside  $< \pm 120$  cm from the foil center), are rejected.

The  $^{116}\text{Cd}$  foils are divided into a low-activity and a high-activity region based on their enrichment levels to provide a more accurate measurement. High-energy hot spots are rejected. Individual region vertex projections for the low- and medium-activity regions are shown in Figure 6.2.

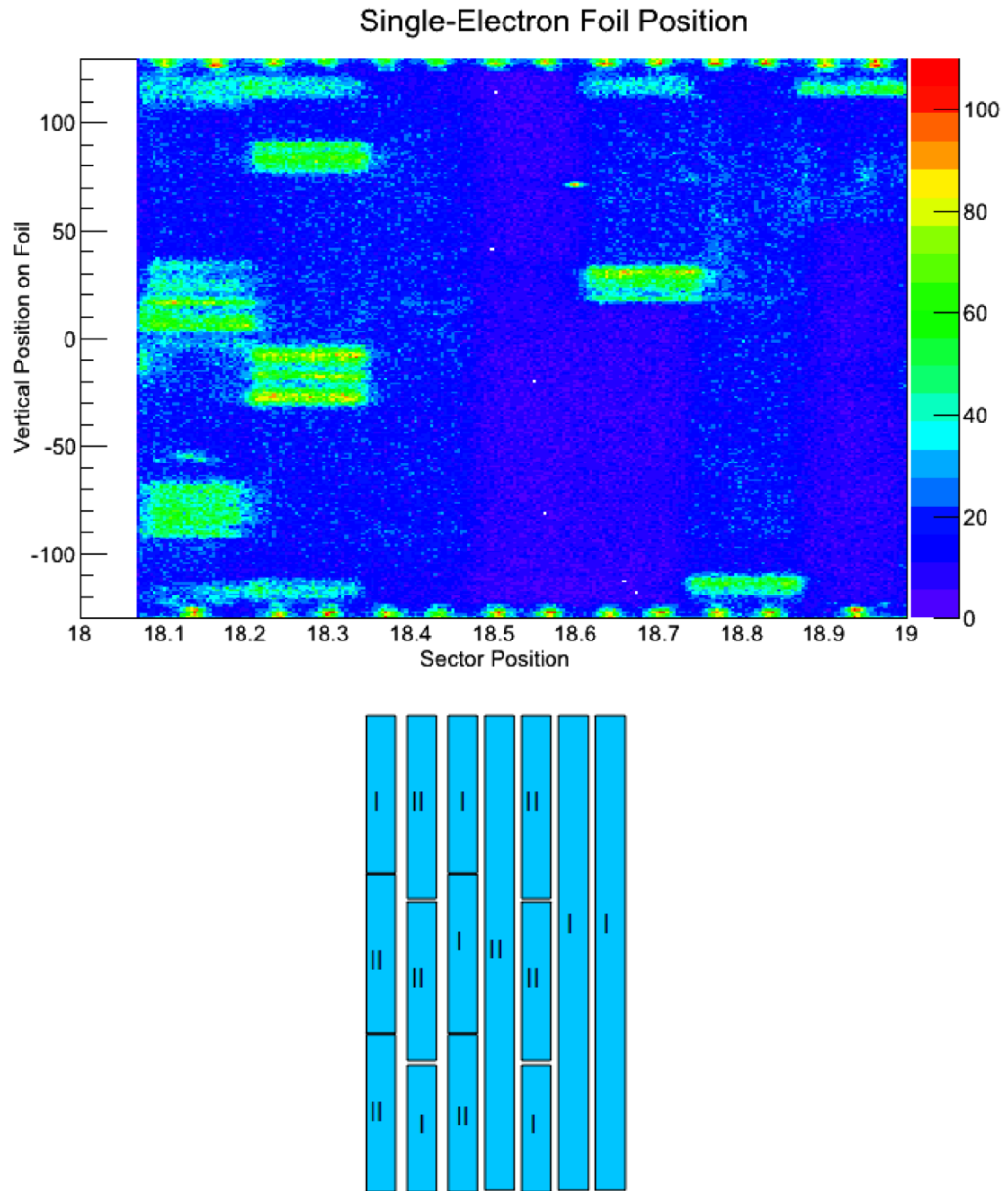


Figure 6.1: Top: Positions of  $^{116}\text{Cd}$  single-electron events on the source foil. The X axis refers to the sector position in NEMO-3.  $^{116}\text{Cd}$  occupied the entirety of sector 18. Bottom: View of individual foils composing Sector 18. I and II refer to the  $^{116}\text{Cd}$  productions.

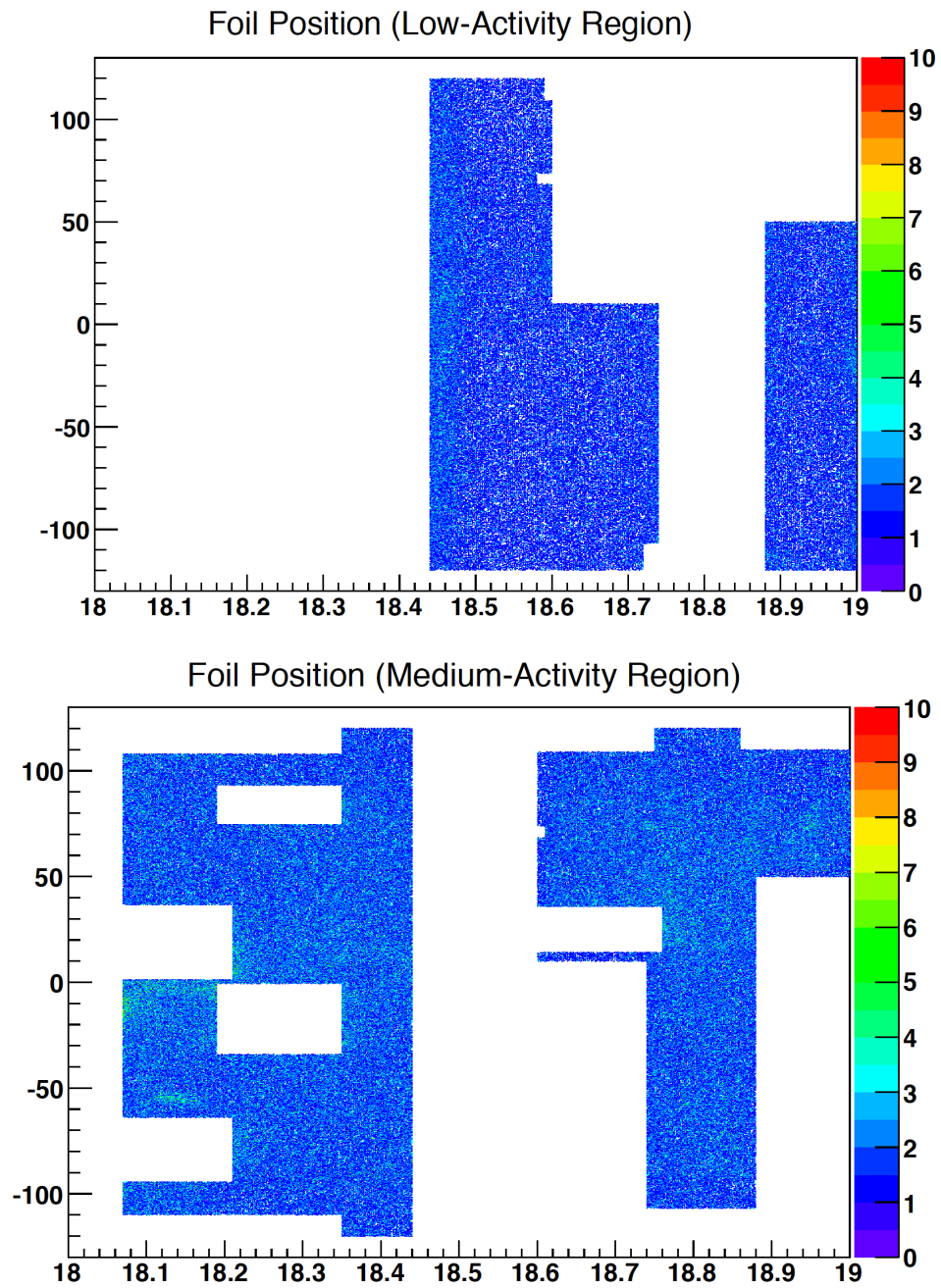


Figure 6.2: Vertex positions of single-electron events in the low- (top) and medium-activity (bottom) regions of the  $^{116}\text{Cd}$  foil.

### 6.2.1 Phase I

Measured single-electron energy spectra are shown for the low-activity (medium-activity) region in figures 6.2.1 and 6.2.1) in Phase I with best-fit values for the isotopes  $^{40}\text{K}$ ,  $^{234m}\text{Pa}$ , and  $^{210}\text{Bi}$  shown in yellow, orange, and cyan, respectively. Measured best-fit activities for these isotopes are given in Table 6.1.

Isotope	Location	Low-Activity Region Activity (mBq)	Medium-Activity Region Activity (mBq)
$^{40}\text{K}$	Internal Source Foil	$3.39 \pm 0.05$	$8.39 \pm 0.04$
$^{234m}\text{Pa}$	Internal Source Foil	$0.36 \pm 0.10$	$1.01 \pm 0.12$
$^{210}\text{Bi}$	Foil Surfaces	$(2.12 \pm 0.01) \times 10^3$	

Table 6.1: Summary of background isotopes measured in the single-electron channel for  $^{116}\text{Cd}$  in Phase I. Spectra for  $^{214}\text{Bi}$  (yellow),  $^{234m}\text{Pa}$ , and  $^{40}\text{K}$  (cyan) are shown with best-fit values to the data (black points) after the inclusion of combined internal (blue), external (dark green), and radon (light green) backgrounds.

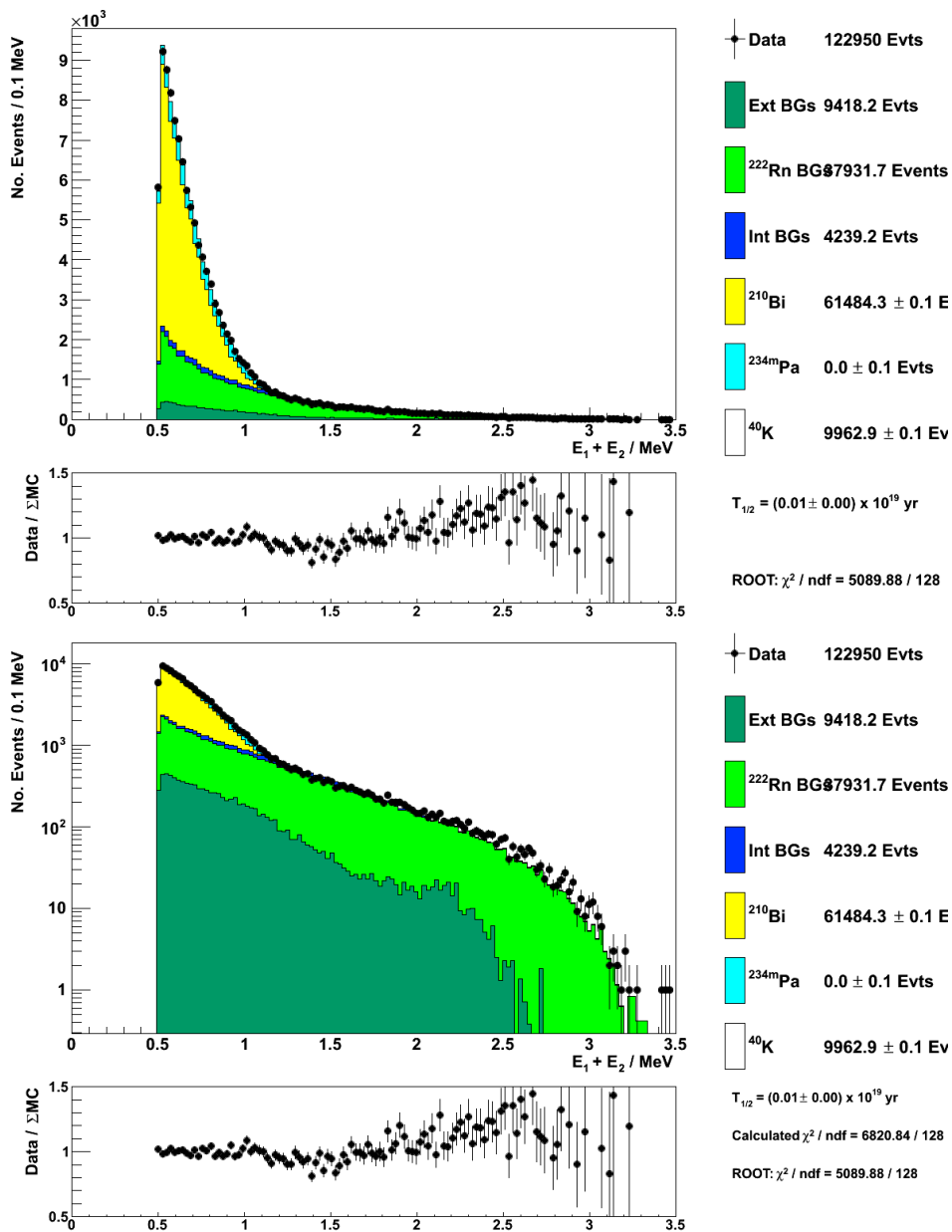


Figure 6.3: Electron energy spectrum for the low-activity Phase I data set in linear (top) and log (bottom) scales. Spectra for  $^{210}\text{Bi}$  (yellow),  $^{234m}\text{Pa}$ , and  $^{40}\text{K}$  (cyan) are shown with best-fit values to the data (black points) after the inclusion of combined internal (blue), external (dark green), and radon (light green) backgrounds.



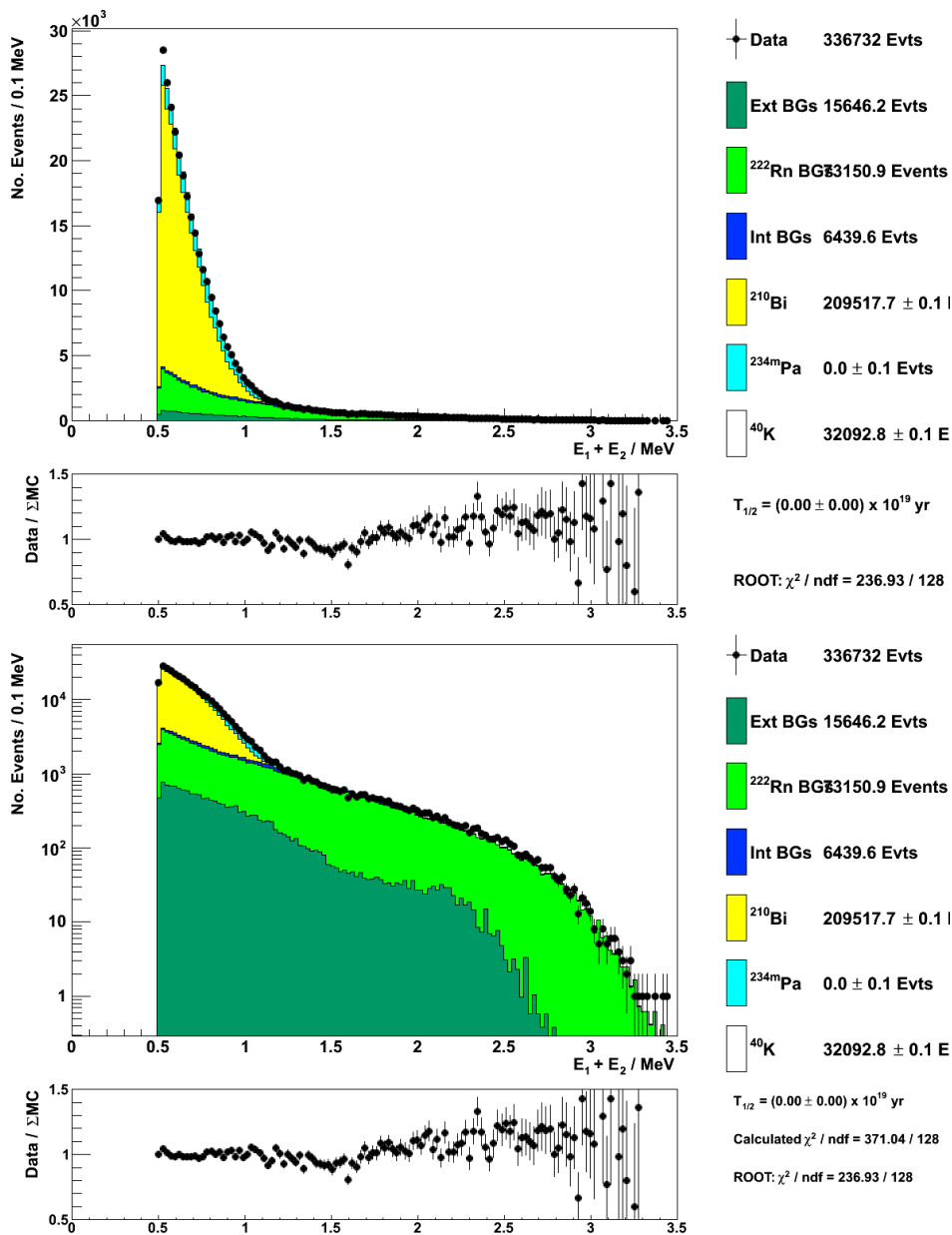


Figure 6.4: Electron energy spectrum for the medium-activity Phase I data set in linear (top) and log (bottom) scales. Spectra for  $^{210}\text{Bi}$  (yellow),  $^{234m}\text{Pa}$ , and  $^{40}\text{K}$  (cyan) are shown with best-fit values to the data (black points) after the inclusion of combined internal (blue), external (dark green), and radon (light green) backgrounds.

### 6.2.2 Phase II

Measured single-electron energy is shown for the low-energy region (Figure 6.2.2) and medium-energy region (Figure 6.2.2) in Phase II with best-fit values for the isotopes  $^{40}\text{K}$ ,  $^{234m}\text{Pa}$ , and  $^{210}\text{Bi}$  shown in yellow, orange, and cyan respectively. Measured best-fit activities for these isotopes are given in Table 6.2.2.

Isotope	Location	Low-Activity Region Activity (mBq)	Medium-Activity Region Activity (mBq)
$^{40}\text{K}$	Internal Source Foil	$3.370 \pm 0.10$	$8.40 \pm 0.11$
$^{234m}\text{Pa}$	Internal Source Foil	$0.36 \pm 0.38$	$0.997 \pm 0.35$
$^{210}\text{Bi}$	Foil Surfaces	$(1.25 \pm 0.01) \times 10^3$	

Table 6.2: Summary of background isotopes measured in the single-electron channel for Phase II in  $^{116}\text{Cd}$ .

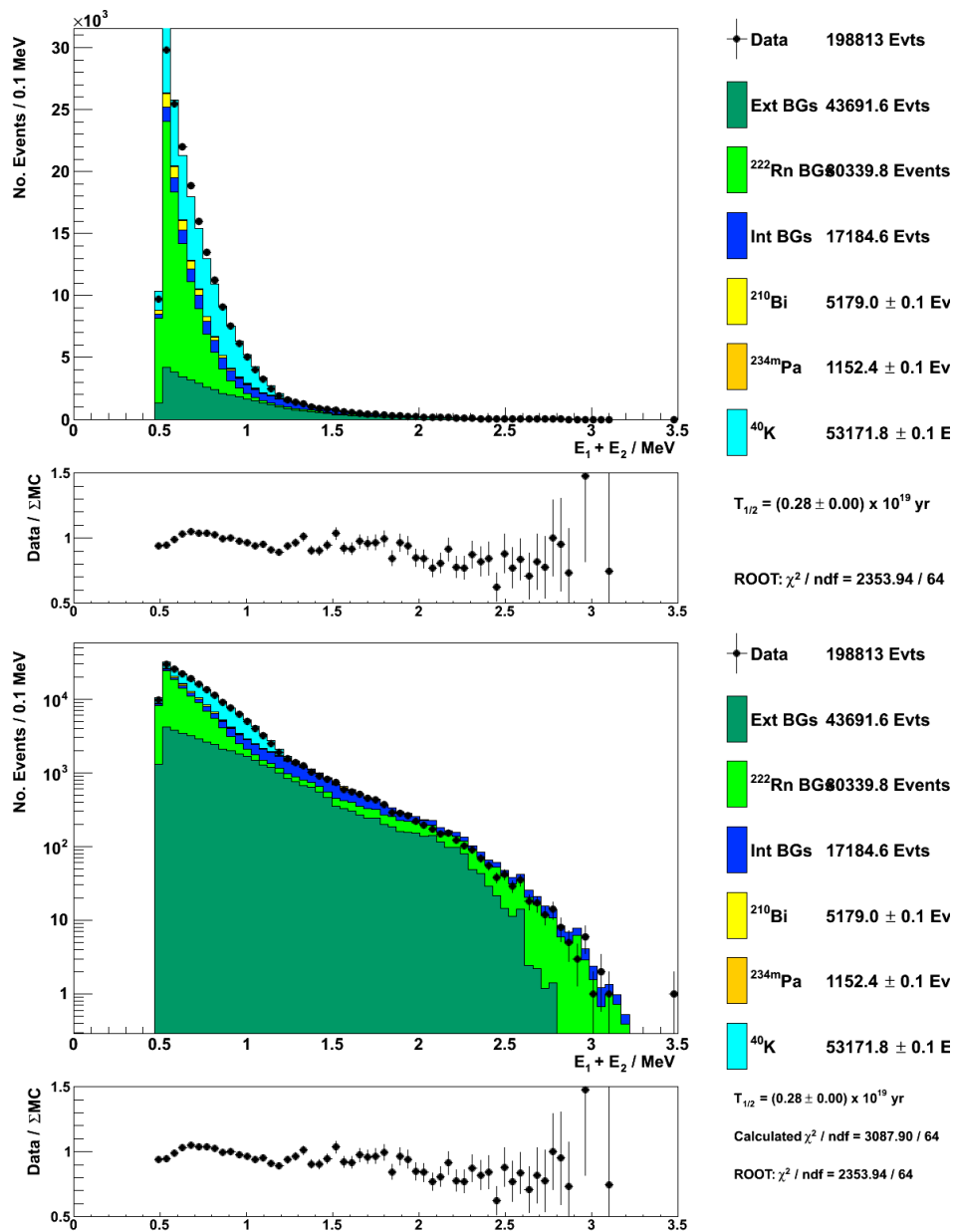


Figure 6.5: Electron energy spectrum for the low-activity Phase II data set in linear (top) and log (bottom) scales. Spectra for  $^{210}\text{Bi}$  (yellow),  $^{234m}\text{Pa}$ , and  $^{40}\text{K}$  (cyan) are shown with best-fit values to the data (black points) after the inclusion of combined internal (blue), external (dark green), and radon (light green) backgrounds.

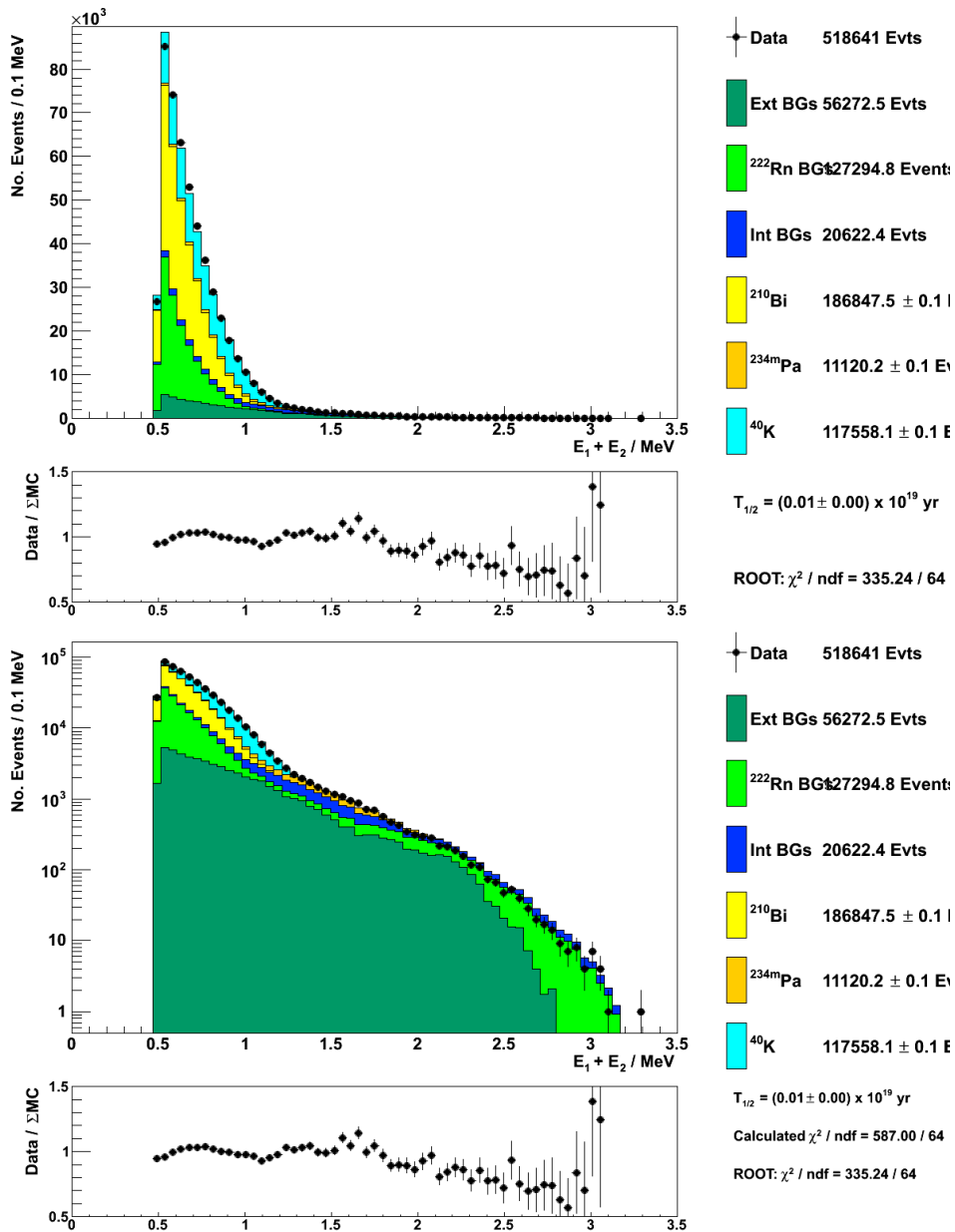


Figure 6.6: Electron energy spectrum for the medium-activity Phase II data set in linear (top) and log (bottom) scales. Spectra for  $^{210}\text{Bi}$  (yellow),  $^{234m}\text{Pa}$ , and  $^{40}\text{K}$  (cyan) are shown with best-fit values to the data (black points) after the inclusion of combined internal (blue), external (dark green), and radon (light green) backgrounds.

### 6.3 $^{82}\text{Se}$ Foil Description

As noted in section 3.2.3, the  $^{82}\text{Se}$  foils were made in two different batches, known to have slightly different enrichment values. In addition, several high-activity “hot spots” were also known to be present from prior experience from their usage in NEMO-2. Furthermore, the relatively high-activity  $^{207}\text{Bi}$  calibration source windows also contributed to background in their vicinity. A plot of single-electron event vertices projected onto the foil before and after removing these hot spots is shown in Figure 6.7.

### 6.4 $^{82}\text{Se}$ One-Electron Results

#### 6.4.1 Phase I

The fitted electron energy spectrum for the  $^{82}\text{Se}$  sectors is shown in Figure 6.4.1. The isotopes  $^{40}\text{K}$  and  $^{234m}\text{Pa}$  are fitted separately for Se(I) and Se(II) sectors, while  $^{210}\text{Bi}$  is fitted as an external background and displayed in orange and cyan, respectively, in the Se(I) sectors and grey and red in Se(II). Best-fit values are given in table 6.3.

Phase I			
Isotope	Location	Se(I) Activity	Se(II) Activity
$^{40}\text{K}$	Internal Source Foil	$(5.82 \pm 0.63) \times 10^{-2}$	$(4.26 \pm 1.4) \times 10^{-2}$
$^{234m}\text{Pa}$	Internal Source Foil	$(1.25 \pm 0.43) \times 10^{-2}$	$(4.24 \pm 1.4) \times 10^{-2}$
$^{210}\text{Bi}$	Foil Surfaces	$2.66 \pm 0.01$	

Table 6.3: Summary of background isotopes measured in the single-electron channel.

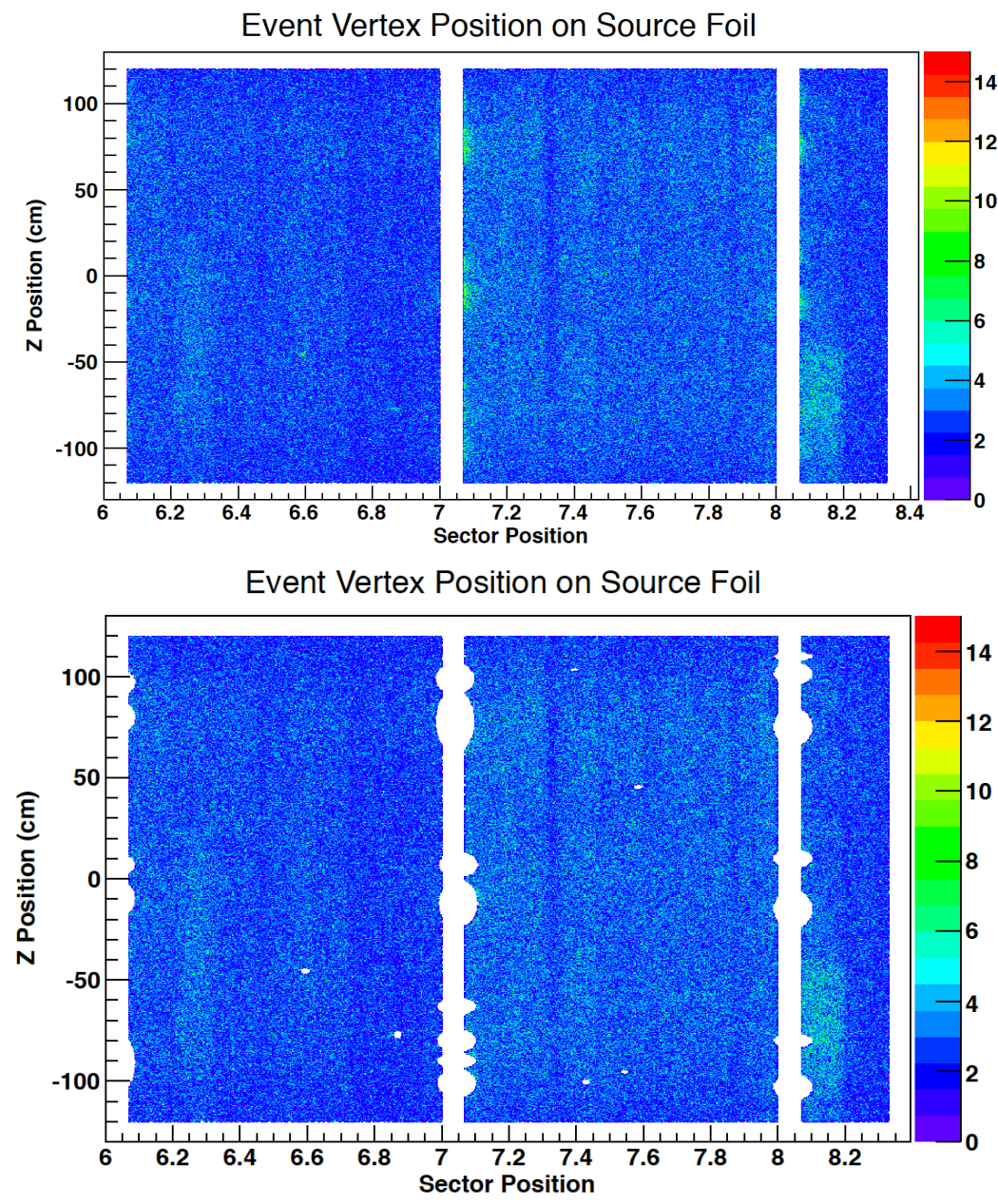


Figure 6.7: Single-electron event vertices projected onto the source foil in the  $^{82}\text{Se}$  sectors before (top) and after (bottom) removing high-activity “hot spots”.

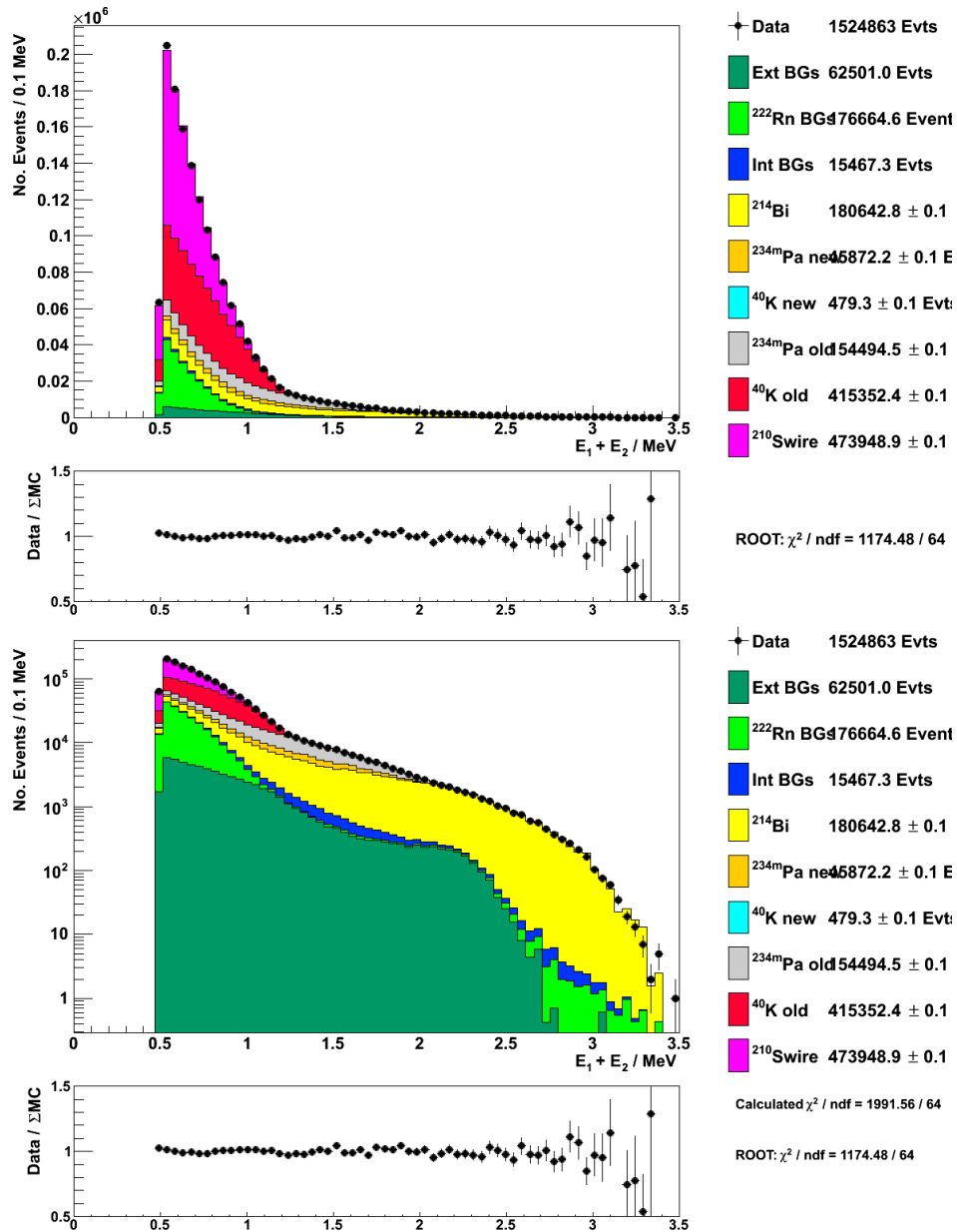


Figure 6.8: Electron energy spectrum for the  $^{82}\text{Se}$  Phase I data set in linear (top) and log (bottom) scales. Best-fit values for  $^{234m}\text{Pa}$   $^{40}\text{K}$  are shown for the Se(I) (Se(II)) sample in orange and cyan (grey and red). Best-fit values of  $^{214}\text{Bi}$  and  $^{210}\text{Bi}$  are shown in yellow and pink.



### 6.4.2 Phase II

The fitted electron energy spectrum for the  $^{82}\text{Se}$  sectors is shown in Figure 6.4.1.  $^{40}\text{K}$  is fitted separately for Se(I) and Se(II) sectors, while  $^{210}\text{Bi}$  is fitted as an external background. These isotopes are shown in orange and cyan, respectively, in the Se(I) sector and in grey and red in Se(II). Best-fit values are given in table 6.4.2.

Isotope	Location	Se(I) Activity	Se(II) Activity
$^{40}\text{K}$	Internal Source Foil	$4.30 \pm 2.07$	$5.40 \pm 2.32$
$^{234m}\text{Pa}$	Internal Source Foil	$1.51 \pm 1.23$	$(1.78 \pm 0.08) \times 10^{-2}$
$^{210}\text{Bi}$	Foil Surfaces	$1.69 \pm 0.01$	

Table 6.4: Summary of background isotopes measured in the single-electron channel.

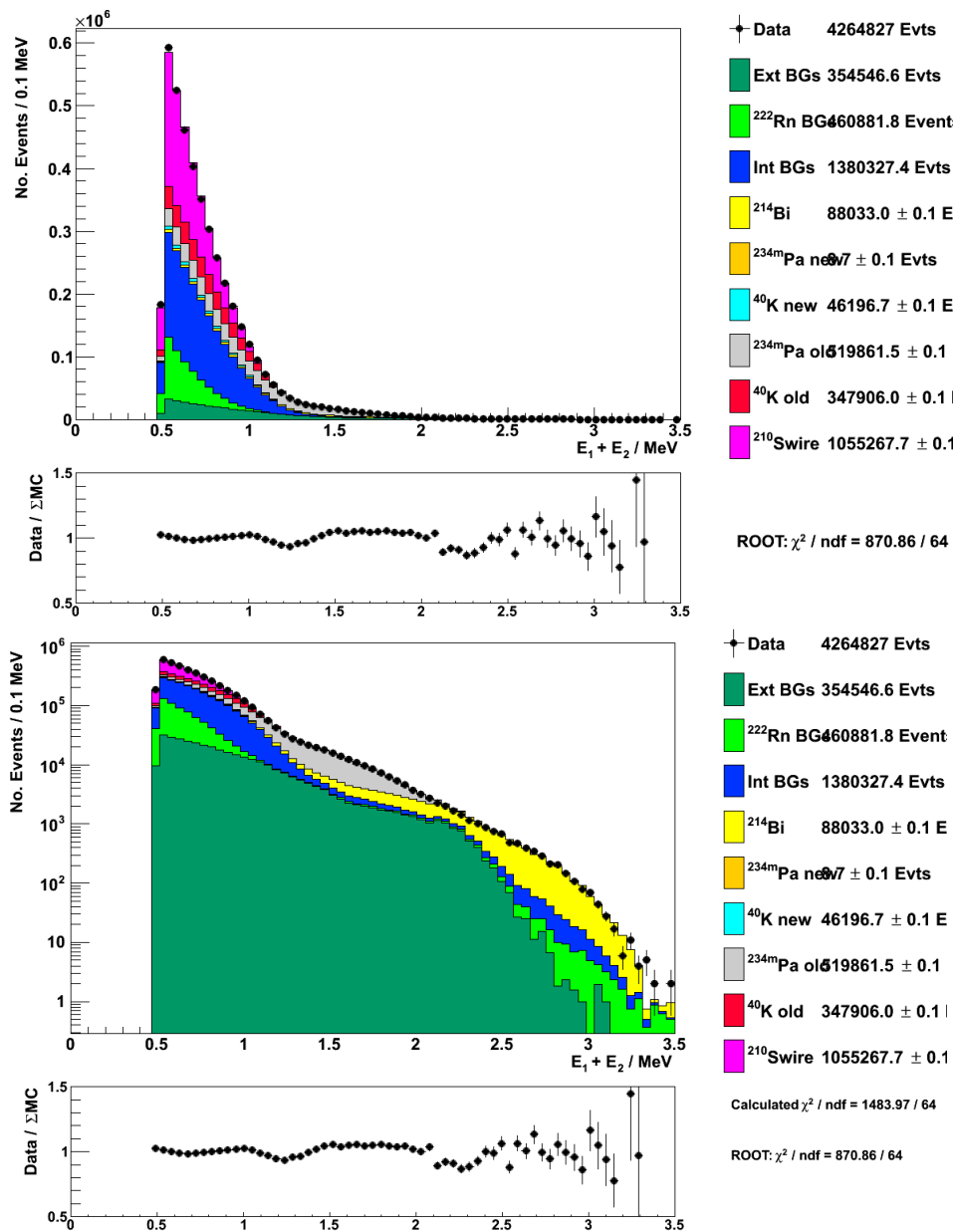


Figure 6.9: Electron energy spectrum for the  $^{82}\text{Se}$  Phase II data set in linear (top) and log (bottom) scales. Best-fit values for  $^{234m}\text{Pa}$   $^{40}\text{K}$  are shown for the Se(I) (Se(II)) sample in orange and cyan (grey and red). Best-fit values of  $^{214}\text{Bi}$  and  $^{210}\text{Po}$  are shown in yellow and pink.

## 6.5 Single-electron Measurement Summary

Single-electron events recorded in NEMO-3 have been used to measure the contamination from  $\beta$  emitters originating in the NEMO-3 internal source foil, detector structure, and radon present in the detector. Cadmium source foils have been divided into low- and medium-activity regions for analysis, and each has been analyzed separately to fit the levels of  $^{210}\text{Bi}$ ,  $^{40}\text{K}$ , and  $^{234m}\text{Pa}$  contamination. The same  $\beta$ -emitting contaminants were measured in the Selenium source foils, with internal contamination from  $^{40}\text{K}$  and  $^{234m}\text{Pa}$  fitted separately for the two Selenium enrichment regions. Results were reported for all foil regions in both Phase I and Phase II of NEMO-3 data taking.

Background levels have been measured more precisely *in situ* than previously-measured HPGe limits, allowing development of a more accurate background model for the  $2\nu\beta\beta$  and  $0\nu\beta\beta$  channels.

## Chapter 7

### Electron- $\gamma$ Background Measurements

In combination with the single-electron channel as described in chapter 6, the electron- $\gamma$  (1e1 $\gamma$ ) and electron- $\gamma\gamma$  (1e2 $\gamma$ ) channels are utilized in measuring the contamination in NEMO-3. The 1e1 $\gamma$  and 1e2 $\gamma$  channels are particularly sensitive to the pernicious isotopes  $^{208}\text{Tl}$  and  $^{214}\text{Bi}$ , both of which are  $\beta$  emitters which decay to excited nuclear states. Detailed information about decays of these isotopes relevant to NEMO-3 is available in Appendix G.

This chapter will describe the selection and measurement of backgrounds in the 1e1 $\gamma$  and 1e2 $\gamma$  channels and provide results to be used in the final background model of NEMO-3 for double beta decays.

#### 7.1 Electron- $\gamma$ Selection Requirements

To accurately model the background contamination in the electron- $\gamma$  channel, selection cuts were chosen to best reconstruct events from the target isotopes  $^{214}\text{Bi}$  and  $^{208}\text{Tl}$ . Cuts are separated by type, moving outward from the source foil.

### 7.1.1 Foil Vertex Cuts

Beginning in the source foil, events are selected to match final-state topologies of desired electron- $\gamma$  events. Electron tracks are extrapolated to an origin in the source foil, selecting only those that arise in an appropriate position for the analysis. Selection requirements are also applied to select against high-energy “hot spots” which are observed to have unacceptable levels of background contaminants. a description of individual selection requirements on track vertices is presented below.

- Events originate in the source foil.
- Events originate in the correct sector of the source foil (Sector 18 for  $^{116}\text{Cd}$ , and Sectors 6 - 8 for  $^{82}\text{Se}$ , as described in sections 3.2.4 and 3.2.3, respectively.
- Events must not originate in high-contamination hot spots.
- Events originate with a vertical foil position of  $< \pm 120$  cm from the center.

### 7.1.2 Tracking Cuts

Selection requirements are applied on the reconstructed particle tracks within the tracking chamber, requiring that particles have tracks characteristic of electrons which exit the source foil, traverse the tracking chamber, and enter the calorimeter. Photons are non-ionizing particles, and thus do not leave tracks in the chamber. Electron tracks must have sufficient length to allow for calculation of internal and external time-of-flight hypotheses, which are then

applied to further distinguish between events originating in the foil and those arising elsewhere. Individual selection requirements are described below.

- Events contain one track consistent with electron curvature and associated to one scintillator and one scintillator hit unassociated to any track.
- Electron tracks must register a hit in the first two layers of Geiger cells (0 or 1).
- Events which hit inner layer petals are rejected.
- Electrons which hit outer layer petals must register a hit in Geiger layer 4 or 5.
- Electrons which hit main wall calorimeters must register a hit in the last two Geiger layers (7 or 8).
- Electron tracks must be a minimum of 50 cm.
- Internal time-of-flight probability for the event must be greater than 10%.
- External time-of-flight probability for the event must be less than 1%.

### 7.1.3 Calorimetry Cuts

Calorimetric requirements are applied to ensure that each selected electron deposits sufficient energy for accurate measurement by the NEMO-3 calorimeter, as well as to reduce scattering from neighboring scintillators and mis-measurement from noisy PMTs. Photons recorded in the calorimeter must be unassociated to any tracks. Additionally, laser time corrections must also exist in the database to ensure accurate event timing for the calculation of time-of-flight hypotheses.

- Electrons must deposit a minimum of 500 keV in the scintillator.
- $\gamma$ s must deposit a minimum of 200 keV in the scintillator.
- Electrons must enter the front face of the scintillator.
- The PMT associated with the track must have a laser time correction.
- The PMT associated with the track must not have excessive electronic noise.

## 7.2 $^{116}\text{Cd}$ Electron- $\gamma$ Results

This section describes the measurement of  $^{214}\text{Bi}$  and  $^{208}\text{Tl}$  contamination in the  $^{116}\text{Cd}$  sector of NEMO-3. Best fits for the background model are shown broken down by phase (I and II) and are shown separately for the low- and medium-activity regions.

### 7.2.1 Phase I

Energy spectra for the emitted electron and  $\gamma$  ray are shown for the low-activity region (medium-activity region) in Figure 7.2 (Figure 7.3). Combined electron- $\gamma$  energies are shown in figures 7.1 and 7.4. Best-fit values for isotopes fitted in the electron- $\gamma$  channel are presented in Table 7.2.1 for the medium- and low-activity regions.

Isotope	Location	Medium Activity Region Activity (Bq)	Low Activity Region Activity (Bq)
$^{214}\text{Bi}$	Foil Surface	$(8.54 \pm 0.66) \times 10^{-2}$	$(7.67 \pm 0.05) \times 10^{-2}$
$^{208}\text{Tl}$	Foil Internal	$(4.0 \pm 0.01) \times 10^{-5}$	$(1.70 \pm 0.05) \times 10^{-2}$
$^{214}\text{Bi}$	Wire Surface	$1.12 \pm 0.02$	

Table 7.1: Summary of measured background activities in the electron- $\gamma$  channel for Phase I.

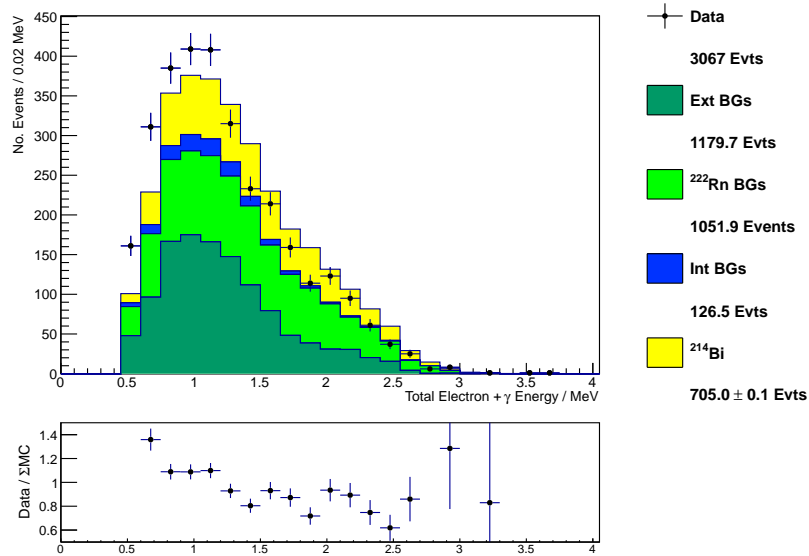


Figure 7.1: Combined electron- $\gamma$  energy for the Phase I low-activity region  $^{116}\text{Cd}$  data set. The  $^{214}\text{Bi}$  spectrum (yellow) has been fitted to the data (shown as black points) after inclusion of internal (blue), external (dark green), and radon (light green) backgrounds. The contribution from  $^{208}\text{Tl}$  is too small to be visible.



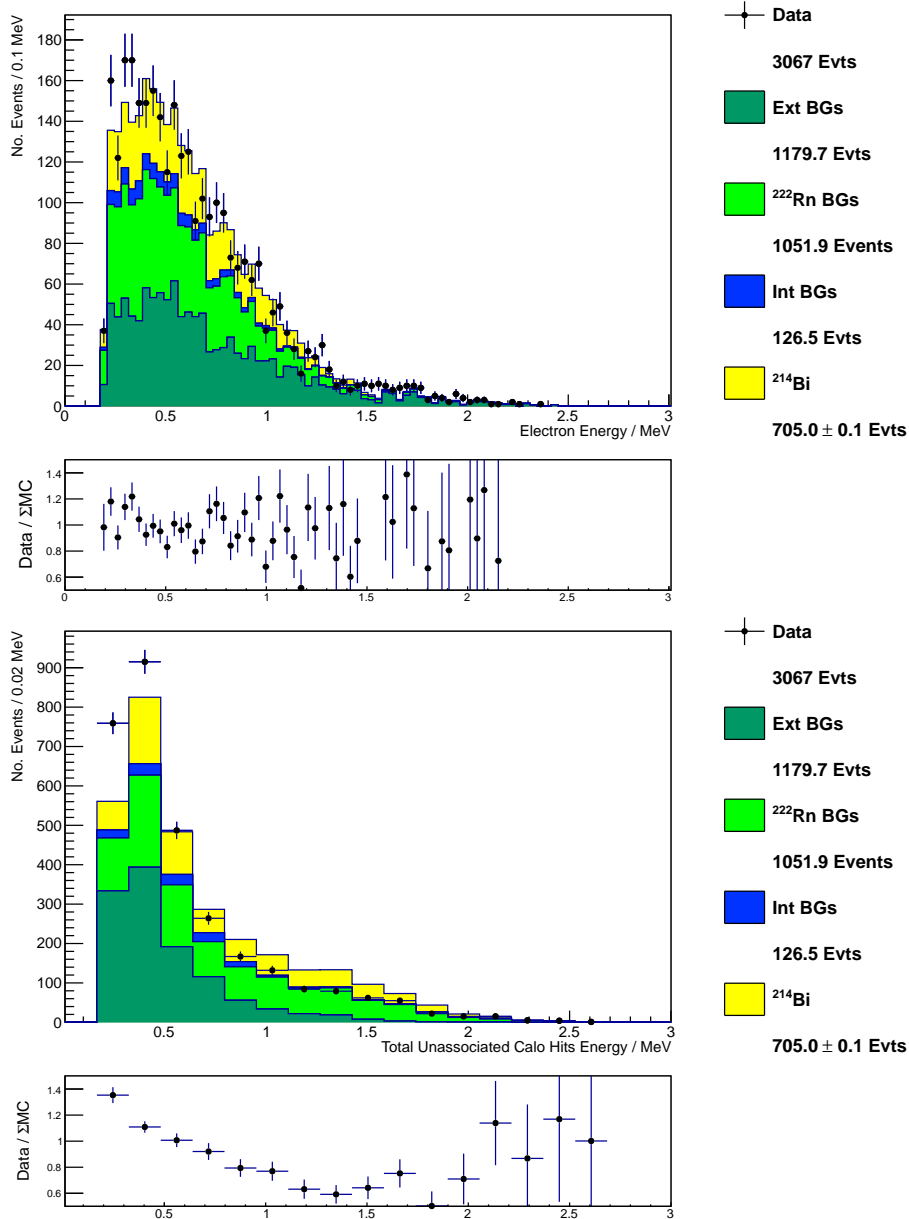


Figure 7.2: Electron (top) and  $\gamma$  (bottom) energy for the Phase I low-activity region  $^{116}\text{Cd}$  data set. The  $^{214}\text{Bi}$  spectrum (yellow) has been fitted to the data (shown as black points) after inclusion of internal (blue), external (dark green), and radon (light green) backgrounds. The contribution from  $^{208}\text{Tl}$  is too small to be visible.

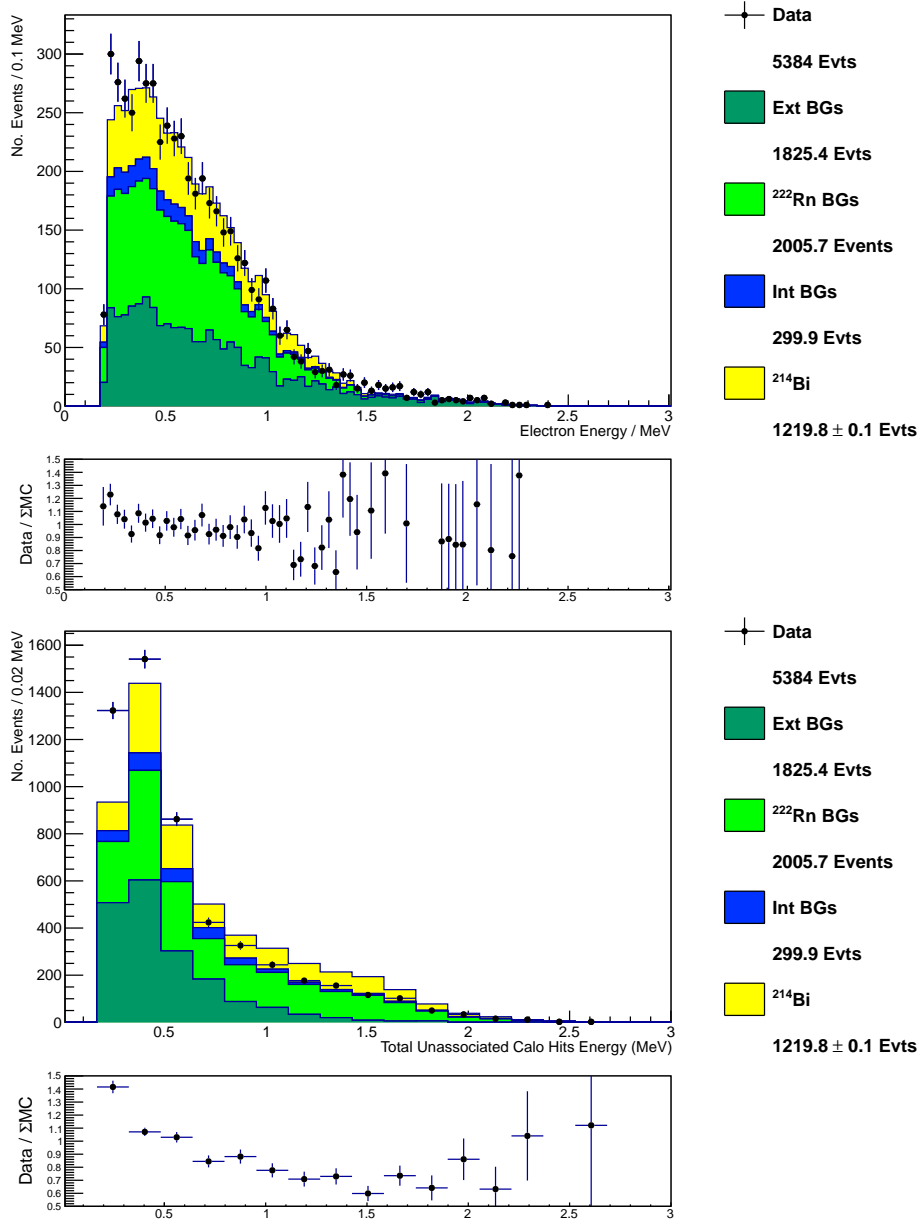


Figure 7.3: Electron (top) and  $\gamma$  (bottom) energy for the Phase I medium-activity region  $^{116}\text{Cd}$  data set. The  $^{214}\text{Bi}$  spectrum (yellow) has been fitted to the data (shown as black points) after inclusion of internal (blue), external (dark green), and radon (light green) backgrounds. The contribution from  $^{208}\text{Tl}$  is too small to be visible.

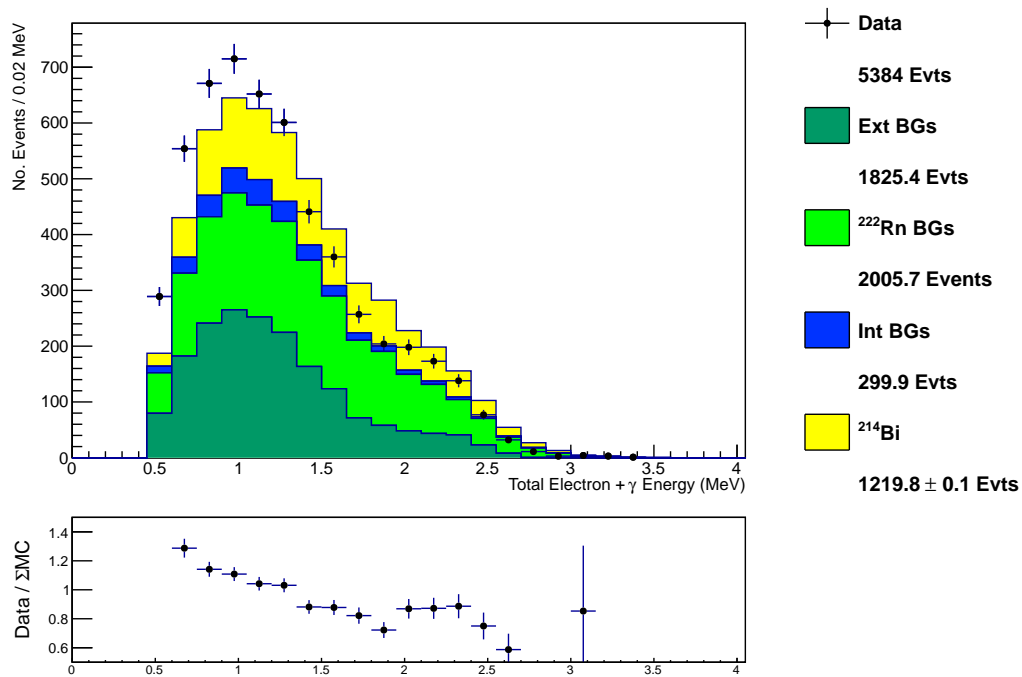


Figure 7.4: Combined electron- $\gamma$  energy for the Phase I medium-activity region  $^{116}\text{Cd}$  data set. The  $^{214}\text{Bi}$  spectrum (yellow) has been fitted to the data (shown as black points) after inclusion of internal (blue), external (dark green), and radon (light green) backgrounds. The contribution from  $^{208}\text{Tl}$  is too small to be visible.

### 7.2.2 Phase II

This section presents results of measurements of electron- $\gamma$  emitters in Phase II of NEMO-3. Energy spectra for the emitted electron and  $\gamma$  ray are shown for the low-activity region (medium-activity region) in Figure 7.5 (Figure 7.11). Combined electron- $\gamma$  energies are shown in figures 7.6 and 7.12.

Isotope	Location	Se(I) Activity ( Bq)	Se(II) Activity ( Bq)
$^{214}\text{Bi}$	Foil Surfaces	$(2.38 \pm 0.28) \times 10^{-2}$	$(3.42 \pm 0.20) \times 10^{-2}$
$^{208}\text{Tl}$	Foil Internal	$(1.75 \pm 0.12) \times 10^{-5}$	$(4.00 \pm 0.08) \times 10^{-5}$
$^{214}\text{Bi}$	Wire Surfaces	$0.20 \pm 0.02$	$0.20 \pm 0.02$

Table 7.2: Summary of measured background activities in the  $^{116}\text{Cd}$  electron- $\gamma$  channel for Phase II.

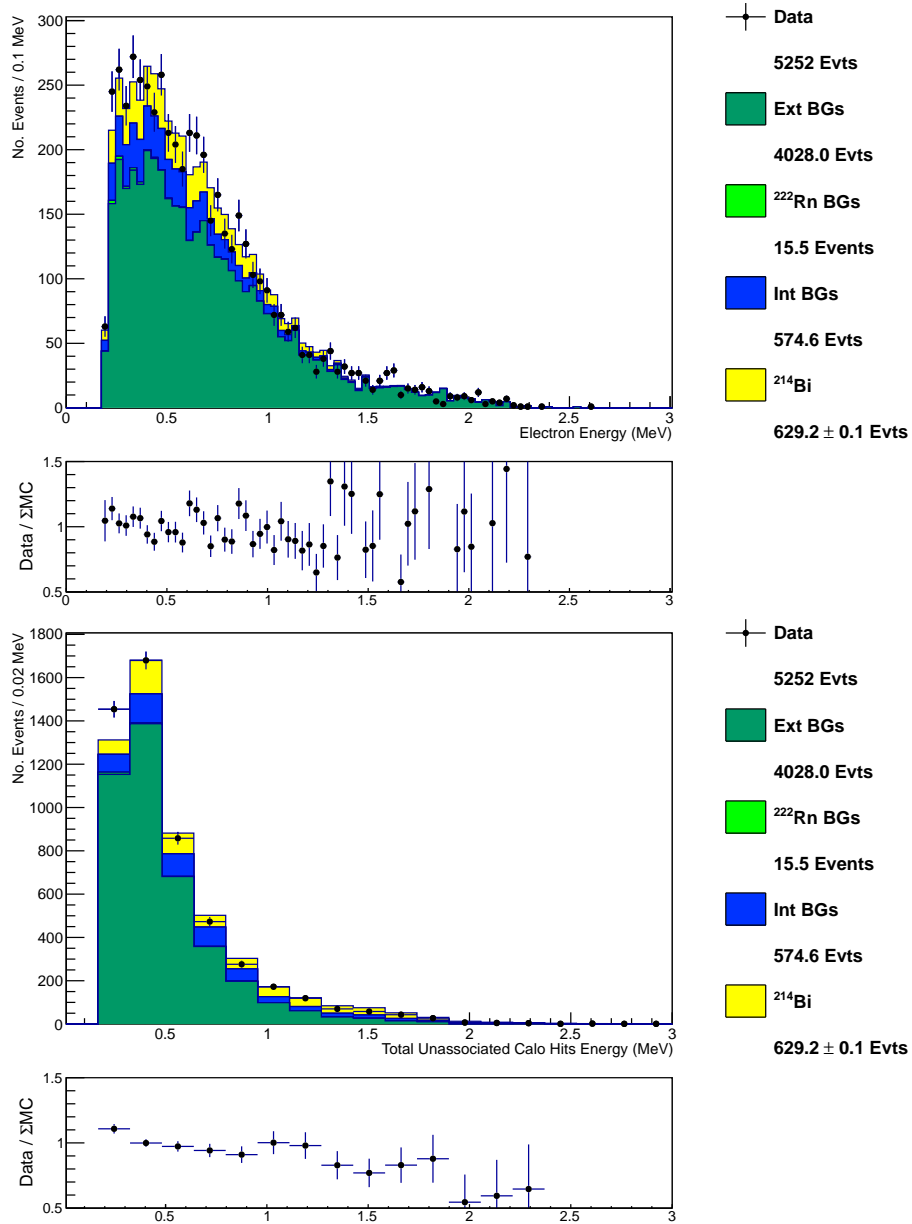


Figure 7.5: Electron energy for the Phase II low-activity region  $^{116}\text{Cd}$  data set. The  $^{214}\text{Bi}$  spectrum (yellow) has been fitted to the data (shown as black points) after inclusion of internal (blue), external (dark green), and radon (light green) backgrounds. The contribution from  $^{208}\text{Tl}$  is too small to be visible.

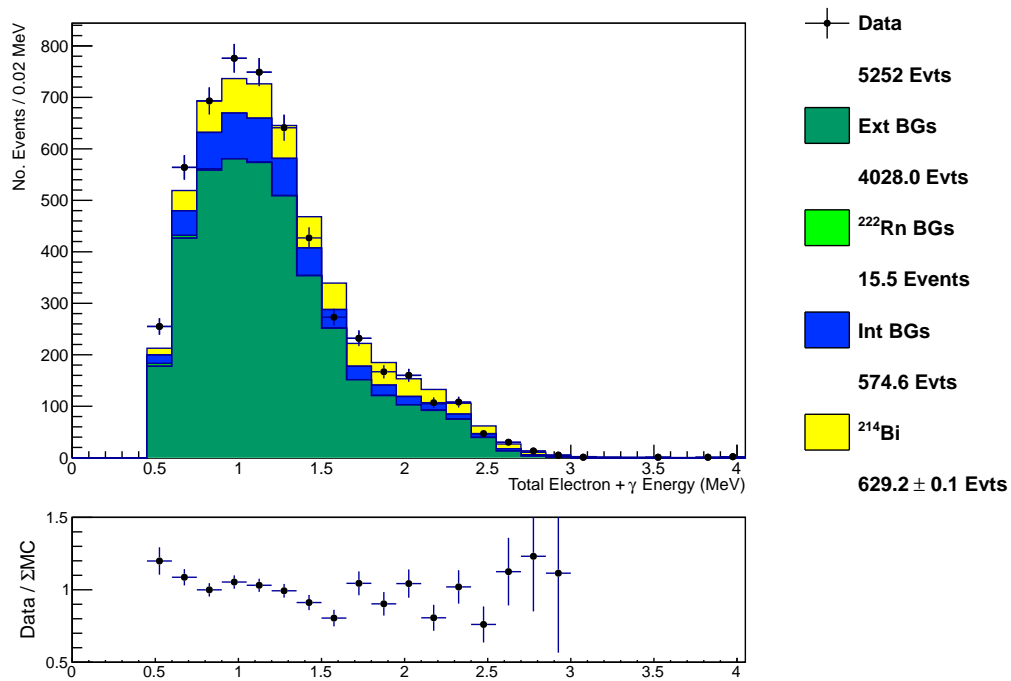


Figure 7.6: Combined electron- $\gamma$  energy for the Phase II low-activity region  $^{116}\text{Cd}$  data set. The  $^{214}\text{Bi}$  spectrum (yellow) has been fitted to the data (shown as black points) after inclusion of internal (blue), external (dark green), and radon (light green) backgrounds. The contribution from  $^{208}\text{Tl}$  is too small to be visible.

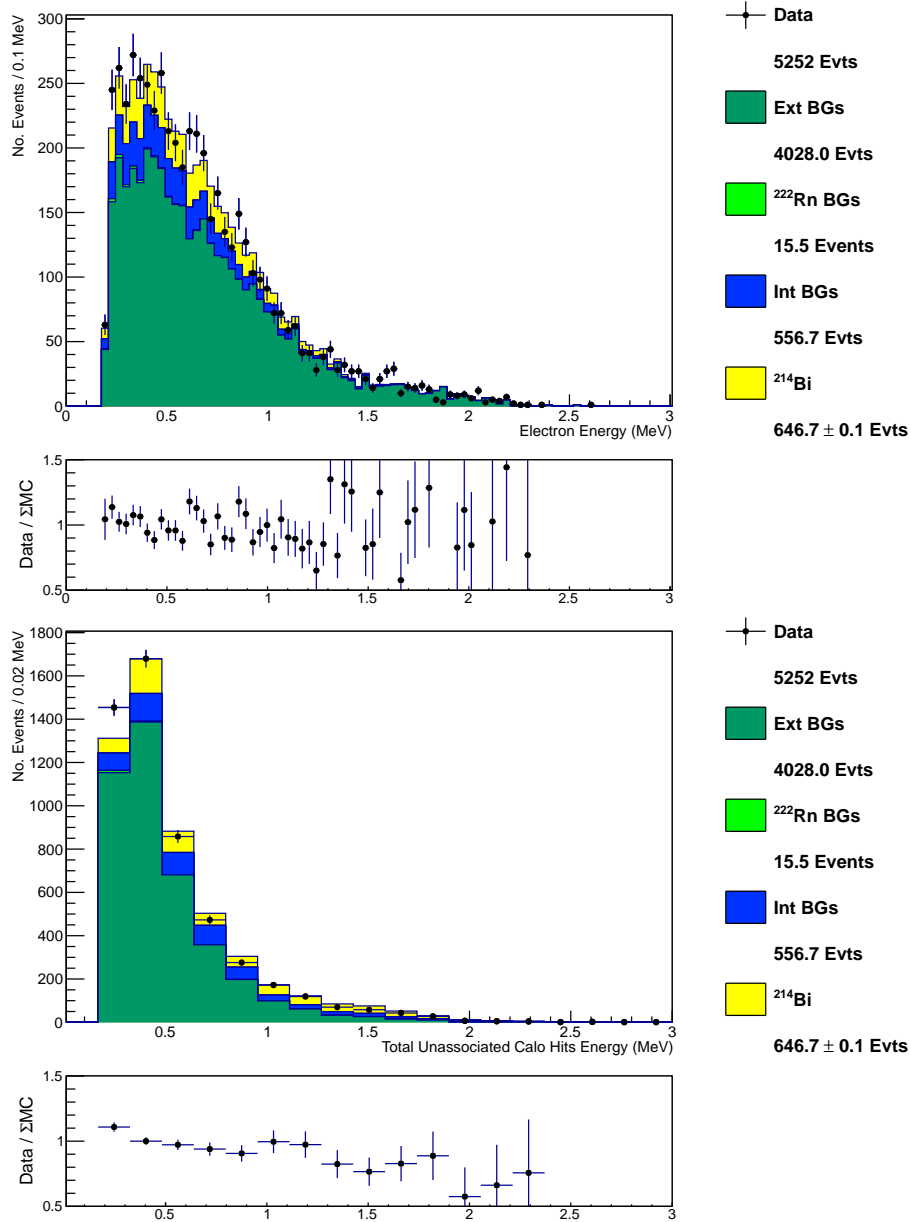


Figure 7.7: Electron energy for the Phase II medium-activity region  $^{116}\text{Cd}$  data set. The  $^{214}\text{Bi}$  spectrum (yellow) has been fitted to the data (shown as black points) after inclusion of internal (blue), external (dark green), and radon (light green) backgrounds. The contribution from  $^{208}\text{Tl}$  is too small to be visible.

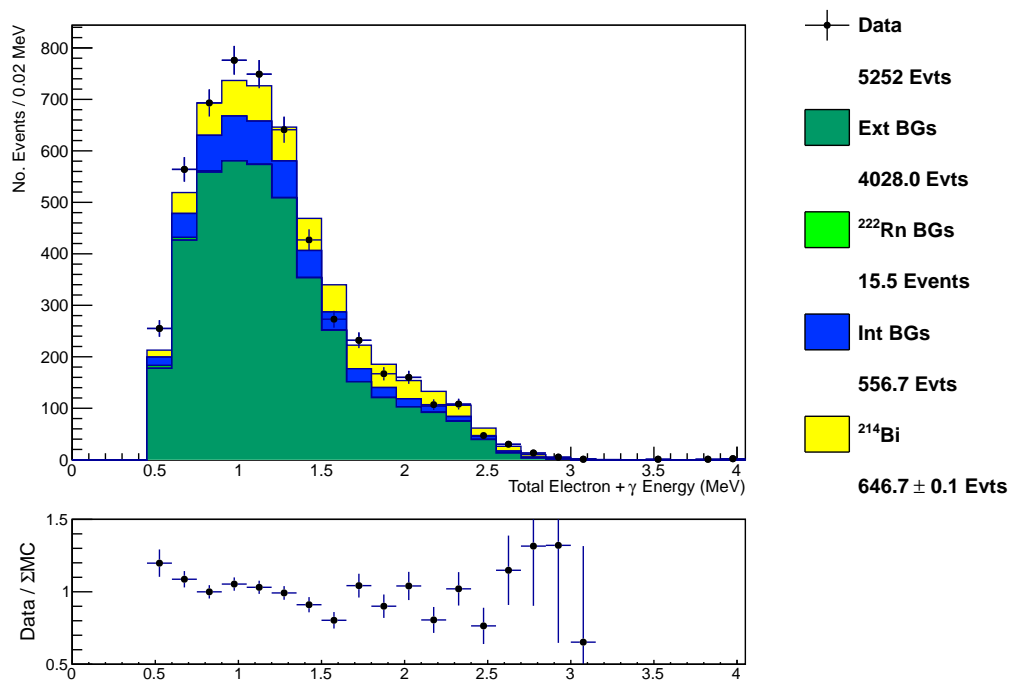


Figure 7.8: Combined electron- $\gamma$  energy for the Phase II medium-activity region  $^{116}\text{Cd}$  data set. The  $^{214}\text{Bi}$  spectrum (yellow) has been fitted to the data (shown as black points) after inclusion of internal (blue), external (dark green), and radon (light green) backgrounds. The contribution from  $^{208}\text{Tl}$  is too small to be visible.



### 7.3 $^{82}\text{Se}$ Electron- $\gamma$ Results

This section will describe the results of measurements of the  $^{82}\text{Se}$  foils using the electron- $\gamma$  channel. Results are presented separately for Phase I and Phase II.

#### 7.3.1 Phase I

Measured electron and  $\gamma$  energies from events in the  $^{82}\text{Se}$  foils are shown individually in Figure 7.9. The combined electron- $\gamma$  energy is shown in Figure 7.10. Table 7.3 presents best-fit values for measured isotopes in both Se(I) and Se(II) foil sections.

Isotope	Location	$^{82}\text{Se}$ (I) Activity (Bq)	Se (II) Activity (Bq)
$^{214}\text{Bi}$	Foil Surface	$(5.17 \pm 0.05) \times 10^{-2}$	$(5.17 \pm 0.05) \times 10^{-2}$
$^{208}\text{Tl}$	Foil Internal	$(0.46 \pm 0.67) \times 10^{-3}$	$(0.55 \pm .0.74) \times 10^{-3}$
$^{214}\text{Bi}$	Foil Surface	$1.44 \pm 0.02$	$1.44 \pm 0.02$

Table 7.3: Summary of measured background activities for  $^{82}\text{Se}$  in the electron- $\gamma$  channel for Phase I.

### 7.3.2 Phase II

This section presents results of measurements of electron- $\gamma$  emitters in Phase II of NEMO-3. Energy spectra for the emitted electron and  $\gamma$  ray are shown for the low-activity region (medium-activity region) in Figure 7.5 (Figure 7.11). Combined electron- $\gamma$  energies are shown in figures 7.6 and 7.12.

Isotope	Location	$^{82}\text{Se}$ (I) activity (Bq)	Se (II) activity (Bq)
$^{214}\text{Bi}$	Foil Surface	$(6.30 \pm 0.06) \times 10^{-3}$	$(6.30 \pm 0.05) \times 10^{-2}$
$^{208}\text{Tl}$	Foil Internal	$(0.36 \pm 0.60) \times 10^{-3}$	$(1.75 \pm 1.32) \times 10^{-3}$
$^{214}\text{Bi}$	Foil Surface	$1.44 \pm 0.02$	$(1.7 \pm 0.02) \times 10^{-2}$

Table 7.4: Summary of measured background activities for  $^{82}\text{Se}$  in the electron- $\gamma$  channel for Phase II.

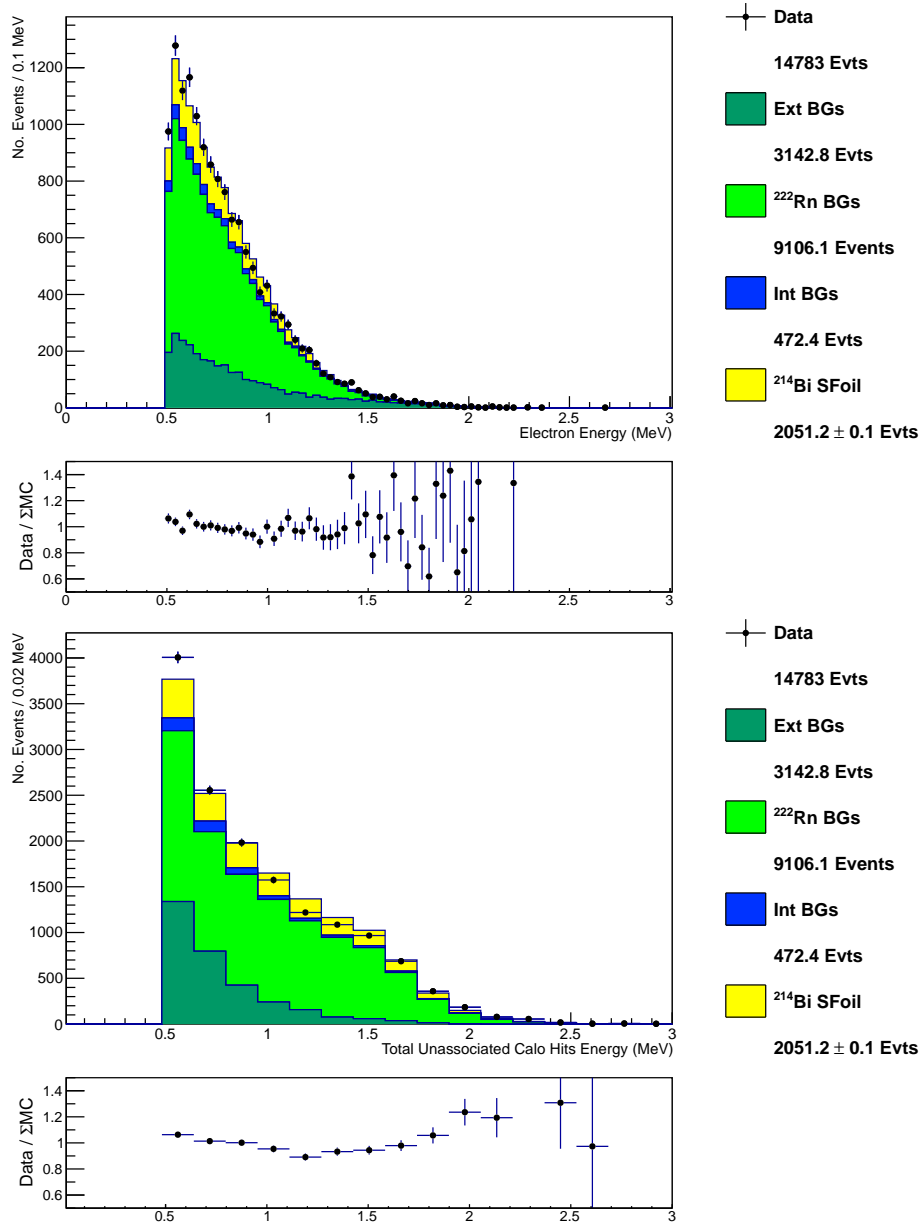


Figure 7.9: Electron (top) and  $\gamma$  (bottom) energy for the Phase I  $^{82}\text{Se}$  data set. The  $^{214}\text{Bi}$  spectrum (yellow) has been fitted to the data (shown as black points) after inclusion of internal (blue), external (dark green), and radon (light green) backgrounds. The contribution from  $^{208}\text{Tl}$  is too small to be visible.

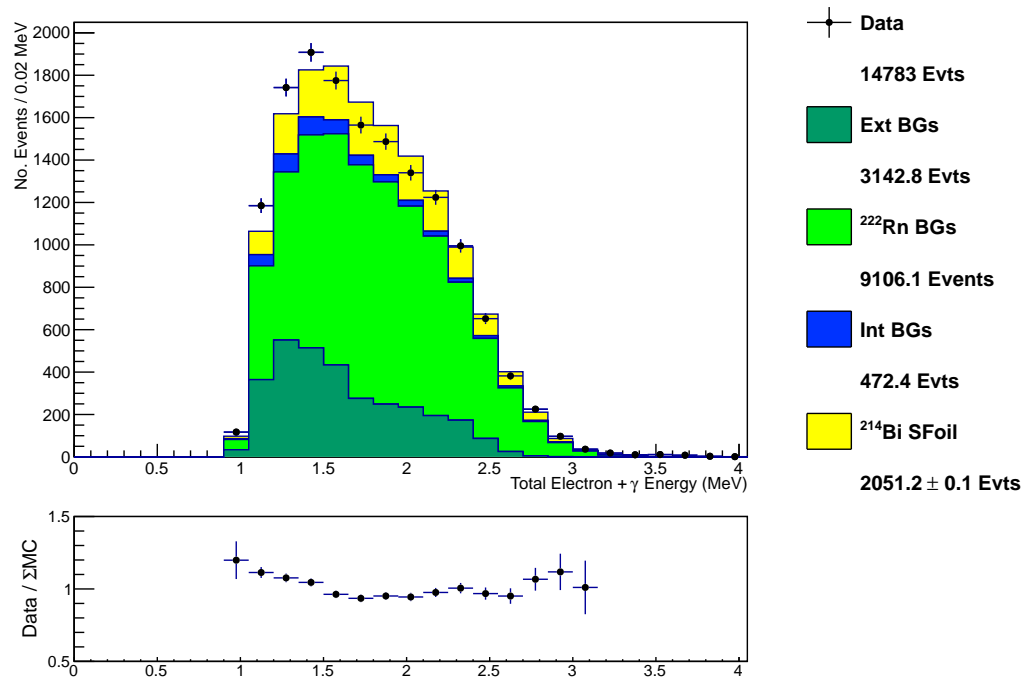


Figure 7.10: Combined electron- $\gamma$  energy for the Phase I  $^{82}\text{Se}$  data set. The  $^{214}\text{Bi}$  spectrum (yellow) has been fitted to the data (shown as black points) after inclusion of internal (blue), external (dark green), and radon (light green) backgrounds. The contribution from  $^{208}\text{Tl}$  is too small to be visible.

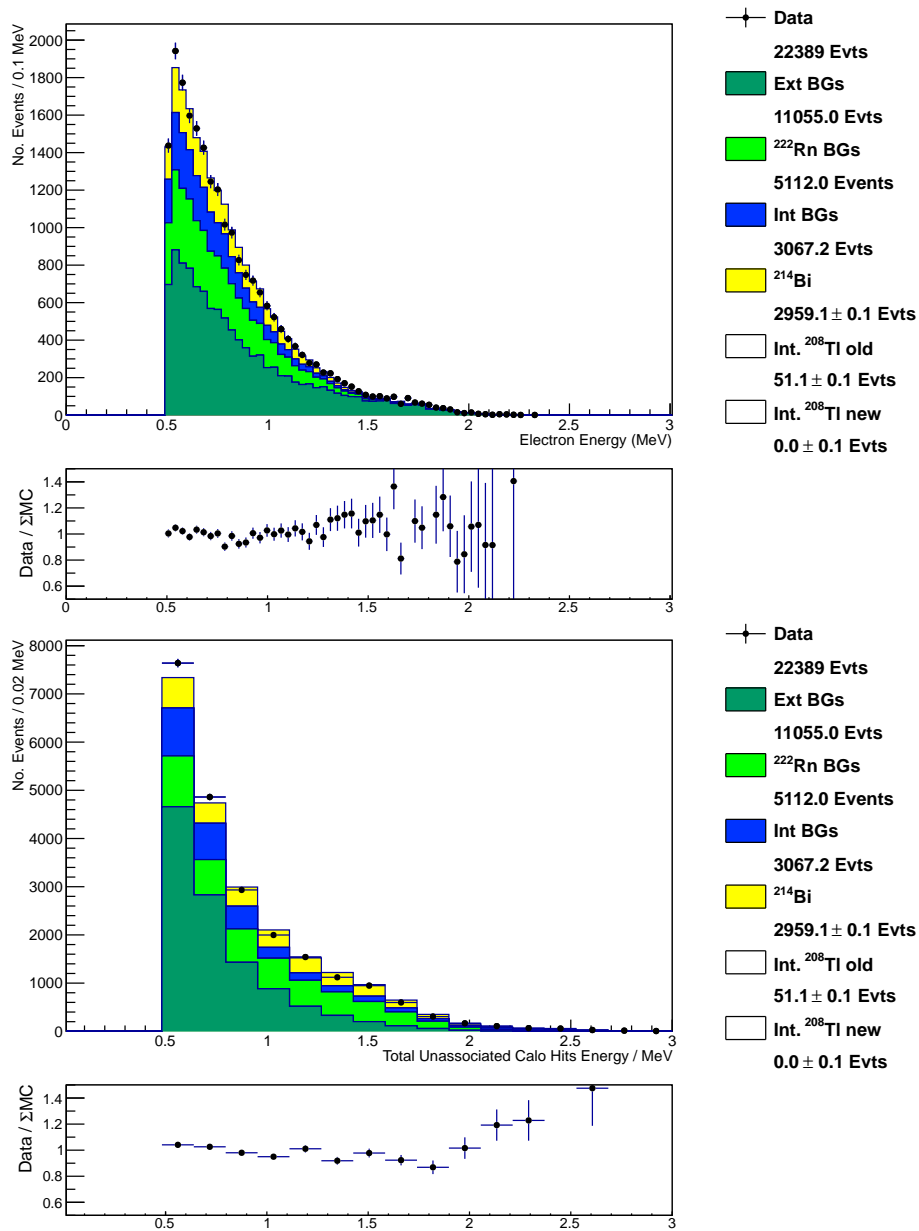


Figure 7.11: Electron (top) and  $\gamma$  (bottom) energy for the Phase II  $^{82}\text{Se}$  data set. The  $^{214}\text{Bi}$  spectrum (yellow) has been fitted to the data (shown as black points) after inclusion of internal (blue), external (dark green), and radon (light green) backgrounds. The contribution from  $^{208}\text{Tl}$  is too small to be visible.

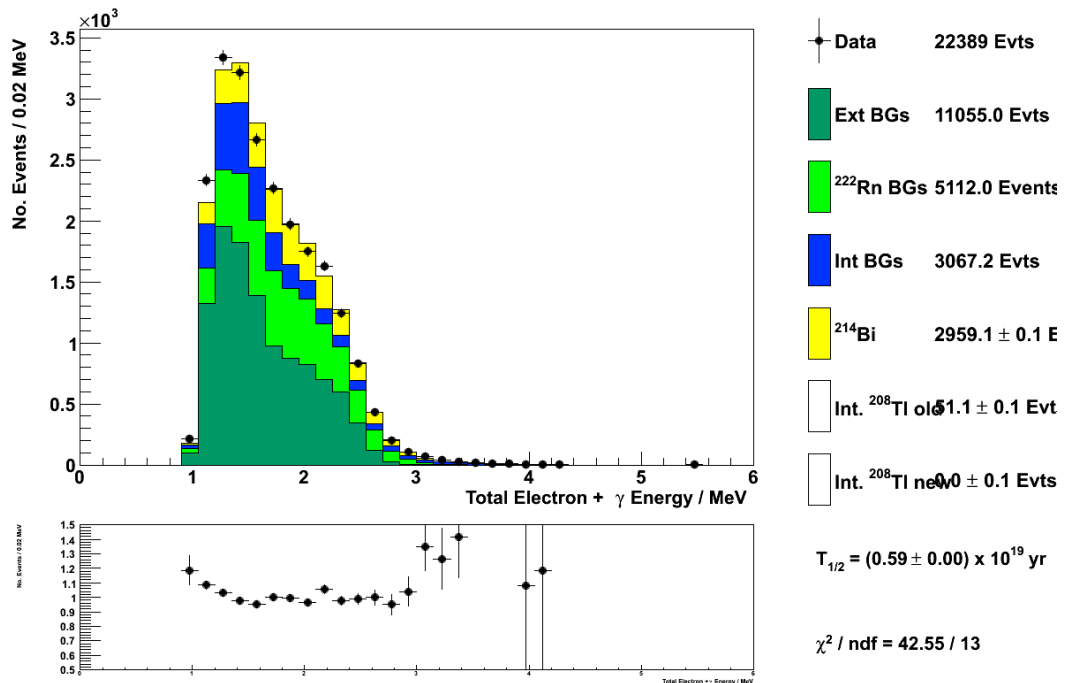


Figure 7.12: Combined electron- $\gamma$  energy for the Phase II  $^{82}\text{Se}$  data set. The  $^{214}\text{Bi}$  spectrum (yellow) has been fitted to the data (shown as black points) after inclusion of internal (blue), external (dark green), and radon (light green) backgrounds. The contribution from  $^{208}\text{Tl}$  is too small to be visible.

## 7.4 Electron- $\gamma\gamma$ Channel

As another check on the internal  $^{208}\text{Tl}$  contamination in NEMO-3, particularly in the source foils, the electron- $\gamma\gamma$  topology was exploited. This channel is dominated by  $^{208}\text{Tl}$  events originating in the source foil, and can be used to measure this isotope largely independent of other contaminants.

Electron emission in  $^{208}\text{Tl}$  is accompanied by a 2,615 keV  $\gamma$  ray, along with a  $\gamma$  of either 583 or 860 keV. Selection cuts are chosen in a manner similar to those of the electron- $\gamma$  channel, with the following additional requirements:

- Events contain one electron and two  $\gamma$  events unassociated to any track.
- The greater-energy  $\gamma$  must have energy greater than 1,800 keV.
- The lesser-energy  $\gamma$  must have energy greater than 200 keV.

The requirement that one  $\gamma$  ray be above 1,800 keV in particular suppresses most other backgrounds, most notably  $^{214}\text{Bi}$ , leaving a sample dominated by  $^{208}\text{Tl}$ .

### 7.4.1 $^{116}\text{Cd}$ Electron- $\gamma\gamma$ Results

Electron- $\gamma\gamma$  measurements were performed over the combined low- and medium-energy region in  $^{116}\text{Cd}$  to maximize available statistics. Results of fitting the internal  $^{208}\text{Tl}$  Monte Carlo to the data - background spectra are shown for the electron energy spectrum in Figure 7.13 and combined  $\gamma$  energies in Figure 7.14. The fitted value of  $^{208}\text{Tl}$  for  $^{116}\text{Cd}$  is  $(0.30 \pm 0.03) \times 10^{-3}$  Bq, in agreement with HPGe limits.

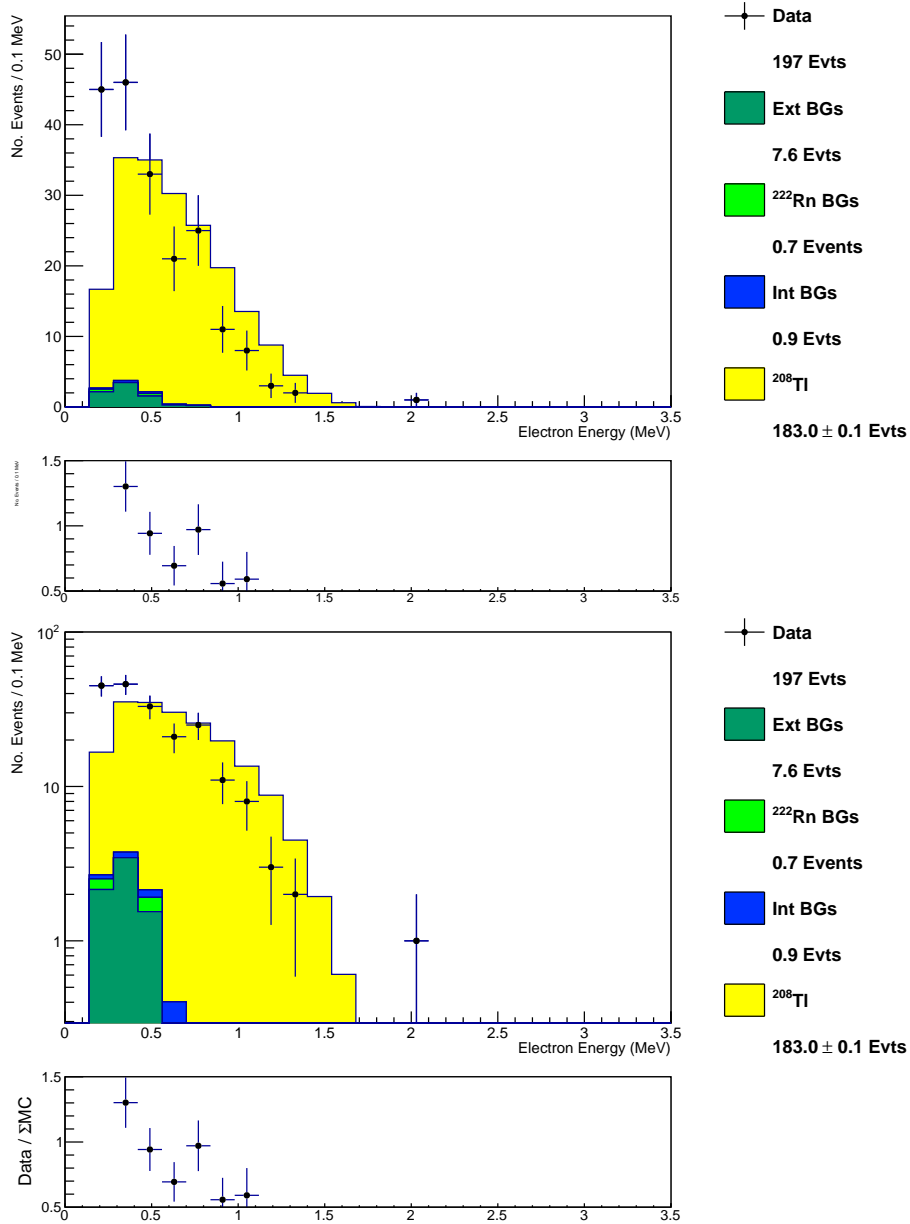


Figure 7.13: Electron energy spectrum for the  $e\gamma$  channel in  $^{116}\text{Cd}$  in linear (top) and log (bottom) scale. The best-fit value to the data (shown as black points) for the contribution from  $^{208}\text{Tl}$  is shown in yellow.



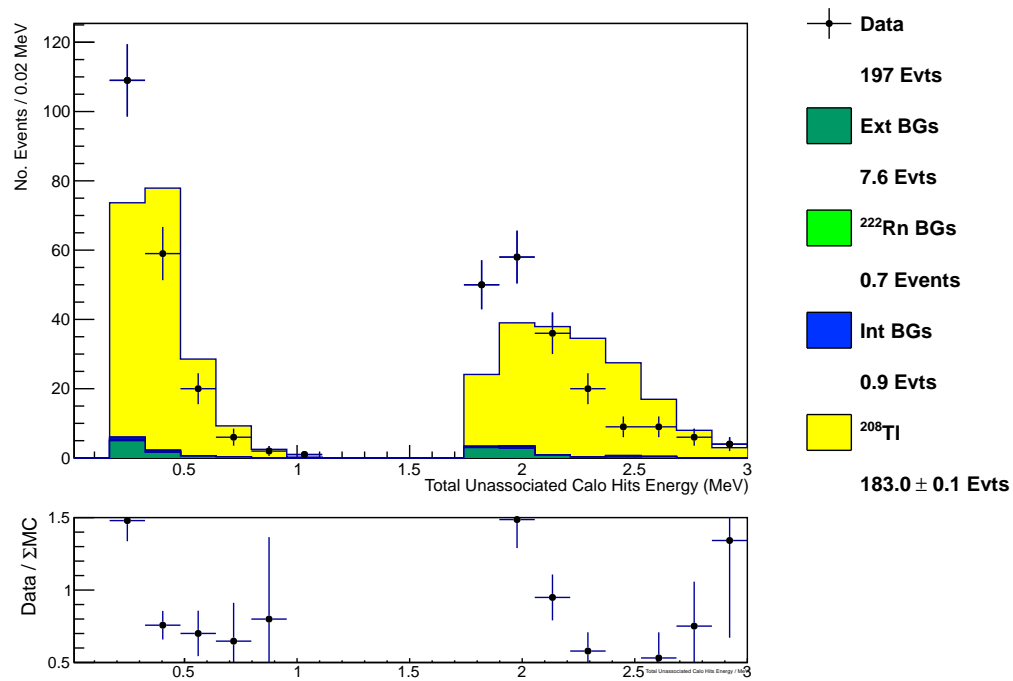


Figure 7.14: Combined  $\gamma$  energy spectra for the  $e\gamma\gamma$  channel in  $^{116}\text{Cd}$  in linear (top) and log (bottom) scale. The best-fit value to the data (shown as black points) for the contribution from  $^{208}\text{Tl}$  is shown in yellow.

#### 7.4.2 $^{82}\text{Se}$ Electron- $\gamma\gamma$ Results

Electron- $\gamma\gamma$  measurements were performed separately for the Se(I) and Se(II) samples, as previously-measured values taken by HPGe reported different limits in the two sections. Results of fitting the  $^{208}\text{Tl}$  Monte Carlo to the data - background spectra for each sector are shown below. Electron energies are shown for the Se(I) sector in Figure 7.15 and for the Se(II) sector in Figure 7.17. Fitted results of the  $\gamma$  energies are shown for Se(I) in Figure 7.16 and for Se(II) in figure 7.18.

Internal source foil  $^{208}\text{Tl}$  values are measured at  $(1.36 \pm 0.04) \times 10^{-3}$  Bq (Se(I)) and  $(1.75 \pm 0.15) \times 10^{-3}$  Bq (Se(II)). Both measurements taken in the  $^{82}\text{Se}$  sectors are in conflict with HPGe measurements taken of the foils, suggesting that better  $\gamma$  identification techniques could be employed in future studies to constrain the number of selected events.

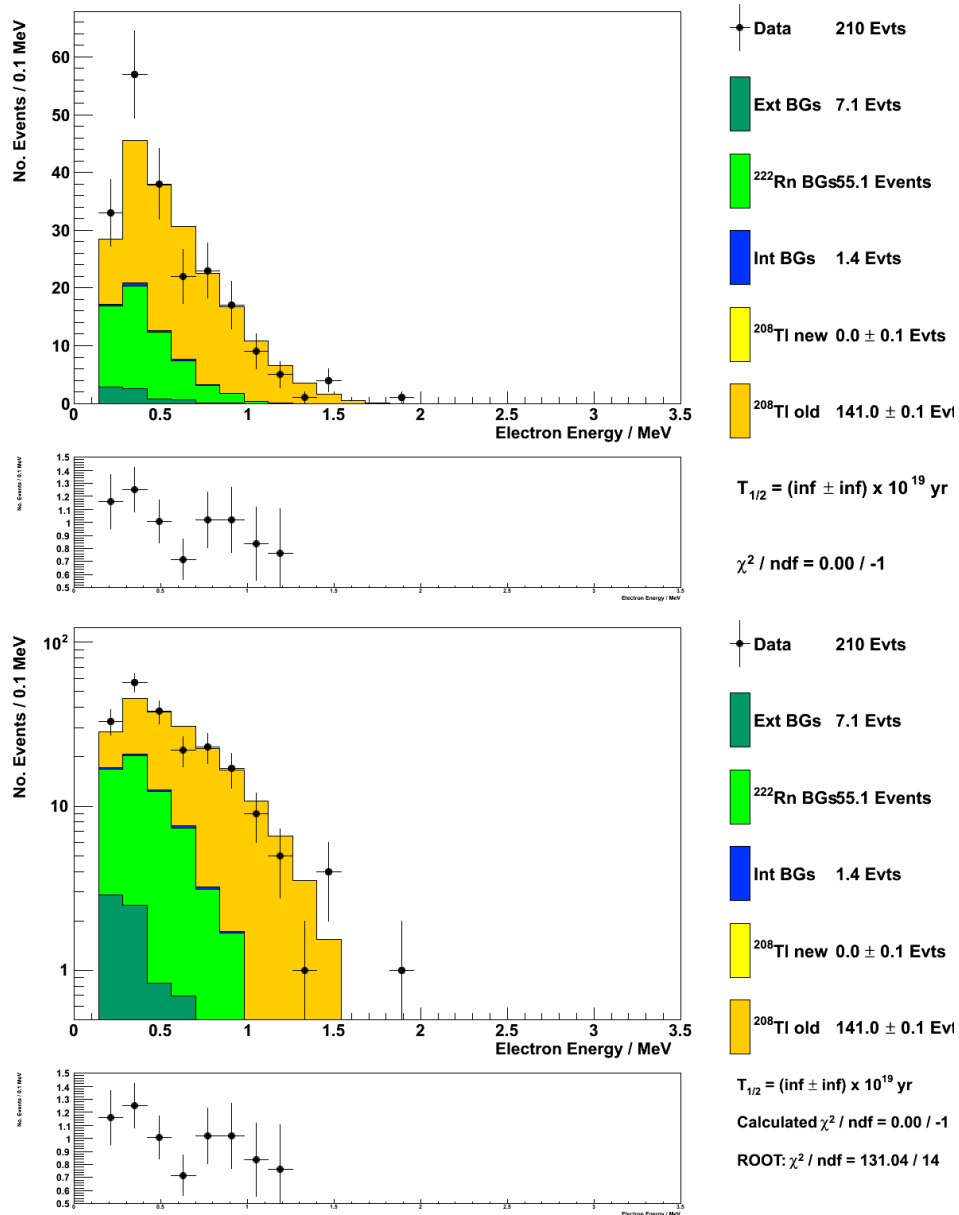


Figure 7.15:  $e\gamma\gamma$  channel electron energy distributions for the Se(I) sample. The best-fit value to the data (shown as black points) for the contribution from <sup>208</sup>Tl is shown in orange.

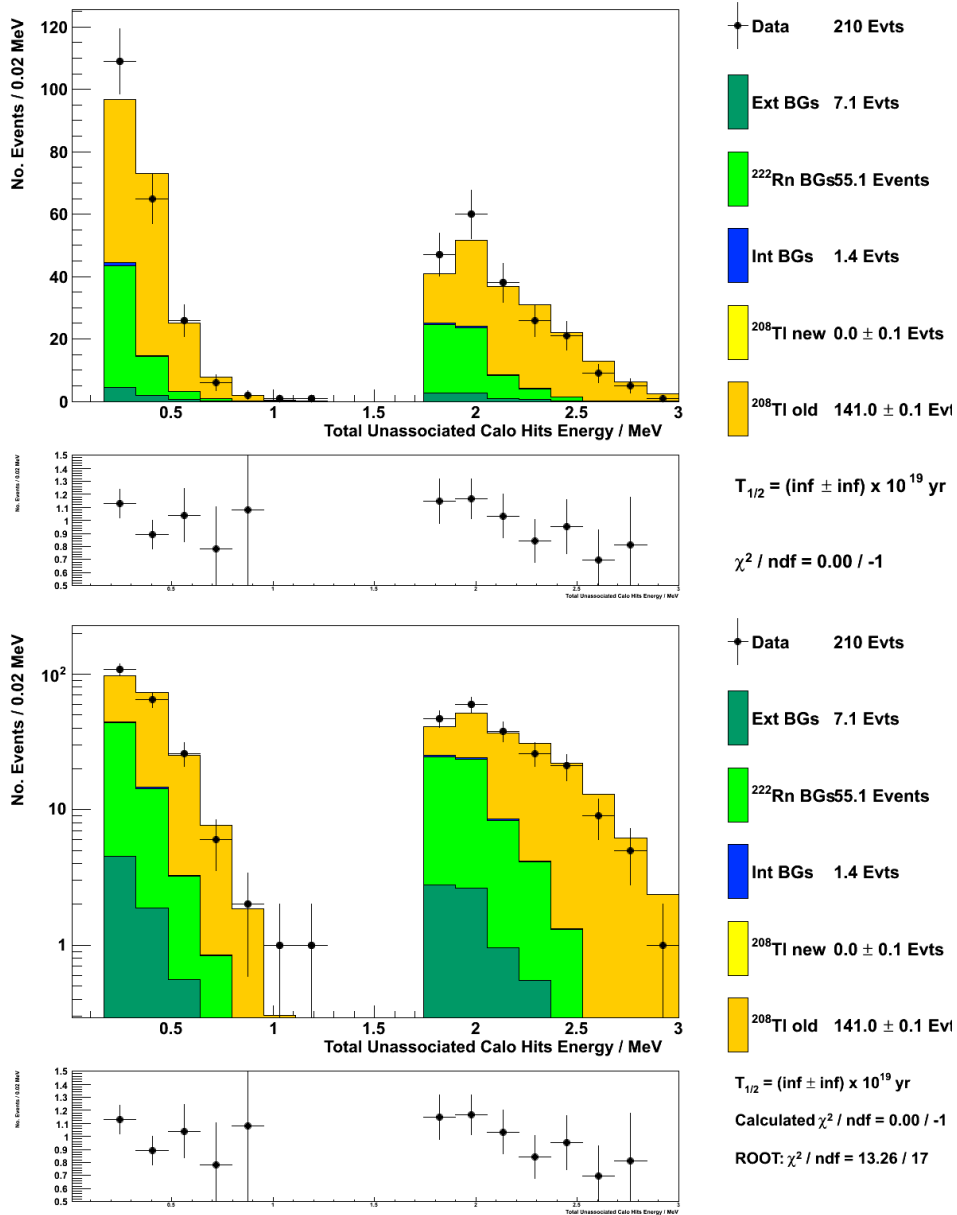


Figure 7.16:  $e\gamma\gamma$  channel electron energy distributions for the Se(I) sample. The best-fit value to the data (shown as black points) for the contribution from  $^{208}\text{Tl}$  is shown in orange.

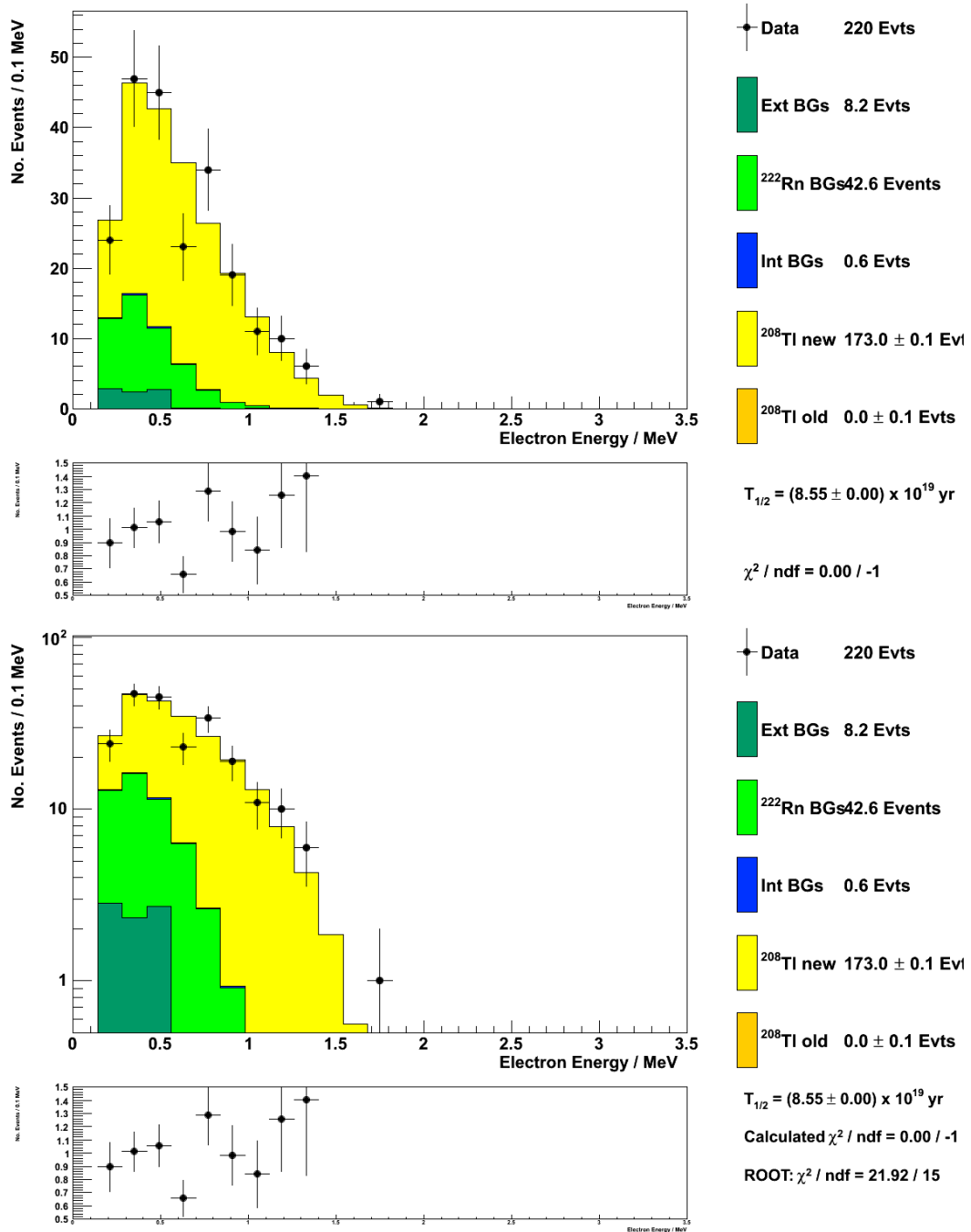


Figure 7.17:  $e\gamma\gamma$  channel electron energy distributions for the Se(II) sample. The best-fit value to the data (shown as black points) for the contribution from  $^{208}\text{Tl}$  is shown in yellow.

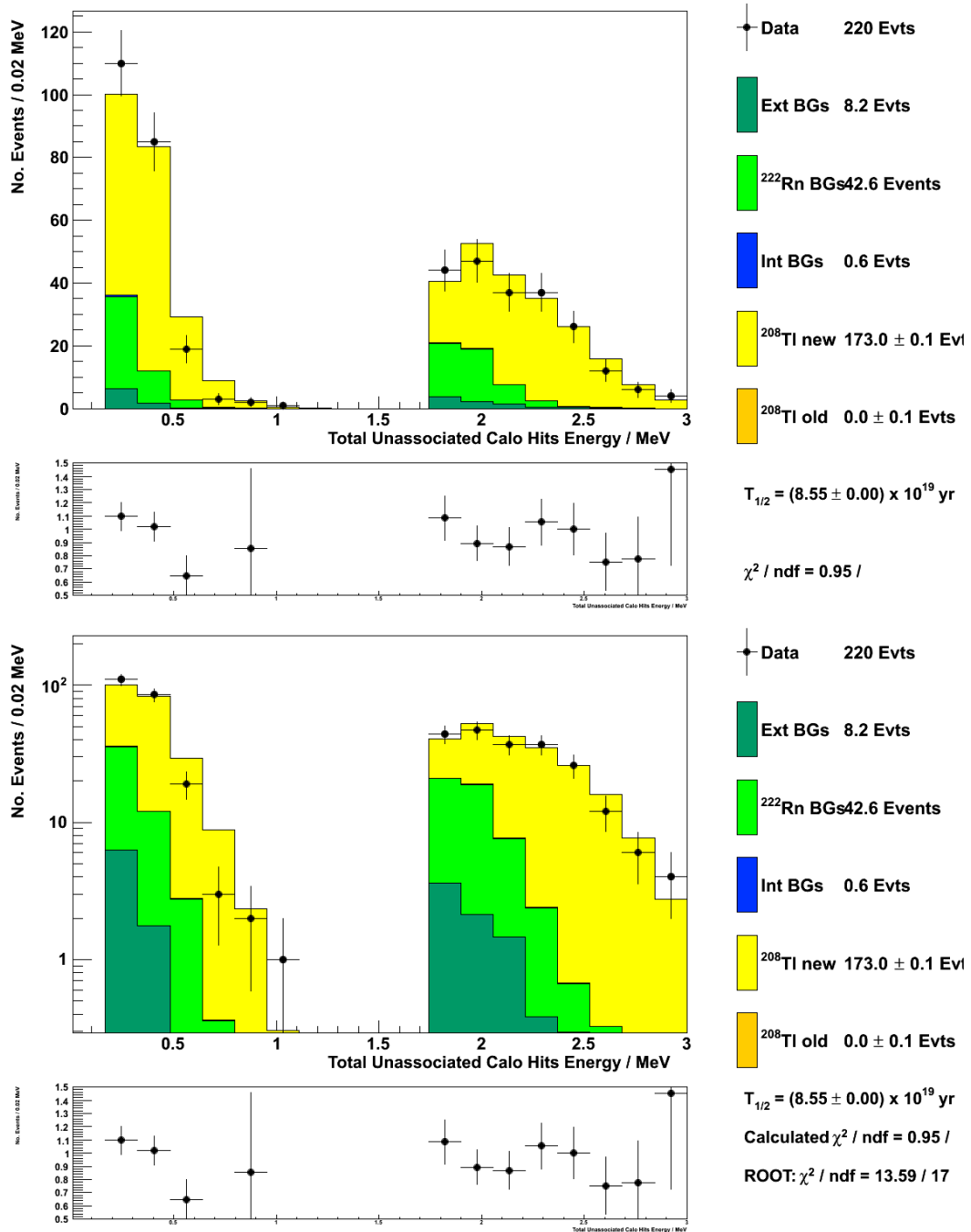


Figure 7.18:  $e\gamma\gamma$  channel electron energy distributions for the Se(II) sample. The best-fit value to the data (shown as black points) for the contribution from  $^{208}\text{Tl}$  is shown in yellow.

## 7.5 Electron- $\gamma$ Measurement Summary

In combination with the single-electron channel measurements taken in chapter 6, further refinements to the background model have been made using electron-gamma events, particularly for the pernicious isotopes of  $^{214}\text{Bi}$  and  $^{208}\text{Tl}$ . Events with an electron and two gammas were also investigated for use in constraining  $^{208}\text{Tl}$ , but the results were found to be in tension with measured HPGe values for the  $^{82}\text{Se}$  samples.

The results of these chapters can now be used to make a background model for both  $^{116}\text{Cd}$  and  $^{82}\text{Se}$ . Accurate determination of contaminant radioisotopes in the single electron, electron- $\gamma$ , and electron- $\gamma\gamma$  channels has provided for the development of this model at levels more sensitive than HPGe measurements, contributing to a more accurate measurement of the  $2\nu\beta\beta$  half-life and ultimately the  $0\nu\beta\beta$  process.

## Chapter 8

### Two Electron Channel Analysis

The measurement of two-neutrino double beta decay is a major physics goal of NEMO-3, both for its own sake in addition to the a way to provide an estimate of the irreducible background the tail of the spectrum contributes to the neutrinoless decay signal window.

This measurement is carried out using the background model developed with input from the single electron and electron-gamma channels described earlier. The  $2\nu\beta\beta$  signal Monte Carlo is fitted to the background-subtracted data spectrum using a log-likelihood fit to determine the overall signal activity, which is converted to a decay half-life.

In this chapter, the measurement of  $^{116}\text{Cd}$  to the ground state of  $^{116}\text{Sn}$  and  $^{82}\text{Se}$  to the ground state of  $^{82}\text{Kr}$  via the  $2\nu\beta\beta$  transition are described. Optimization of the selection criteria for both isotopes and a comparison of the HSD and SSD hypotheses for  $^{116}\text{Cd}$  are also discussed before the determination of a final  $2\nu\beta\beta$  half-life result is presented.



## 8.1 Two Electron Selection Requirements

Final selection cuts are given below, in order of origin in the source foil to interaction with the calorimeter.

### 8.1.1 Vertex requirements

Beginning in the source foil, events are selected to match final-state topologies of desired two-electron events. Electron tracks are extrapolated to an origin in the source foil, selecting only those that arise in an appropriate position for the analysis. Selection requirements are also applied to select against high-energy “hot spots” which are known from other channels to have unacceptable levels of background contaminants. Furthermore, events whose track vertices are too far apart are rejected, as desired events originate in a single nucleus. A description of individual selection requirements on track vertices is presented below.

- Reconstructed foil vertices are in the correct foil sectors (sector 18 for  $^{116}\text{Cd}$ , sectors 6-8 for  $^{82}\text{Se}$ ).
- Events originating in high-activity hot spots are rejected.
- Reconstructed foil vertices are within 2 cm in the XY direction.
- Reconstructed foil vertices are within 4 cm in the Z direction.
- Events must be within  $\pm 120$  cm of the foil center in the Z direction.

### 8.1.2 Tracking requirements

Selection requirements are applied on the reconstructed particle tracks within the tracking chamber, requiring that particles have tracks characteristic

of electrons which exit the source foil, traverse the tracking chamber, and enter the calorimeter. Electron tracks must have sufficient length to allow for calculation of internal and external time-of-flight hypotheses, which are then applied to further distinguish between events originating in the foil and those arising elsewhere. Individual selection requirements are described below.

- Two tracks are reconstructed with curvature consistent with negative charge.
- Tracks must be associated with fired scintillators.
- Total track length exceeds 60 cm.
- Each track has a Geiger hit in the first two layers of cells (0 or 1).
- Tracks ending at internal petal scintillators are rejected.
- Tracks ending at external petal scintillators are required to have a Geiger hit in layer 4 or 5.
- Tracks ending at main wall calorimeters are required to have a Geiger hit in layer 7 or 8.
- Tracks must have a calculated internal probability greater than 1%.
- Tracks must have a calculated external probability less than 1%.
- Events with a delayed  $\alpha$  track are rejected.
- Events must have  $\leq 2$  Geiger hits which are not assigned to a track.

### 8.1.3 Calorimeter requirements

Calorimetric requirements are applied to ensure that each selected electron deposits sufficient energy for accurate measurement by the NEMO-3

calorimeter, as well as to reduce scattering from neighboring scintillators and mis-measurement from noisy PMTs. Additionally, laser time corrections must also exist in the database to ensure accurate event timing for the calculation of time-of-flight hypotheses.

- Each electron must have an energy greater than 200 keV, and the combined energy must be greater than 400 keV.
- Electrons must enter the scintillator at the front face.
- Electron events are rejected if they are in adjacent scintillators, including diagonals.
- Laser time corrections must exist for the activated scintillators.

## 8.2 Selection criteria optimization

to determine the most beneficial criteria for distinguishing between signal-like and background-like events, analysis cuts were studied on a blinded set composing approximately 20% of the total NEMO-3 data. To determine the usefulness of a given cut, the efficiency  $\epsilon$ , purity  $\pi$ , and  $\epsilon \times \pi$  were measured for varying values of each variable under consideration while all others were held constant. Selected signal to background and signal to square root of background ratios were also considered in the determination; in general, greater values of  $\epsilon$ , purity,  $\epsilon \times \pi$ , S/B, and  $S/\sqrt{B}$  are desirable.

Efficiency is defined as the ratio of selected final signal events to total generated signal events, and purity is defined as

$$\pi = \frac{S}{(S + B)} \tag{8.1}$$

for S signal and B background events. Detailed results from the selection optimization are given in Appendix E.

### 8.3 Systematic uncertainties

A full understanding of measurements of the  $2\nu\beta\beta$  spectrum requires a detailed knowledge of the uncertainty introduced by the detector used; in NEMO-3, a great deal of effort has been expended to ensure that the systematic uncertainties are well-understood. Uncertainties are introduced in:

- Source enrichment percentage (mass):
  - 0.2% uncertainty on  $^{116}\text{Cd}$  mass; see discussion in section 3.2.4
  - 0.5% uncertainty on  $^{82}\text{Se}$  mass
- External background Monte Carlo uncertainty of 10% [90]
- Internal background Monte Carlo uncertainty of 5% [90]
- Calorimeter energy resolution uncertainty of 1% [94]
- $2\nu\beta\beta$  signal efficiency uncertainty, calculated at 5% [95] and comprised of:
  - Electron track  $\Delta XY$  vertex uncertainty
  - Electron track  $\Delta Z$  vertex uncertainty
  - Positron misidentification of 3% at high energy ( $>3$  MeV) [78]
  - Uncertainty of geometric acceptance of events in the NEMO-3 detector

To determine the effect of each individual uncertainty on the final  $T_{1/2}^{2\nu\beta\beta}$ , each systematic was varied independently and propagated through the signal fitting and  $T_{1/2}$  calculation; the results were added in quadrature to determine an overall systematic uncertainty value. A detailed description of each calculation is given below.

As discussed in section 4.3, the  $2\nu\beta\beta$  half-life (equation 4.12) is linear in both mass and signal efficiency; therefore, variations in these quantities are passed directly in the overall systematic uncertainty.

The uncertainty in signal efficiency is introduced by the imperfect modelling of the NEMO-3 detector in GEANT-3, as well as uncertainty in the track reconstruction algorithm.

Uncertainty of external (including radon) background Monte Carlo is largely due to imperfect knowledge of  $\gamma$ -ray flux in the detector. To determine the effect such an error, each background was re-scaled to reflect the maximal case of 10% increase (decrease), after which the  $2\nu\beta\beta$  signal was fitted to the data - background spectrum and the half-life recalculated to give an upper (lower) half-life value. Internal backgrounds were simulated at 5% uncertainty and within their individual statistical error in analogous fashion to provide upper and lower half-life values.

Calorimeter energy resolution uncertainty was simulated by adding a “smearing” term to each electron energy prior to making selection cuts. The smearing term  $G$  consisted of the 1% uncertainty multiplied by a randomly-

generated number following a Gaussian distribution with  $\mu = 0$  and  $\sigma = 1$ , giving a “smeared” energy of

$$E \rightarrow E \times (1 + 0.01G) \quad (8.2)$$

The energy spectra thus modified were then passed through the selection cuts and fitting procedure as normal.

A summary of systematics for  $^{116}\text{Cd}$  is shown in table 8.3, and table 8.3 presents a summary of systematics for  $^{82}\text{Se}$ .

## 8.4 Two-Electron Results

In this section, the agreement of data and MC after all data selection cuts have been applied will be presented and discussed for individual data sets and ultimately for the combined set of data for the lifetime of NEMO-3 for both  $^{116}\text{Cd}$  and  $^{82}\text{Se}$ .

### 8.4.1 $^{116}\text{Cd}$ Two-Electron Measurements

After fitting the  $2\beta 2\nu$  signal in each of the four data sets, all data sets were added together for a final half-life measurement. Figure 8.1 shows the combined two-electron energy distribution for the entire selected cadmium data set. Greater- and lesser-energy electron spectra are shown in Figure 8.2. This section assumes that the decay occurs via the SSD hypothesis. Following the discussion of results, a comparison of the SSD and HSD hypotheses is discussed.

Systematic	Uncertainty	$T_{1/2}^{2\nu\beta\beta}$ Uncertainty
Mass	0.2%	0.2%
Signal efficiency	5%	5%
External Background Monte Carlo	10%	0.6%
Internal Background Monte Carlo	5%	<0.1%
Calorimeter Energy Resolution	1%	0.26%
Total		5.05%

Table 8.1: Summary of systematic uncertainties for  $^{116}\text{Cd}$ .

Measured cosine values between electron tracks and calculated internal time-of-flight probability are shown in Figure 8.8. Vertex distributions shown by sector and vertical position are shown in figure 8.4. Results and figures of merit for the combined data set are summarized in table 8.3.

Systematic	Uncertainty	$T_{1/2}^{2\nu\beta\beta}$ Uncertainty
Mass	0.5%	0.5%
Signal efficiency	5%	5%
External Background Monte Carlo	10%	0.5%
Internal Background Monte Carlo	5%	1.5%
Calorimeter Energy Resolution	1%	<0.1%
Total		5.25%

Table 8.2: Summary of systematic uncertainties for  $^{82}\text{Se}$ .



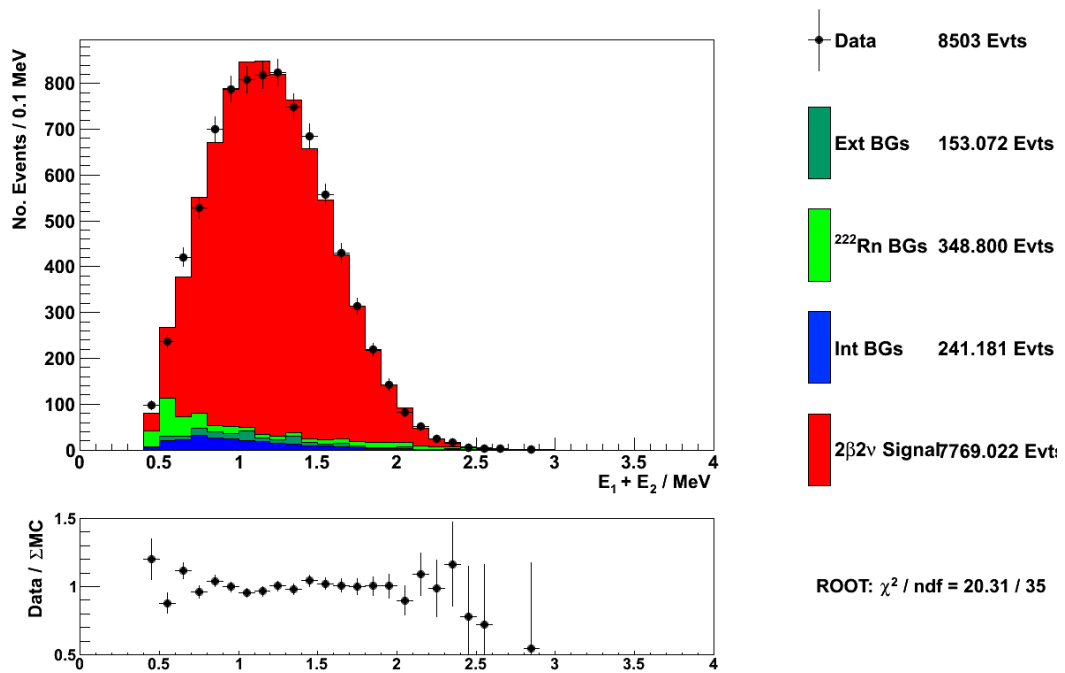


Figure 8.1: Two-electron combined energy for the combined  $^{116}\text{Cd}$  data set. The best-fit value for the  $2\nu\beta\beta$  combined electron-energy spectrum is shown in red, fitted to the data (shown as black points) after the inclusion of internal (blue), external (dark green), and radon (light green) backgrounds.

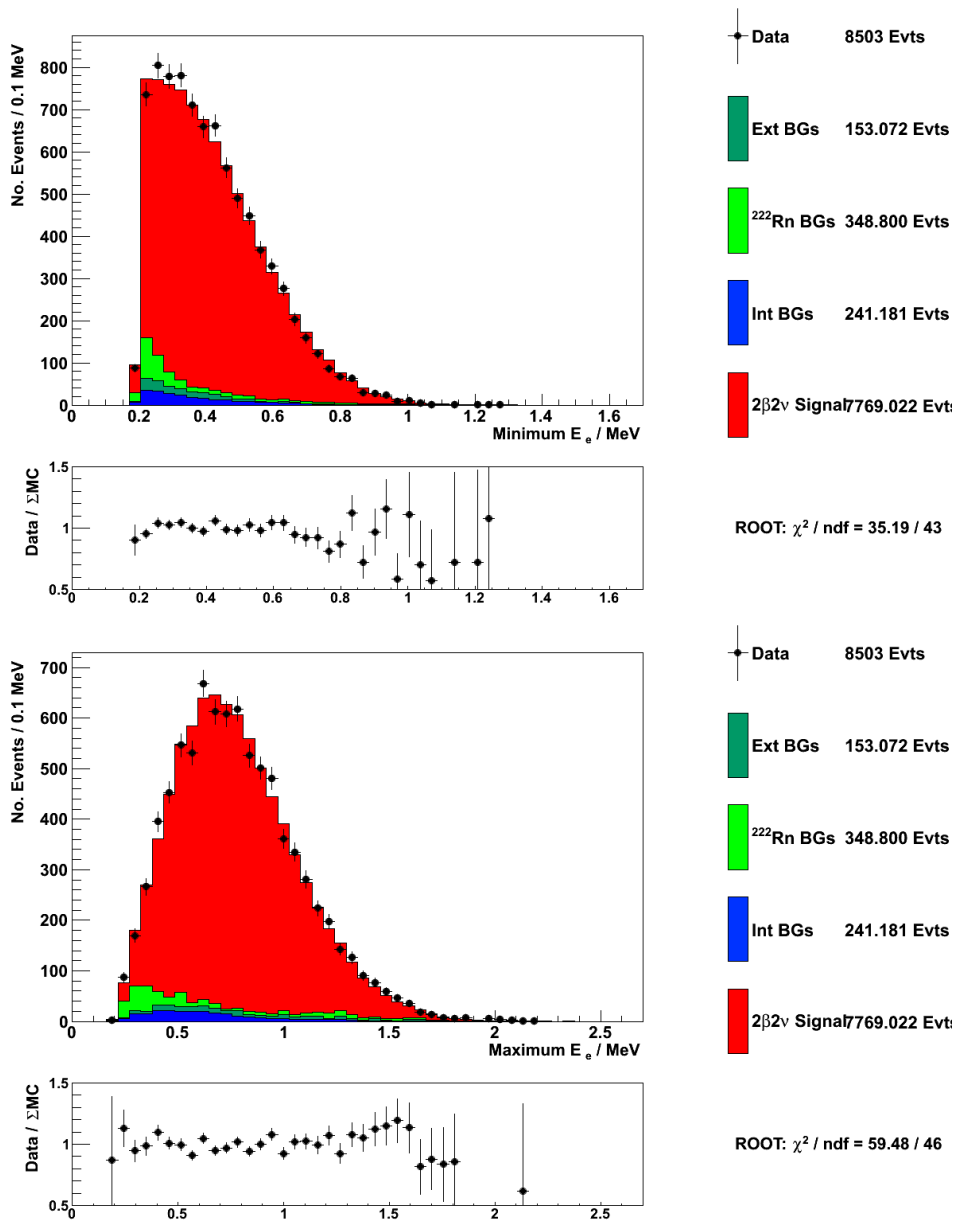


Figure 8.2: Energy of the lesser-energy electron for the combined  $^{116}\text{Cd}$  data set. The  $2\nu\beta\beta$  spectrum fitted in the total energy histogram (Figure 8.1) is displayed in red. Data are shown as black points, along with internal (blue), external (dark green), and radon (light green) backgrounds.

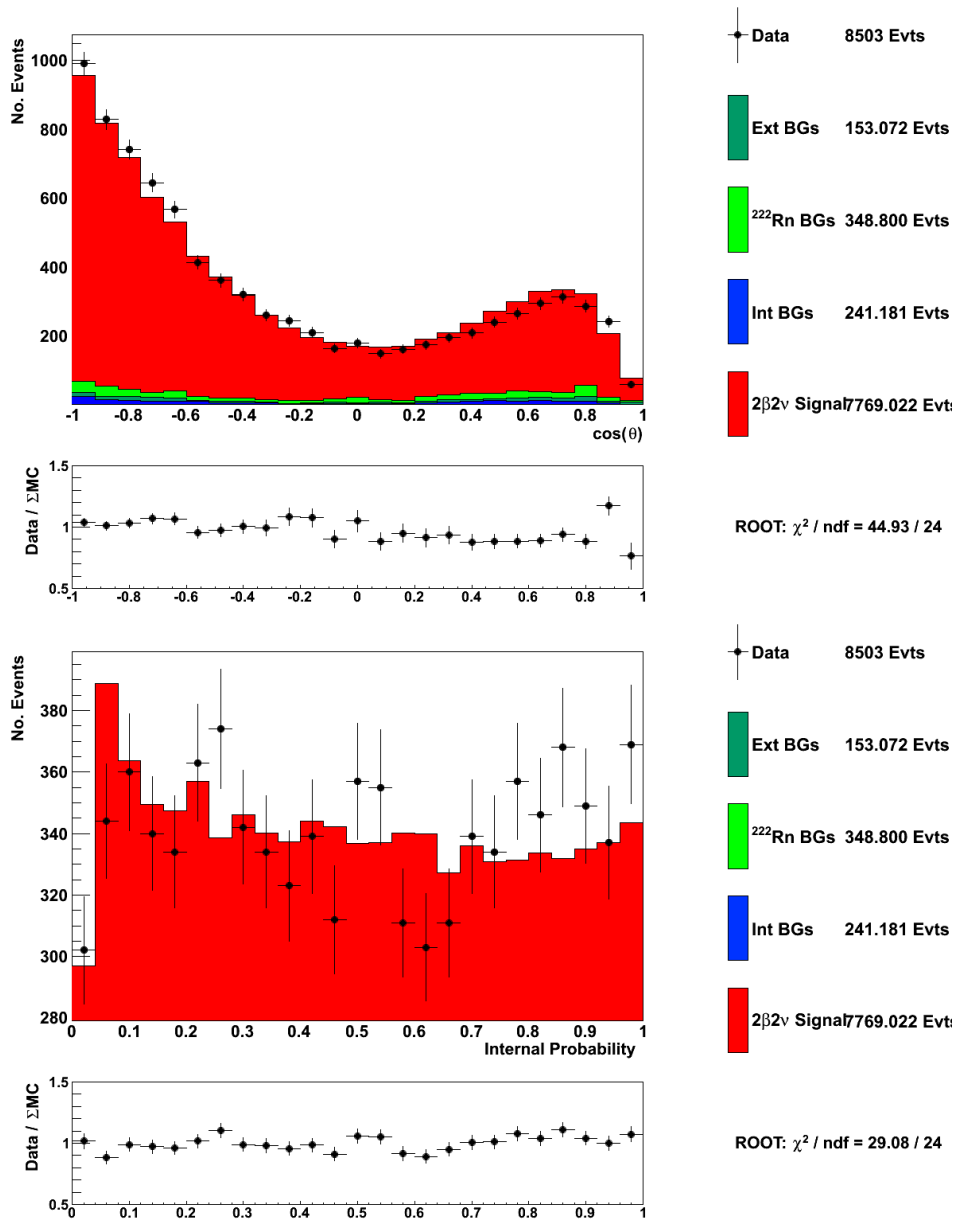


Figure 8.3: Cosine between electron tracks (top) and internal probability (bottom) for the combined  $^{116}\text{Cd}$  data set. The  $2\nu\beta\beta$  spectrum fitted in the total energy histogram (Figure 8.1) is displayed in red. Data are shown as black points, along with internal (blue), external (dark green), and radon (light green) backgrounds.

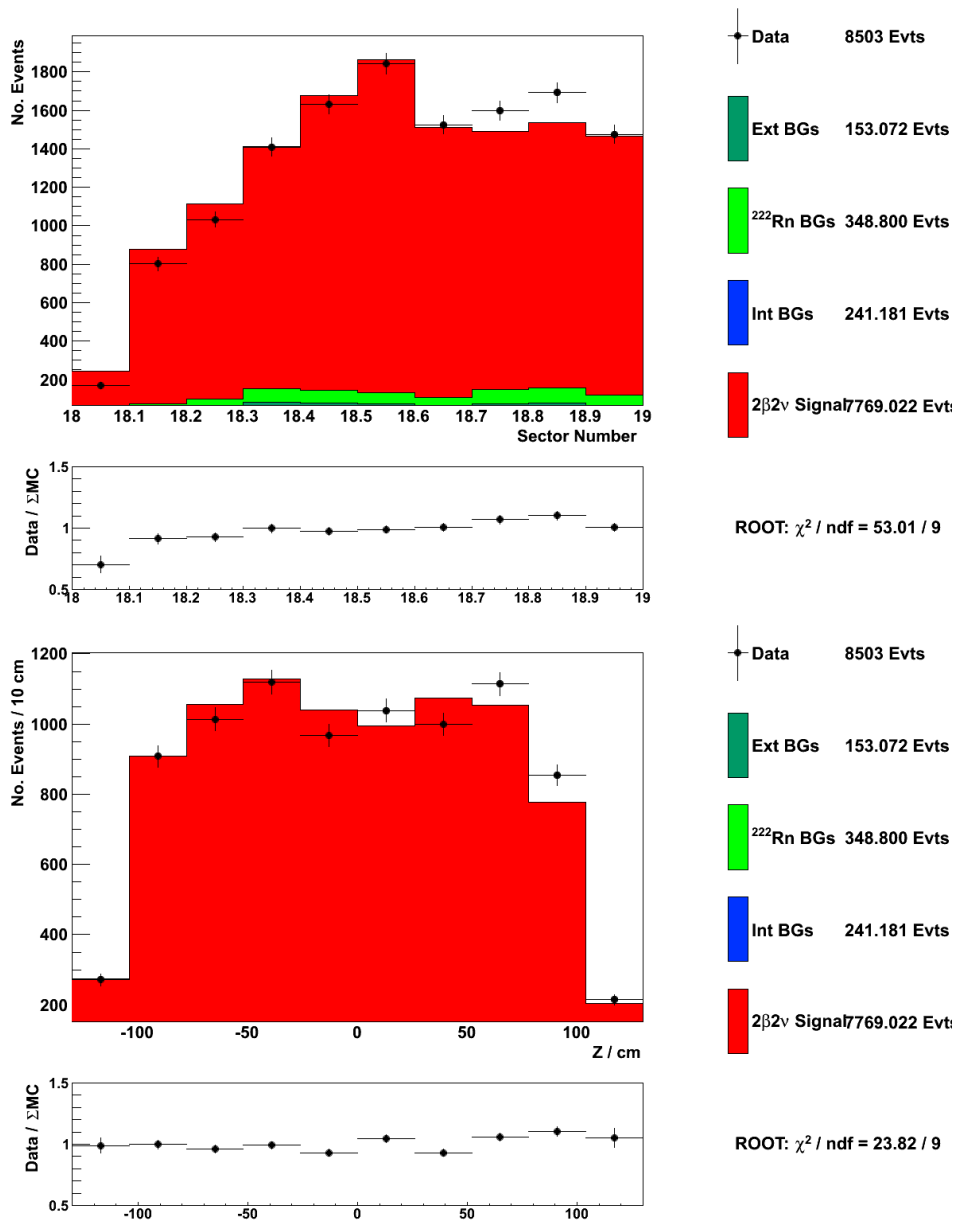


Figure 8.4: Vertex sector (top) and Z (bottom) position for the combined  $^{116}\text{Cd}$  data set. The  $2\nu\beta\beta$  spectrum fitted in the total energy histogram (Figure 8.1) is displayed in red. Data are shown as black points, along with internal (blue), external (dark green), and radon (light green) backgrounds.

Combined $^{116}\text{Cd}$ Data Set	
Data events	8503
Signal events	7769
Internal BG events	241
External BG events	153
Radon BG events	348
Total BG events	742
$\frac{\text{Signal}}{\text{Background}}$	10.47
$\frac{\text{Signal}}{\sqrt{\text{Background}}}$	285.21
Signal efficiency	3.26%
Signal Purity	83.7%
$T_{\frac{1}{2}} (\times 10^{19} \text{ yr})$	$(2.90 \pm 0.03^{stat} \pm 0.15_{syst})$

Table 8.3: Summary of  $^{116}\text{Cd}$  results for the combined data set.

## 8.5 SSD and HSD hypotheses

Because  $^{116}\text{Cd}$  decays via the  $1^+$  state of its intermediate daughter nucleus, it is a candidate for decay via single-state dominance (SSD) wherein only the lowest-lying state of the intermediate nucleus contributes to the nuclear matrix element for the decay. To differentiate between the single-state and higher states dominance hypotheses, a study has been carried out using Monte Carlo generated based on each model. Results were then compared based on goodness of fit tests between the signal and background-subtracted data spectrum in both total energy and minimum energy spectra.

Results of fits using both the SSD and HSD hypotheses are given in table 8.4.

Model	Total Energy $\chi^2$	Minimum Electron Energy $\chi^2$
SSD	20.31 / 35	35.19 / 43
HSD	25.40 / 35	48.66 / 43

Table 8.4:  $\chi^2$  results for SSD and HSD spectra for relevant observables.

Compared to the SSD fits, the HSD  $\chi^2/\text{NDF}$  is worsened in both the total and minimum energy distributions, indicating that the SSD hypothesis is favored. Under the HSD hypothesis, the  $2\nu\beta\beta$  transition half-life is increased

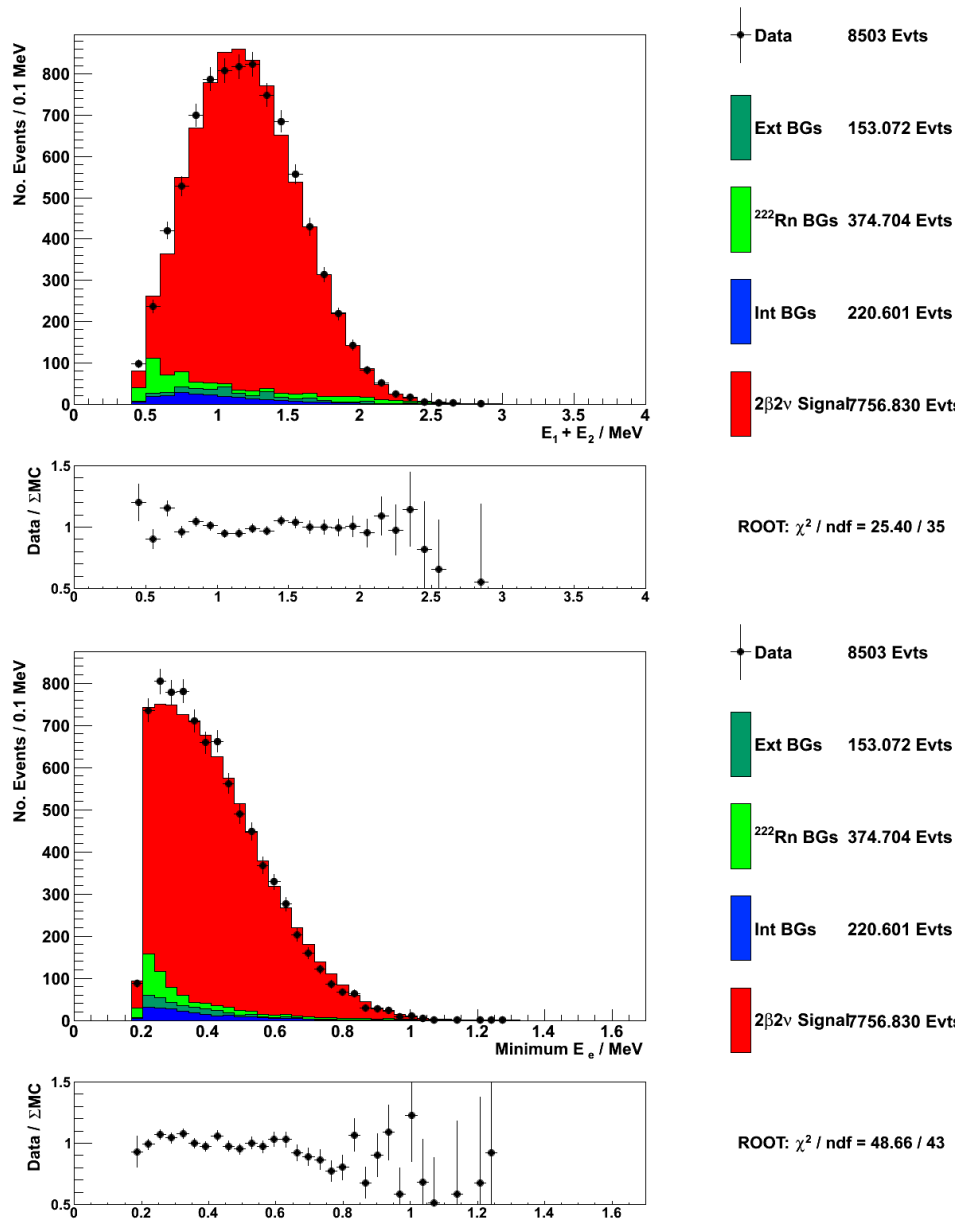


Figure 8.5: Total (top) and minimum (bottom) electron energies for fitted  $^{116}\text{Cd}$  signal under the higher states dominance hypothesis. The fitted  $2\nu\beta\beta$  spectrum under the HSD hypothesis shown in red, fitted to the data (shown as black points) after inclusion of internal (blue), external (dark green), and radon (light green) backgrounds.

to

$$T_{1/2}^{2\nu} = (3.13 \pm 0.03^{stat} \pm 0.17_{syst}) \times 10^{19} \text{ yr} \quad (8.3)$$

### 8.5.1 $^{82}\text{Se}$ Two-Electron Measurements

Results for the total data set of  $^{82}\text{Se}$  are presented in this section. Figure 8.6 shows the total electron energy spectrum. Minimum and maximum energy electron energy spectra are presented in Figure 8.7, and the cosine between electrons is shown in Figure 8.8. Source foil vertex distributions are shown by sector number and vertical position in Figure 8.9.

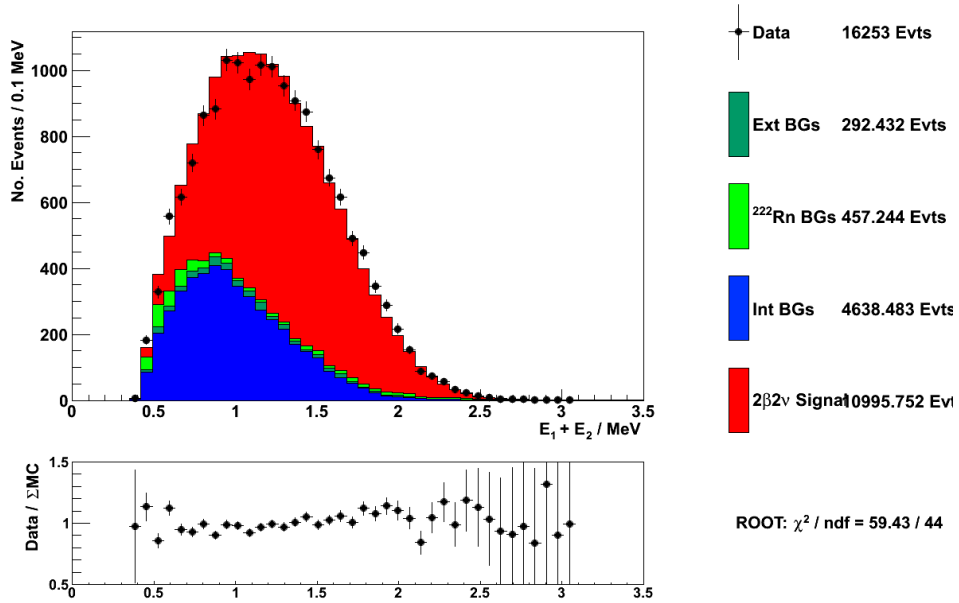


Figure 8.6: Two-electron combined energy for the combined  $^{82}\text{Se}$  data set. The best-fit value for the  $2\nu\beta\beta$  combined electron-energy spectrum is shown in red, fitted to the data (shown as black points) after the inclusion of internal (blue), external (dark green), and radon (light green) backgrounds.



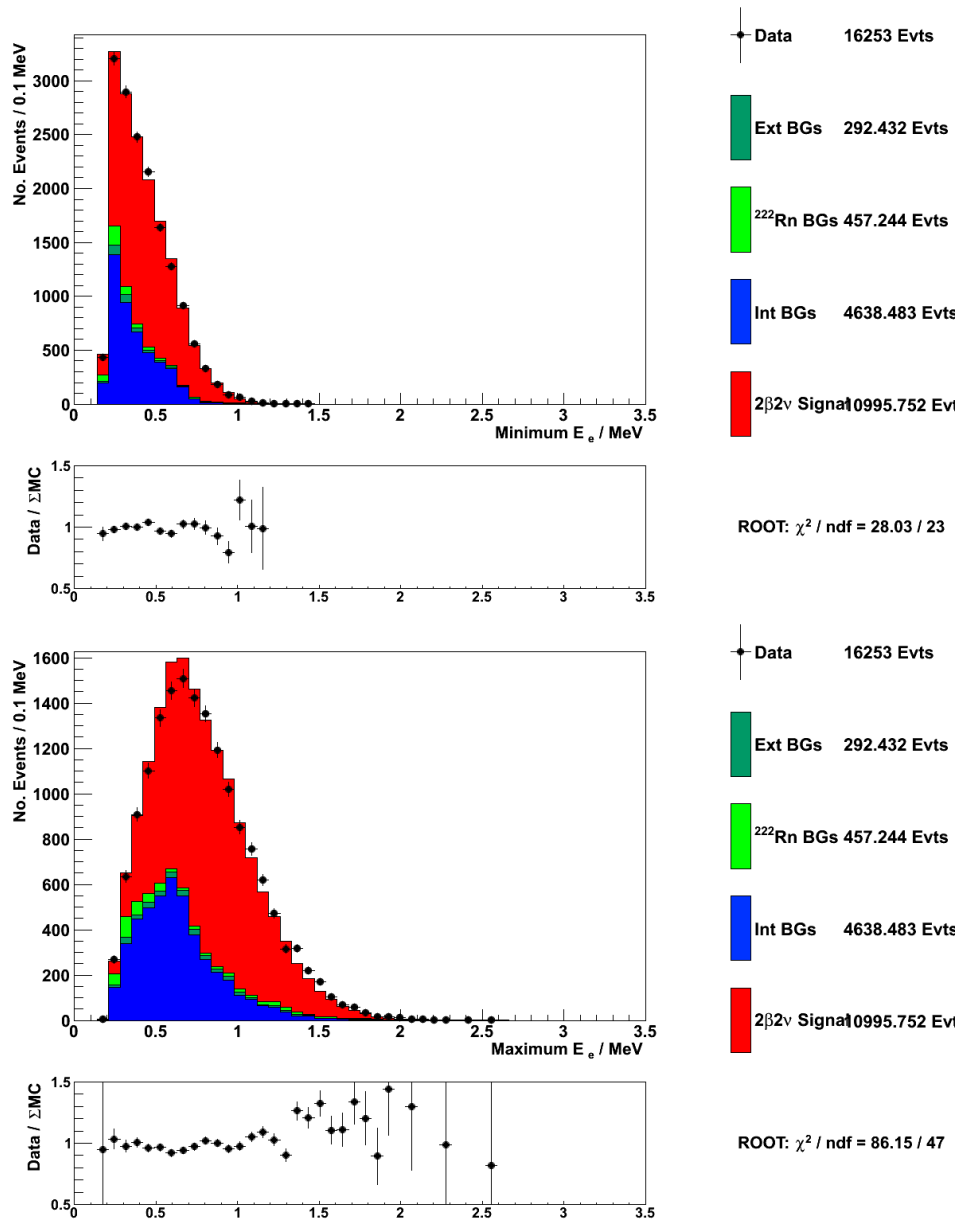


Figure 8.7: Energy of the lesser- (top) and greater-(bottom) energy electron for the combined  $^{82}\text{Se}$  data set. The  $2\nu\beta\beta$  spectrum fitted in the total energy histogram (Figure 8.6) is displayed in red. Data are shown as black points, along with internal (blue), external (dark green), and radon (light green) backgrounds.

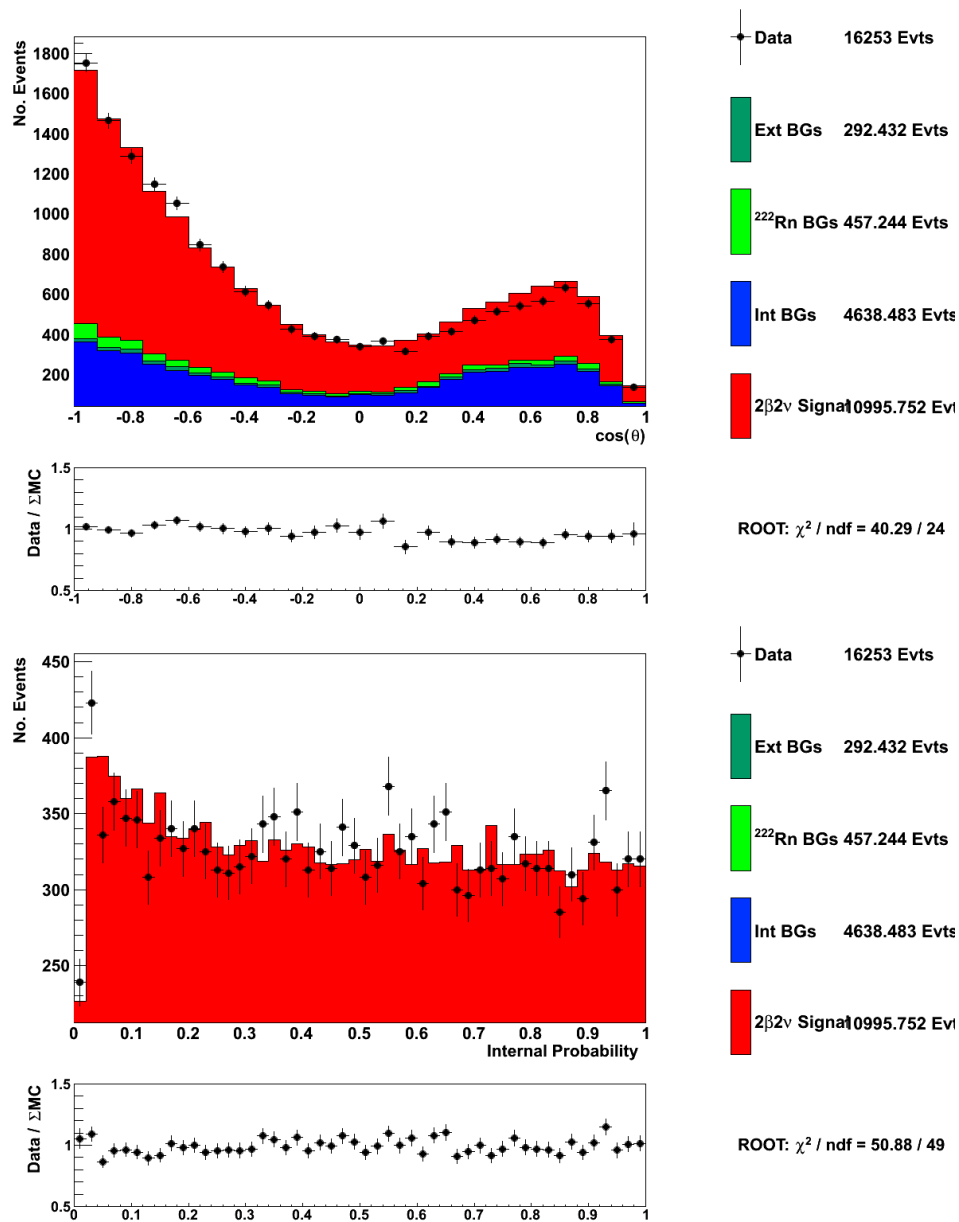


Figure 8.8: Cosine between electron tracks (top) and internal probability (bottom) for the combined  $^{82}\text{Se}$  data set. The  $2\nu\beta\beta$  spectrum fitted in the total energy histogram (Figure 8.6) is displayed in red. Data are shown as black points, along with internal (blue), external (dark green), and radon (light green) backgrounds.

Combined $^{82}\text{Se}$ Data Set	
Data events	16253
Signal events	10995.75
Internal BG events	4638.48
External BG events	292.43
Radon BG events	457.48
Total BG events	5388.16
$\frac{\textit{Signal}}{\textit{Background}}$	2.04
$\frac{\textit{Signal}}{\sqrt{\textit{Background}}}$	149.80
Signal efficiency	2.70%
Signal Purity	67%
$T_{1/2} (\times 10^{19} \text{ yr})$	$10.62 \pm 0.11^{stat} \pm 0.56_{syst}$

Table 8.5: Summary of  $^{82}\text{Se}$  results for the combined data set.

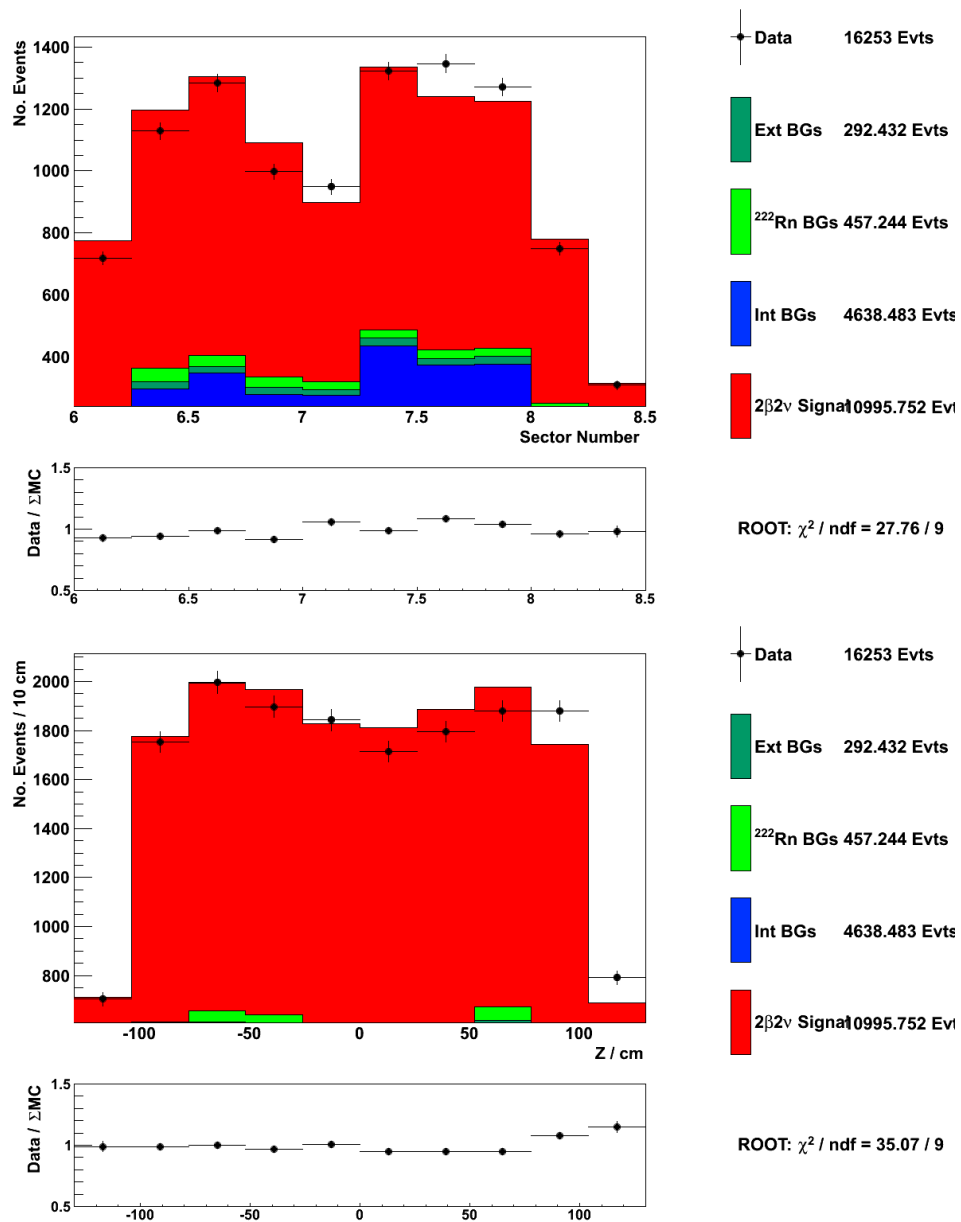


Figure 8.9: Vertex sector (top) and Z (bottom) position for the combined  $^{82}\text{Se}$  data set. The  $2\nu\beta\beta$  spectrum fitted in the total energy histogram (Figure 8.6) is displayed in red. Data are shown as black points, along with internal (blue), external (dark green), and radon (light green) backgrounds.

## 8.6 Summary and Conclusions

Using a background model developed from HPGe measurements and background values measured *in situ* in the single electron and electron-gamma channels, a set of requirements has been developed and tested to select and identify  $2\nu\beta\beta$  events. These events have been used to measure the  $2\nu\beta\beta$  transition half-life for the decay to the ground state of  $^{116}\text{Cd}\rightarrow^{116}\text{Sn}$

$$T_{1/2}^{2\nu}(^{116}\text{Cd}) = (2.90 \pm 0.03^{\text{stat}} \pm 0.15_{\text{syst}}) \times 10^{19} \text{ yr} \quad (8.4)$$

in agreement with both previously published NEMO results [96] and the Solotvina experiment [72]. The single-states dominance and higher-states dominance hypotheses have been investigated for  $^{116}\text{Cd}$ , finding that the SSD matches the data better with respect to the HSD in both total and minimum electron energy spectra, suggesting that the decay proceeds via the SSD transition.

The  $2\nu\beta\beta$  transition half-life for the decay to the ground state of  $^{82}\text{Se}\rightarrow^{82}\text{Kr}$  has also been measured at

$$T_{1/2}^{2\nu}(^{82}\text{Se}) = 10.62 \pm 0.11^{\text{stat}} \pm 0.56_{\text{syst}} \times 10^{19} \text{ yr} \quad (8.5)$$

in statistical agreement with previous measurements of  $^{82}\text{Se}$  from prior NEMO results [96] and the 1992 Elliott experiment [76].

Results from these measurements will be used as the major component of the background model to the  $0\nu\beta\beta$  process in both  $^{116}\text{Cd}$  and  $^{82}\text{Se}$ .  $2\nu\beta\beta$  results may also be used to constrain the two-neutrino nuclear matrix elements for their respective isotopes.

## Chapter 9

### Search for the Neutrinoless Transition

In this chapter, the transitions of  $^{116}\text{Cd}$  to the ground state of  $^{116}\text{Sn}$  and  $^{82}\text{Se}$  to the ground state of  $^{82}\text{Kr}$  via  $0\nu\beta\beta$  transitions are described. Lower limits of half-lives are presented for the Light Majorana Exchange (LME) process, describing  $0\nu\beta\beta$  by a light massive neutrino; Right Handed Current (RHC), mediated by neutrinos which couple to right-handed leptons; and four Majoron-emitting models of neutrinoless transition. Nuclear matrix elements and phase-space factors and their use in determining an effective neutrino mass are discussed and neutrino mass limits are presented.

#### 9.1 Limit Calculation

The  $0\nu\beta\beta$  limit is calculated using the procedure described in chapter 4.4. Expected background events are considered to be the backgrounds as described in chapters 5, 6, and 7. In addition, the  $2\nu\beta\beta$  spectrum as measured in chapter 8 is also considered as a background to the  $0\nu\beta\beta$  signal. Each of the  $0\nu\beta\beta$  models discussed in section 2.3.1 will be considered separately.

### 9.1.1 Selection Criteria and Data Set

The  $0\nu\beta\beta$  signal is selected using the same criteria as the  $2\nu\beta\beta$  set, as described in section 8.1, in accordance with the principle of blind analysis. The overall data set is recorded for 1707.79 days, for a total exposure of 1.65 kg y for  $^{116}\text{Cd}$  and 3.75 kg y for  $^{82}\text{Se}$ .

### 9.1.2 NEMO-3 Sensitivity

Before considering the limit set on the  $0\nu\beta\beta$  half-life, it is instructive to consider the expected sensitivity of the NEMO-3 detector. Referring to section 4.4.1, for a time of 1695.31 days, the expected sensitivity at 90% C.L. (corresponding to  $n_\sigma = 1.645$ ) is

$$T_{1/2}^{0\nu} = 1.09 \times 10^{23} \text{ yr} \quad (9.1)$$

for  $^{116}\text{Cd}$  and

$$T_{1/2}^{0\nu} = 3.01 \times 10^{23} \text{ yr} \quad (9.2)$$

for  $^{82}\text{Se}$ .

### 9.1.3 Nuclear Matrix Elements and Phase-Space Values

To relate the half-life limit to a limit on the effective neutrino mass, the  $0\nu\beta\beta$  nuclear matrix element  $M^{0\nu}$  and phase-space factor  $G^{0\nu}$  must be known. While the phase-space factor is exactly calculable, the NME is subject to a range of values depending on the approximation technique used. NMEs for  $^{116}\text{Cd}$  and  $^{82}\text{Se}$  are shown in tables 9.1.3 and 9.1.3 below [97].

In addition to differences between models, an additional spread is introduced in the choice of Gamow-Teller coupling constant  $g_A$  used in the calculation of of NME. To account for a known discrepancy between calculated and measured Gamow-Teller matrix elements [33] (see section 2.4), the true value of  $g_A$  is customarily “quenched” to a value of 1.00 [97, 98]. NMEs using both of these values are considered in the calculation of the effective neutrino mass.

$^{116}\text{Cd}$		
$G^{0\nu} = 1.894 \times 10^{-25} \text{ yr}^{-1}$		
$g_A$ value	RQRPA	QRPA
1.25	$1.43 \pm 0.03$	$1.56 \pm 0.03$
1.00	$1.22 \pm 0.02$	$1.31 \pm 0.02$

Table 9.1: Phase-space factor and nuclear matrix element values for  $^{116}\text{Cd}$ .

## 9.2 Neutrinoless Transition Search Results for $^{116}\text{Cd}$

This section describes the calculation of half-life limits for  $^{116}\text{Cd}$  in the Light Majorana Exchange, Right-Handed Current, and Majoron-emitting



$^{82}\text{Se}$		
$G^{0\nu} = 1.079 \times 10^{-25} \text{ yr}^{-1}$		
$g_A$ value	RQRPA	QRPA
1.25	$2.12 \pm 0.04$	$2.36 \pm 0.04$
1.00	$1.91 \pm 0.02$	$2.10 \pm 0.05$

Table 9.2: Phase-space factor and nuclear matrix element values for  $^{82}\text{Se}$ .

mechanisms. Spectra are shown for each  $0\nu\beta\beta$  process, and the calculated half-life limits at 90% confidence level are given. Where applicable, these results are related to limits on effective neutrino mass  $\langle m_\nu \rangle$  and RHC coupling values.

### 9.2.1 Light Majorana Exchange Mechanism

The Light Majorana Exchange mechanism, described in section 2.3.2, is the most widely discussed  $0\nu\beta\beta$  mechanism. Phenomenologically, it occurs as a monoenergetic peak at the  $Q_{\beta\beta}$  value, as only electrons are present to carry energy from the decay. Using the process described in section 4.4.2, the LME Monte Carlo energy spectrum is rescaled by a decreasing activity until

a 90% confidence level of signal exclusion is reached.

Once this activity limit has been reached, the number of events in the  $0\nu\beta\beta$  spectrum can be considered excluded at 90% confidence level and the activity readily converted to a half-life by using formula 4.12.

The  $0\nu\beta\beta$  spectrum is shown as an overlay on the data and total background in Figure 9.1, where the background includes the  $2\nu\beta\beta$  spectrum. The window around the  $Q_{\beta\beta}$  signal region is shown in detail in linear scale on the right of the same figure.

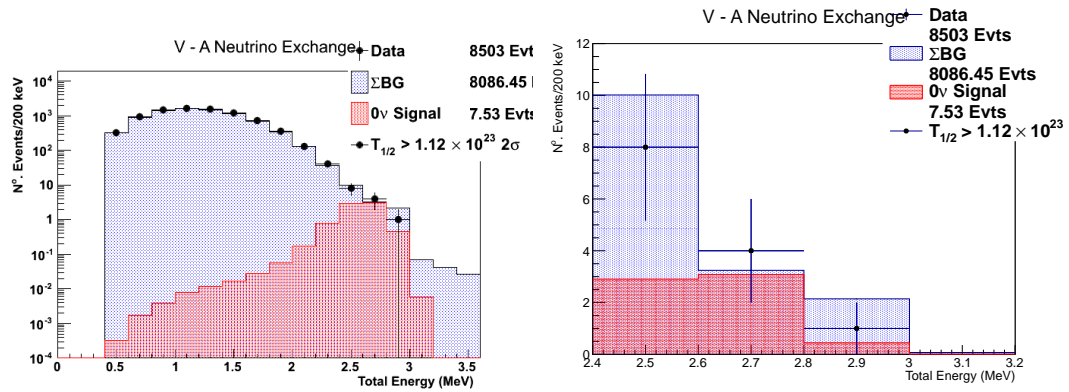


Figure 9.1:  $0\nu\beta\beta$  spectrum of  $^{116}\text{Cd}$  excluded at 90% C.L. shown in red as an overlay on the total background. All backgrounds, including the measured  $2\nu\beta\beta$  spectrum, are shown in blue. Data points are shown in black.

At 90% Confidence Level, the  $0\nu\beta\beta$  spectrum contains 7.53 events, corresponding to a half-life of  $1.12 \times 10^{23}$  years.

### 9.2.2 Signal Windows

To determine the optimal signal window and thus place the strongest limit on  $0\nu\beta\beta$  [99], a variety of ranges were considered. Beginning with the full spectrum, the number of bins considered in the limit calculation was reduced, with the window centered around the  $Q_{\beta\beta}$  values of 2.802 and 2.995 MeV, respectively. Results of the limit calculations are shown in Table 9.2.2.

$^{116}\text{Cd}$ ( $Q_{\beta\beta}$ : 2.802 MeV)					
Window (Total Electron Energy, MeV)	Full Spectrum	1.8 - 3.0	2.1 - 3.0	2.3 - 3.0	2.6 - 3.0
$0\nu\beta\beta$ Signal Events (90% C.L.)	7.25	7.18	7.13	6.96	6.20
$0\nu\beta\beta$ Efficiency (%)	12.23	12.11	12.02	10.46	5.74
$T_{1/2}^{0\nu}$	1.12	1.12	1.12	1.12	1.12

Table 9.3: Results of calculating the  $^{116}\text{Cd}$   $0\nu\beta\beta$  half life for various signal windows.

### 9.2.3 Effective neutrino Mass Calculation

After calculating a half-life limit for the  $0\nu\beta\beta$  process, the results can be combined with the phase-space factor and nuclear matrix elements to pro-

duce a limit on effective neutrino mass. Because of the discrepancies between calculated NME values, the result is a range on the upper limit of effective neutrino mass.

In the case of  $^{116}\text{Cd}$ , the limit on the neutrino mass is:

$$\langle m_\nu \rangle \leq (4.33 - 5.54) eV \quad (9.3)$$

### 9.2.4 Right-Handed Currents

A procedure identical to that used for the LME was applied for computation of right-handed current 90% confidence level limit. No events are observed above background for the  $0\nu\beta\beta$  decay via the right-handed current mechanism, with a lower half-life limit set at  $6.02 \times 10^{22}$  yr at 90% C.L., corresponding to 7.61 events excluded. The full spectrum and a detail of the peak region are shown in Figure 9.2.

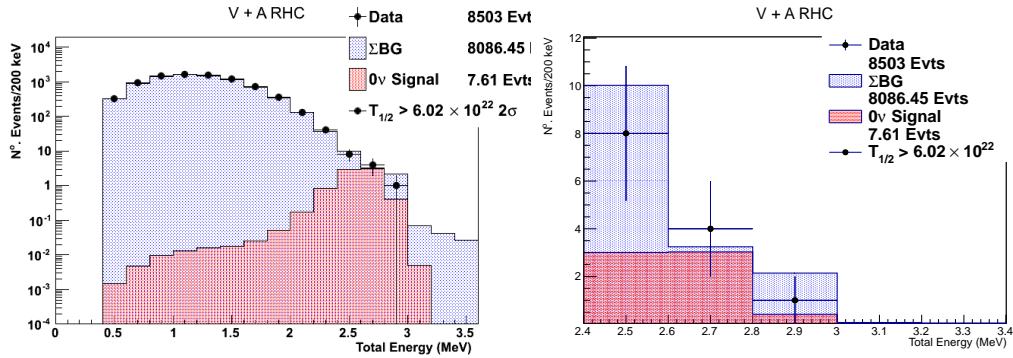


Figure 9.2: Right-Handed Current (V + A) spectrum of  $^{116}\text{Cd}$  excluded at 90% C.L. shown as an overlay on the total background. All backgrounds, including the measured  $2\nu\beta\beta$  spectrum, are shown in blue. Data points are shown in black.

### 9.2.5 Majoron-Emitting Models

The same procedure for calculating half-life limits was applied to Majoron-emitting models, but in contrast to the LME and RHC cases, there is no single signal window to be used in the calculation. As a result, only full-spectrum calculations were taken. Results are summarized in table 9.4.

No events are observed in any of the Majoron-emitting modes; lower half-life limits and excluded events are shown in table 9.4. Electron energy spectra for Majoron modes compared to the background-subtracted data are shown in Figure 9.3.

Spectral Index	n = 1	n = 2	n = 3	n = 7
Events excluded at 90% C.L.	78.43	220.74	414.23	306.75
Signal efficiency	8.70	7.10	5.62	2.08
$T_{1/2}(\times 10^{21}) \geq$	7.66	2.22	0.94	0.47

Table 9.4: Summary of results for Majoron-emitting models in  $^{116}\text{Cd}$ .

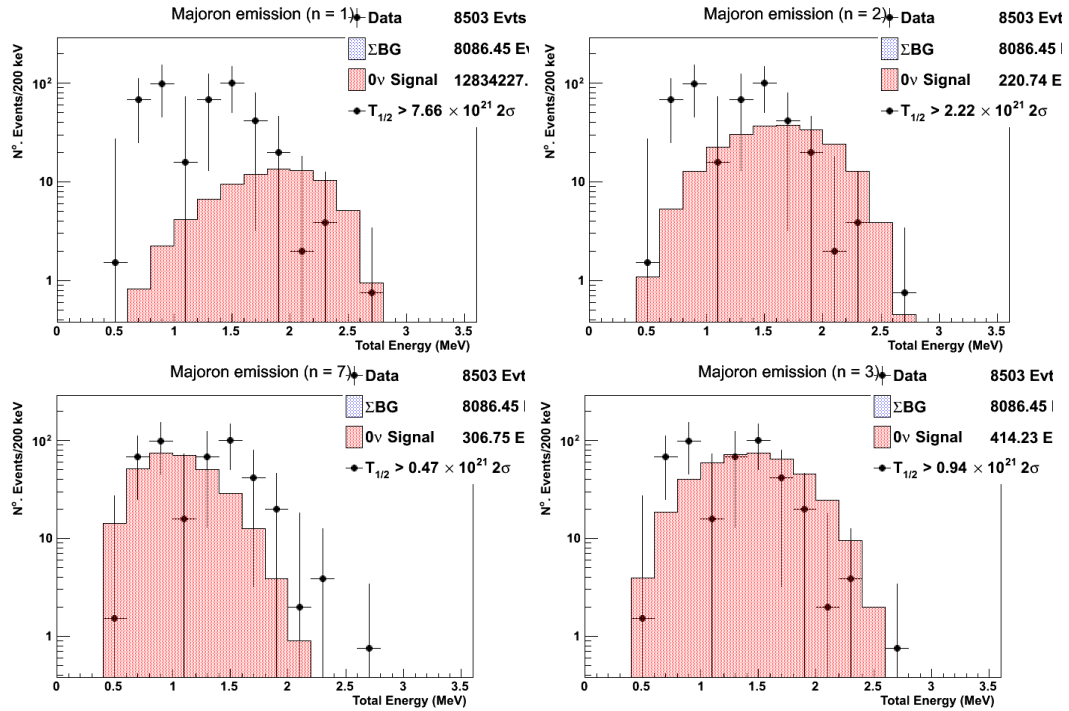


Figure 9.3: Spectra of Majoron-emitting modes in  $^{116}\text{Cd}$ , shown in red. Data are shown as black points after subtraction of all backgrounds, including the measured  $2\nu\beta\beta$  spectrum. Clockwise starting from top left, they are the  $n=1$ ,  $n=2$ ,  $n=5$ , and  $n=7$  modes.

### 9.3 Neutrinoless Transition Search Results for $^{82}\text{Se}$

For calculation of the  $^{82}\text{Se}$   $0\nu\beta\beta$  half-life limits, procedures identical to those used in the analysis of  $^{116}\text{Cd}$  were used. Results for the Light Majorana Exchange are shown in section 9.3.1, Right-Handed Current results are given in section 9.3.3, and limits for Majoron-emitting models are given in section 9.3.4. Where applicable, these quantities are related to the effective neutrino mass  $\langle m_\nu \rangle$  and RHC coupling constant values.

#### 9.3.1 Light Majorana Exchange Mechanism

The  $0\nu\beta\beta$  spectrum is shown as an overlay on the data and total background in Figure 9.4, where the background includes the  $2\nu\beta\beta$  spectrum.

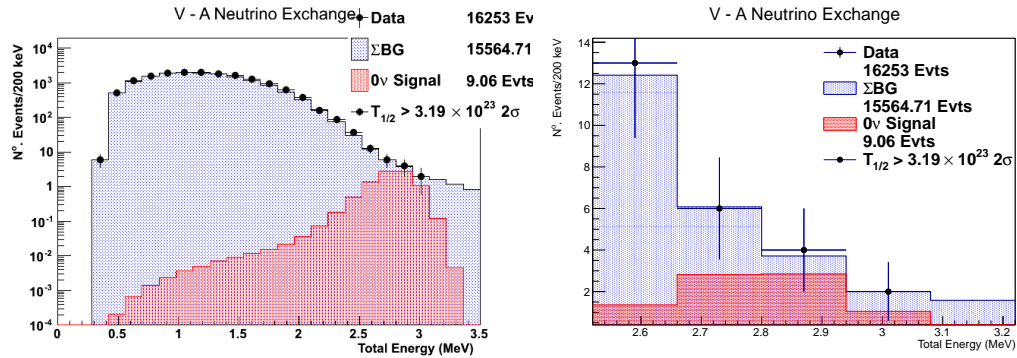


Figure 9.4:  $0\nu\beta\beta$  spectrum of  $^{82}\text{Se}$  excluded at 90% C.L. shown in red as an overlay on the total background, shown in blue and including the  $2\nu\beta\beta$  spectrum. Data points are displayed in black.

At 90% Confidence Level, the  $0\nu\beta\beta$  spectrum contains 9.06 events, corresponding to a half-life of  $3.19 \times 10^{23}$  years.

### 9.3.2 Effective Neutrino Mass Calculation

Having calculated a half-life limit for the  $0\nu\beta\beta$  process, the results can be combined with the phase-space factor and nuclear matrix elements to calculate a limit on effective neutrino mass. Because of the discrepancies between calculated NME values, the result is a range on the upper limit of effective neutrino mass.

For  $^{82}\text{Se}$ , the limit is calculated to be:

$$\langle m_\nu \rangle \leq (2.28 - 2.82) \text{ eV} \quad (9.4)$$

### 9.3.3 Right-Handed Currents

A procedure identical to that used for the LME was applied for computation of right-handed current 90% confidence level limit. No events above background were observed, setting a lower half-life limit for  $0\nu\beta\beta$  decay via the right-handed current mechanism at  $7.93 \times 10^{22}$  yr, corresponding to 9.17 events. Results are shown in Figure 9.5, with the RHC spectrum overlaid on the combined background spectrum, including  $2\nu\beta\beta$  events.

### 9.3.4 Majoron-Emitting Models

The same procedure for calculating half-life limits was applied to Majoron-emitting models. However, because their spectra cover ranges similar to those of the  $2\nu\beta\beta$  spectrum, there is no single signal window to be used in the calculation. As a result, only full-spectrum calculations were taken. Total electron



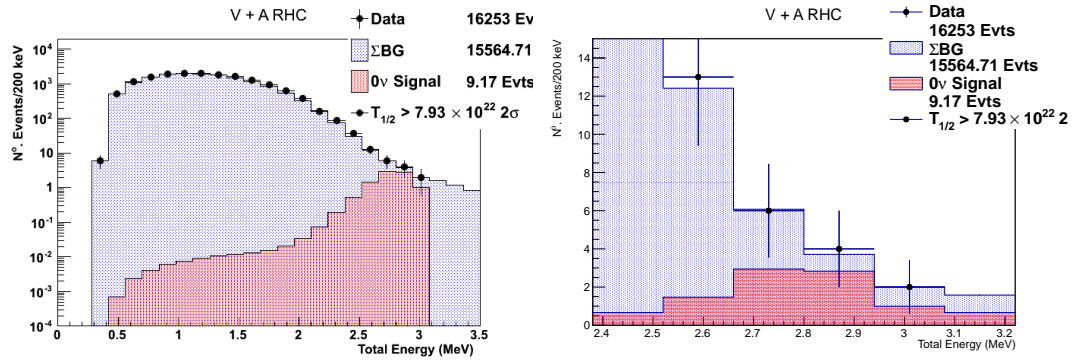


Figure 9.5: Right-handed current ( $V + A$ ) spectrum of  $^{82}\text{Se}$  excluded at 90% C.L. shown in red as an overlay on the total background, shown in blue and including the measured  $2\nu\beta\beta$  spectrum. Data points are displayed in black.

energy spectra for Majoron modes are shown overlaid on the background subtracted data in Figure 9.6.

Results for Majoron-emitting modes are summarized in table 9.5.

Spectral Index	n = 1	n=2	n = 3	n = 7
Events excluded at 90% C.L.	144.80	393.48	583.83	428.55
Signal efficiency	9.91%	8.33	6.88%	2.90%
$T_{1/2}(\times 10^{21}) \geq$	6.89	2.07	1.15	0.66

Table 9.5: Summary of results for Majoron-emitting models in  $^{82}\text{Se}$ .

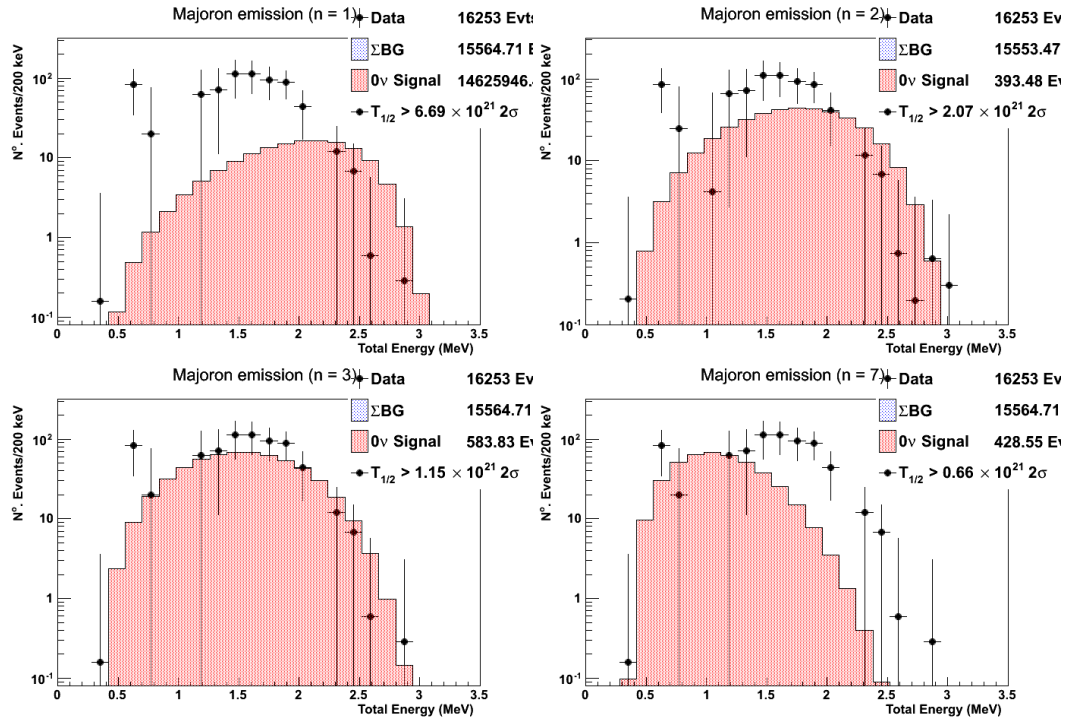


Figure 9.6: Majoron-emitting model spectra for  $^{82}\text{Se}$ , shown in red. Data are shown as black points after subtraction of all backgrounds, including the measured  $2\nu\beta\beta$  spectrum. Clockwise starting from top left, they are the  $n=1$ ,  $n=2$ ,  $n=5$ , and  $n=7$  modes.

## 9.4 Discussion and Conclusions

Neutrinoless double-beta decay processes have been considered for both  $^{116}\text{Cd}$  and  $^{82}\text{Se}$ , including the Light Majorana Exchange mechanism, Right-Handed Currents, and Majoron emitting modes. No neutrinoless double beta decay events were observed above expected background, and thus only lower limits could be set. In  $^{116}\text{Cd}$ , a  $0\nu\beta\beta$  half-life limit of

$$T_{1/2}^{0\nu}(90\%C.L.) \geq 1.12 \times 10^{23} \text{ yr} \quad (9.5)$$

has been set for  $^{116}\text{Cd}$  in the Light Majorana Exchange mechanism, corresponding to 7.53 neutrinoless events excluded and an effective neutrino mass of

$$\langle m_\nu \rangle \leq (4.33 - 5.54) \text{ eV} \quad (9.6)$$

This limit improves upon the previously-reported value of  $1.6 \times 10^{22}$  yr from NEMO-3 [96], indicating an improvement of almost an order of magnitude from using the full data set in measurements. However, it remains below the current half-life limit set by the Solotvina experiment [72] of  $1.7 \times 10^{23}$  yr. Effective neutrino masses calculated from all considered NMEs are given in Table 9.6.

Neutrinoless decay half-life limits have been set for  $^{82}\text{Se}$ , with a Light Majorana Exchange half-life limit of

$$T_{1/2}^{0\nu}(90\%C.L.) \geq 3.19 \times 10^{23} \text{ yr} \quad (9.7)$$

corresponding to 9.06 excluded events and an effective neutrino mass of

$$\langle m_\nu \rangle \leq (2.28 - 2.82) \text{ eV} \quad (9.8)$$

NME Type	Value	$\langle m_{\beta\beta} \rangle$ (eV)
QRPA ( $g_A = 1.25$ )	1.53	5.54
QRPA ( $g_A = 1.00$ )	1.31	4.80
RQRPA ( $g_A = 1.25$ )	1.43	5.24
RQRPA ( $g_A = 1.00$ )	1.22	4.33

Table 9.6: Summary of effective neutrino masses by calculated nuclear matrix element for  $^{116}\text{Cd}$ .

falling slightly below previously-reported values from NEMO [96]. A summary of effective neutrino masses by NME is given in Table 9.7.

While both results fall below current world-best limits, these data may still be considered as useful points in constraining  $\langle m_\nu \rangle$  and calculations of neutrinoless nuclear matrix elements.

In addition to the Light Majorana Exchange process, the Right Handed Current (V + A) and Majoron-emitting processes were also considered. In both cases, no events were observed above predicted background, so lower half-life limits were set in both  $^{116}\text{Cd}$  and  $^{82}\text{Se}$ .

NME Type	Value	$\langle m_{\beta\beta} \rangle$ (eV)
QRPA ( $g_A = 1.25$ )	2.36	2.82
QRPA ( $g_A = 1.00$ )	2.10	2.64
RQRPA ( $g_A = 1.25$ )	2.12	2.62
RQRPA ( $g_A = 1.00$ )	1.91	2.28

Table 9.7: Summary of effective neutrino masses by calculated nuclear matrix element for  $^{82}\text{Se}$ .

## Chapter 10

### The SuperNEMO Detector

The SuperNEMO detector is a planned next-generation double-beta decay detector to be built as a successor to SuperNEMO. Utilizing experience from the NEMO-3 experiment as well as an increased mass of source material, SuperNEMO is intended to provide an increase in  $0\nu\beta\beta$  half-life sensitivity of one to two orders of magnitude with respect to NEMO-3. SuperNEMO will be installed in an extension of the LSM, near the site of the NEMO-3 detector, thus retaining the same 4,800 m.w.e. overhead as NEMO-3.

The experiment plans to continue the search for  $0\nu\beta\beta$  decay using a similar philosophy and technique as that of NEMO-3, but using the improved mass, radiopurity, and instrumentation to probe regions inaccessible to NEMO-3.

#### 10.1 Detector Description

SuperNEMO is being developed as a modular experiment, ultimately containing 20 sectors which can be constructed individually and added as they are completed. Each module will be entirely self-contained and able to commence data taking immediately following its completion. A demonstrator

module will be installed first, with slightly more source material than future planned modules, to demonstrate the sensitivity of the new detector.

In contrast to NEMO-3, the SuperNEMO detector will be rectangular in shape, with each source foil housed in a separate module. an exploded view of a planned module is shown in Figure 10.1.

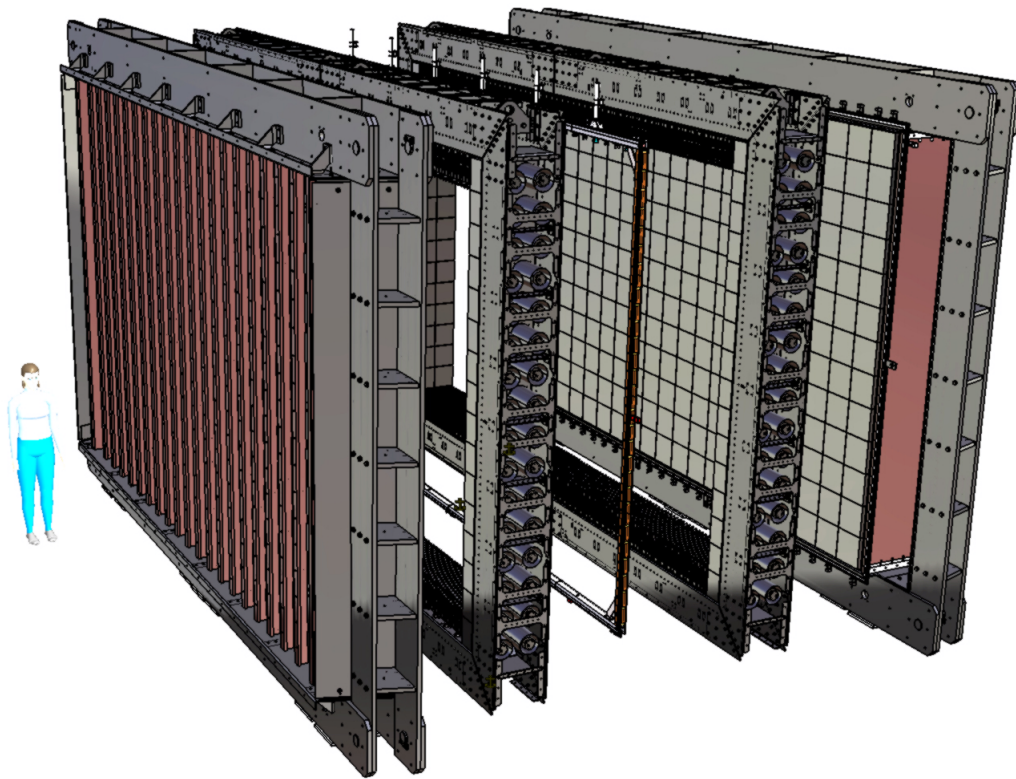


Figure 10.1: Exploded view of the SuperNEMO detector.

## 10.2 Source Material

At present, each of the 20 planned SuperNEMO modules is planned to house approximately 5 kg of  $^{82}\text{Se}$ , with the exception of the demonstrator module, which will contain 7 kg, ultimately totaling approximately 100 kg of source material. However, because the modular nature of the experiment allows for additions after data taking has commenced, if it becomes possible through unforeseen advances in enrichment in other isotopes, it is also conceivable that another isotope such as  $^{48}\text{Ca}$  or  $^{96}\text{Zr}$  could be added for further study.

## 10.3 Tracker

SuperNEMO plans to use a tracker similar to that of NEMO-3, differing only in the arrangement of the Geiger cells. Each module plans to use several thousand octagonal drift cells similar to those described in Section 3.3.1 [100]. Extensive testing of the tracker arrangement has been carried out, including studies of drift chamber design and size, wire size and material, and gas mixture [101].

To further reduce the risk of contamination on the tracker wires, a wiring robot was developed to automate the construction process. Because there are a planned 260,000 wires to be installed across all 20 modules, this presents an opportunity to greatly reduce the amount of contamination distributed throughout SuperNEMO.



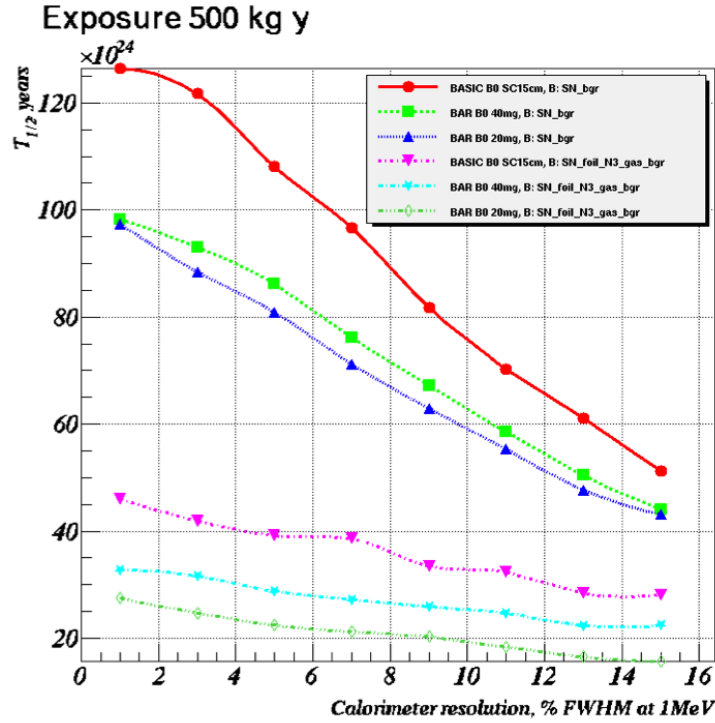


Figure 10.2: Predicted SuperNEMO half-life sensitivity as a function of calorimeter resolution at 1 MeV. Individual curves represent predicted sensitivities given differing levels of background contaminants present.

## 10.4 Calorimeter

To achieve the desired half-life sensitivity for SuperNEMO, the overall calorimeter resolution must be less than 8% FWHM at 1 MeV, corresponding to 4% FWHM at 3 MeV, near the Q-value for the relevant double beta decays. This represents an improvement with respect to the NEMO-3 resolution of approximately a factor of two. Predicted sensitivity as a function of calorimeter resolution for SuperNEMO is presented graphically in Figure 10.2.

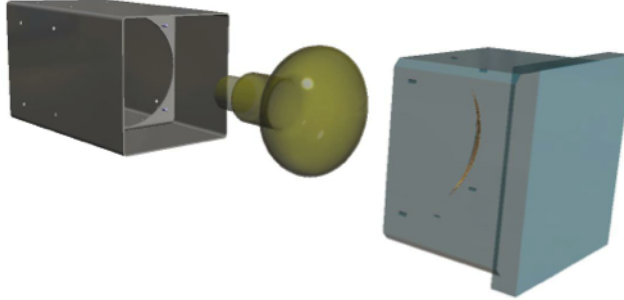


Figure 10.3: Exploded view of a main wall optical module in SuperNEMO, showing the hemispherical cutout to be bonded directly to the PMT.

To achieve this goal, several avenues have been pursued.

- Construction of main wall scintillators in poly-vinyl-toluene (PVT), where possible. PVT scintillates at 10,000 photons/MeV, compared to the estimated 8,000 photons/MeV for polystyrene (PS).
- Removal of the light guide connecting scintillator to PMT in main wall scintillators. This was incorporated in the design by making a hemispherical cutout in the scintillator which can be bonded directly to the PMT, as shown in Figure 10.3.
- Use of larger PMTs to increase light collection efficiency.

The calibration system has also been improved with respect to NEMO-3, including the removal of calibration tubes and windows which presented a barrier to  $^{207}\text{Bi}$  electrons. Windows in particular were also significantly less radiopure than the adjacent source foils, and introduced contamination in the surrounding areas. The new system is contained almost entirely outside of the

detector when not in use, and the sources are guided into place using a weight centered on a guiding wire. Development and testing of this system has been carried out at the University of Texas.

## 10.5 Radiopurity

As discussed in section 4.4.1, sensitivity to  $0\nu\beta\beta$  signal is largely dependent upon the reduction of background. Therefore, a major effort has been made during the research and development phase of SuperNEMO to reduce the amount of background present in the final detector. To reach the stated sensitivity goals, limits have been set regarding acceptable activity of troublesome radioisotopes, at  $2\ \mu\text{Bq}/\text{kg}$  for  $^{208}\text{Tl}$  and  $10\ \mu\text{Bq}/\text{kg}$  for  $^{214}\text{Bi}$ ; all other isotopes must fall below those limits. A major portion of the effort to develop and clean materials in order to reach stated radiopurity goals has been carried out by the University of Texas group.

## 10.6 SuperNEMO versus NEMO-3

A summary of planned SuperNEMO properties with and a comparison to NEMO-3 is presented in table 10.1. Upgrades in terms of candidate isotope mass, projected signal efficiency, required contamination levels, and calorimeter resolution are presented, along with the resulting projected increases in sensitivity to  $0\nu\beta\beta$  half-life thus the effective neutrino mass  $\langle m_\nu \rangle$ .

	NEMO-3	SuperNEMO
Isotope	$^{100}\text{Mo}, ^{82}\text{Se}, ^{116}\text{Cd}$ $^{96}\text{Zr}, ^{48}\text{Ca}, ^{130}\text{Te}, ^{150}\text{Nd}$	$^{82}\text{Se}$
Mass	10 kg	$\geq 100$ kg
Signal Efficiency	18%	$> 30\%$
$^{208}\text{Tl}$ foil activity	$< 20 \mu\text{Bq/kg}$	$< 2 \mu\text{Bq/kg}$
$^{214}\text{Bi}$ foil activity	$< 300 \mu\text{Bq/kg}$	$< 10 \mu\text{Bq/kg}$
Energy res. at 3 MeV	8% FWHM	4% FWHM
Half-life sensitivity	$\simeq 10^{24}$ yr	$\simeq (1 - 2) \times 10^{26}$ yr
$m_\nu$ sensitivity	$\simeq (0.3 - 0.9)$ eV	$\simeq (0.05 - 0.1)$ eV

Table 10.1: Comparison of NEMO-3 and SuperNEMO parameters [100].

## Chapter 11

### Simulations of SuperNEMO Scintillators

To achieve the stated sensitivity goal for the SuperNEMO experiment, a detailed knowledge of the scintillator response is of the utmost importance. As part of the ongoing research and development effort for the SuperNEMO detector, detailed simulations of the scintillators were carried out using the GEANT4 development package [102].

Following the model developed for the NEMO-3 detector [84], a model of each scintillator variety proposed for the SuperNEMO experiment was developed to determine the optimal design for the detector and understanding of photon behavior inside the optical module.

This chapter describes the simulation of optical modules to be used within the SuperNEMO modules, including the blocks ultimately chosen for use in SuperNEMO as well as several relevant types which were simulated for comparison during research and development.

#### 11.1 Scintillator Types

The final design of the SuperNEMO calorimeter calls for three distinct scintillator blocks, each to be placed in a distinct section of the calorimeter.

*Main wall* blocks cover the walls facing the isotopic source foils, and as they are intended to be the main component in electron energy measurements, require the best overall energy resolution. *X-wall* blocks are placed at the ends of the foils, and *V-wall* blocks are to be above and below the foils; both are to be used largely for tagging  $\gamma$ -rays and background rejection, and thus their required minimum energy resolution is less strict than that of the main wall blocks. A description of each scintillator type is given in table 11.1.1.

### 11.1.1 Photomultiplier Tubes

For the case of both X- and V-walls, the scintillators are coupled to 5" Hamamatsu PMTs via a poly-methyl-methacrylate light guide bonded to the top face of the scintillator. In the case of the main wall blocks, however, the PMT is bonded directly to the PMT in a hemispherical section cut out of the top face of the scintillator.

An exception to this setup occurs in the main wall blocks at the edge of each wall. Such blocks are partially overlapped by adjacent X- and V-blocks, and as such their fiducial volume is reduced. Because of the consequent loss of efficacy of these blocks, they are bonded to 5" PMTs, which have a reduced quantum efficiency and photocathode area, but were available for reuse after their removal from NEMO-3.

Block Type	Height (mm)	Width (mm)	Depth (mm)	Attached PMT
Main wall	256.8	256.8	194.0	8" 5" (Edge blocks)
X wall	256.8	256.8	194.0	5"
V wall	308.0	310.0	150.0	5"

Table 11.1: Description of scintillator blocks in SuperNEMO.

## 11.2 Materials

In addition to the specific geometry of each variety of scintillator, the choice of material is also crucial in determining the properties of each optical module. Two different scintillator plastics were considered for use in SuperNEMO scintillators: Poly-vinyl-tolulene (PVT) manufactured by Eljen [103], and Polystyrene (PS), manufactured by ENVINET. Both PVT and PS are doped with a p-terphenyl (pTP) primary fluor and a wavelength shifter 1,4-di-(5-phenyl-2-oxazolyl) benzene (POPOP). PVT light yield is quoted as 10,000 photons/MeV [103], while the light yield for PS is estimated at 8,000 photons/MeV.

Main wall scintillators with 8" PMTs are bonded directly to the PMT with an optical glue; in the case of scintillators with PMMA light guides, as

described in section 11.1.1, the light guide is bonded to the PMT with the same optical glue.

The scintillator is surrounded by a Teflon wrapping on four sides, and wrapped with a reflective Mylar covering. A 0.5 mm air gap is simulated between the scintillator and Mylar covering.

### 11.2.1 Material Properties

Simulations done for SuperNEMO scintillators followed the model developed in reference [84] in using  $\lambda$ -dependent properties in the optical modules, including absorption and emission spectra, bulk absorption length, and reflectivity of all materials present.

### 11.2.2 Simulation Results

To determine the resolution for a given scintillator block, the entrance face was divided into 25 separate sections arranged as a  $5 \times 5$  grid. 2,500 electrons with an energy of 1 MeV were simulated incident normal to the block face at each section, with the energy resolution at each position calculated as

$$R_{FWHM} = \frac{2 \ln 2 \sqrt{2}}{\sqrt{N_{pe}}} \quad (11.1)$$

where  $N_{pe}$  is the number of photoelectrons detected in the photomultiplier.

Simulation results are presented below for each of the three types of scintillator blocks to be used in SuperNEMO. Figure 11.1 shows the simulated energy resolution for each of the 25 electron entrance points on the block face for the main wall scintillator with PVT and an 8" PMT.



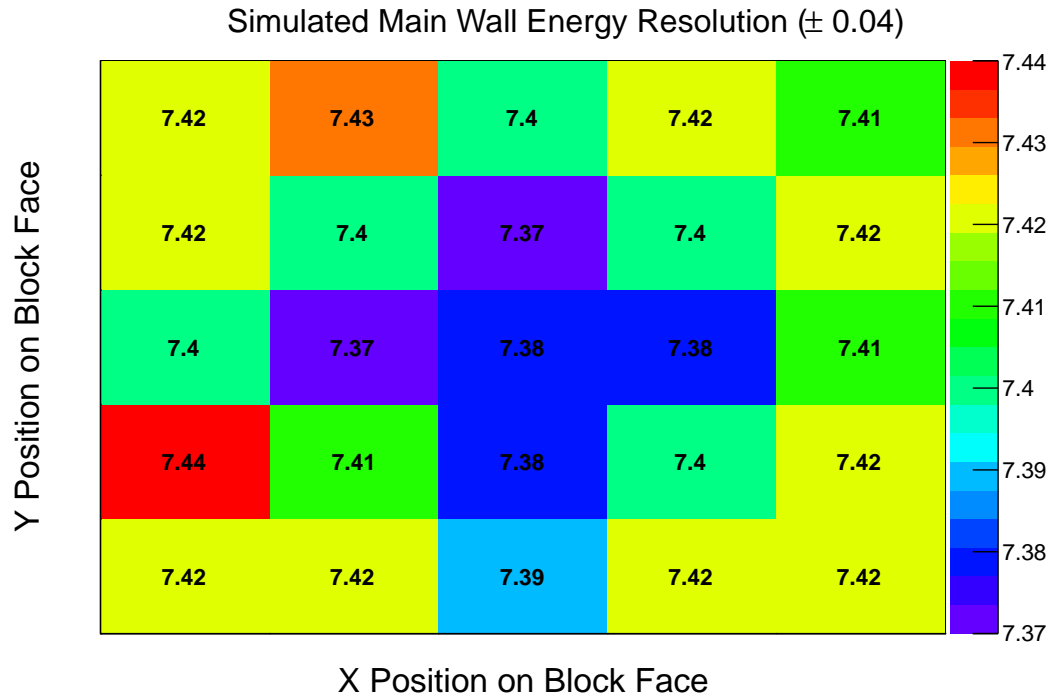


Figure 11.1: Simulated energy resolution for a main wall block to be used in SuperNEMO.

Figure 11.2 presents the simulated resolutions for the X and V walls. Simulation results are summarized in table 11.2, along with measured values taken within the collaboration [104], where available.

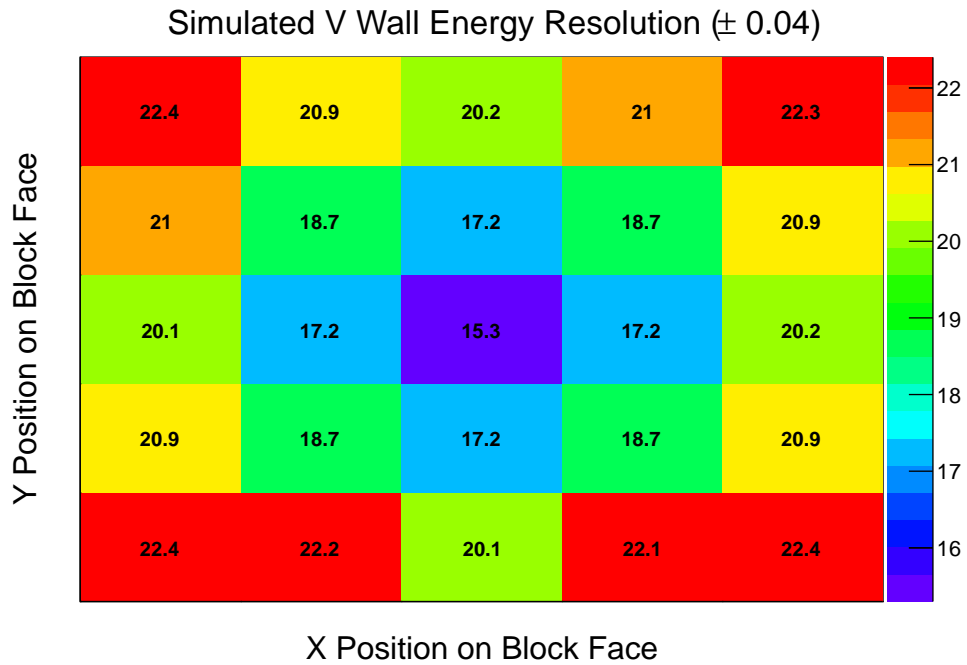
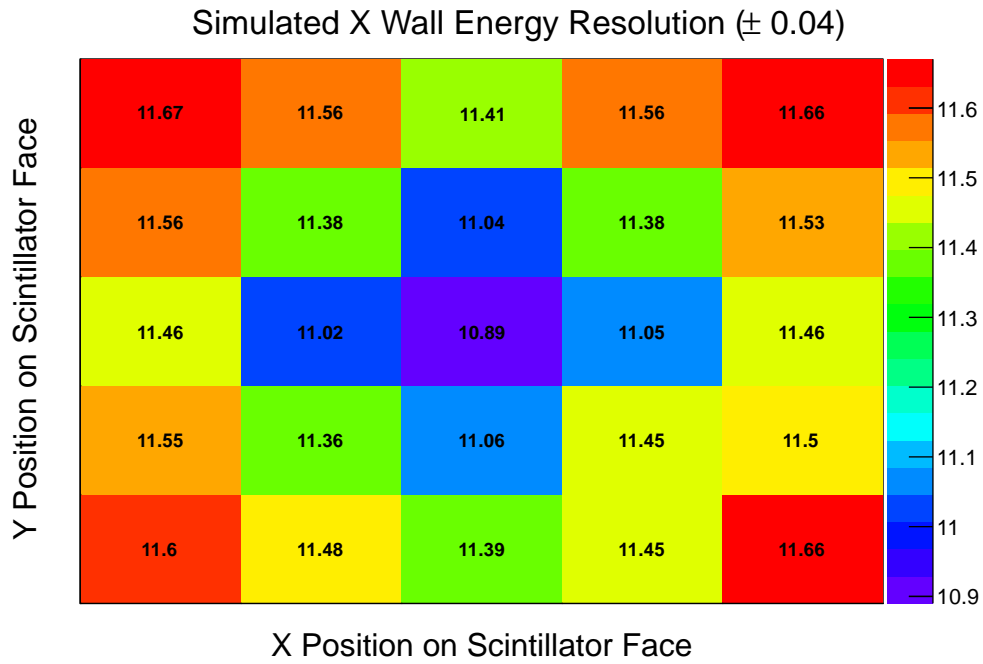


Figure 11.2: Simulated energy resolution for an X- (top) and V-wall (bottom) block to be used in SuperNEMO.

Block Type	Material	PMT	Average Resolution	Center Resolution	Measured Resolution
Main wall	PVT	8"	7.41%	7.38%	$(7.3 - 7.5) \pm 0.1\%$
		5"	13.14	12.62	–
	PS	8"	8.28%	8.25%	–
		5"	13.24	12.62%	–
X Wall	PS	5"	11.38%	10.89%	11 - 12%
V Wall	PS	5"	19.21%	15.3%	13 - 14% (edges excluded)

Table 11.2: Summary of SuperNEMO scintillator simulation results.

Note that for V Wall blocks, the measured results in table 11.2 are only for the  $176 \times 176 \text{ mm}^2$  area at the center of the block, corresponding to approximately 32% of the total block face, as the V Wall blocks were too large for the apparatus to measure.

### 11.3 Summary and Conclusion

Building off of a model developed for NEMO-3, the GEANT4 toolkit was used to produce simulations of all scintillator block types to be used in the forthcoming SuperNEMO detector. Detailed simulations were carried out utilizing measured spectral properties of all optical module components and

found to be in agreement with experimental values for all scintillator modules to be utilized in the SuperNEMO detector.

This work provides a detailed model of calorimeter response and photon transport in SuperNEMO. Simulations developed in this model were shown to be predictive of measurements, and thus useful as a tool for research and development of SuperNEMO as well as future detectors.

## Chapter 12

### Conclusions and Outlook

This dissertation details the measurement of two-neutrino double beta decay ( $2\nu\beta\beta$ ) and the search for neutrinoless double beta decay ( $0\nu\beta\beta$ ) in the transitions  $^{116}\text{Cd}\rightarrow^{116}\text{Sn}$  and  $^{82}\text{Se}\rightarrow^{82}\text{Kr}$  using the unique combination of tracking and calorimetry capabilities in the NEMO-3 detector.

The NEMO-3 detector and the tracking and calorimetry techniques were described, followed by an explanation of the analysis procedures and tools used in extracting physics information taken from the data, and the model of natural background radioactivity was discussed. The single-electron channel was used to improve the model of background contaminants *in situ*, particularly in the source foils, and the electron-gamma channel was studied to determine the amounts of  $^{214}\text{Bi}$  and  $^{208}\text{Tl}$  in NEMO-3.

The measured background model was used in the determination of  $2\nu\beta\beta$  half-lives. Using the full data set taken during the running of NEMO-3, an exposure of 1.65 kg·y was used to measure the  $2\nu\beta\beta$  half-life of  $^{116}\text{Cd}$  at

$$T_{1/2}^{2\nu} = 2.90 \pm 0.03(\text{stat}) \pm 0.15(\text{syst}) \times 10^{19} \text{ yr} \quad (12.1)$$

under the SSD hypothesis and

$$T_{1/2}^{2\nu} = 3.13 \pm 0.03(\text{stat}) \pm 0.17(\text{syst}) \times 10^{19} \text{ yr} \quad (12.2)$$

under the HSD hypothesis.  $\chi^2$  fits to both total and minimum energy electron spectra indicate that decay via the SSD hypothesis is favored.

The results of the SSD hypothesis are in agreement with the value measured by the Solotvina experiment, and represent the best measured uncertainties to date.

The final data set for  $^{82}\text{Se}$  corresponded to an exposure of 3.75 kg·y, used to measure a  $2\nu\beta\beta$  half-life of

$$T_{1/2}^{2\nu} = 10.62 \pm 0.11(\text{stat}) \pm 0.56(\text{syst}) \times 10^{19} \text{ yr} \quad (12.3)$$

for  $^{82}\text{Se}$ .

Lower limits were set at 90% confidence level on the  $0\nu\beta\beta$  half-lives for both  $^{116}\text{Cd}$  and  $^{82}\text{Se}$ , corresponding to upper limits on the effective neutrino mass  $\langle m_\nu \rangle$ . The limit for  $^{116}\text{Cd}$  was found to be

$$T_{1/2}^{0\nu}(90\%C.L.) \geq 1.12 \times 10^{23} \text{ yr} \quad (\langle m_\nu \rangle \leq 4.33 - 5.54 \text{ eV}) \quad (12.4)$$

giving an improvement over previously-quoted NEMO results but falling below the current best limit.

The  $0\nu\beta\beta$  half-life of  $^{82}\text{Se}$  was set at

$$T_{1/2}^{0\nu}(90\%C.L.) \geq 3.19 \times 10^{23} \text{ yr} \quad (\langle m_\nu \rangle \leq 2.28 - 2.82 \text{ eV}) \quad (12.5)$$

falling slightly below previously-quoted values from NEMO.

The development of the next-generation successor to NEMO-3, SuperNEMO, was also discussed, including its stated physics goals and an overview

of the planned detector setup and instrumentation. Planned advances for the new detector allowing for increases of two orders of magnitude in half-life sensitivity are shown, including developments in isotope mass, radiopurity requirements, and calorimetry resolution. Detailed information about the development of calorimetric simulations for the new detector were discussed, demonstrating that the SuperNEMO calorimeter is sufficient to achieve the project's stated half-life sensitivity goal. Simulations were shown to be in agreement with measured data, providing an accurate modeling of the SuperNEMO calorimeters and allowing understanding of the behavior of planned optical modules.

SuperNEMO expects to reach a neutrinoless double beta decay half-life sensitivity of  $10^{26}$  years over the course of its lifetime, generating measurements competitive with other next-generation experiments currently in development.

## Appendices



# Appendix A

## Scintillator details

This appendix gives an overview of and details for scintillators used in the optical modules in NEMO-3. Scintillator types, dimensions, associated PMTs, and number contained in the detector are presented for each area (inner wall, outer wall, and petals).

Table A.2 provides details of the blocks on the internal and external walls of NEMO-3. Table A.3 contains details of the inner and outer petal scintillators. Table A.1 presents the mass fractions of base material and dopants for primary scintillation and wavelength shifting for each of the block types.

Block type	IN	EC	EE	Petal
PS	98.49	98.49	98.49	98.75
pTP	1.50	1.50	1.50	1.20
POPOP	0.01	0.01	0.01	0.05

Table A.1: Mass fraction of scintillator materials by block type.

Block type	IN	EC	EE
Number per sector	34	13	26
Thickness	110 mm	99 mm	99/123 mm
Height	153 mm	200 mm	200 mm
Width	154/138 mm	218/228 mm	218/230 mm
Volume	2.41	4.51	5.01
Associated PMT	3"	5"	5"
Total Number	680	260	520

Table A.2: Vertical wall scintillator characteristics.

Block type	L1	L2	L3	L4
Number per sector	6	6	6	6
Thickness	100 mm	100 mm	100 mm	100 mm
Width	113/126 mm	133/146 mm	174/188 mm	195/208 mm
Length	126 mm	126 mm	126 mm	126
Volume	1.51	1.81	2.31	2.51
Associated PMT	3"	3"	3"	5"
Total Number	120	120	120	120

Table A.3: Petal scintillator characteristics.

## Appendix B

### Double beta decay candidate isotopes

This appendix presents a list of known double beta decay candidate isotopes. The transition, end-point energy (Q-value), relative abundance, and phase-space factors for the two-neutrino and zero-neutrino double beta decay processes [105].

Transition	$Q_{\beta\beta}$ (keV)	$\eta(\%)$	$G^{2\nu}$ ( $\text{yr}^{-1}$ )	$G^{0\nu}$ ( $\text{yr}^{-1}$ )
$^{46}\text{Ca} \rightarrow ^{46}\text{Ti}$	$987 \pm 4$	0.0035	$1.148 \times 10^{-22}$	$1.397 \times 10^{-27}$
$^{48}\text{Ca} \rightarrow ^{46}\text{Ti}$	$4271 \pm 4$	0.187	$3.968 \times 10^{-17}$	$2.439 \times 10^{-25}$
$^{70}\text{Zn} \rightarrow ^{70}\text{Ge}$	$1001 \pm 3$	0.62	$3.155 \times 10^{-22}$	$2.342 \times 10^{-27}$
$^{76}\text{Ge} \rightarrow ^{76}\text{Se}$	$2039.6 \pm 0.9$	7.8	$1.305 \times 10^{-19}$	$2.445 \times 10^{-26}$
$^{80}\text{Se} \rightarrow ^{80}\text{Kr}$	$130 \pm 9$	49.8	$1.220 \times 10^{-28}$	$4.274 \times 10^{-29}$
$^{82}\text{Se} \rightarrow ^{82}\text{Kr}$	$2995 \pm 6$	9.2	$4.348 \times 10^{-18}$	$1.079 \times 10^{-25}$

Table B.1: Table of double beta decay isotopes, with  $Q_{\beta\beta}$  values, isotopic abundance and phase space factors  $G$  for  $2\nu\beta\beta$  and  $0\nu\beta\beta$  processes [105].

Transition	$Q_{\beta\beta}$ (keV)	$\eta(\%)$	$G^{2\nu}$ ( $\text{yr}^{-1}$ )	$G^{0\nu}$ ( $\text{yr}^{-1}$ )
$^{86}\text{Kr} \rightarrow ^{86}\text{Sr}$	$1256 \pm 5$	17.3	$3.333 \times 10^{-21}$	$6.369 \times 10^{-27}$
$^{94}\text{Zr} \rightarrow ^{94}\text{Mo}$	$1145.3 \pm 2.5$	17.4	$2.304 \times 10^{-21}$	$6.369 \times 10^{-27}$
$^{96}\text{Zr} \rightarrow ^{96}\text{Mo}$	$3350 \pm 3$	2.8	$1.927 \times 10^{-17}$	$2.242 \times 10^{-25}$
$^{98}\text{Mo} \rightarrow ^{98}\text{Ru}$	$112 \pm 7$	24.1	$9.709 \times 10^{-29}$	$6.711 \times 10^{-29}$
$^{100}\text{Mo} \rightarrow ^{100}\text{Ru}$	$3034 \pm 6$	9.6	$9.434 \times 10^{-18}$	$1.754 \times 10^{-25}$
$^{104}\text{Ru} \rightarrow ^{104}\text{Pd}$	$1299 \pm 4$	18.7	$9.174 \times 10^{-21}$	$1.202 \times 10^{-26}$
$^{110}\text{Pd} \rightarrow ^{110}\text{Cd}$	$2013 \pm 19$	11.8	$3.984 \times 10^{-19}$	$5.376 \times 10^{-26}$
$^{114}\text{Cd} \rightarrow ^{114}\text{Sn}$	$534 \pm 4$	28.7	$1.443 \times 10^{-23}$	$1.639 \times 10^{-27}$
$^{116}\text{Cd} \rightarrow ^{116}\text{Sn}$	$2802 \pm 4$	7.5	$8.000 \times 10^{-18}$	$1.894 \times 10^{-25}$
$^{122}\text{Sn} \rightarrow ^{122}\text{Te}$	$364 \pm 4$	4.56	$1.047 \times 10^{-24}$	$8.621 \times 10^{-28}$
$^{124}\text{Sn} \rightarrow ^{124}\text{Te}$	$2288.1 \pm 1.6$	5.64	$1.686 \times 10^{-18}$	$1.055 \times 10^{-25}$

Table B.1: Table of double beta decay isotopes, with  $Q_{\beta\beta}$  values, isotopic abundance and phase space factors  $G$  for  $2\nu\beta\beta$  and  $0\nu\beta\beta$  processes [105].

Transition	$Q_{\beta\beta}$ (keV)	$\eta(\%)$	$G^{2\nu}$ ( $\text{yr}^{-1}$ )	$G^{0\nu}$ ( $\text{yr}^{-1}$ )
$^{128}\text{Te} \rightarrow ^{128}\text{Xe}$	$868 \pm 4$	31.7	$8.475 \times 10^{-22}$	$6.993 \times 10^{-27}$
$^{130}\text{Te} \rightarrow ^{130}\text{Xe}$	$2528.8 \pm 4$	33.8	$4.808 \times 10^{-18}$	$1.698 \times 10^{-25}$
$^{134}\text{Xe} \rightarrow ^{134}\text{Ba}$	$847 \pm 10$	10.4	$8.621 \times 10^{-22}$	$7.692 \times 10^{-27}$
$^{136}\text{Xe} \rightarrow ^{136}\text{Ba}$	$2479 \pm 8$	8.9	$4.831 \times 10^{-18}$	$1.812 \times 10^{-25}$
$^{142}\text{Ce} \rightarrow ^{142}\text{Nd}$	$1417.6 \pm 2.5$	11.1	$7.246 \times 10^{-20}$	$1.812 \times 10^{-26}$
$^{146}\text{Nd} \rightarrow ^{146}\text{Sm}$	$56 \pm 5$	17.2	$4.854 \times 10^{-30}$	$1.418 \times 10^{-28}$
$^{148}\text{Nd} \rightarrow ^{148}\text{Sm}$	$1928.3 \pm 1.9$	5.7	$1.070 \times 10^{-18}$	$1.276 \times 10^{-25}$
$^{150}\text{Nd} \rightarrow ^{150}\text{Sm}$	$3367.1 \pm 2.2$	5.6	$1.189 \times 10^{-16}$	$8.000 \times 10^{-25}$
$^{154}\text{Sm} \rightarrow ^{154}\text{Gd}$	$1251.9 \pm 1.5$	22.6	$4.098 \times 10^{-20}$	$4.202 \times 10^{-26}$
$^{160}\text{Gd} \rightarrow ^{160}\text{Dy}$	$1729.5 \pm 1.4$	21.8	$6.623 \times 10^{-19}$	$1.252 \times 10^{-25}$
$^{170}\text{Gr} \rightarrow ^{170}\text{Yd}$	$653.9 \pm 1.6$	14.9	$5.495 \times 10^{-22}$	$1.445 \times 10^{-26}$

Table B.1: Table of double beta decay isotopes, with  $Q_{\beta\beta}$  values, isotopic abundance and phase space factors  $G$  for  $2\nu\beta\beta$  and  $0\nu\beta\beta$  processes [105].

Transition	$Q_{\beta\beta}$ (keV)	$\eta(\%)$	$G^{2\nu}$ ( $\text{yr}^{-1}$ )	$G^{0\nu}$ ( $\text{yr}^{-1}$ )
$^{176}\text{Yb} \rightarrow ^{176}\text{Hf}$	$1078.8 \pm 2.7$	12.6	$3.067 \times 10^{-20}$	$5.714 \times 10^{-26}$
$^{186}\text{W} \rightarrow ^{186}\text{Os}$	$490.3 \pm 2.2$	28.6	$1.302 \times 10^{-22}$	$1.439 \times 10^{-26}$
$^{192}\text{Os} \rightarrow ^{192}\text{Pj}$	$417 \pm 4$	41.0	$5.051 \times 10^{-23}$	$1.299 \times 10^{-26}$
$^{198}\text{Pt} \rightarrow ^{198}\text{Hg}$	$1048 \pm 4$	7.2	$6.135 \times 10^{-20}$	$1.144 \times 10^{-25}$
$^{204}\text{Hg} \rightarrow ^{204}\text{Pb}$	$416.5 \pm 1.9$	6.9	$8.130 \times 10^{-23}$	$1.976 \times 10^{-26}$
$^{232}\text{Th} \rightarrow ^{232}\text{U}$	$858 \pm 6$	100	$5.952 \times 10^{-20}$	$2.519 \times 10^{-25}$
$^{238}\text{U} \rightarrow ^{238}\text{Pu}$	$1145.8 \pm 1.7$	99.275	$6.803 \times 10^{-19}$	$5.952 \times 10^{-25}$

Table B.1: Table of double beta decay isotopes, with  $Q_{\beta\beta}$  values, isotopic abundance and phase space factors  $G$  for  $2\nu\beta\beta$  and  $0\nu\beta\beta$  processes [105].

# Appendix C

## Time-of-Flight Calculation Details

This appendix details the method of calculating internal and external time-of-flight (TOF) probabilities for two-particle events in NEMO-3.

For events in which at least two scintillators are activated, the time discrepancy between hits can be used to compute the likelihood that the event originated in the source foil. For every such event, two hypotheses are constructed: the *internal* and *external* hypothesis. In the internal hypothesis, events are assumed to originate inside the foil, traverse the tracking chamber and cause a scintillator response. In the external hypothesis, events are assumed to originate outside the foil, cross the tracking chamber and source foil, and activate two or more scintillators. In each hypothesis, a time difference  $t_{th}$  is calculated based on the assumed origin for each particle and compared to the time  $t_m$  measured in the calorimeter.

The time differences  $\Delta t_{th}$  are calculated as

$$\Delta t_{th} = \frac{l_1}{v_1} \pm \frac{l_2}{v_2} \tag{C.1}$$

where the + is for the internal hypothesis and the - is external. For  $\gamma$  rays,  $v$  is  $c$ ; for electrons, the velocity is calculated using the electron momentum; however, because the momentum is not directly observable it must be calculated from the



measured energy. Using the relationships

$$E^2 = (E_k + m)^2 = p^2 + m^2 \rightarrow p^2 = E_k^2 + 2E_k m \quad (\text{C.2})$$

and

$$\frac{v}{c} = \frac{pc}{E}, \quad (\text{C.3})$$

the velocity is calculated as

$$v(E_k) = \frac{\sqrt{E_k^2 + 2E_k m c}}{E_k + m} \quad (\text{C.4})$$

The uncertainties for  $\Delta t_i$ ,  $\sigma_{th}^2$  and  $\sigma_m^2$ , are calculated as

$$\sigma_t^2 = \left(\frac{\partial t}{\partial l}\right)^2 \sigma_l^2 + \left(\frac{\partial t}{\partial v}\right)^2 \sigma_v^2 \quad (\text{C.5})$$

assuming  $\sigma_l \ll \sigma_t$ ,

$$\sigma_t^2 = \left(\frac{\partial t}{\partial v}\right)^2 \sigma_v^2 \quad (\text{C.6})$$

Referring to equation C.4,

$$\left(\frac{\partial v}{\partial E}\right)^2 = \frac{m^4}{(E_k + m)^2} \frac{1}{E_k^2 + 2E_k m} \quad (\text{C.7})$$

Taking advantage of this and that

$$\left(\frac{\partial t}{\partial v}\right)^2 = \frac{l^2}{v^4} = \frac{t^2}{v^2}, \quad (\text{C.8})$$

$$\sigma_t^2 = \left(\frac{\partial t}{\partial v}\right)^2 \left(\frac{\partial v}{\partial E}\right)^2 \sigma_E^2 \quad (\text{C.9})$$

and thus

$$\sigma_t^2 = t^2 \frac{m^4}{(E_k + m)^2 (E_k)^2 (E_k + 2m)^2} \sigma_E^2 \quad (\text{C.10})$$

Using these calculated values, a  $\chi^2$  value is calculated as

$$\chi^2 = \frac{(\Delta t_m - \Delta t_{th})^2}{\sigma_m^2 + \sigma_{th}^2} \quad (\text{C.11})$$

The probability for the hypothesis  $i$  is calculated as

$$P(\chi_i^2) = 1 - \frac{2}{\pi} \int_0^{\chi_i^2} e^{-u^2} du \quad (\text{C.12})$$

where

$$u = \frac{1}{1 + \sqrt{2\chi_i^2}} \quad (\text{C.13})$$

## Appendix D

### Neutrinoless Decay Kinetic Observables

This appendix presents observables from simulated  $0\nu\beta\beta$  Monte Carlo sets. In addition to the limit calculations specified in chapter 9, neutrinoless signals can be differentiated from the  $2\nu\beta\beta$  tail and other backgrounds by individual electron energies, energies of lowest- and highest-energy electrons, and minimum versus maximum energy distributions.

Figure D.1 shows the simulated two-electron energy distributions for the Light Majorana Exchange, Right Handed Current, and four Majoron-emitting processes. Figure D.2 displays individual electron energies for the same processes. Figures D.3 and D.3 present spectra of greater and lesser energy electrons, respectively. Distributions of minimum versus maximum energy electrons are shown in Figure D.5, and the cosine of the angle between electron tracks is presented in Figure D.6.

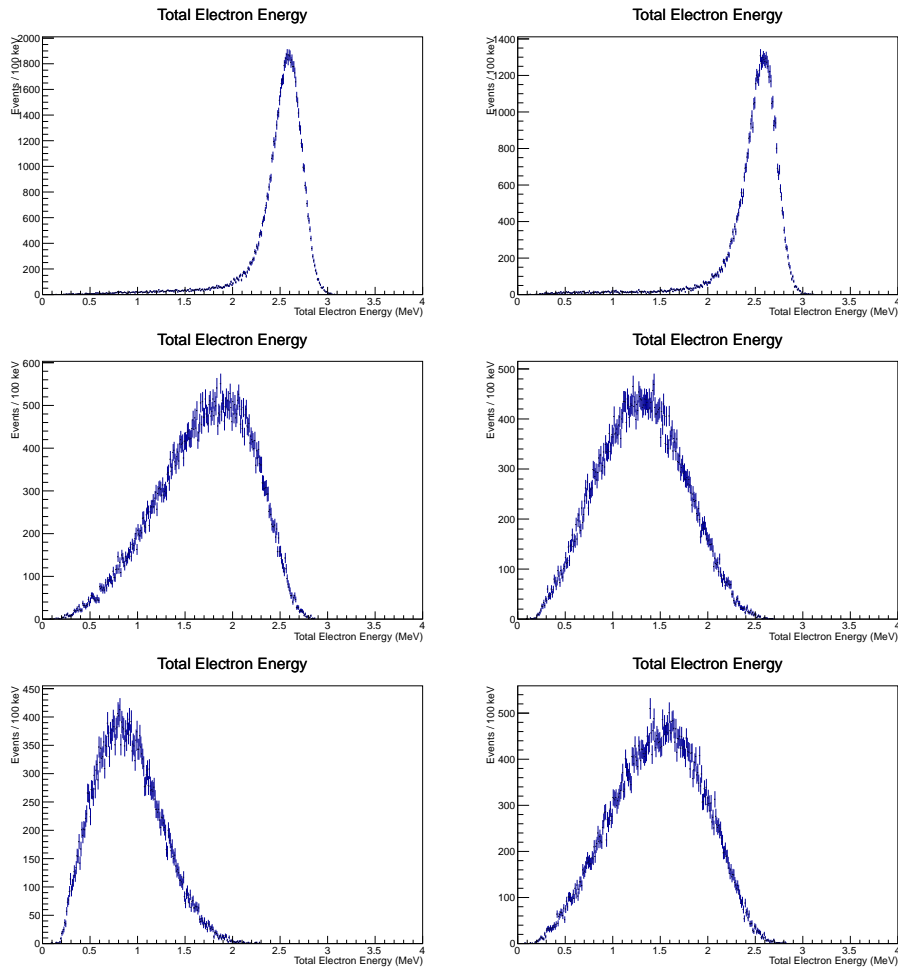


Figure D.1: Total electron energy distributions for Light Majorana Exchange, Right Handed Current, and Majoron-emitting  $0\nu\beta\beta$  models.

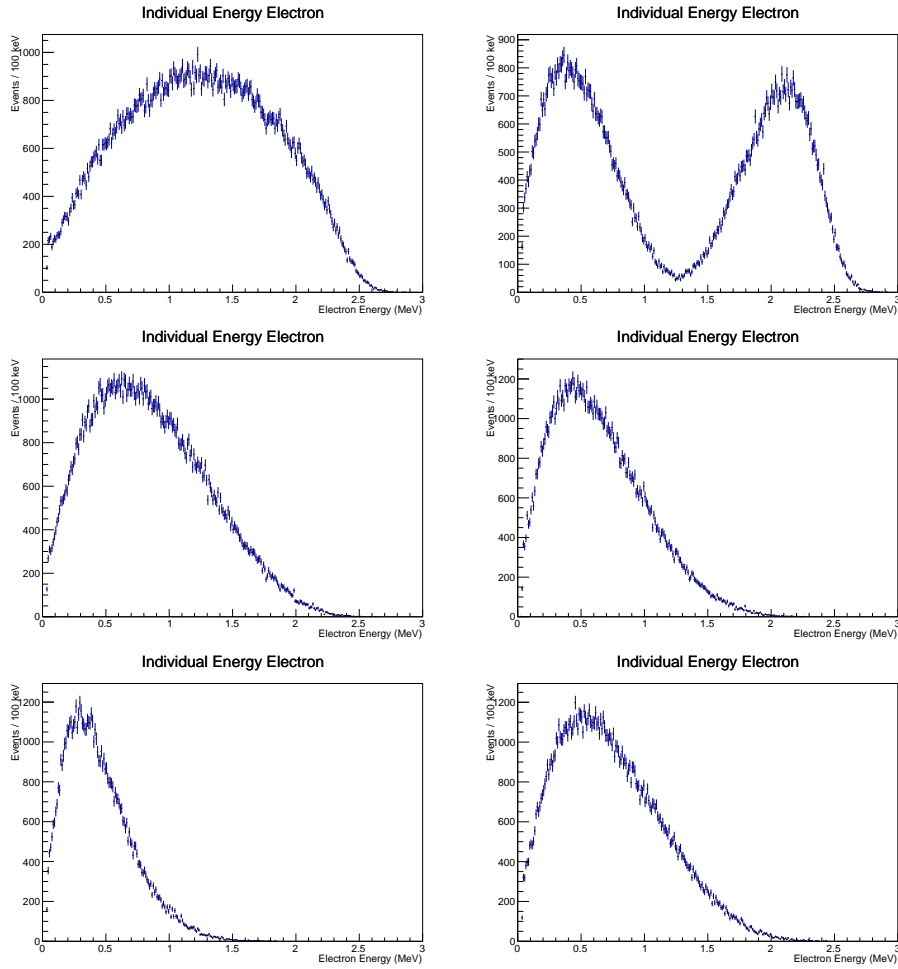


Figure D.2: Individual electron energy distributions for Light Majorana Exchange, Right Handed Current, and Majoron-emitting  $0\nu\beta\beta$  models.

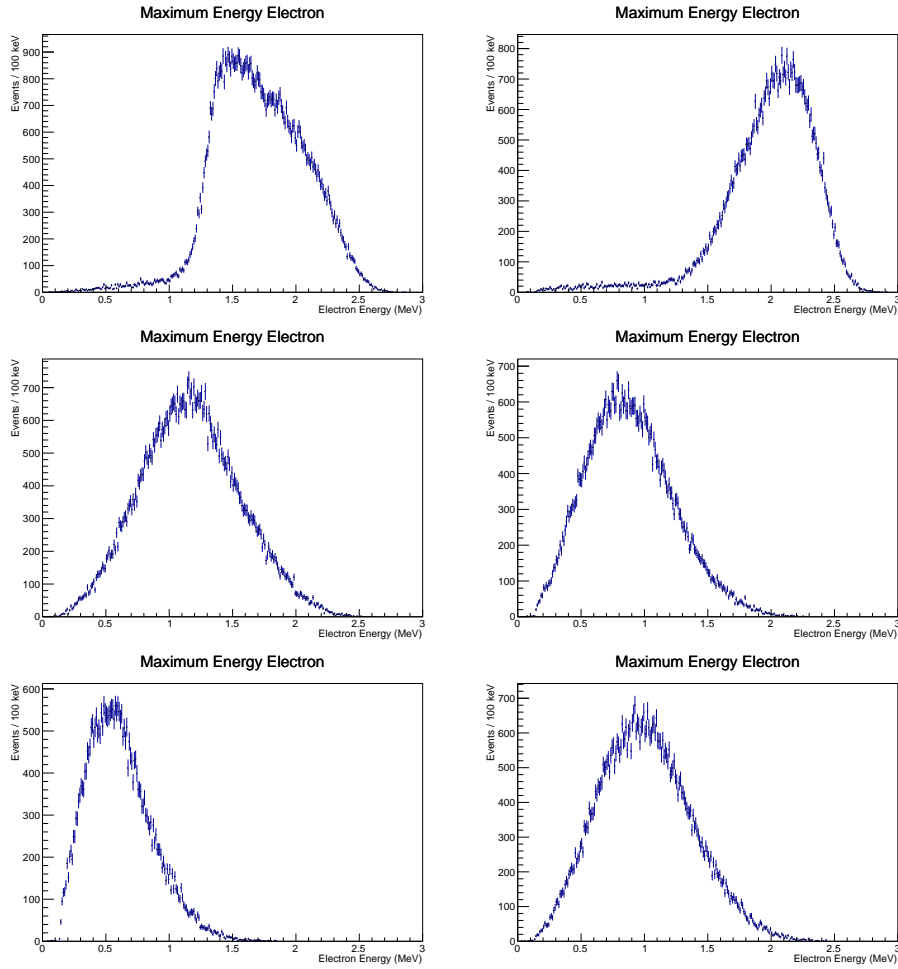


Figure D.3: Maximum electron energy distributions for Light Majorana Exchange, Right Handed Current, and Majoron-emitting  $0\nu\beta\beta$  models.

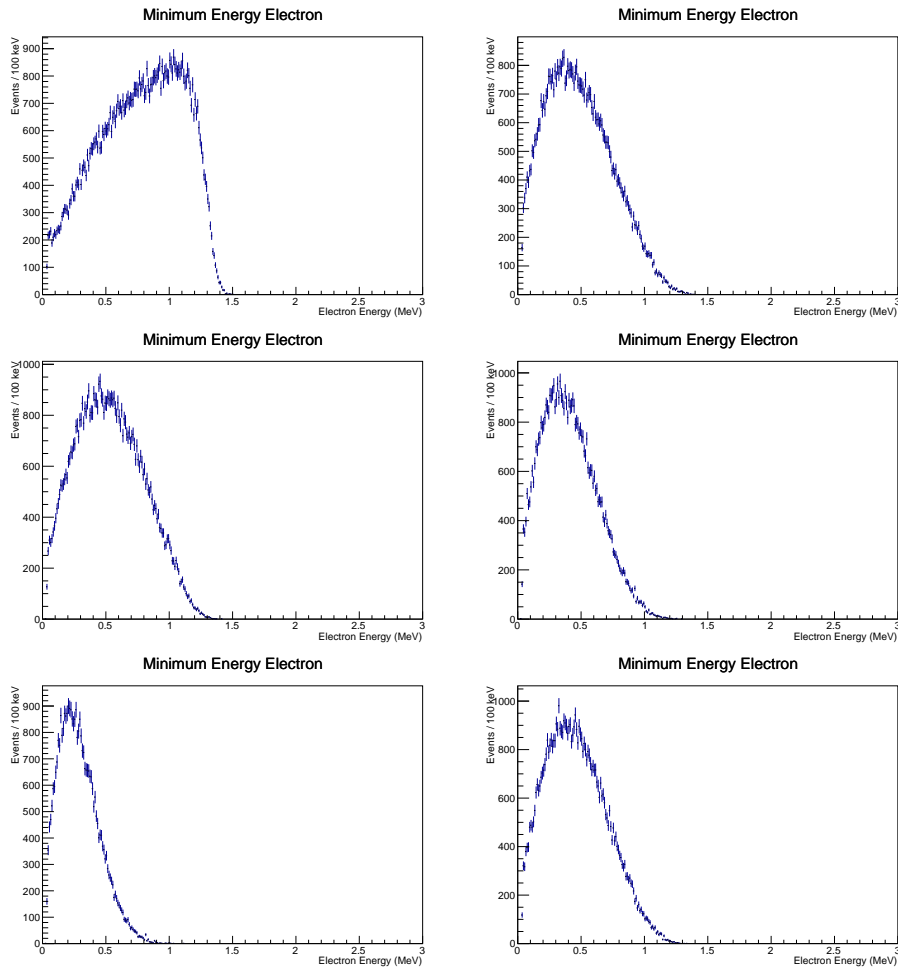


Figure D.4: Minimum electron energy distributions for Light Majorana Exchange, Right Handed Current, and Majoron-emitting  $0\nu\beta\beta$  models.

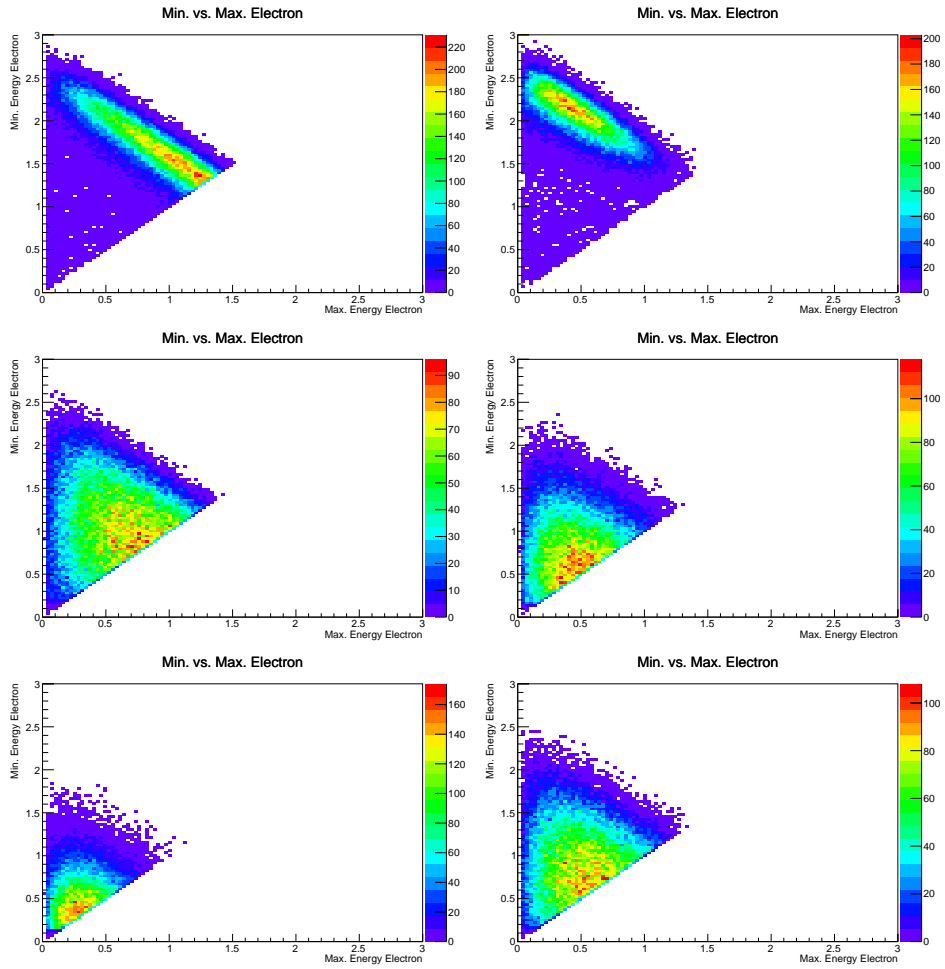


Figure D.5: Maximum vs. Minimum electron energy distributions for Light Majorana Exchange, Right Handed Current, and Majoron-emitting  $0\nu\beta\beta$  models.



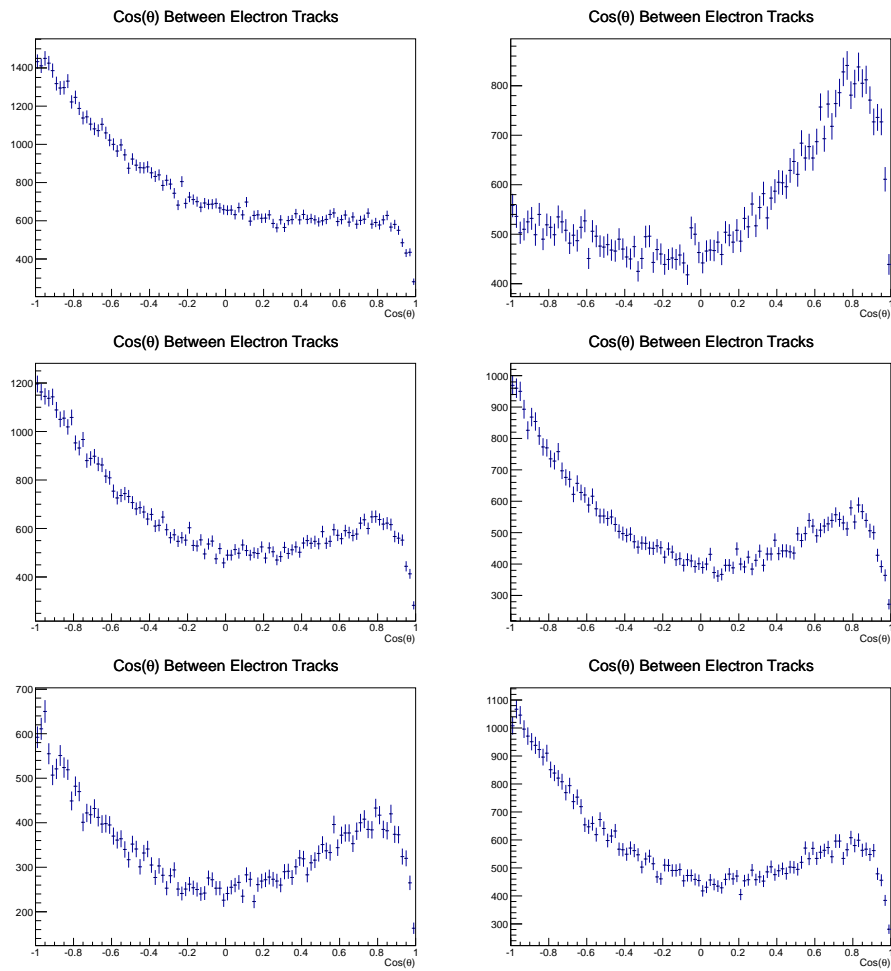


Figure D.6: Cosine between electron tracks distributions for Light Majorana Exchange, Right Handed Current, and Majoron-emitting  $0\nu\beta\beta$  models.

# Appendix E

## Cut Optimization Details

This appendix gives details of the optimization of selection cuts for the two-electron channel analysis. To minimize the chance of influencing the outcome of the overall analysis, a reduced data set consisting of every fifth file of the final data set was used. Selection criteria were considered based on the following figures of merit:

- Efficiency ( $\epsilon$ ): The fraction of signal Monte Carlo selected versus the total generated.
- Purity ( $\pi$ ): The ratio of selected signal to the sum of selected signal events  $S$  and background events  $B$  after fitting ( $\frac{S}{S+B}$ ).
- The product of efficiency and purity ( $\epsilon \times \pi$ ).
- The ratio of selected signal to background events ( $S / B$ ) after fitting.
- The ratio of selected signal to the square root of background events ( $S / \sqrt{B}$ ) after fitting.

In general,  $\epsilon \times \pi$  was considered to be the most judicious figure of merit for decisions.

Selection cut optimization was carried out by changing individual selection criteria while holding others constant. Selection was applied to the data, signal, and all background Monte Carlo. The selected data and MC sets were propagated

through the analysis as described in Chapter 4, including background calculation and signal fitting. The figures of merit described above were then calculated based on these results. Selected cuts are listed in Section 8.1.

Most selection criteria considered were based on continuous distributions such as electron energy. Selection criteria for these were applied at intervals described above each table. Several criteria, such as Geiger cell hits, were based on a discrete distribution, and cuts were applied at each available level. In addition, “binary” cuts such as electron charge selection could only be considered as with or without application of the cut.

## **E.1 Cut Descriptions and Values**

A selection cut was applied based on the minimum energy of each electron. This cut is constrained at the lower end by the resolution of NEMO-3, at approximately 200 keV. Above this level, cuts were considered in units of 100 keV. Results from this selection are shown in Table E.1.

Variable	Value	$\epsilon$	$\pi$	$\epsilon \times \pi$	Signal / Background	Signal / $\sqrt{BG}$
Minimum Single-electron Energy	200 keV	0.000503	0.913978	0.000459	10.624880	252.230115
	300 keV	0.000377	0.930459	0.000350	13.380010	245.032442
	400 keV	0.000251	0.932797	0.000234	13.880234	203.866845
	500 keV	0.000145	0.933614	0.000135	14.063438	155.733836
	600 keV	0.000145	0.933614	0.000135	14.063438	155.733836

Table E.1: Optimization details for Minimum Single-electron Energy cuts.

Internal time-of-flight probabilities are generated based on timing information from scintillators, as described in Appendix C. The listed cut is the minimum allowable calculated internal probability for the two electron tracks in the event. Results of applying this cut are presented in Table E.2.

Variable	Value	$\epsilon$	$\pi$	$\epsilon \times \pi$	Signal / Background	Signal / $\sqrt{BG}$
Internal Probability	0.1	0.000095	0.930186	0.000088	13.323863	122.584197
	0.2	0.000085	0.932101	0.000079	13.727846	117.886518
	0.3	0.000073	0.933956	0.000068	14.141323	110.659552
	0.4	0.000063	0.935405	0.000059	14.481182	104.532825
	0.5	0.000052	0.938635	0.000049	15.295834	97.576244
	0.6	0.000042	0.938684	0.000040	15.308888	87.685073

Table E.2: Optimization details for internal time-of-flight cuts.

To ensure that events originate on the foil, a selection cut was applied based on the position of the first activated Geiger cell in the tracking chamber. The selection considered events which activated cells at or before the specified layer, with layer 0 being the closest to the foil on either side. Results from this selection are shown in Table E.3.

Variable	Value	$\epsilon$	$\pi$	$\epsilon \times \pi$	Signal / Background	Signal / $\sqrt{BG}$
Minimum First Layer Geiger hit	0	0.000373	0.918268	0.000342	11.235168	223.391152
	1	0.000384	0.916595	0.000352	10.989746	224.213927
	2	0.000385	0.916440	0.000353	10.967393	224.410947

Table E.3: Optimization details for Minimum First Geiger Layer cuts.

The magnetic field oriented along the vertical ( $Z$ ) axis of NEMO-3 allowed for discrimination between electrons and positrons. Selection is based on the charge of electrons, reconstructed from their curvature in the magnetic field. The effects of this cut are shown in Table E.4. “No charge cut” denotes the case where this selection is not applied.

Variable	Value	$\epsilon$	$\pi$	$\epsilon \times \pi$	Signal / Background	Signal / $\sqrt{BG}$
Charge	Q < 0	0.000504	0.913867	0.000461	10.609913	252.417992
	no charge cut	0.000503	0.913978	0.000459	10.624880	252.230115

Table E.4: Optimization details for charge cuts.

## Appendix F

### Details of the $^{207}\text{Bi}$ Calibration Source

Measurement of  $2\nu\beta\beta$  and possible detection of  $0\nu\beta\beta$  relies heavily upon accurate measurement of electron energies, and thus a logical choice for a calibration source is a “standard candle” which consistently emits electrons at known energies. For this purpose,  $^{207}\text{Bi}$  was chosen as the calibration source for the NEMO-3 detector and each of the 20 sectors was fitted with a vertical copper tube into which sources were inserted for dedicated calibration runs [78].

$^{207}\text{Bi}$  decays via electron capture to excited states of  $^{207}\text{Pb}$ , which in turn emits internal conversion electrons, of which K lines at 482 and 976 keV are used in the absolute energy calibration.

$^{207}\text{Bi}$  decays via electron capture to the  $\frac{7}{2}^-$  (2340 keV, 7% branching ratio),  $\frac{13}{2}^+$  (1633 keV, 84.2%), and  $\frac{5}{2}^-$  (570 keV, 8.8%) excited states of  $^{207}\text{Pb}$ , with accompanying X-rays or Auger electrons. For a discussion of electron capture, see section 2.2.1. X-ray energies and branching fractions for the  $^{207}\text{Bi} \rightarrow ^{207}\text{Pb}$  decay are summarized in table F.1 [34].

The approximate binding energies of the daughter nucleus  $^{207}\text{Pb}$  ( $Z=82$ ) for the K, L, and M ( $n = 1,2,3$ ) shell electrons are presented in table F.2.

Energy (keV)	Branching Fraction
10.6	36%
72.8	22%
75.0	37%
84.9	1.6%

Table F.1: Summary of X-rays resulting from electron capture in the  $^{207}\text{Bi} \rightarrow ^{207}\text{Pb}$  decay.

A schematic of de-excitation transitions in  $^{207}\text{Pb}$  is presented in Figure F, and a summary of emitted conversion electrons is given in Table F [34, 106].



Shell	Binding Energy ( keV)
K	88
L	22
M	10

Table F.2: Binding energies for the K,L,M shell electrons of  $^{207}\text{Pb}$ .

Transition	$h\nu$	Binding Energy	Energy ( keV)	Shell	Branching Fraction
$\frac{13}{2}^- \rightarrow \frac{5}{2}^-$	1063	88	976	$e_K$	6.1%
$\frac{13}{2}^- \rightarrow \frac{5}{2}^-$	1063	22	1040	$e_L$	1.5%
$\frac{13}{2}^- \rightarrow \frac{5}{2}^-$	1063	10	1060	$e_M$	0.5%
$\frac{5}{2}^- \rightarrow \frac{1}{2}^-$	573	88	482	$e_K$	1.6%
$\frac{5}{2}^- \rightarrow \frac{1}{2}^-$	573	22	553	$e_L$	0.4%

Table F.3: Summary of conversion electrons in  $^{207}\text{Bi} \rightarrow ^{207}\text{Pb}$  decay.

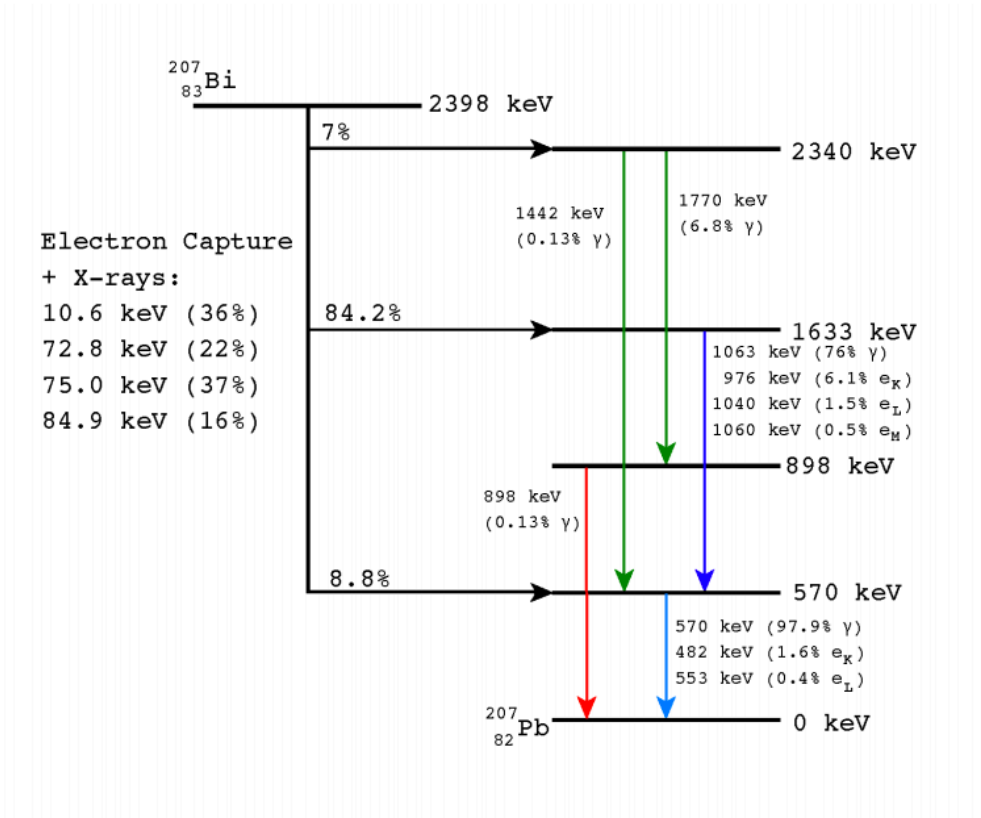


Figure F.1: Decay scheme of  $^{207}\text{Bi}$ . [107]

# Appendix G

## $^{214}\text{Bi}$ and $^{208}\text{Tl}$ decay information

### G.1 Introduction

NEMO-3 and SuperNEMO were both designed with the goal of having extremely low background radiation, a condition necessitated by the relative rarity of both the  $0\nu\beta\beta$  signal and  $2\nu\beta\beta$  decays. In addition, to understand well the systematic uncertainty from the remaining background, a thorough understanding of the background contamination is necessary, particularly in the signal region around the Q-value of each isotope.

The dominant background contribution in the  $2\beta$  energy range above 3 MeV comes from  $^{214}\text{Bi}$  and  $^{208}\text{Tl}$ . Therefore understanding the decay of these two isotopes in particular is of crucial importance to background rejection in the region of expected  $2\beta0\nu$  signal.

### G.2 Decay of $^{214}\text{Bi}$

$^{214}\text{Bi}$  contributes to the background of NEMO-3 primarily via 3 decays, shown in figure G.1:

- 3272 keV  $\beta$  decay directly to the ground state of  $^{214}\text{Po}$ .

- 1855 keV  $\beta$  decay to the 1415 keV excited state of  $^{214}\text{Po}$ , followed by a 1323 keV EC transition with a 99 ps delay.
- 1505 keV  $\beta$  decay to the 1765 keV excited state of  $^{214}\text{Po}$ , with subsequent  $\gamma$  transitions to the ground state which can be Möller scattered to mimic a second electron.

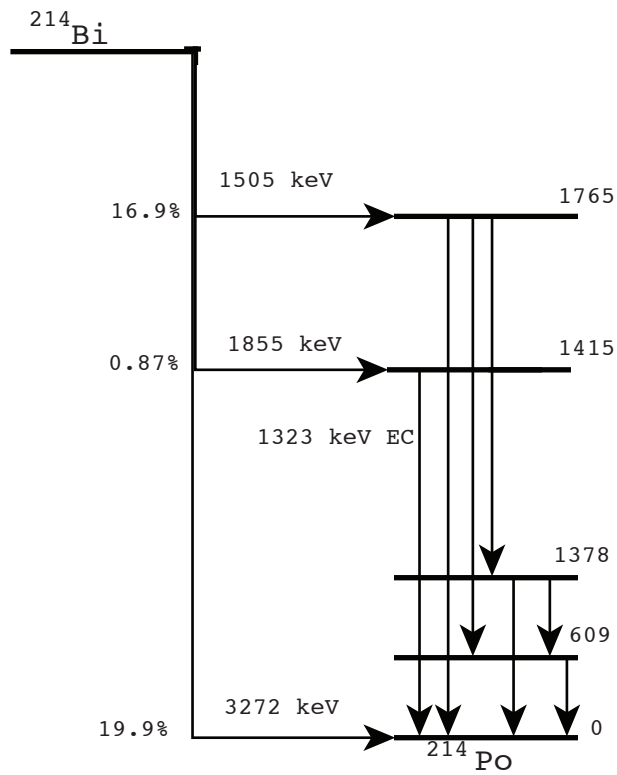


Figure G.1:  $^{214}\text{Bi}$  decays contributing background to the  $\beta\beta$  spectrum.  $\gamma$  transition energies are suppressed for clarity. [107].

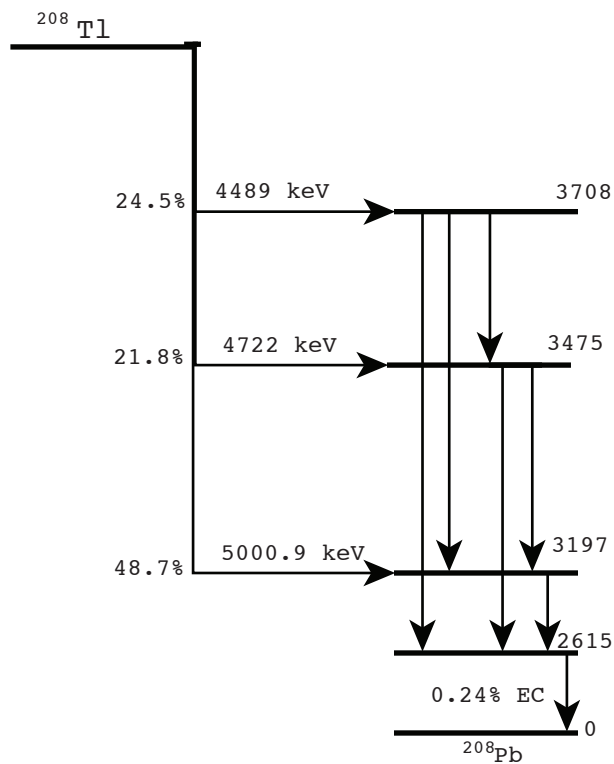


Figure G.2: Three most common decays of  $^{208}\text{Tl}$  contributing background to the  $\beta\beta$  spectrum.  $\gamma$  transition energies are suppressed for clarity [107].

### G.3 Decay of $^{208}\text{Tl}$

$^{208}\text{Tl}$  contributes to the high-energy background in NEMO-3 via a high energy  $\beta$  decay to excited states of  $^{208}\text{Po}$ , all of which  $\gamma$  transition to the 2,615 keV excited state. Decay to the ground state then has a 0.24% probability to transition to the ground state via electron capture. The three most common  $^{208}\text{Tl}\beta$  decays are shown in figure G.2.

# Appendix H

## Background Details

This appendix describes the backgrounds included in the background model for  $^{116}\text{Cd}$  and  $^{82}\text{Se}$ . Backgrounds are organized by geometric location within the NEMO-3 detector, and in order of number of expected events in the final analysis. Backgrounds are presented separately by NEMO-3 phase number and by data set.

### H.1 $^{116}\text{Cd}$

The background model for  $^{116}\text{Cd}$  is described in this section. Tables H.1, H.2, and H.3 present the background model organized by background type (internal, external, radon) and location in the detector. Table H.4 present backgrounds present in each of the  $^{116}\text{Cd}$  data sets by number of expected events.

### H.1.1 Internal Backgrounds

This section describes the model of backgrounds present in the NEMO-3 internal  $^{116}\text{Cd}$  source foil. Activities for the medium- and low-activity sections are shown separately.

Sector	Background	PI Activity (mBq)	PII Activity (mBq)	Source
Low Activity	$^{228}\text{Ac}$	0.664	0.664	HPGe
	$^{212}\text{Bi}$	0.664	0.664	
	$^{214}\text{Bi}$	0.162	0.162	
	$^{137}\text{Cs}$	1.210	1.210	x
	$^{40}\text{K}$	3.393	3.370	Fitted in 1e channel
	$^{234m}\text{Pa}$	0.260	0.260	
	$^{214}\text{Pb}$	0.162	0.162	
	$^{208}\text{Tl}$	$1.7 \times 10^{-2}$	$1.7 \times 10^{-2}$	Fitted in 1e $\gamma$ channel
Medium Activity	$^{228}\text{Ac}$	0.664	0.664	HPGe
	$^{212}\text{Bi}$	0.664	0.664	
	$^{214}\text{Bi}$	0.389	0.389	
	$^{137}\text{Cs}$	1.210	1.210	
	$^{40}\text{K}$	8.39	8.40	Fitted in 1e channel
	$^{234m}\text{Pa}$	1.010	1.010	
	$^{214}\text{Pb}$	0.389	0.389	
	$^{208}\text{Tl}$	$4.1 \times 10^{-2}$	$4.1 \times 10^{-2}$	Fitted in 1e $\gamma$ channel

Table H.1: Table of backgrounds present in the  $^{116}\text{Cd}$  foils.

## H.1.2 External Backgrounds

This section describes the model of external backgrounds measured in the NEMO-3  $^{116}\text{Cd}$  sector. Activities for the medium- and low-activity sections are shown separately.

External Backgrounds					
BG Name	Origin	Isotope	Phase I Activity (Bq)	Phase II Activity (Bq)	Source
EXBG4	Fe Shield	$^{228}\text{Ac}$	1350	1350	modelf
		$^{214}\text{Bi}$	7360	7360	BG Paper
		$^{208}\text{Tl}$	484	484	BG Paper
EXBG6	Internal Tower	$^{60}\text{Co}$	18.4	18.4	BG Paper
EXBG7	Fe Petals	$^{228}\text{Ac}$	8.54	8.54	modelf
		$^{214}\text{Bi}$	9.1	9.1	BG Paper
		$^{60}\text{Co}$	6.09	6.09	BG Paper
		$^{40}\text{K}$	100	100	BG Paper
EXBG8	$\mu$ -metal	$^{208}\text{Tl}$	3.1	3.1	BG Paper
		$^{60}\text{Co}$	14.6	14.6	BG Paper
EXBG11	PMTs	$^{228}\text{Ac}$	8.54	8.54	modelf
		$^{214}\text{Bi}$	324	324	BG Paper
		$^{40}\text{K}$	1078	1078	BG Paper
		$^{208}\text{Tl}$	27	27	BG Paper
EXBG17	Cu Petals	$^{60}\text{Co}$	47.6	47.6	BG Paper
SCII	Inner Scint.	$^{40}\text{K}$	7.59	7.59	modelf
SCIO	Outer Scint.	$^{40}\text{K}$	12.53	12.53	modelf
SCIP	Petal Scint.	$^{40}\text{K}$	1.39	1.39	modelf

Table H.2: Summary of external BG model. 'modelf' refers to default value from recorded measurement.



### H.1.3 Radon Backgrounds

This section describes the model of radon-derived backgrounds measured in the NEMO-3  $^{116}\text{Cd}$  sector. Activities for the medium- and low-activity sections are shown separately.

Radon Backgrounds					
BG Name	Origin	Isotope	Phase I Activity (Bq)	Phase II Activity (Bq)	Source
SWIRE	Wire Surfaces	$^{214}\text{Bi}$	1.21	0.198	Vera's map
		$^{210}\text{Bi}$	8.536	8.536	Vera's map
		$^{214}\text{Pb}$	1.21	0.198	Vera's map
SFOIL	Foil Surface	$^{214}\text{Bi}$	8.54	3.42	Fitted in $1e1\gamma$
		$^{210}\text{Bi}$	0.160	0.160	Vlad's note
		$^{214}\text{Pb}$	8.54	3.42	Fitted in $1e1\gamma$
SSCIN	Scintillator Surfaces	$^{214}\text{Bi}$	0.291	0.291	Vlad's note
		$^{210}\text{Bi}$	28.6	28.6	Vlad's note
		$^{214}\text{Pb}$	0.291	0.291	Vlad's note

Table H.3: Summary of Radon background model.

### H.1.4 Backgrounds Listed by Number of Events

This section presents backgrounds in the  $^{116}\text{Cd}$  sector of NEMO-3, arranged by expected number of events after selection.

Phase I low activity (Bq)			Phase I medium activity (Bq)		
Background	Exp. events	Activity	Background	Exp. events	Activity
exbg11_bi214	5.77	324.00	exbg4_tl208	8.14	484.10
exbg4_bi214	3.84	7359.30	exbg4_bi214	7.68	7359.30
sfoil_bi214	3.50	0.01590	inbg_k40	6.57	0.00339
sfoil_pb214	3.49	0.01590	sfoil_pb214	6.07	0.01590
inbg_k40	3.45	0.00339	sfoil_bi214	6.07	0.01590
exbg4_tl208	2.91	484.10	exbg11_tl208	4.53	26.95800
exbg11_tl208	2.83	26.95800	swire_bi214	42.44	0.00
inbg_ac228	2.80	0.66	inbg_ac228	3.66	0.66
exbg11_k40	2.70	1078.40	swire_pb214	35.89	0.00
swire_bi214	18.96	0.00	exbg11_k40	3.24	1078.40
inbg_bi212	1.83	0.66	inbg_bi212	2.70	0.66
inbg_bi214	1.58	0.16	inbg_pa234m	2.60	0.26
inbg_pa234m	1.44	0.26	inbg_bi214	2.55	0.16
swire_pb214	14.04	0.00	exbg7_tl208	1.26	3.07300
exbg6_co60	0.73	18.42	sfoil_bi210	1.18	0.16
sfoil_bi210	0.59	0.16	exbg11_bi214	10.49	324.00
inbg_pb214	0.42	0.16	exbg7_co60	0.96	6.09
swire_bi210	0.34	0.00	inbg_pb214	0.74	0.16
exbg7_tl208	0.32	3.07300	exbg8_co60	0.43	14.58300
exbg8_co60	0.29	14.58300	scio_k40	0.40	12.53
exbg7_k40	0.29	100.26	sscin_bi214	0.30	0.39334
exbg7_co60	0.24	6.09	exbg7_k40	0.29	100.26
exbg11_ac228	0.20	72.70800	inbg_tl208	0.27	0.02
inbg_tl208	0.16	0.02	exbg11_ac228	0.20	72.70800
sscin_bi214	0.15	0.39334	swire_bi210	0.17	0.00
exbg7_bi214	0.00	9.11600	exbg7_bi214	0.11	9.11600
exbg7_ac228	0.00	8.54300	sscin_pb214	0.06	0.39334
scii_k40	0.00	7.58940	exbg7_ac228	0.00	8.54300
sscin_bi210	0.00	31.99181	scii_k40	0.00	7.58940
scip_k40	0.00	1.39	inbg_pb211	0.00	0.00
exbg4_ac228	0.00	1345.80	sscin_bi210	0.00	31.99181
scio_k40	0.00	12.53	exbg6_co60	0.00	18.42
sscin_pb214	0.00	0.39334	scip_k40	0.00	1.39
inbg_cs137	0.00	0.00121	exbg4_ac228	0.00	1345.8
inbg_pb211	0.00	0.00	inbg_cs137	0.00	0.00121

Table H.4: Summary of backgrounds by final number of expected events in  $^{116}\text{Cd}$  for Phase I.

## H.2 $^{82}\text{Se}$

### H.2.1 Internal Backgrounds

This section describes the model of backgrounds present in the NEMO-3 internal  $^{82}\text{Se}$  source foil. Activities for the Se(I) and Se(II) sections are shown separately.

Sector	Background	PI Activity (mBq)	PII Activity (mBq)	Source
Se(I)	$^{228}\text{Ac}$	0.664	0.664	HPGe
	$^{212}\text{Bi}$	0.664	0.664	
	$^{214}\text{Bi}$	0.162	0.162	
	$^{137}\text{Cs}$	1.210	1.210	x
	$^{40}\text{K}$	3.393	3.370	Fitted in 1e channel
	$^{234m}\text{Pa}$	0.260	0.260	
	$^{214}\text{Pb}$	0.162	0.162	
	$^{208}\text{Tl}$	$1.7 \times 10^{-2}$	$1.7 \times 10^{-2}$	x
Se(II)	$^{228}\text{Ac}$	0.664	0.664	HPGe
	$^{212}\text{Bi}$	0.664	0.664	
	$^{214}\text{Bi}$	0.389	0.389	
	$^{137}\text{Cs}$	1.210	1.210	
	$^{40}\text{K}$	8.39	8.40	Fitted in 1e channel
	$^{234m}\text{Pa}$	1.010	1.010	
	$^{214}\text{Pb}$	0.389	0.389	
	$^{208}\text{Tl}$	$4.1 \times 10^{-2}$	$4.1 \times 10^{-2}$	x

## H.2.2 External Backgrounds

This section describes the model of external backgrounds measured in the NEMO-3  $^{82}\text{Se}$  sectors. Activities for the Se(I) and Se(II) sections are shown separately.

External Backgrounds					
BG Name	Origin	Isotope	Phase I Activity ( Bq)	Phase II Activity ( Bq)	Source
EXBG4	Fe Shield	$^{228}\text{Ac}$	1350	1350	modelf
		$^{214}\text{Bi}$	7360	7360	BG Paper
		$^{208}\text{Tl}$	484	484	BG Paper
EXBG6	Internal Tower	$^{60}\text{Co}$	18.4	18.4	BG Paper
EXBG7	Fe Petals	$^{228}\text{Ac}$	8.54	8.54	modelf
		$^{214}\text{Bi}$	9.1	9.1	BG Paper
		$^{60}\text{Co}$	6.09	6.09	BG Paper
		$^{40}\text{K}$	100	100	BG Paper
EXBG8	$\mu$ -metal	$^{208}\text{Tl}$	3.1	3.1	BG Paper
		$^{60}\text{Co}$	14.6	14.6	BG Paper
EXBG11	PMTs	$^{228}\text{Ac}$	8.54	8.54	modelf
		$^{214}\text{Bi}$	324	324	BG Paper
		$^{40}\text{K}$	1078	1078	BG Paper
		$^{208}\text{Tl}$	27	27	BG Paper
EXBG17	Cu Petals	$^{60}\text{Co}$	47.6	47.6	BG Paper
SCII	Inner Scint.	$^{40}\text{K}$	7.59	7.59	modelf
SCIO	Outer Scint.	$^{40}\text{K}$	12.53	12.53	modelf
SCIP	Petal Scint.	$^{40}\text{K}$	1.39	1.39	modelf

Table H.5: Summary of external BG model. 'modelf' refers to default value from recorded measurement.

### H.2.3 Radon Backgrounds

This section describes the model of radon-derived backgrounds measured in the NEMO-3  $^{82}\text{Se}$  sectors. Activities for the Se(I) and Se(II) sections are shown separately.

Radon Backgrounds					
BG Name	Origin	Isotope	Phase I Activity ( Bq)	Phase II Activity ( Bq)	Source
SWIRE	Wire Surfaces	$^{214}\text{Bi}$	1.21	0.198	Vera's map
		$^{210}\text{Bi}$	8.536	8.536	Vera's map
		$^{214}\text{Pb}$	1.21	0.198	Vera's map
SFOIL	Foil Surface	$^{214}\text{Bi}$	8.54	3.42	Fitted in $1e1\gamma$
		$^{210}\text{Bi}$	0.160	0.160	Vlad's note
		$^{214}\text{Pb}$	8.54	3.42	Fitted in $1e1\gamma$
SSCIN	Scintillator Surfaces	$^{214}\text{Bi}$	0.291	0.291	Vlad's note
		$^{210}\text{Bi}$	28.6	28.6	Vlad's note
		$^{214}\text{Pb}$	0.291	0.291	Vlad's note

## Bibliography

- [1] J. Schechter and J. Valle, “Neutrinoless Double beta Decay in  $SU(2) \times U(1)$  Theories,” *Phys.Rev.*, vol. D25, p. 2951, 1982.
- [2] J. Chadwick, “Intensitätsverteilung im magnetischen Spectrum der  $\gamma$ -Strahlen von radium B + C,” *Verh. Phys. Gesell.*, vol. 16, pp. 383–391, 1914.
- [3] E. Fermi, “Versuch einer theorie der  $\beta$ -strahlen,” *Z. Phys*, vol. 1, pp. 161–177, 1934.
- [4] F. Reines and C. L. Cowan, “A Proposed Experiment to Detect the Free Neutrino,” *Phys. Rev.*, vol. 90, pp. 492–493, 1953.
- [5] F. Reines and C. L. Cowan, “The neutrino,” *Nature*, vol. 178, pp. 446–449, 1956.
- [6] G. Danby *et al.*, “Observation of High-Energy Neutrino Reactions and the Existence of Two Kinds of Neutrinos,” *Phys. Rev. Lett.*, vol. 9, pp. 36–44, 1962.
- [7] K. Kodama *et al.*, “Final tau-neutrino results from the DONuT experiment,” *Phys. Rev.*, vol. D78, p. 052002, 2008.
- [8] M. E. Peskin and D. V. Schroeder, *An Introduction to quantum field theory*. Reading, USA: Addison-Wesley, 1995.

- [9] S. Weinberg, “A Model of Leptons,” *Phys. Rev. Lett.*, vol. 19, pp. 1264–1266, 1967.
- [10] S. L. Glashow, “Partial Symmetries of Weak Interactions,” *Nucl. Phys.*, vol. 22, pp. 579–588, 1961.
- [11] S. L. Glashow, J. Iliopoulos, and L. Maiani, “Weak Interactions with Lepton-Hadron Symmetry,” *Phys. Rev.*, vol. D2, pp. 1285–1292, 1970.
- [12] J. Goldstone, A. Salam, and S. Weinberg, “Broken Symmetries,” *Phys. Rev.*, vol. 127, pp. 965–970, 1962.
- [13] R. Davis, D. S. Harmer, and K. C. Hoffman, “Search for neutrinos from the sun,” *Phys. Rev. Lett.*, vol. 20, pp. 1205–1209, May 1968.
- [14] J. N. Bahcall, N. A. Bahcall, and G. Shaviv, “Present status of the theoretical predictions for the  $^{37}\text{Cl}$  solar-neutrino experiment,” *Phys. Rev. Lett.*, vol. 20, pp. 1209–1212, May 1968.
- [15] B. Pontecorvo, T. D. Blokhintseva, I. G. Pokrovskaya, M. G. Sapozhnikov, and S. M. Bilenky, *B. Pontecorvo selected scientific works: recollection on B. Pontecorvo*. Bologna: Societ Italiana di Fisica, 1997.
- [16] B. Pontecorvo, “Mesonium and anti-mesonium,” *Sov.Phys.JETP*, vol. 6, p. 429, 1957.
- [17] Z. Maki, M. Nakagawa, and S. Sakata, “Remarks on the unified model of elementary particles,” *Prog.Theor.Phys.*, vol. 28, pp. 870–880, 1962.

- [18] N. Cabibbo, “Unitary symmetry and leptonic decays,” *Phys. Rev. Lett.*, vol. 10, pp. 531–533, Jun 1963.
- [19] M. Kobayashi and T. Maskawa, “CP Violation in the Renormalizable Theory of Weak Interaction,” *Prog.Theor.Phys.*, vol. 49, pp. 652–657, 1973.
- [20] S. Abe *et al.*, “Precision Measurement of Neutrino Oscillation Parameters with KamLAND,” *Phys.Rev.Lett.*, vol. 100, p. 221803, 2008.
- [21] B. Aharmim *et al.*, “Combined Analysis of all Three Phases of Solar Neutrino Data from the Sudbury Neutrino Observatory,” *Phys.Rev.*, vol. C88, p. 025501, 2013.
- [22] P. Adamson *et al.*, “Measurement of Neutrino and Antineutrino Oscillations Using Beam and Atmospheric Data in MINOS,” *Phys.Rev.Lett.*, vol. 110, p. 251801, 2013.
- [23] K. Abe *et al.*, “Evidence of Electron Neutrino Appearance in a Muon Neutrino Beam,” *Phys.Rev.*, vol. D88, p. 032002, 2013.
- [24] D. M. Webber, “An Improved Measurement of Electron Antineutrino Disappearance at Daya Bay,” *Nucl.Phys.Proc.Suppl.*, vol. 233, pp. 96–101, 2012.
- [25] S. R. Elliott, “Introduction to the double-beta decay experimental program,” 2006.
- [26] S. M. Bilenky, C. Giunti, and W. Grimus, “Phenomenology of neutrino oscillations,” *Prog. Part. Nucl. Phys.*, vol. 43, pp. 1–86, 1999.



- [27] S. M. Bilenky, “Majorana neutrino mixing,” *J. Phys.*, vol. G32, p. R127, 2006.
- [28] T. Tomoda, “Double beta decay,” *Rept. Prog. Phys.*, vol. 54, pp. 53–126, 1991.
- [29] M. Blennow, E. Fernandez-Martinez, J. Lopez-Pavon, and J. Menendez, “Neutrinoless double beta decay in seesaw models,” *Journal of High Energy Physics*, vol. 2010, no. 7, pp. 1–31, 2010.
- [30] K. Zuber, “Double beta decay,” *Contemp. Phys.*, vol. 45, pp. 491–502, 2004.
- [31] W. Rodejohann, “Neutrinoless double beta decay and particle physics,” *International Journal of Modern Physics E*, vol. 20, pp. 1833–1930, 2012.
- [32] P. Marmier and E. Sheldon, *Physics of Nuclei and Particles*. 111 Fifth Avenue, New York, New York 10003: Academic Press, Inc., 1969.
- [33] S. S. M. Wong, *Introductory Nuclear Physics*. Englewood Cliffs, New Jersey 07632: Prentice Hall, 1990.
- [34] R. D. Evans, *The Atomic Nucleus*. Malabar, Florida: Krieger Publishing Company, 1955.
- [35] E. Caurier, F. Nowacki, and A. Poves, “Nuclear-structure aspects of the neutrinoless  $\beta\beta$ -decays,” *The European Physical Journal A*, vol. 36, no. 2, pp. 195–200, 2008.
- [36] M. DOI, T. KOTANI, and E. TAKASUGI, “Double beta decay and majorana neutrino,” *Progress of theoretical physics. Supplement*, pp. 1–175, mar 1986.

- [37] M. Hirsch, H. V. Klapdor-Kleingrothaus, S. G. Kovalenko, and H. Pas, “On the observability of Majoron emitting double beta decays,” *Phys. Lett.*, vol. B372, pp. 8–14, 1996.
- [38] M. Doi, T. Kotani, and E. Takasugi, “The Neutrinoless Double Beta Decay with Majoron Emission,” *Phys. Rev.*, vol. D37, p. 2575, 1988.
- [39] R. N. Mohapatra, A. Perez-Lorenzana, and C. A. de S Pires, “Neutrino mass, bulk Majoron and neutrinoless double beta decay,” *Phys. Lett.*, vol. B491, pp. 143–147, 2000.
- [40] P. Bamert, C. P. Burgess, and R. N. Mohapatra, “Multi - Majoron modes for neutrinoless double beta decay,” *Nucl. Phys.*, vol. B449, pp. 25–48, 1995.
- [41] R. Mohapatra and E. Takasugi, “Neutrinoless Double Beta Decay With Double Majoron Emission,” *Phys.Lett.*, vol. B211, p. 192, 1988.
- [42] M. Morita, *Beta Decay and Muon Capture*. Reading, Massachusetts: W. A. Benjamin, Inc., 1973.
- [43] E. Litvinova and V. Tselyaev, “Microscopic description of nuclear vibrations: Relativistic QRPA and its extensions with quasiparticle-vibration coupling,” 2013.
- [44] F. Simkovic, A. Faessler, V. Rodin, P. Vogel, and J. Engel, “Anatomy of nuclear matrix elements for neutrinoless double-beta decay,” *Phys. Rev.*, vol. C77, p. 045503, 2008.

- [45] A. Faessler, V. Rodin, and F. Simkovic, “Nuclear matrix elements for neutrinoless double-beta decay and double-electron capture,” *J.Phys.*, vol. G39, p. 124006, 2012.
- [46] J. Zofka, “Application of the hartree-fock method in nuclear theory,” *Czech. J. Phys.*, vol. 20, p. 926, 1970.
- [47] J. Barea and F. Iachello, “Neutrinoless double- $\beta$  decay in the microscopic interacting boson model,” *Phys. Rev. C*, vol. 79, p. 044301, Apr 2009.
- [48] J. Abad, A. Morales, R. Nunez-Lagos, and A. F. Pacheco, “A dynamical mechanism for the two neutrino double beta decay,” *Nuovo Cim.*, vol. A75, pp. 173–190, 1983.
- [49] R. Dvornicky, F. Simkovic, and A. Faessler, “Nuclear and particle physics aspects of the  $2\nu\beta\beta$ -decay of  $^{150}\text{Nd}$ ,” *AIP Conf. Proc.*, vol. 942, pp. 28–32, 2007.
- [50] S. V. Semenov, F. Simkovic, V. V. Khrushchev, and P. Domin, “Contribution of the lowest  $1+$  intermediate state to the  $2\nu\beta\beta$ -decay amplitude,” *Phys. Atom. Nucl.*, vol. 63, pp. 1196–1199, 2000.
- [51] O. Moreno *et al.*, “Single and low-lying states dominance in two-neutrino double-beta decay,” *J. Phys.*, vol. G36, p. 015106, 2009.
- [52] H. Akimune, H. Ejiri, M. Fujiwara, I. Daito, T. Inomata, *et al.*, “GT strengths studied by  $(\text{He-3,t})$  reactions and nuclear matrix elements for double beta decays,” *Phys.Lett.*, vol. B394, pp. 23–28, 1997.

- [53] S. Rakers *et al.*, “Low-lying GT+ strength in In-116 from a (d,He-2) reaction experiment and its implications for Cd-116 double beta decay,” *Phys. Rev.*, vol. C71, p. 054313, 2005.
- [54] H. Klapdor-Kleingrothaus, I. Krivosheina, A. Dietz, and O. Chkvorets, “Search for neutrinoless double beta decay with enriched Ge-76 in Gran Sasso 1990-2003,” *Phys.Lett.*, vol. B586, pp. 198–212, 2004.
- [55] H. V. Klapdor-Kleingrothaus, A. Dietz, H. L. Harney, and I. V. Krivosheina, “Evidence for Neutrinoless Double Beta Decay,” *Mod. Phys. Lett.*, vol. A16, pp. 2409–2420, 2001.
- [56] C. Aalseth, F. Avignone, R. Brodzinski, W. Hensley, H. Miley, *et al.*, “Recent results of the IGEX Ge-76 double-beta decay experiment,” *Phys.Atom.Nucl.*, vol. 63, pp. 1225–1228, 2000.
- [57] M. Agostini *et al.*, “Results on neutrinoless double beta decay of  $^{76}\text{Ge}$  from GERDA Phase I,” *Phys.Rev.Lett.*, vol. 111, p. 122503, 2013.
- [58] S. Umehara, T. Kishimoto, I. Ogawa, R. Hazama, H. Miyawaki, *et al.*, “Neutrinoless double-beta decay of Ca-48 studied by Ca F(2)(Eu) scintillators,” *Phys.Rev.*, vol. C78, p. 058501, 2008.
- [59] I. Ogawa *et al.*, “Study of Ca-48 double beta decay by CANDLES,” *J.Phys.Conf.Ser.*, vol. 375, p. 042018, 2012.

- [60] A. Gando *et al.*, “Limit on Neutrinoless  $\beta\beta$  Decay of Xe-136 from the First Phase of KamLAND-Zen and Comparison with the Positive Claim in Ge-76,” *Phys.Rev.Lett.*, vol. 110, no. 6, p. 062502, 2013.
- [61] V. Lozza, “Neutrinoless double beta decay search with SNO+,” *EPJ Web Conf.*, vol. 65, p. 01003, 2014.
- [62] F. C. Wellstood, C. Urbina, and J. Clarke, “Hot-electron effects in metals,” *Phys. Rev. B*, vol. 49, pp. 5942–5955, Mar 1994.
- [63] C. Arnaboldi *et al.*, “Results from a search for the  $0\nu\beta\beta$ -decay of  $^{130}\text{Te}$ ,” *Phys. Rev.*, vol. C78, p. 035502, 2008.
- [64] E. Andreotti, C. Arnaboldi, F. Avignone, M. Balata, I. Bandac, *et al.*, “ $^{130}\text{Te}$  Neutrinoless Double-Beta Decay with CUORICINO,” *Astropart.Phys.*, vol. 34, pp. 822–831, 2011.
- [65] D. Artusa *et al.*, “Searching for neutrinoless double-beta decay of  $^{130}\text{Te}$  with CUORE,” 2014.
- [66] M. Auger *et al.*, “Search for Neutrinoless Double-Beta Decay in  $^{136}\text{Xe}$  with EXO-200,” *Phys.Rev.Lett.*, vol. 109, p. 032505, 2012.
- [67] The NEXT Collaboration and others, “Present status and future perspectives of the NEXT experiment,” *arXiv*, jul 2013.
- [68] R. Winter, “Search for double beta decay in cadmium and molybdenum,” *Phys. Rev.*, vol. 99:1, p. 88, 1955.

- [69] K. Kume *et al.*, “Double beta decays of Mo-100 and Cd-116 studied by means of ELEGANT V,” (Osaka, Japan), March 1996. Prepared for 15th RCNP Osaka International Symposium on Nuclear Physics Frontiers with Electroweak Probes (FRONTIER 96): Quark Nuclear Physics with GeV Photons and Symmetry Problems.
- [70] K. Zuber, “COBRA: Double beta decay searches using CdTe detectors,” *Phys. Lett.*, vol. B519, pp. 1–7, 2001.
- [71] T. Bloxham *et al.*, “First results on double beta decay modes of Cd, Te and Zn isotopes with the COBRA experiment,” *Phys. Rev.*, vol. C76, p. 025501, 2007.
- [72] F. A. Danevich *et al.*, “Double beta decay of Cd-116. Final results of the Solotvina experiment and CAMEO project,” *Nucl. Phys. Proc. Suppl.*, vol. 138, pp. 230–232, 2005.
- [73] F. A. Danevich *et al.*, “Search for 2 beta decay of cadmium and tungsten isotopes: Final results of the Solotvina experiment,” *Phys. Rev.*, vol. C68, p. 035501, 2003.
- [74] F. A. Danevich *et al.*, “New results of  $^{116}\text{Cd}$  double beta decay study with  $^{116}\text{CdWO}_4$  scintillators,” *Phys. Rev.*, vol. C62, p. 045501, 2000.
- [75] W. Lin, O. Manuel, G. Cumming, D. Krstic, and R. Thorpe, “Geochemically Measured Half-Lives of  $^{82}\text{Se}$  and  $^{130}\text{Te}$ ,” *Nucl. Phys.*, vol. A481, pp. 477–483, 1988.

- [76] S. Elliott, A. Hahn, M. Moe, M. Nelson, and M. Vient, “Double beta decay of Se-82,” *Phys.Rev.*, vol. C46, pp. 1535–1537, 1992.
- [77] R. Arnold, C. Augier, J. Baker, A. Barabash, D. Blum, *et al.*, “Double beta decay of Zr-96,” *Nucl.Phys.*, vol. A658, pp. 299–312, 1999.
- [78] C. Augier, “Experience nemo 3 avantages et limitations: Prospective pour la physique double beta,” May 2005.
- [79] T. Bernatowicz, J. Brannon, R. Brazzle, R. Cowsik, C. Hohenberg, and F. Podosek, “Neutrino mass limits from a precise determination of  $\beta\beta$ -decay rates of  $^{128}\text{Te}$  and  $^{130}\text{Te}$ ,” *Phys. Rev. Lett.*, vol. 69, pp. 2341–2344, Oct 1992.
- [80] N. Takaoka, Y. Motomura, and K. Nagao, “Half-life of  $^{130}\text{Te}$  double- $\beta$  decay measured with geologically qualified samples,” *Phys. Rev. C*, vol. 53, pp. 1557–1561, Apr 1996.
- [81] R. Arnold *et al.*, “Double beta decay of 82se,” *Nuclear Physics A*, vol. 636, no. 2, pp. 209 – 223, 1998.
- [82] I. Vanushin, “NEMO-3 Internal memorandum on the measurements of cadmium installed in NEMO-3,” 1999.
- [83] V. Kovalenko, “Laser time corrections (ltcs) for the nemo3 data,” 2006. NEMO note IPHC&JINR-1.
- [84] J. Argyriades *et al.*, “Spectral modeling of scintillator for the NEMO-3 and SuperNEMO detectors,” *Nucl.Instrum.Meth.*, vol. A625, pp. 20–28, 2011.

- [85] O. A. Ponkratenko, V. I. Tretyak, and Y. G. Zdesenko, “The Event generator DECAY4 for simulation of double beta processes and decay of radioactive nuclei,” *Phys. Atom. Nucl.*, vol. 63, pp. 1282–1287, 2000.
- [86] “Geant detector description and simulation tool cern program library long writeup w5013.” [http://wwwasdoc.web.cern.ch/wwwasdoc/geant\\_html3/geantall.html](http://wwwasdoc.web.cern.ch/wwwasdoc/geant_html3/geantall.html), 1995. Accessed: 2014-01-23.
- [87] F. T. Avignone, III, S. R. Elliott, and J. Engel, “Double Beta Decay, Majorana Neutrinos, and Neutrino Mass,” *Rev. Mod. Phys.*, vol. 80, pp. 481–516, 2008.
- [88] O. Cremonesi, “Neutrino masses and Neutrinoless Double Beta Decay: Status and expectations,” 2010.
- [89] T. Junk, “Confidence level computation for combining searches with small statistics,” *Nucl. Inst. Meth. A*, vol. 434, p. 435, 1999.
- [90] J. Argyriades *et al.*, “Measurement of the background in the NEMO 3 double beta decay experiment,” *Nucl. Instrum. Meth.*, vol. A606, pp. 449–465, 2009.
- [91] C. Marquet *et al.*, “Influence of neutrons and gamma-rays in the Frejus underground laboratory on the NEMO experiment,” *Nucl. Instrum. Meth.*, vol. A457, pp. 487–498, 2001.
- [92] V. Chazal, R. Brissot, J. Cavaignac, B. Chambon, M. de Jesus, D. Drain, Y. Giraud-Heraud, C. Pastor, A. Stutz, and L. Vagneron, “Neutron background measurements in the underground laboratory of modane,” *Astroparticle Physics*, vol. 9, no. 2, pp. 163 – 172, 1998.



- [93] A. Nachab, “Radon monitoring in nemo3,” 2008. NEMO-3 internal memorandum.
- [94] R. Arnold *et al.*, “Technical design and performance of the NEMO 3 detector,” *Nucl. Instrum. Meth.*, vol. A536, pp. 79–122, 2005.
- [95] V. Vasiliev, “Studying nemo tracking device systematics with  $^{207}\text{Bi}$  electron source.,” 2004. NEMO-3 internal memorandum.
- [96] A. Barabash and V. Brudanin, “Investigation of double beta decay with the NEMO-3 detector,” *Phys.Atom.Nucl.*, vol. 74, pp. 312–317, 2011.
- [97] V. A. Rodin, A. Faessler, F. Simkovic, and P. Vogel, “Assessment of uncertainties in QRPA  $0\nu\beta\beta$ -decay nuclear matrix elements,” *Nucl. Phys.*, vol. A766, pp. 107–131, 2006.
- [98] V. Rodin, A. Faessler, F. Simkovic, and P. Vogel, “Uncertainties in the  $0\nu\beta\beta$ -decay nuclear matrix elements,” *Czech.J.Phys.*, vol. 56, pp. 495–503, 2006.
- [99] O. Helene, “Determination of the upper limit of a peak area,” *Nucl. Instrum. Meth.*, vol. A300, pp. 132–136, 1991.
- [100] A. Barabash, “SuperNEMO double beta decay experiment,” 2011.
- [101] I. Nasteva, “The SuperNEMO double beta decay experiment,” 2007.
- [102] S. A. *et al.* [GEANT4 Collaboration], “Geant4: A simulation toolkit,” *Nucl. Instrum. Meth. A*, vol. 506, p. 250, 2003.

- [103] “Ej-200.” [www.eljentechnology.com/index.php/component/content/article/31-general/48-ej-200](http://www.eljentechnology.com/index.php/component/content/article/31-general/48-ej-200). Accessed: 2014-01-26.
- [104] G. Lutter, “NEMO-3 internal presentation on the measurements of Proposed SuperNEMO scintillator blocks,” 2011.
- [105] F. Boehm and P. Vogel, *Physics of massive neutrinos*. Cambridge, UK: Univ. Pr., 1992.
- [106] D. Alburger and A. Sunyar, “Decay of  $\text{bi}^{207}$ ,” *Journal Name: Physical Review (U.S.) Superseded in part by Phys. Rev. A, Phys. Rev. B: Solid State, Phys. Rev. C, and Phys. Rev. D*, Aug 1955.
- [107] R. B. Firestone, *Table of Isotopes*. Lawrence Berkeley National Laboratory, University of California: John Wiley & Sons, Inc., 1996.

# Vita

Zachary John Liptak was born in Norwalk, Ohio, the son of Ronald M. Liptak and Constance S. Liptak. He received the Bachelor of Science degree in Physics and the Bachelor of Arts degree in Japanese from the University of Notre Dame. He began graduate studies in High Energy Physics at the University of Texas at Austin in June of 2009.

He currently resides at 1044 Camino la Costa #3067, Austin, TX 78752. He can be reached at [liptak@ph.utexas.edu](mailto:liptak@ph.utexas.edu).

Permanent address: 7670 Paulin Dr.  
Poland, OH 44514

This dissertation was typeset with L<sup>A</sup>T<sub>E</sub>X<sup>†</sup> by the author.

---

<sup>†</sup>L<sup>A</sup>T<sub>E</sub>X is a document preparation system developed by Leslie Lamport as a special version of Donald Knuth's T<sub>E</sub>X Program.